Electrocatalytic Refinery toward Green Production of Chemicals through N_2 and CO_2 Electroreduction

Dazhi Yao

School of Chemical Engineering and Advanced Materials

Faculty of Science, Engineering, and Technology

A thesis submitted for the degree of Doctor of Philosophy

The University of Adelaide

November 2022

Contents

Abstract

The depletion of fossil fuels and rapid environmental deterioration call for the development of clean and sustainable energy supplies for the future. Recently, the electrocatalytic refinery (e-refinery) is emerging as a more sustainable and environmentally benign strategy to harness renewable energy for the production of value-added chemicals. As the second most produced chemical in the world, ammonia has played a significant role in agriculture and chemical engineering, and now severs as one promising medium for hydrogen storage, due to its higher energy density. Thus, exploration of strategies to produce ammonia (NH_3) powered by renewable energy with decreased carbon emissions has raised widespread interests among researchers. Up till now, two main routes with lower carbon emission levels have been proposed: (1) steam methane reforming coupled Haber-Bosch process (SMR-HB) with carbon capture and storage technologies (SMR-HB + CCS) and (2) direct electrocatalytic nitrogen (N_2) reduction reaction (NRR) in aqueous conditions. For the CCS, electrocatalytic reduction of carbon dioxide (CO_2) to other carbonaceous products is regarded as the highly effective pathway. However, the difficulty to achieve these two routes is to develop electrocatalysts for effective activation and conversion of the reactants (like N_2 and CO_2). Therefore, this Thesis aims to design and synthesize novel nanostructured materials as efficient electrocatalysts for N_2 and CO_2 reduction reactions. In conjunction with the electrocatalyst engineering, detailed investigations on catalyst "structure-to-performance" correlations are also elaborated to guide the design of catalysts for future applications in other fields.

In this Thesis, a systematic review on the roadmap towards electrocatalytic green NH_3 production is provided (Chapter 2). This chapter critically evaluates the challenges of NRR and discusses several emerging strategies for green ammonia synthesis beyond conventional catalyst design and engineering, including

electrocatalytic nitrogen oxidation, electrocatalytic nitrate reduction, bio-electrocatalysis and redox-mediated electrocatalysis.

The first study of this Thesis (Chapter 3) focuses on a comprehensive and accurate evaluation of NRR performance by employing in situ fragmented bismuth nanoparticles as a promising candidate for ambient NRR. NRR performance is rigorously evaluated in both neutral and acid electrolyte through ionic chromatograph and isotope labelling testing. Online differential electrochemical mass spectrometry (DEMS) detects the production of NH_3 and N_2H_2 during NRR, suggesting a possible pathway through two-step reduction and decomposition.

The second section of this Thesis (Chapter 4 and 5) explores novel strategies for efficient CO_2 fixation to produce value-added chemicals via electrocatalytic CO_2 reduction (CRR). In/ex situ characterizations unravel the in-depth understanding on the complicated surface reconstruction of Bi-MOFs under CRR conditions, which can be controlled using electrolyte and potential mediation. The intentionally reconstructed Bi catalyst exhibits excellent activity and selectivity for formate production. It is also revealed that unsaturated surface Bi atoms are formed during reconstruction and become the active sites. The optimized CO_2-to-CO performance is achieved on the asymmetric dual-atom NiCu catalysts which are distributed within threshold distance on the N-doped graphene. The simulation results and electrocatalytic experiments unravel the inter-metal interaction with a threshold effect. The random distribution algorithm and mathematical modelling establish the relationship between diatomic distance and metal loading amount, benefiting the design of dual-atom catalysts for other electrocatalytic reactions and applications.

In the third part of this Thesis (Chapter 6), a simple and straightforward strategy based on the "adsorption-sonication" route is developed for the synthesis of noble-metal single atom catalysts (SACs) on C_3N_4, including Pd, Pt, Ag, and Au. It is found the Pt SACs on the C_3N_4 (Pt-CN) exhibit promising electrocatalytic nitrate reduction

for ammonia production. The Pt-CN achieves the maximized FE for ammonia of 80.42% at –0.45 V versus reversible hydrogen electrode (vs RHE) and the highest ammonia yield of 10.65 μmol cm^{-2} h^{-1} at –0.8 V in 0.1 M KNO$_3$/0.5 M K$_2$SO$_4$ electrolyte. This work deepens the understanding of the growth mechanism of SACs, explores some new insights into employing traditional wet chemistry in SACs preparation, and also paves the way for their future industrial production and application.

Declaration

I certify that this work contains no material which has been accepted for the award of any other degree or diploma in my name, in any university or other tertiary institution and, to the best of my knowledge and belief, contains no material previously published or written by another person, except where due reference has been made in the text. In addition, I certify that no part of this work will, in the future, be used in a submission in my name, for any other degree or diploma in any university or other tertiary institution without the prior approval of the University of Adelaide and where applicable, any partner institution responsible for the joint-award of this degree.

I acknowledge that copyright of published works contained within this thesis resides with the copyright holder(s) of those works.

I also give permission for the digital version of my thesis to be made available on the web, via the University's digital research repository, the Library Search and also through web search engines, unless permission has been granted by the University to restrict access for a period of time.

Signed: …………………………   Date: ………………………………… 28/09/20n

Acknowledgements

First and foremost, I would like to express my heartfelt gratitude to my principal supervisor, Prof. Shi-Zhang Qiao, and my co-supervisor, Dr. Cheng Tang for their patient and continuous instruction, professional supervision and enthusiastic encouragement throughout my PhD candidature. I also extend my sincere appreciation to Associate Professor Yan Jiao for her guidance on theoretical simulations. Without their ongoing support and encouragement, this Thesis would not be possible. I commend their enormous dedication to students supervision and research.

I would like to thank all group members of Professor Qiao's group for their support and assistance both in the labs and in daily life. Special thanks go to Yanzhao Zhang, Dr. Anthony Vasileff, Dr. Laiquan Li, Dr. Xing Zhi, Dr. Chaochen Xu, Dr. Pengtang Wang, and Xianlong Zhou for their huge help in my research projects, and valuable instructions on my electrocatalysis and material characterization skills. I would also extend my thanks to Dr. Fangxi Xie, Dr. Huanyu Jin, Dr. Bingquan Xia, Huan Li, Xin Xu, Junyu Zhang, and Yingjie Gao for their helpful discussions and involvement in my research and their friendship. It has been a great pleasure working alongside the intelligent and hard-working people in Prof. Qiao's group.

I feel also grateful for many research and technical staff whose work paves the crucial way for my completion of this Thesis. My deepest gratitude goes to Dr. Qiuhong Hu for her generous support with the analytical equipment, Dr. Roy Lehmann, Dr. Ay Ching Hee, Tom Wilson, David Bowler and Jason Peak for their exceptional technical skills and general support, Dr. Ashley Slattery for his TEM imaging, Philip Clements for the NMR testing, Ken Neubauer for his help with SEM, and Dr. Sarah Gilbert for her ICP-MS measurements. Many thanks go to the XPS measurement assistance from Prof. Haolan Xu, Dr. Huimin Yu and Dr. Ting Gao at the University of South

Australia (UniSA), and AFM measurement instructions from Prof. Youhong Tang at Flinders University.

My special gratitude goes to the professional staff, Dr. Bernt Johannessen from the Australian Synchrotron (ANSTO) for the generous help and professional guidance on the application of synchrotron beamline, testing and data analysis. Many thanks to the members of Adelaide University's finance and purchasing team, who assisted me a lot in all kinds of trivial issues concerning purchasing and saved valuable time for me.

I would also like to acknowledge the University of Adelaide, the China Scholarship Council (CSC) and Australia Research Council (ARC) for financial support, Adelaide microscopy and Australian Synchrotron (ANSTO) for technical support and valuable beamline grant.

Finally, my deepest appreciation goes out to my family and friends for their encouragement and support all through my studies. Thanks for my Mum, Dad, and grandparents for their forever support. Without their unconditional trust and love, I could not have completed my PhD research. And sincere gratitude goes to my friends in China and Australia for their encouragement and care, as well as affirmation, which make me feel full of hope for the future!

Chapter 1

Introduction

1.1 Project Significance

Ammonia (NH_3) is the one of the most important chemicals in our daily life, which not only serves as a source of modern agriculture (such as fertilizer) but also can be developed as a promising clean energy carrier.[1-3] For the production of ammonia in industry, Haber-Bosch (H-B) process has been the most commonly adopted strategy.[3-5] However, the H-B method consumes huge quantities of fossil fuels, and requires harsh conditions such as high temperature (400–500 °C) and high pressure (100–200 bar), which exhausts 1.4 % of global annual energy consumption and produces carbon emission to pollute the environment.[3, 5-7] Therefore, developing methods for green ammonia synthesis is of great urgency and importance.

Recently, electrocatalytic refinery (e-refinery), due to its inherent merits including using renewable and clean energy and ease of operation, has been widely employed in energy chemistry and fuel production.[8] Specifically, e-refinery represents various electrocatalytic processes that can efficiently convert renewable feedstocks (e.g., air, water, CO_2, biomass derivates) to transportable fuels (e.g., NH_3, C_2H_5OH), commodity chemicals (e.g., CO, H_2, C_2H_4, CH_3OH), and even speciality chemicals.[8] For green ammonia synthesis, in addition to direct electrocatalytic nitrogen (N_2) reduction reaction (NRR) in aqueous conditions, the electrocatalysis-coupled routes exhibit high technology readiness and low carbon emissions. Particularly, the water electrolyzer coupled HB process (eH_2O + HB), and steam methane reforming coupled HB process with carbon capture and storage technologies (SMR-HB + CCS) are two most promising routes.[9] However, the main bottleneck for employing e-refinery for green ammonia synthesis lies in the development of efficient electrocatalysts with high activity, selectivity, and stability for the desired transformation reactions. This Thesis aims at the rational design and development of efficient nanomaterials for NRR and CO_2 reduction reaction (CRR) through detailed investigations of catalyst

structure on working conditions. Combining a series of ex-situ and in-situ characterizations, as well as theoretical simulations, reaction mechanisms and "structure-to-performance" correlations are discussed and established as the principles for designing electrocatalysts, which are expected to inspire future advances in electrocatalysis and other related fields.

1.2 Research Objectives

The main goal of this Thesis is to discover promising, effective and stable electrocatalysts as the candidates to fulfil electrocatalytic N_2 and CO_2 reduction to meet different demands of the green ammonia synthetic routes. To achieve this, a combination of electrochemistry, in situ spectroscopy, theoretical computations, and material physiochemical characterizations was utilized. Specifically, the objectives were to:

- Find promising electrocatalysts for direct N_2 electroreduction (NRR).
- Investigate and modulate catalyst surface reconstruction in CRR.
- Rationally design electrocatalysts for optimized CRR performance.
- Explore indirect green ammonia synthesis via electrocatalytic nitrate reduction (NitRR).

1.3 Thesis Outline

This Thesis presents the outcomes of my PhD research and is presented as a sequence of journal publications. The Chapters in this Thesis are presented as follows:

- Chapter 1 summarizes the background of the Thesis and outlines the project scope and key contributions to the field of e-refinery for sustainable production of chemicals.
- Chapter 2 provides a review of recent literature covering the electrocatalytic green ammonia production strategies beyond the ambient aqueous synthesis.

- Chapter 3 investigates the direct ammonia electrosynthesis through electrochemical N_2 reduction based on in situ fragmented Bi electrocatalyst, and discusses the possible reaction pathway.

- Chapter 4 unravels the surface reconstruction of Bi-MOFs under the CRR working condition by combining in situ spectroscopy, ex situ scanning transmission electron microscopy (STEM) and theoretical computations.

- Chapter 5 discusses the correlation of inter-metal distance in the NiCu dual-atom catalysts with the CRR performance. New insights into the design and development of dual-atom catalysts (DACs) and their "structure-to-performance" correlation are also gained.

- Chapter 6 presents a novel and simple strategy for the fabrication of noble-metal single-atom catalysts (SACs) on the carbon-based matrix, and explores their practical application of nitrate electroreduction for ammonia production.

- Chapter 7 presents the conclusions and provides some outlooks for future work on NRR, CRR and other e-refinery reactions.

1.4 References

[1] L. Li, C. Tang, B. Xia, H. Jin, Y. Zheng, S. Z. Qiao, *ACS Catal.* 2019, *9*, 2902.

[2] J. G. Chen, R. M. Crooks, L. C. Seefeldt, K. L. Bren, R. M. Bullock, M. Y. Darensbourg, P. L. Holland, B. Hoffman, M. J. Janik, A. K. Jones, M. G. Kanatzidis, P. King, K. M. Lancaster, S. V. Lymar, P. Pfromm, W. F. Schneider, R. R. Schrock, *Science* 2018, *360*, 7.

[3] S. L. Foster, S. I. P. Bakovic, R. D. Duda, S. Maheshwari, R. D. Milton, S. D. Minteer, M. J. Janik, J. N. Renner, L. F. Greenlee, *Nat. Catal.* 2018, *1*, 490.

[4] B. H. R. Suryanto, H. L. Du, D. B. Wang, J. Chen, A. N. Simonov, D. R. MacFarlane, *Nat. Catal.* 2019, *2*, 290.

[5] C. Tang, S.-Z. Qiao, *Chem. Soc. Rev.* 2019, *48*, 3166.

[6] S. Z. Andersen, V. Čolić, S. Yang, J. A. Schwalbe, A. C. Nielander, J. M. McEnaney, K. Enemark-Rasmussen, J. G. Baker, A. R. Singh, B. A. Rohr, M. J. Statt, S. J. Blair, S. Mezzavilla, J. Kibsgaard, P. C. K. Vesborg, M. Cargnello, S. F. Bent, T. F. Jaramillo, I. E. L. Stephens, J. K. Nørskov, I. Chorkendorff, *Nature* 2019, *570*, 504.

[7] D. R. MacFarlane, P. V. Cherepanov, J. Choi, B. H. R. Suryanto, R. Y. Hodgetts, J. M. Bakker, F. M. Ferrero Vallana, A. N. Simonov, *Joule* 2020, *4*, 1186.

[8] C. Tang, Y. Zheng, M. Jaroniec, S.-Z. Qiao, *Angew. Chem. Int. Ed.* 2021, *60*, 19572.

[9] M. Wang, M. A. Khan, I. Mohsin, J. Wicks, A. H. Ip, K. Z. Sumon, C. T. Dinh, E. H. Sargent, I. D. Gates, M. G. Kibria, *Energy Environ. Sci.* 2021, *14*, 2535

Chapter 2

Literature Review: Electrocatalytic Green Ammonia Production beyond Ambient Aqueous Nitrogen Reduction

2.1 Introduction and Significance

Achieving carbon neutrality is one of the most important and challenging goals for the world during the coming decades. Ammonia, one of the world's most important chemicals, is dominantly used for fertilizer production to underpin modern agriculture, and recently attracts increasing interest as an energy-dense, carbon-neutral carrier for renewable energy. The present Haber-Bosch process for NH_3 production is energy-, emission-, and capital-intensive. Alternatively, electrocatalysis technologies have potentials for green ammonia production with decreased carbon emissions, higher compatibility with renewable energy sources, and flexible operation. Present research work dominantly focuses on the design and synthesis of efficient electrocatalysts, identification of actual catalytic active sites, and elucidation of reaction pathways and mechanism. However, such trial-and-error research cannot effectively address the intrinsic limitations from nitrogen activation and reaction system, and the achieved performance is still far from feasibility. Aiming at obvious technological and performance breakthroughs, a critical assessment and insightful discussion of new opportunities and strategies beyond catalyst design and ambient aqueous nitrogen reduction is urgently anticipated.

The combination of materials science and chemical engineering is very likely the best way to design and develop more advanced, clean and green synthesis approach. In contrast with literature that focuses on electrocatalyst design and mechanism understanding, we try to identify the right battle to fight. Starting by discussing the roadmap for the development of green ammonia production technologies, this review presents recent advances and further opportunities in the effective coupling of water electrolyzers and the Haber-Bosch synthesis loop. Some new strategies beyond materials science are also included to boost electrocatalytic nitrogen reduction performance. Besides, emerging electrocatalytic processes are discussed to close the the anthropogenic nitrogen cycle. For example, the electrocatalytic ammonia

production performance can be potentially boosted by electrolyte effect, operation pressure, Li-mediated reaction, reactor innovation, new N-transformation reactions, and redox-mediated catalysis.

Accordingly, this Chapter highlights the crucial roles and opportunites of research in materials synthesis, processing, reaction engineering and catalysis on accelerating the development of green ammonia production..

2.2 Electrocatalytic Green Ammonia Production beyond Ambient Aqueous Nitrogen Reduction

This Chapter includes work published in the journal article Chem. Eng. Sci. 2022, 257, 117735. It presents a review of recent literature covering the roadmap towards green NH_3 and critically assessing the challenges of NRR. Perspectives are focusing on several emerging strategies beyond conventional catalyst design and engineering under ambient aqueous conditions.

Statement of Authorship

Title of Paper	Electrocatalytic green ammonia production beyond ambient aqueous nitrogen reduction
Publication Status	☑ Published ☐ Accepted for Publication ☐ Submitted for Publication ☐ Unpublished and Unsubmitted work written in manuscript style
Publication Details	D. Yao, C. Tang, P. Wang, H. Cheng, H Jin, L. X. Ding, S. Z. Qiao, Chemical Engineering Science, 117735

Principal Author

Name of Principal Author (Candidate)	Dazhi Yao
Contribution to the Paper	Collected the related information, devised the idea and structure with supervisors, wrote and reviewed the manuscript.
Overall percentage (%)	70%
Certification:	This paper reports on original research I conducted during the period of my Higher Degree by Research candidature and is not subject to any obligations or contractual agreements with a third party that would constrain its inclusion in this thesis. I am the primary author of this paper.
Signature	Date 28/09/2022

Co-Author Contributions

By signing the Statement of Authorship, each author certifies that:

i.   the candidate's stated contribution to the publication is accurate (as detailed above);

ii.   permission is granted for the candidate in include the publication in the thesis; and

iii. the sum of all co-author contributions is equal to 100% less the candidate's stated contribution.

| Name of Co-Author	Cheng Tang
Contribution to the Paper	Gathered the information, discussed the framework, wrote and edited the manuscript
Signature	Date 28/09/2022

Name of Co-Author	Pengtang Wang
Contribution to the Paper	Gathered the information, wrote part of manuscript and wrote some part of the manuscript
Signature	Date 28/09/2022

Name of Co-Author	Hui Cheng		
Contribution to the Paper	Discussion and revision of manuscript		
Signature		Date	28/09/2022

Name of Co-Author	Huanyu Jin		
Contribution to the Paper	Gathered the information, wrote part of manuscript, and helped with conceptualization		
Signature		Date	28/09/2022

Name of Co-Author	Liang-Xin Ding		
Contribution to the Paper	Discussion and revision of manuscript		
Signature		Date	28/09/2022

Name of Co-Author	Shi-Zhang Qiao		
Contribution to the Paper	Supervision of the work, discussion of the whole manuscript, revision and conceptualization		
Signature		Date	28/09/2022
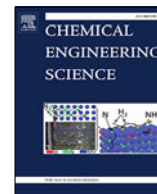
Review

Electrocatalytic green ammonia production beyond ambient aqueous nitrogen reduction

Dazhi Yao [a], Cheng Tang [a,*], Pengtang Wang [a], Hui Cheng [b], Huanyu Jin [a], Liang-Xin Ding [b], Shi-Zhang Qiao [a,*]

[a] School of Chemical Engineering and Advanced Materials, The University of Adelaide, Adelaide, SA 5005, Australia
[b] School of Chemistry and Chemical Engineering, South China University of Technology, Guangzhou 510640, China

HIGHLIGHTS

- Roadmap for the development of green ammonia production technologies.
- Effective coupling of water electrolyzers and the Haber-Bosch synthesis loop.
- Promising strategies to boost electrocatalytic nitrogen reduction performance.
- New electrocatalytic processes to close the anthropogenic nitrogen cycle.

GRAPHICAL ABSTRACT

ARTICLE INFO

ABSTRACT

Ammonia (NH_3), the second highest produced chemical in the world, is dominantly used for fertilizer production to underpin the modern agriculture, and recently attracts increasing interest as an energy-dense, carbon-neutral carrier for renewable energy. The present Haber-Bosch process for NH_3 production is energy-, emission-, and capital-intensive. Therefore, recent research efforts have been devoted to developing efficient alternatives with decreased carbon emissions, higher compatibility with renewables, and flexible operation. Electrocatalysis technologies represent a crucial role and great potentials, especially the electrocatalytic nitrogen reduction reaction (NRR). However, the achieved performance is still far from feasibility due to the intrinsic limitations from nitrogen activation and reaction system. In this Review, we first discussed the roadmap towards green NH_3, critically assessed the challenges of NRR, and then focused on several emerging strategies beyond conventional catalyst design and engineering under ambient aqueous conditions, including electrolyte effect, operation pressure, Li-mediated reaction, reactor innovation, new N-transformation reactions, and redox-mediated catalysis.

© 2022 Elsevier Ltd. All rights reserved.

Contents

* Corresponding authors.
  E-mail addresses: cheng.tang@adelaide.edu.au (C. Tang), s.qiao@adelaide.edu.au (S.-Z. Qiao).

1. Introduction

Achieving carbon neutrality is one of the most important and challenging goals for the world during the coming decades. It is crucial to help limit the long-term rise in average global temperature to well below 1.5 °C above pre-industrial levels, consistent with The Glasgow Climate Pact. Up to date, more than 130 countries have committed to carbon neutrality, and over 90% of them set a net-zero carbon emissions target by 2050. The Energy sector is the major source of global carbon emissions (>75%) and holds the key to responding to the world's climate challenge (Agency, 2021a, 2021b). In the net zero scenario, half of total energy consumption in 2050 will be supplied by electricity, and 90% of global electricity comes from renewable sources with solar and wind together accounting for ~70% (Agency, 2021b). It is noteworthy that renewable electricity is intrinsically seasonal, intermittent, remote, and geographic, leading to extensive demand for ramping flexibility and high-efficient storage and transport. Advanced batteries for electrochemical energy storage will be predominantly used to provide short-term flexibility, while energy-dense fuels need to be developed for long-term storage, seasonal balancing, and long-distance transport in the form of chemical energy (Tang et al., 2021). Although green hydrogen (H_2) produced by water electrolyzers has attracted extensive research efforts and policy support as one of the most promising carbon-free energy carriers, the high cost and safety risk for H_2 storage and transport significantly limit the development of hydrogen energy industry (Jiang and Fu, 2021).

Among various alternatives, ammonia (NH_3) shows great potential as an ideal energy-dense liquid fuel to carry green H_2 and renewable energy (ARPA-E, 2016; Li et al., 2021g; Wang et al., 2018). Advantages of NH_3 include: 1) a large hydrogen content of 17.6 wt%, 2) a high volumetric energy density of 4.32 kWh L^{-1} in liquid, 3) facile liquefaction at moderate conditions (1.0 MPa at 25 °C or 0.1 MPa at –33 °C), 4) a high safety level with much narrower explosion limit (15–28%), 5) complete industry chains and standards for NH_3 production, storage, transport and use, and; 6) catalytic decomposition to supply CO_x-free H_2 for fuel cells (Jiang and Fu, 2021; Schüth et al., 2012; Tang and Qiao, 2019). The dominant technology for artificial NH_3 synthesis nowadays is the ingenious Haber–Bosch (HB) process, which underpins the modern fertilizers and agriculture to feed half of the global population. However, the fossil fuel-based HB process consumes 1–2% of global energy and generates ~1% of global energy-related carbon emissions. Besides, to gain economic benefits at scale the NH_3 plants are centralized and in a huge size, leading to low compatibility with renewable energy. Therefore, it is highly demanded to develop decentralized, fossil fuel-free, and carbon-neutral process for green NH_3 production (Smith et al., 2020; Tang and Qiao, 2019; Wang, M. et al., 2021).

During the past few years, several promising routes have been explored to produce NH_3 with modular reactors, decreased carbon emissions, and higher compatibility with renewable electricity (MacFarlane et al., 2020; Wang, M. et al., 2021). As shown in Fig. 1, main NH_3 synthesis routes can be classified in the following sections according to the technology readiness level and carbon
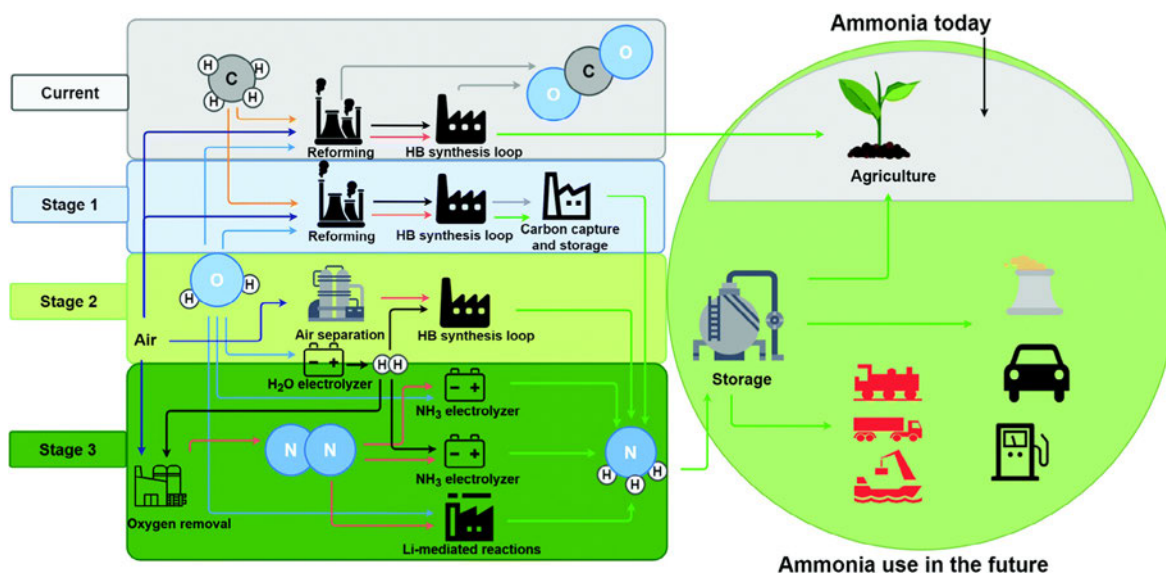

Fig. 1. The roadmap of NH_3 synthesis technologies. (Reproduced from (Wang, M. et al., 2021) with permission from The Royal Society of Chemistry).

emission level (Wang, M. et al., 2021): 1) steam methane reforming coupled HB process (SMR-HB), 2) SMR-HB with carbon capture and storage technologies (SMR-HB + CCS), 3) water electrolyzer coupled HB process (eH$_2$O + HB), 4) direct electrocatalytic nitrogen (N$_2$) reduction reaction (NRR) in aqueous conditions, 5) electrocatalytic reduction of N$_2$ with H$_2$ (H$_2$-NRR), and; 6) lithium (Li)-mediated electrocatalytic NRR (Li-NRR). The Route 3 uses water electrolyzers to replace emission-intensive SMR process for H$_2$ production, while the Routes 4–6 conduct electrocatalytic NRR at ambient conditions to replace HB process. Extensive research efforts have been devoted to these electrocatalysis processes, focusing on the design and synthesis of efficient electrocatalysts, identification of actual catalytic active sites, and elucidation of reaction pathways and mechanism (Li et al., 2021d; Qing et al., 2020; Suryanto et al., 2019). However, the achieved performance is still far from feasibility and cannot compete with the current HB process. Specifically, the electrocatalytic NRR suffers from a poor Faradaic efficiency (FE, < 30%) and low NH$_3$ yield (2–3 orders of magnitude lower than that of HB process) because of the large energy barrier for N$_2$ activation, low solubility of N$_2$ in aqueous solutions, and competing hydrogen evolution reaction (HER) (Zhao et al., 2021). Aiming at obvious technological and performance breakthroughs, a critical assessment and insightful discussion of new opportunities and strategies beyond catalysts design and ambient aqueous NRR is urgently anticipated.

To address the challenges in green NH$_3$ synthesis and dilemmas in electrocatalytic NRR, this Review critically assesses recent research efforts and emerging directions. Notably, in contrast with literatures focusing on electrocatalysts design and mechanism understanding, we try to identify the right battle to fight. For the (eH$_2$O + HB) route, we discuss the status and challenges of water electrolyzers, as well as the efficient integration with HB process. For electrocatalytic NRR, we highlight a series of intrinsically effective opportunities to boost N$_2$ activation or suppress H$_2$ evolution, from aspect of electrolyte effect, operation pressure, Li-mediated reaction, and reactor innovation. We also evaluate several new electrocatalytic processes for nitrogen fixation and green NH$_3$ synthesis, such as electrocatalytic nitrogen oxidation, electrocatalytic nitrate reduction, bioelectrocatalysis and redox-mediated electrocatalysis. We conclude by providing a broader perspective on the roles and opportunities of electrocatalysis to achieve green NH$_3$ synthesis towards carbon neutrality.

2. Green hydrogen coupled Haber–Bosch process

Using green H$_2$ from water splitting for HB NH$_3$ industry has been considered as one of the most promising hybrid synthesis approaches for clean energy storage (Dana et al., 2016; Tang et al., 2021; Wang et al., 2018). This route can directly transform the existing HB plants into green NH$_3$ industries without major disruption (Fig. 2a) (Smith et al., 2020). Although this concept is easy to propose and not new, it has only attracted considerable attention in recent years owing to the commercialization of water electrolyzers and the decline of renewable electricity price. Many companies are investing in pilot-scale (eH$_2$O + HB) plants powered by wind or solar electricity worldwide. For example, green NH$_3$ demonstration programs are currently operational in Oxford (30 kg per day, developed by Siemens) and Fukushima (20 kg per day, developed by Fukushima Renewable Energy Institute) (Brown, 2018). Yara, partnering with ENGIE, is developing a green NH$_3$ project next to their Pilbara fertilizer plant in Western Australia (Atchison, 2021). A 10 MW solar farm and electrolyzer is announced to be installed and operational by the end of 2022, producing 625 tons of green H$_2$ and 3,500 tons of green NH$_3$ annually.

The success of such green NH$_3$ industry relies on 1) increased energy efficiency of water electrolyzers and 2) small-scale, distributed and agile HB loop process (Smith et al., 2020). Today, various water electrolyzers are commercially available from many companies such as Siemens, Cummins, Proton Onsite, and Nel Hydrogen (Buttler and Spliethoff, 2018), which have successfully reached MW-scale power capacity at > 1000 Nm^3 h^{-1} per stack. Compared to other kinds of electrolyzers, proton exchange membrane (PEM) electrolyzers show a lot of advantages such as the compact and modular design, high current density, high system efficiency, fast response, dynamic operation, and high H$_2$ purity. However, the cost competitiveness is still limited by the high price of green H$_2$ production. Currently, renewable-powered water electrolyzers run at > US\$4 per kg of H$_2$, three times more expensive than SMR process (US\$1.3–1.5 per kg of H$_2$) (Lagadec and Grimaud, 2020). The cost is expected to be substantially decreased in 2030 with larger PEM scales (~US\$0.5 M MW^{-1}), improved performance (3 A cm^{-2} at 1.8 V), and cheaper renewable electricity (<US\$0.02 kWh^{-1}) (Peterson et al., 2020; Wang, M. et al., 2021). A most recent study revealed that the replacement of SMR process by renewable-powered water electrolyzer can significantly
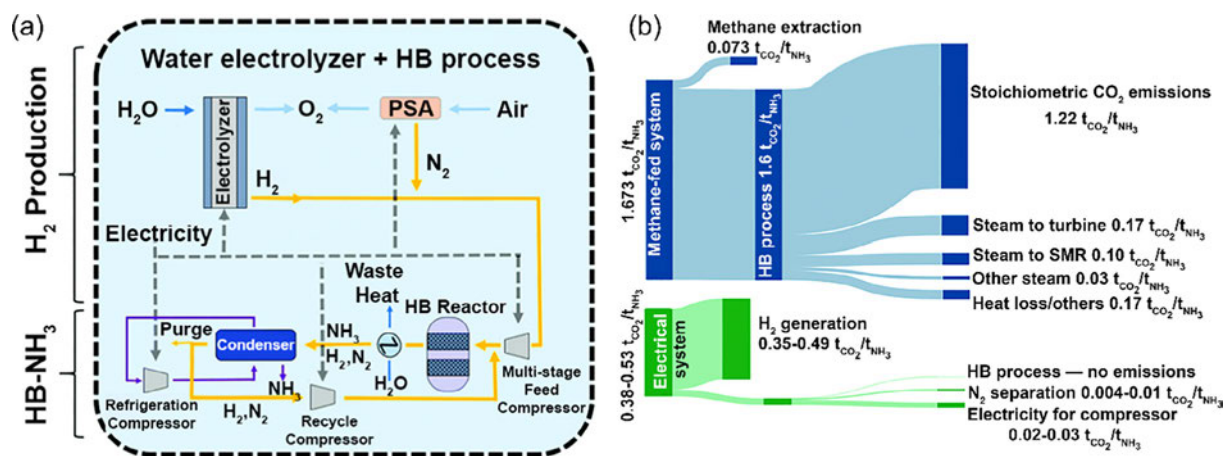

Fig. 2. Green H$_2$ coupled HB process for green NH$_3$ synthesis. (a) Schematic of the (eH$_2$O + HB) process with H$_2$ and NH$_3$ production stages. (b) Sankey diagram showing the attributions of direct CO$_2$-eq emissions arising from the (eH$_2$O + HB) process. (Reproduced from (Smith et al., 2020) with permission from The Royal Society of Chemistry). (For interpretation of the references to colour in this figure legend, the reader is referred to the web version of this article.)

decrease the associated CO_2 emissions for NH_3 manufacturing by ~75% from 1.5 to 0.38 tons of CO_2 per ton of NH_3 (Fig. 2b) (Smith et al., 2020).

Furthermore, the use of renewable electricity and PEM-based green H_2 systems provides new opportunities to optimize the coupled HB synthesis loop (Smith et al., 2020). The high purity and pressure (~80 bar) of produced H_2 make the purge, gas compression, and electronic motors unnecessary, thus increasing the energy efficiency of the HB synthesis loop by 50% (~4.2 GJ per ton of NH_3). The conventional HB process is typically operated continuously to prevent the damage of catalysts; however, the intermittency of renewable electricity from wind or solar demands a dynamic operation of PEM electrolyzers and HB synthesis loop. Therefore, in addition to improving the energy efficiency of water splitting, more efforts are required to explore advanced HB processes with lower pressure, alternative ammonia separation techniques, faster response time, smaller scale, and less capital (Smith et al., 2020).

3. Promising opportunities to enhance direct electrocatalytic NRR

To improve the electrocatalytic activity and selectivity of NRR, previous research efforts dominantly focus on exploring new electrocatalysts and optimizing their electronic structures (Cui et al., 2018; Li et al., 2019a; Qing et al., 2020; Suryanto et al., 2019; Tang and Qiao, 2019; Yao et al., 2020). However, the resulting performance enhancement is still highly restricted due to the ultralow solubility of N_2 in aqueous electrolyte, large energy barrier for N≡N bond dissociation, and highly active HER competition (Cai et al., 2021; Lazouski et al., 2019). With the deepening of mechanism study and advance in electrochemical technologies, more effective and targeted approaches beyond electrocatalysts design have been proposed, including the engineering of electrolytes,

implementation of new N_2 reduction mechanism, and operation of NRR under more favourable conditions and devices.

3.1. Non-aqueous electrolyte and ion effects

Optimization of electrolyte can readily enhance N_2 solubility and discriminatively regulate NRR/HER activity (Cui et al., 2018; Tang and Qiao, 2019). By choosing different solvents, the solubility, diffusion and mass transport of N_2 could be greatly altered (Battino et al., 1984; Liu et al., 2019). The modulation of proton transport/-supply to anode can favourably promote NRR with inhibited HER (Liu et al., 2021; Zhou et al., 2017).

Using non-aqueous solvent–water hybrid electrolyte is one promising method to promote NRR performance. Compared with water, alcohols feature a relatively low proton-donating ability (Ashida et al., 2019; Nedić et al., 2011) and higher N_2 solubility (Jia et al., 2019). The methanol–water electrolyte with water volumetric content of 0.16% (Ren et al., 2021) and 2-propanol–water electrolyte with water volumetric content of 10% (Kim et al., 2016) were employed in previous works to successfully achieve high FE towards NH_3 formation. With modulated local proton concentration and microenvironment (Fig. 3a), the methanol–water electrolyte enabled a record high FE of 75.9 ± 4.1% and NH_3 yield of 262.5 ± 7.3 g $g_{cat}^{-1}h^{-1}$, nearly 8-fold enhanced compared with that in aqueous electrolytes (Ren et al., 2021). Furthermore, the NRR performance was revealed to exhibit a volcano-like relationship with the proton-donating ability of solvents (Fig. 3b). However, electro-reduction of alcohols to form alkoxides (e.g., CH_3O^-) and H_2 appears to be common for alcohol–water hybrid systems, indicating the importance of addressing stability issues (Kim et al., 2016). Different from conventional solvents, ionic liquids (ILs) totally consist of anions and cations by ionic bonds and exhibit liquid state under ambient conditions (Zhou et al., 2017). ILs possess many advantages as electrochemical electrolytes, including a wide
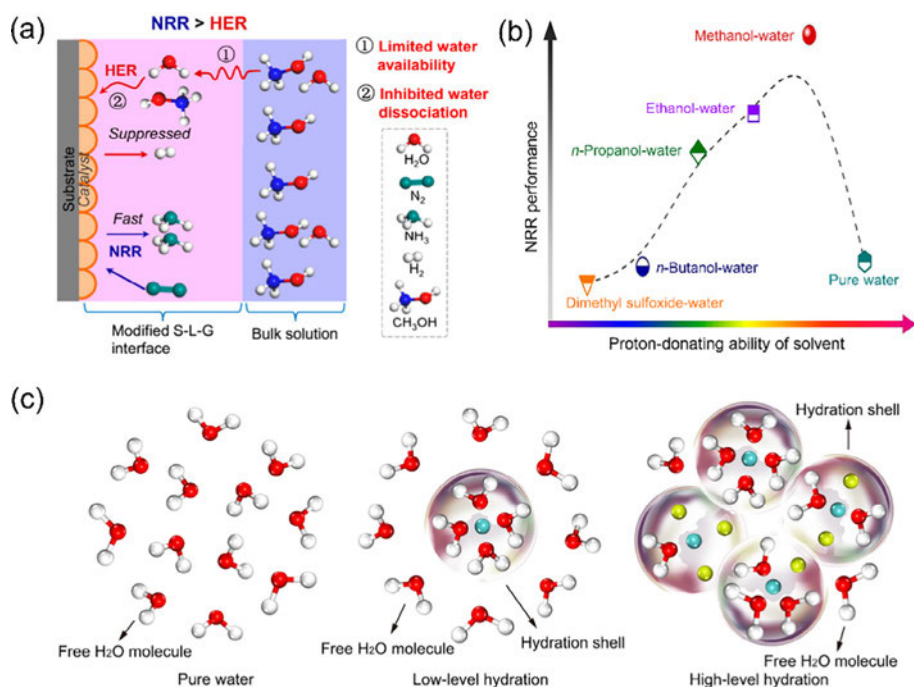

Fig. 3. Non-aqueous electrolyte and ion effects to enhance direct electrocatalytic NRR. (a) Schematic of NRR and HER processes at the solid-liquid-gas interface of methanol–water electrolyte. (b) Volcano-like correlation between NRR activity and different electrolytes with various proton-donating ability. (Reproduced from (Ren et al., 2021) with permission from American Chemical Society). (c) Illustration of hydration shells in pure water, a low-level hydration system, and a high-level hydration system. The cyan, yellow, red, and white spheres represent Li, Cl, O, and H atoms, respectively. (Reproduced from (Wang et al., 2021c) with permission from Springer Nature). (For interpretation of the references to colour in this figure legend, the reader is referred to the web version of this article.)

electrochemical window, non-volatility, high conductivity, and high stability (Liu et al., 2010; Quinn et al., 2002; Rosen et al., 2011). In addition, N_2 is more soluble in ILs than in pure water (Battino et al., 1984; Suryanto et al., 2018), and fluorination of ILs can further improve the mole fraction solubility of N_2 (Kang et al., 2019; Zhang et al., 2018). Inspired by these unique merits, a hydrophobic, highly N_2-soluble, and fluorinated IL was designed for NRR, rendering a high NH_3 FE of 60% on a nanostructured Fe catalyst under ambient conditions (Zhou et al., 2017).

The composition and concentration of supporting electrolyte, namely ion effects, also influence the electrocatalytic NRR performance. For example, potassium cations (K^+) were reported to promote NRR performance over bismuth (Bi) catalysts and noble metallic catalysts including Au, Ag and Pt (Gao et al., 2019; Hao et al., 2019). Density functional theory (DFT) computations revealed that K^+ ions lowered the energy barrier required by the potential-determining step over Bi catalysts. Simultaneously, proton transfer could be retarded in the presence of high-concentration K^+, which would be concentrated near the catalyst surface (Hao et al., 2019). The influence of high-concentration solute ions was further investigated recently by combining molecular dynamics simulations, *in situ* Fourier transform infrared (FTIR), *in situ* X-ray diffraction (XRD), and *in situ* Raman spectra (Wang et al., 2021c). In the aqueous 10 M LiCl electrolyte, N_2 was ideally enriched within the Stern layer and only finite free-H_2O molecules were available with others involved in lithium hydration (Fig. 3c). The balance between N_2 supply and proton activity obtained a superior NH_3 FE of 71 ± 1.9% and yield of $(9.5 ± 0.4) × 10^{-10}$ mol cm^{-2} s^{-1} at −0.3 V vs. reversible hydrogen electrode (RHE).

In fact, considering the complexity of electrolyte/electrode interface and impurities in chemicals, some "false-positive" results may be unconsciously obtained (Choi et al., 2020; Li et al., 2019b). Some co-existing ions from the supporting electrolyte and the leached ions from catalysts reconstruction lead to the exaggerated and erroneous ammonia yield (Zhao et al., 2019). Also, the pH of the electrolyte solution, reaction time, and the linear range of ammonia quantification need to be carefully evaluated before determination (Yao et al., 2020; Zhao et al., 2019). Other external strategies including gas cleaning by acid trap and pre-catalysis under Argon, combined with isotope labelling nuclear magnetic resonance (NMR) verification, are recommended to conduct as an protocol for standard NRR tests (Andersen et al., 2019; Choi et al., 2020; Iriawan et al., 2021; Tang and Qiao, 2019). Therefore, the rigid operation for NRR experiments is a prerequisite to understand the ion effect for NRR with direct and solid evidence to confirm the roles of specific ion engagement.

The introduction of non-aqueous electrolyte, especially the organic solvents, obstacles the ammonia separation from the reaction system and their industrial-scale application. Additionally, changes in solvent polarity have a non-negligible effect on UV–Vis assays, further hindering the accurate quantification of ammonia yield (Liang et al., 2016; Lazouski et al., 2019; Zhao et al., 2019). For ILs electrolyte, it is still challenging to find desirable ILs with matched electrochemical potential window for NRR, without leaving influence on the ammonia production and determination simultaneously (McEnaney et al., 2017; Ong et al., 2011; Zhou et al., 2017). The stability of ILs, especially under electrical field, needs to be investigated before application (McEnaney et al., 2017; Zhou et al., 2017). More importantly, the viscosity of ILs is usually dependent on the change of temperature (Ghatee et al., 2010), which will affect the N_2 diffusion and mass transfer in the ILs. Furthermore, the techno-economic assessment of ILs needs to be taken into consideration for the actual application (Gnahm and Kolb, 2011; Zhang et al., 2012; Plechkova and Seddon, 2008), including synthesis of ILs with specific cations and anions, purification and pre-treatment, and recyclability. Therefore, it is important

to choose a suitable quantification method for different reaction systems, and there is a long way to go for industrial-scale application of non-aqueous NRR.

3.2. Lithium-mediated NRR

Due to the highly negative standard reduction potential of lithium (Li^+/Li, −3.04 V vs. standard hydrogen electrode), Li can easily dissociate N≡N bonds under ambient conditions. Therefore, Li-mediated nitrogen activation offers a novel and promising pathway for NH_3 electrosynthesis (Li et al., 2021d). In 1993, this concept was first demonstrated via electrolysis with a near-aprotic solvent as follows (Tsuneto et al., 1993): 1) plating out metallic Li from a Li-salt, 2) as-deposited Li reacting with N_2 to form Li_3N, and 3) Li_3N protonation to generate NH_3 by a suitable proton source. However, the current efficiency for NH_3 production on this proposed model is still a major problem, together with the poor cyclicity and limited mechanism understanding (Li et al., 2021b). Recent efforts have been endeavoured to enhance the Li-mediated ammonia electrosynthesis from the perspective of above-mentioned three steps.

Lithium plating is favourable in non-aqueous media due to the vigorous reaction between metallic Li and water ($Li + H_2O → LiOH + 1/2 H_2$). For example, propylene carbonate (PC) was used for Li deposition, complemented with aqueous anodic electrolyte through an expensive Li^+-conducting glass ceramic material (LISICON) (Kim et al., 2018). After Li nitridation in N_2 and Li_3N hydrolysis in diluted sulfuric acid, NH_4^+ was formed with a high FE of 52.3%. This system was further optimized by polymethyl methacrylate (PMMA) reinforcement to improve the immiscibility and avoid using expensive LISICON membranes (Kim et al., 2019). Alternatively, LiOH electrolysis in a LiCl–KCl/LiOH–LiCl controlled molten salt mixture was proposed to yield high efficiency for Li production (Fig. 4a) (McEnaney et al., 2017). The absence of protons and carbonates mitigated both by-products (e.g., Li_2CO_3) and HER, leading to a high overall current efficiency of 88.5% to NH_3. Tetrahydrofuran (THF) electrolyte with lithium salts and additional proton sources (e.g., ethanol) was also widely used for Li-mediated NRR (Lazouski et al., 2020; Lazouski et al., 2019; Li et al., 2021b; Suryanto et al., 2021).

The reaction rate of Li_3N formation also plays a crucial role on enhancing NRR activity. It was noticed that NH_3 yields increased at higher partial pressures of N_2 (Tsuneto et al., 1994). The formation of Li_3N was revealed to be the rate-limiting step for NH_3 production, and the reaction rate exhibited a first order dependence on N_2 with N_2 transport limitations at higher current densities (Fig. 4b) (Lazouski et al., 2019). It was also verified by another simple kinetic model (Schwalbe et al., 2020), that increasing the mass transport of N_2 led to a much higher FE for NH_3 formation. Therefore, the use of gas diffusion electrodes to improve N_2 transport provides promising enhancement for Li-mediated electrocatalytic NRR system (Lazouski et al., 2020).

The choice of proton sources for Li_3N protonation significantly affects the long-term stability of Li-mediated routine (Andersen et al., 2020; Lazouski et al., 2020). Ethanol was first used as a sacrificial proton donor (Tsuneto et al., 1993), but solvent decomposition was suggested to occur alongside the ethanolysis of Li_3N and thus restrict continuous operation. With an ingenious design of anode reaction and reactor configuration, ethanol can be regenerated from the ethoxide by protons produced from H_2 oxidation reaction (HOR) at the anode (Lazouski et al., 2020). LiCl–KCl–CsCl eutectic mixture (Murakami et al., 2003) and phosphate molten salt electrolyte (Musgrave et al., 2021) can also bind protons, thus providing high diffusion rates in favour of N—H bond formation. A phosphonium salt-based proton shuttle was devised to solve the long-term stability of proton sources (Suryanto et al., 2021). As
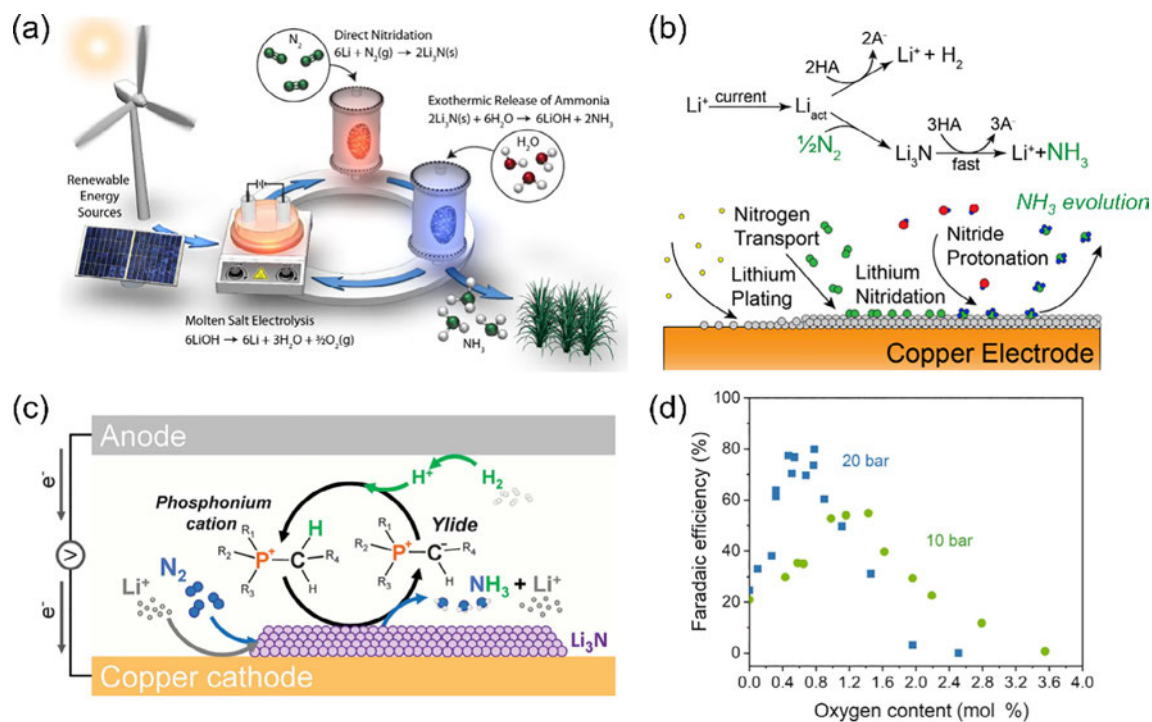
Fig. 4. Lithium-mediated NRR. (a) Schematic of Li deposition by molten salt electrolysis. (Reproduced from (McEnaney et al., 2017) with permission from The Royal Society of Chemistry). (b) Schematic of the kinetic studies and chemistry of Li-mediated NRR. (Reproduced from (Lazouski et al., 2019) with permission from Elsevier). (c) Schematic of Li-mediated NRR based on a phosphonium proton shuttle. (Reproduced from (Suryanto et al., 2021) with permission from AAAS). (d) Influence of oxygen content on the resulting FE for NH_3 electrosynthesis. (Reproduced from (Li et al., 2021b) with permission from AAAS).

shown in Fig. 4c, the phosphonium cation stably shuttled the HOR-derived protons from the anode and then donated them to reduced nitrogen at the cathode to form an ylide and release NH_3. As the proton shuttle was not consumed in NRR, 20-hour stability was achieved with a significant NH_3 yield of 53 ± 1 nmol cm^{-2} s^{-1} and a high FE of $69 \pm 1\%$.

Besides the factors on the reaction-based process, other physical practices to enhance activity and stability of Li-mediated NRR have been studied, including increase of the electrode area (Li et al., 2022), and implementation of continuous (Lazouski et al., 2019) or cycling procedures (McEnaney et al., 2017). Notably, contaminations in the feeding N_2 may have a counterintuitively positive effect on both the FE and the stability of NRR, which also sheds light on the underlying mechanism. Most recently, it was reported that adding 0.6 to 0.8 mol% O_2 into 20 bar of N_2 achieved a record-high NH_3 FE of up to $78.0 \pm 1.3\%$ (Fig. 4d) (Li et al., 2021b). Inspired by studies in Li–air batteries and supported by theoretical microkinetic modelling, such enhancement was ascribed to the decreased Li diffusion rate through the solid electrolyte interface (SEI) layer formed in the presence of O_2. XRD and X-ray photoelectron spectroscopy (XPS) analysis revealed that O_2 induced the formation of a more homogeneous and uniform SEI layer for increased cyclability and stability.

Despite these advances, the Li-mediated NRR system is not ideal. The sensitivity of Li to water and oxygen requires harsh operation conditions and limits its application to the non-aqueous system. All reagents must be carefully pre-treated and employed in the glove box if needed (Andersen et al., 2019). According to the REFUEL program of the US Department of Energy, the target for ammonia electrosynthesis is a FE of 90% at 300 mA cm^{-2} and an energy efficiency (EE) of 60% (ARPA-E, 2016; Li et al., 2021b). However, the present system could only achieve a low EE (~26% assuming 80% of FE) far from the practical application (Li et al., 2021b). Long-term stability and recycling need to be improved due to the

irreversible Li loss during the reaction (Li et al., 2021d). The variation and vague understanding on SEI layer also hinders the optimization of stability and performance of the whole NRR system (Li et al., 2021d; McEnaney et al., 2017; Westhead et al., 2021). Hopefully, with the development of characterization tools and battery science, the stability and effectiveness of Li-mediated NRR could be facilitated to the practical application scale (Li et al., 2021b; Westhead et al., 2021).

3.3. NRR under pressure

As the concentration of N_2, as a reactant, in aqueous solution is very low, the adsorption efficiency of N_2 on catalyst during electrolysis will be severely reduced compared with that of protons or H_2O involved in HER, resulting in inhibited NH_3 yield and FE. According to the Henry's law, the solubility of a gas in liquid is proportion to the equilibrium partial pressure of the gas. Therefore, the dissolved N_2 concentration in water and N_2 supply to catalyst surface is expected to be increased under higher partial pressure of N_2. It is an emerging and promising research direction for electrocatalytic NRR under pressure, but also a new challenge (Cheng et al., 2019; Zou et al., 2020).

The primary challenge for breakthrough of pressurized NRR is the rational design and assembly of electrochemical cell devices with pressure. In 2019, it was realized for the first time by moving the routine reactor directly into the pressurized kettle in the form of an open system (Cheng et al., 2019). The pressurized environment can promote the dissolution of N_2, accelerate the $N\equiv N$ bond activation, and inhibit the competing HER (Fig. 5a). Compared with atmospheric pressure conditions, the NRR performance under N_2 pressure of 0.7 MPa was improved with the maximum NH_3 yield increased from 13.10 to 13.55 μg cm^{-2}h^{-1}, and maximum NH_3 FE from 0.26% to 14.74% (Fig. 5b). With a well-designed integrated pressurized electrolytic cell (Fig. 5c), the N_2 pressure can be
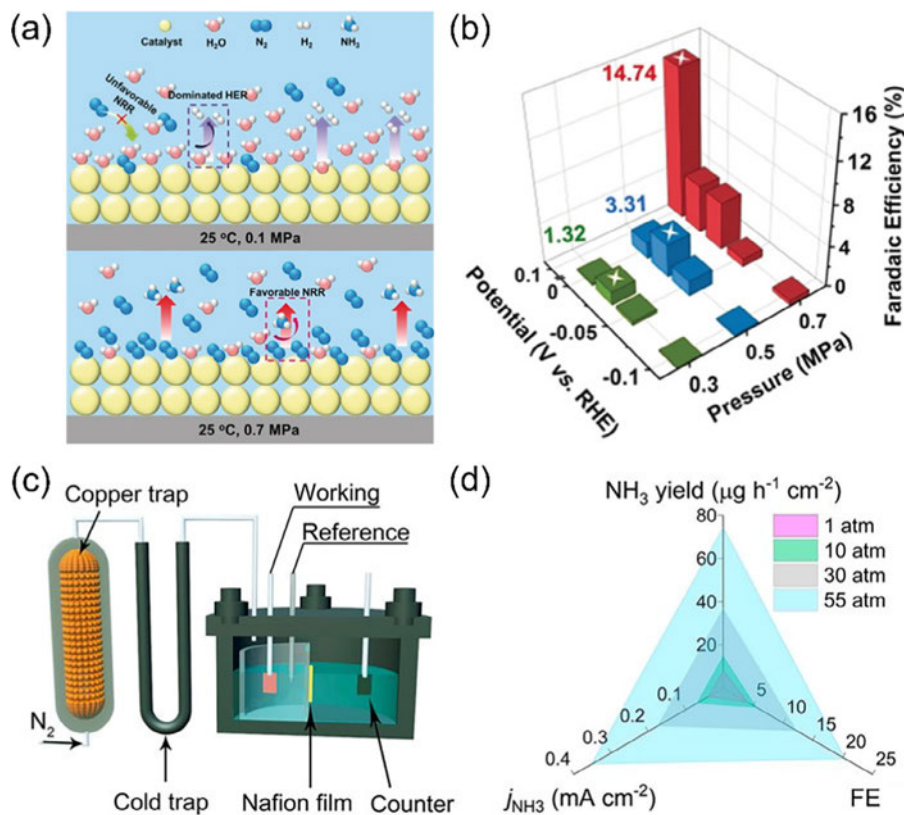
Fig. 5. Enhanced NRR under pressure. (a) Schematic of NRR versus HER on a catalyst surface under ambient condition and pressurized condition. (b) NH$_3$ FE of Fe$_3$Mo$_3$C/C catalyst under different pressurized conditions. (Reproduced from (Cheng et al., 2019) with permission from Wiley-VCH). (c) Schematic of an integrated pressurized electrolytic cell. (d) Comparison of the NH$_3$ yield, NH$_3$ FE, and NRR partial current density versus the exerted N$_2$ pressure. (Reproduced from (Zou et al., 2020) with permission from National Academy of Sciences).
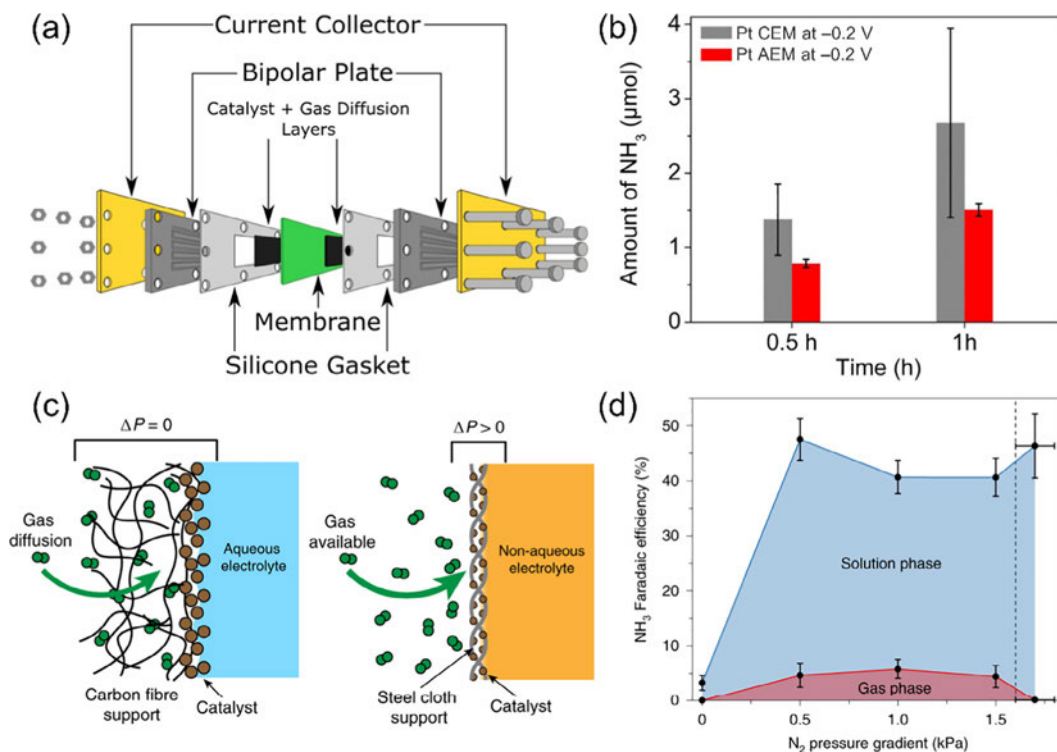

Fig. 6. NRR in flow cells. (a) Schematic of the MEA configuration for NRR tests. (b) The NH$_3$ yield and FE on noble metal catalysts tested in flow cells with AEM or CEM membranes. (Reproduced from (Nash et al., 2017) with permission from IOP Publishing). (c) Schematic of GDEs with an aqueous or non-aqueous electrolyte. In the case of non-aqueous electrolyte, a pressure gradient across the cloth is required to prevent complete catalyst flooding due to the lack of substantial capillary action. (d) The effect of pressure gradients across GDEs on the NH$_3$ FE at 15 mA cm^{-2}. (Reproduced from (Lazouski et al., 2020) with permission from Springer Nature).

applied to as high as 55 atm (Zou et al., 2020). The electrocatalytic NRR performance was gradually enhanced with the increase of N_2 pressure (Fig. 5d). At 55 atm, the maximum NH_3 yield reached 74.15 μg $cm^{-2}h^{-1}$ with a high NH_3 FE of 20.36%. DFT computations revealed that the driving force for N_2 adsorption as end-on $*N_2$ on the catalyst surface increased by 9.62 kJ mol^{-1} under 55 atm, which significantly facilitated NRR and in turn suppressed HER.

Although there are encouraging breakthroughs in pressurized devices for electrocatalytic NRR, several major issues are demanded to be addressed. First, the greatly improved N_2 adsorption on the catalyst surface will restrain the adsorption of protons, and ultimately inhibit the hydrogenation reduction of N_2. It is critical to balance the adsorption of N_2 and protons under pressure conditions. Second, the gas tightness and durability of pressurized devices should be carefully evaluated. Oxygen produced at the anode may exert destructive pressure on the membrane separating cathode/anode zones or harm the stability of catalysts in an open system. Third, although the pressurized condition enhances N_2 solubility and thus improves the NRR selectivity, N_2 diffusion requires further improvement to increase the reaction rate. More advances in pressurized electrocatalytic NRR and other reactions are anticipated by optimizing the reactor design and interface engineering (Li et al., 2020b).

3.4. Flow cells

Given the inherently slow diffusion and terrible solubility of N_2 in aqueous media, using the continuous flow reactors (denoted as flow cells) is also an effective strategy to enhance the NRR performance (Furuya and Yoshiba, 1989; Wei et al., 2021; Yang et al., 2018). It is because the flow cells can continuously circulate N_2 and products to and away from electrodes, which can greatly overcome the problem of N_2 supply and transport limitations in H-type cells.

Currently, the widely studied NRR flow cells are membrane electrode assembly (MEA) reactors (Kugler et al., 2014; Lazouski et al., 2020; Wei et al., 2021). As shown in Fig. 6a (Nash et al., 2017), such compact architecture utilizes a polymer electrolyte membrane to separate the anode and cathode, meanwhile transfer the ions while attenuating product crossover (Chen et al., 2021; Weekes et al., 2018). A highly porous gas diffusion layer (GDL) loaded with catalysts (denoted as gas diffusion electrode, GDE) is located between the electrode and membrane to promote the contact of supplied N_2 and electrocatalyst during NRR, and thus increase the upper limit of reaction rates. Based on this, the NRR efficiency in flow cells is not only related to the electrocatalyst performance, but also depends on GDL and membrane components (Hasnat et al., 2009; Lees et al., 2022; Liu and Xu, 2010). In 2017, the electrocatalytic NRR was first investigated in a MEA flow cell, and the influence of membrane components on NRR performance was studied via using both cation and anion exchange membranes (CEMs and AEMs) (Nash et al., 2017). The authors demonstrated that NH_3 yields for noble metal catalysts were higher in CEMs than those in AEMs, while this trend was reversed for NH_3 FE because of the relatively slow kinetics of HER in alkaline solutions (Fig. 6b).

The flow cell configuration can be integrated with the Li-mediated NRR approach to achieve further enhanced performance (Lazouski et al., 2020). Generally, the GDLs are hydrophobic carbon substrate for aqueous flow cells, which however cannot enable effective gas–liquid contact in non-aqueous solvents, such as THF. Instead, a stainless steel cloth-based support was used as the GDL to support *in situ* plated Li metal and a pressure gradient across the GDL was maintained to control the non-aqueous electrolyte penetration (Fig. 6c) (Lazouski et al., 2020). The non-aqueous Li-mediated NRR in a flow cell achieved a NH_3 partial current density of 8.8 ± 1.4 mA cm^{-2} and a high NH_3 FE of 35 ± 6% (Fig. 6d).
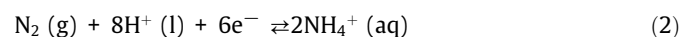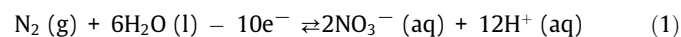
Although flow cells can improve NRR performance in both aqueous and non-aqueous electrolytes, many aspects of system engineering and catalyst design require further development. It is noticeable that the time-dependent ammonia yields are not on the same numerical scale (Yang et al., 2018). Also, the ammonia can pass through the membrane or be adsorbed on the membrane and even oxidized on the counter electrode (Hanifpour et al., 2020; Ren et al., 2019a, 2019b). Such phenomenon can cause significant errors in ammonia measurement ($\sim$30%), which challenges the accurate quantification of produced ammonia and the long-term stable operation (Ren et al., 2019a, 2019b). Water flooding issue is another challenge that needs to be solved in flow cells. Once flooding happens, the cathode diffusion layer and catalyst layer are saturated with water (Pan et al., 2021). The limited solubility and diffusion of N_2 in water will obstacle the adsorption and activation of N_2 onto the catalyst surface, thus lowering the thermodynamics and kinetics of NRR (Pan et al., 2021). Nevertheless, recent advances in the CO_2 flow cell electrolyzers can provide some useful suggestions for the design and improvement of NRR flow cells (Leonard et al., 2020a; Leonard et al., 2020b; Niu et al., 2021; Yang et al., 2021). With more understandings and strategies for better flow cell configurations, the stability and longevity for NRR flow cell could be further improved.

4. Emerging strategies for electrocatalysis-enabled green ammonia synthesis

Despite recent advances and the above-mentioned new opportunities for electrocatalytic NRR, the performance of NH_3 electrosynthesis is still highly limited by the intrinsic challenges of NRR. Increasing research interest has been attracted to explore new strategies for electrocatalytic nitrogen fixation and NH_3 production, such as nitrogen oxidation followed by nitrate/nitric oxide reduction. Specifically, Fig. 7a summarizes possible routes for nitrogen transformations towards NH_3 synthesis, which will be highlighted in the following sections.

4.1. Electrocatalytic nitrogen oxidation

As a counterpart of NRR, electrocatalytic nitrogen oxidation reaction (NOR) is also a vital procedure for sustainable nitrogen cycle and fixation (Lim et al., 2021; Wang et al., 2022). According to the Pourbaix diagram for the N_2-H_2O system, N_2 is unstable towards nitrate under moderate electrooxidation conditions (Chen et al., 2018). Thus, electrooxidation of N_2 into nitrate is theoretically feasible (Equation 1) and could be regarded as a promising avenue for replacement of the conventional nitrate synthesis (Ostwald process) to reduce the energy consumption and greenhouse gas emission (Kuang et al., 2020). More importantly, electrocatalytic NOR could effectively couple with NRR as a full electrochemical cell via just using ambient N_2 and water as the feedstock. Theoretical calculation reveals that NOR-NRR coupling cell would require a lower cell voltage (1.08 V) than that of water splitting (1.23 V) to operate in neutral or alkaline electrolyte (Chen et al., 2018). Green NH_3 and nitrate can be simultaneously generated in cathode and anode to directly yield NH_4NO_3 (Equation 2,3), thereby boosting the efficiency for nitrogen fixation (Chen et al., 2018).

$$N_2 \ (g) + 6H_2O \ (l) - 10e^- \rightleftarrows 2NO_3^- \ (aq) + 12H^+ \ (aq) \qquad (1)$$

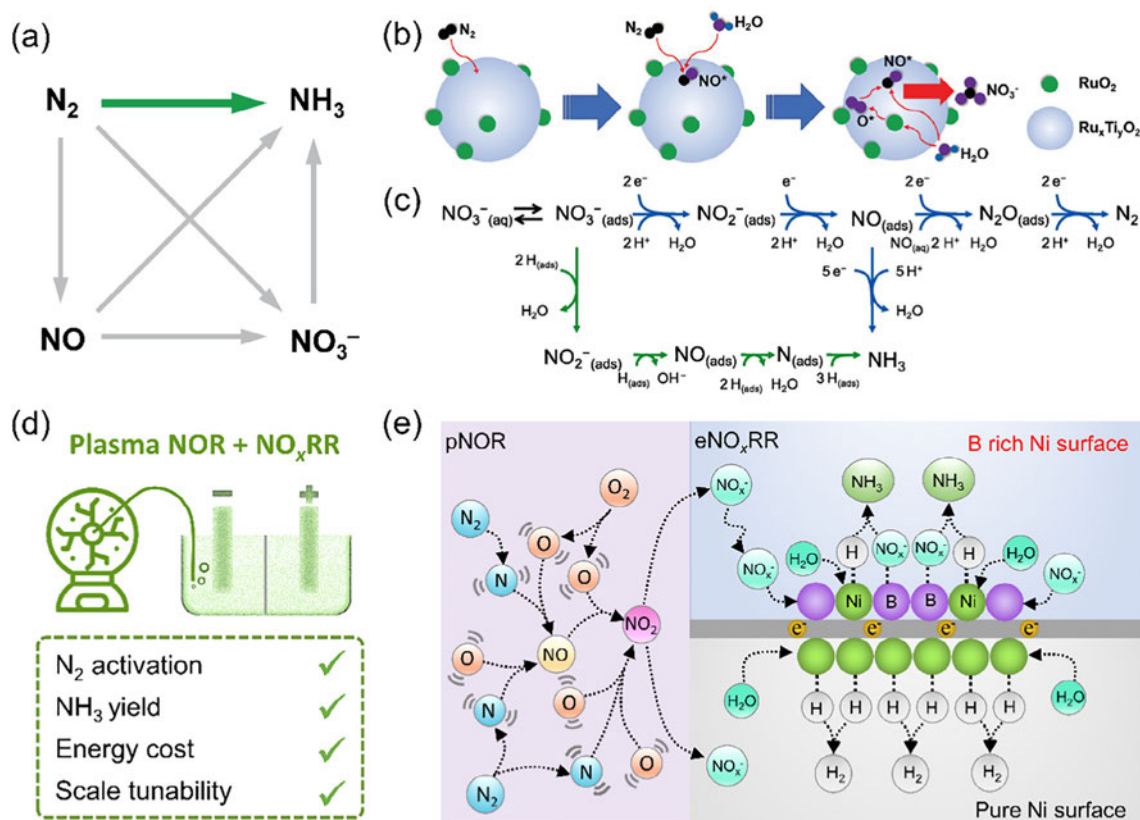$$N_2 \ (g) + 8H^+ \ (l) + 6e^- \rightleftarrows 2NH_4^+ \ (aq) \qquad (2)$$

Fig. 7. Electrocatalytic nitrogen oxidation and nitrate reduction reactions. (a) Possible routes for nitrogen transformations towards NH₃ synthesis. (b) Schematic of the NOR mechanism on Ru/TiO₂ composite electrocatalysts. (Reproduced from (Kuang et al., 2020) with permission from Wiley-VCH). (c) Reaction pathway and mechanisms for NO$_x$RR mediated by electron transfer (blue arrow) and atomic hydrogen (green arrow). (Reproduced from (Zhang et al., 2021) with permission from Elsevier). (d) Renewable N₂-to-NH₃ conversion through integration of plasma-driven N₂ oxidation and electrocatalytic NO$_x$RR and (e) corresponding mechanism. (Reproduced from (Li et al., 2021c) with permission from Wiley-VCH). (For interpretation of the references to colour in this figure legend, the reader is referred to the web version of this article.)

$$N_2 \text{ (g)} + 3H_2O \text{ (l)} \rightleftharpoons NH_4^+ \text{ (aq)} + NO_3^- \text{ (aq)} + H_2 \text{ (g)} \qquad (3)$$
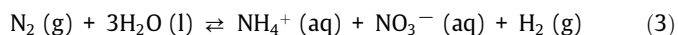
Assuming a reasonable FE of 10% for both cathodic (NRR) and anodic (NOR) reactions due to the competing water splitting reactions, the 60 mol of electrons input could provide at least 6 mol of electrons to drive pure NRR with 1 mol of N₂ consumed, or drive NRR-NOR coupling cell with (1 + 0.6) mol of N₂ converted. Therefore, the NRR-NOR coupling cell exhibits much higher energy efficiency for N₂ fixation.

For NOR, the proposed N₂-to-nitrate process involves two main stages: electrochemical activation of inert N₂ into the key *NO intermediate and the following reduction of *NO intermediate to *NH₃ (Anand et al., 2021; Kuang et al., 2020). However, the specific reaction pathways vary from report to report. In the first stage, the adsorbed *N₂ is oxidized to form a *N₂OH intermediate, which will experience various redox intermediates, such as *N₂O, *N₂OOH, *N₂O₂, *NO₂, *NOH and *NO intermediates (Han et al., 2021; Kuang et al., 2020; Li et al., 2021e). In the second stage, the active *NO intermediate will react with *O from water splitting or adjacent lattice O of catalyst to form *NO₃ (Dai et al., 2020; Han et al., 2021). Therefore, the key factor for designing highly efficient and selective NOR electrocatalysts is to promote N₂ adsorption and activation and regulate the competing oxygen evolution reaction (OER) activity for moderate *O supply. For example, a Ru-doped TiO₂/RuO₂ catalyst was proposed to boost electrooxidation of N₂ into nitrate (Kuang et al., 2020). The doped Ru$^{\delta+}$ sites in TiO₂ lattice with upshifted d-band center functioned as the main active sites for N₂ oxidation, while the induced RuO₂ provided optimal OER active sites to promote the redox transformation of *NO to nitrate (Fig. 7b), leading to a considerable nitrate yield of 161.9 μmol g$_{cat}^{-1}$-

h^{-1} and a high nitrate FE of 26.1%. In the case of ZnFe$_x$Co$_{2-x}$O₄, theoretical and experimental results revealed that Fe assisted the first N—O bond formation on the *N site, while high-oxidation-state Co stabilized the absorbed *OH for the second and third N—O bond formation (Dai et al., 2020). In addition to the boosted NOR activity, another worthy thing is that the surface chemistry and structure of electrocatalysts would dynamically change during NOR process (Dai et al., 2020; Fang et al., 2020; Han et al., 2021). Thus, tracing the catalyst evolution and probing the active species is also important and urgent for NOR to exactly understand the reaction mechanism, which can be conducted with the aid of isotope-labelling tests, *in situ* spectra and online differential electrochemical mass spectrometry (DEMS) (Li et al., 2021e).

Although NOR offers a new route for electrocatalytic nitrogen fixation, it apparently faces similar challenges as NRR, including the ultralow solubility of N₂ in aqueous electrolyte, high dissociation energy of N≡N bonds, and the parasitic OER competition. Therefore, the further research of NOR is recommended to investigate the efficacy of above-mentioned opportunities for NRR, such as non-aqueous electrolyte, high-concentration salt effect, flow cell, and pressurized reaction. The stability of electrolytes and catalysts under highly positive potentials applied for NOR requires deliberate evaluation.

4.2. Electrocatalytic nitrate reduction

Nitrate (NO₃⁻) is a common contaminant in agricultural and industrial wastewater runoff, and can be removed by electrocatalytic denitrification into N₂ (Duca and Koper, 2012). However,

the N$_2$ product is valueless, making such denitrification a waste of nitrogen-rich fertilizers. Recently, this research area attracted renewed interest to directly reduce NO$_3^-$ into NH$_3$ as an alternative and sustainable production process for NH$_3$ (van Langevelde et al., 2021; Zhang et al., 2021). This strategy can pave a way to fertilizer recovery and recycling in the route of N$_2$ → NH$_3$ → NO$_3^-$ → NH$_3$ (Greenlee, 2020).

The electrocatalytic reduction of NO$_3^-$ to N$_2$ or NH$_3$ goes through various intermediates, such as *NO$_2$, NO$_2^-$, *NO, *N$_2$O and *NH$_2$OH (Fig. 7c) (Duca and Koper, 2012; Zhang et al., 2021). Without the need to break or form N—N bonds, electrocatalytic nitrate reduction reaction (NO$_x$RR) to NH$_3$ is intrinsically easier with a higher selectivity and yield (Li et al., 2019b). Up to date, a series of transition metal-based catalysts have been reported for high-performance NO$_x$RR, especially Cu-based materials (Chen et al., 2020a; Wang, Yuhang et al., 2020; Wang, Yuting et al., 2020), Ti/TiO$_2$-based materials (Jia et al., 2020; McEnaney et al., 2020), Ni-based materials (Li et al., 2021c), and Fe single-atom catalysts (Li et al., 2021a; Wu et al., 2021). For example, a high NH$_3$ yield of 5.56 mol g$_{cat}^{-1}$h^{-1} with nearly 100% selectivity was obtained over strained Ru nanoclusters in alkaline electrolyte (pH = 14) with 1 M NO$_3^-$ (Li et al., 2020a). Experimental and theoretical study revealed that the tensile lattice strains endowed hydrogen radicals (·H) as the dominant reactive species to accelerate intermediate hydrogenation and restrain hydrogen dimerization. A copper-incorporated crystalline 3,4,9,10-perylenetetracarboxylic dianhydride (PTCDA) catalyst exhibited a high NH$_3$ yield of 436 ± 85 μg cm^{-2}h^{-1} and a maximum FE of 85.9% at −0.4 V vs. RHE in neutral electrolyte (pH = 7) with 500 ppm NO$_3^-$ (Chen et al., 2020a). The unique electronic structure of Cu suppressed HER and boosted the formation of N—H bonds, while the PTCDA structure facilitated protons and electrons transfer to the active Cu sites. However, the resulting NH$_3$ yields and selectivity are revealed to highly depend on operation conditions, such as the pH of electrolyte, nitrate concentration, and applied potential (McEnaney et al., 2020; van Langevelde et al., 2021), which requires extra caution and investigation in further studies. Besides, the catalyst durability remains to be improved.

It is noteworthy that such approach cannot realize complete sustainability because nitrate is industrially produced by the Ostwald process of NH$_3$, and the concentration of NO$_3^-$ in natural wastewater streams is too low for electrocatalysis (van Langevelde et al., 2021). Therefore, the study of large-scale concentration of real wastewater or exploration of new renewable nitrate sources is crucial for the practical application of electrocatalytic NO$_x$RR process. Recently, electrocatalytic oxidation of nitric oxide (NO) in exhausted gas has been demonstrated for nitrate synthesis over defective carbon cloth (Wang et al., 2021a). NO itself can also be electrocatalytically reduced to NH$_3$ at a remarkable rate of 517.1 μmol cm^{-2}h^{-1} and FE of 93.5% over a Cu foam electrode (Long et al., 2020). Another promising strategy is plasma-driven N$_2$ oxidation to NO$_x$, followed by alkaline absorption to generate an aqueous mixture of NO$_3^-$ and NO$_2^-$ (Li et al., 2021c; Sun et al., 2021). The integration of plasma-driven N$_2$ oxidation and electrocatalytic NO$_x$RR can realize highly efficient NH$_3$ production from air with advantages in yield, selectivity, energy cost, and scale tunability (Fig. 7d and e) (Li et al., 2021c).

4.3. Bioelectrocatalysis and redox-mediated electrocatalysis

In nature, biological nitrogen fixation to NH$_3$ occurs efficiently through the enzyme nitrogenase (Foster et al., 2018). Bioinspired mechanism investigation and catalysis design is believed to be very beneficial to the enhancement of electrocatalytic nitrogen fixation. By interfacing oxidoreductase enzymes to the solid electrode surface, electron transfer between the enzyme and the electrode can be finely tailored, resulting in bioelectrocatalysis (Milton and Minteer, 2019). According to the pattern of electron transfer, it
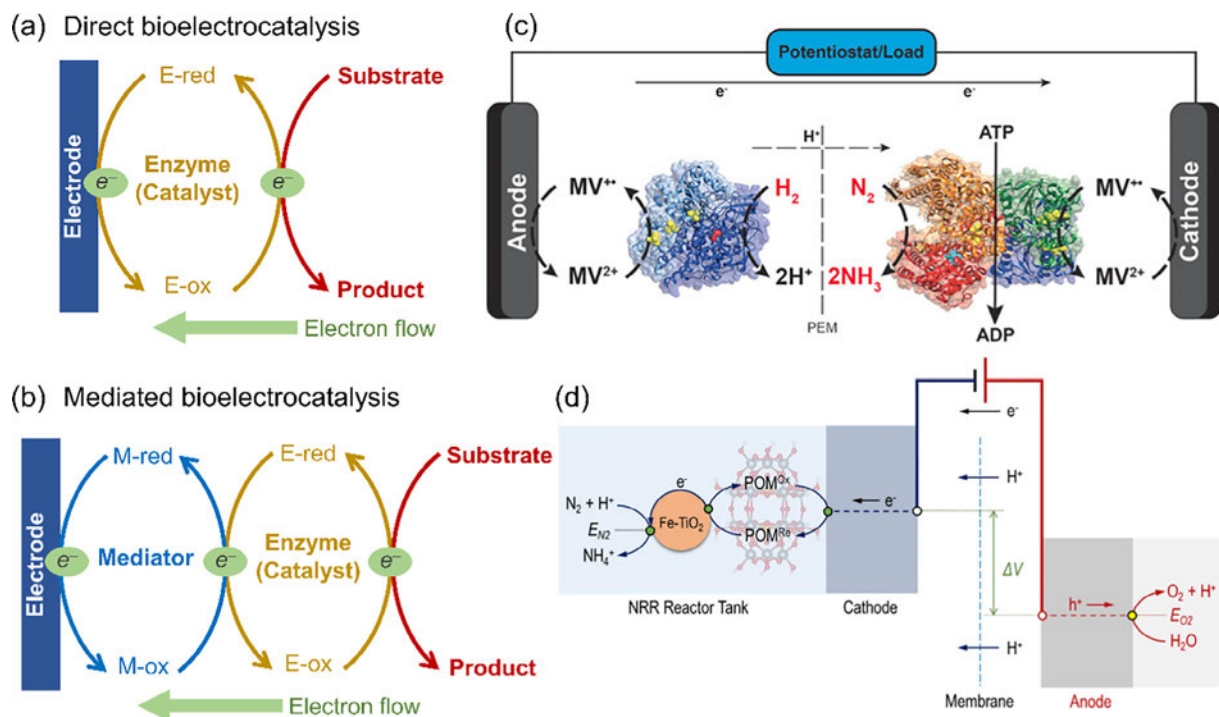

Fig. 8. Bioelectrocatalysis and redox-mediated electrocatalysis for NRR to NH$_3$. (a) Schematic of direct bioelectrocatalysis with direct electron transfer. (b) Schematic of mediated bioelectrocatalysis with redox-mediated electron transfer. E, S, M, red, and ox represent enzyme (or catalyst), substrate, mediator, reduced state, oxidized state, respectively. (c) MV-mediated NRR using nitrogenase Fe/MoFe proteins as the catalyst. (Reproduced from (Milton et al., 2017) with permission from Wiley-VCH). (d) Working principle of the POM-mediated NRR based on a close-loop electrochemical-chemical cycle. (Reproduced from (Wang et al., 2021d) with permission from Wiley-VCH). (For interpretation of the references to colour in this figure legend, the reader is referred to the web version of this article.)

Table 1
Performance comparison of some representative NRR systems with the quantification method.

Catalyst/Electrode	Electrolyte	NH₃ Yield	Faradaic Efficiency	Ammonia Detection Method			Reference
2D mosaic Bi nanosheet	0.1 M Na$_2$SO$_4$	2.54 ± 0.16 µg cm^{-2}h^{-1} @ −0.8 V vs RHE	10.46 ± 1.45% @ −0.8 V vs RHE	Indophenol blue			Li et al., 2019a
Fragmented Bi nanoparticle	0.1 M Na$_2$SO$_4$	3.25 ± 0.08 µg cm^{-2}h^{-1} @ −0.7 V vs RHE	12.11 ± 0.84% @ −0.6 V vs RHE	Indophenol blue	IC[c]	NMR[d]	Yao et al., 2020
Bi nanocrystal	0.5 M K$_2$SO$_4$	200 mmol g^{-1}h^{-1} (0.052 mmol cm^{-2}h^{-1}) @ −0.6 V vs RHE	66% @ −0.6 V vs RHE	Nessler's reagent	Ammonia kit	NMR	Hao et al., 2019
Ag nanotriangle	0.5 M K$_2$SO$_4$	58.5 mg$_{NH3}$ g$_{Ag}^{-1}$ h^{-1} @ −0.25 V vs RHE	25% @ −0.25 V vs RHE	Nessler's reagent	Indophenol blue	NMR	Gao et al., 2019
Deposited Li/stainless-steel cloth	1 M LiBF$_4$/0.11 M EtOH/THF	0.410 ± 0.038 µg cm^{-2} s^{-1} @ 20 mA cm^{-2}	39.5 ± 1.7% @ −10 mA cm^{-2}	Indophenol blue		NMR	Cai et al., 2021
Deposited Li/Copper	1 M LiBF$_4$/0.1 M EtOH/THF	7.9 ± 1.6 nmol cm^{-2} s^{-2} @ −15 mA cm^{-2}	18.5 ± 2.9% @ −8 mA cm^{-2}	Indophenol blue		NMR	Lazouski et al., 2019
Boron-doped carbon paper/ exfoliated proton-filtering COF	0.1 M HCl	287.2 ± 10.0 µg h^{-1} mg$_{cat}^{-1}$ @ −0.3 V vs RHE	54.5 ± 1.1% @ −0.3 V vs RHE	Indophenol blue		NMR	Liu et al., 2021
Activated B-rich COFs/NC	0.1 M KOH	12.53 µg h^{-1} mg^{-1} $_{cat}$ @ −0.2 V vs RHE	45.43% @ −0.2 V vs RHE	Indophenol blue		NMR	Liu et al., 2019
Fluorine doped tin oxide (FTO) glass/stainless steel cloth (SSC)	[P$_{6,6,6,14}$][eFAP] /[C$_4$mpyr][eFAP]	on SSC: 14 mg m^{-2}h^{-1} @ −0.8 V vs NHE	on FTO: 60.0 ± 0.6% @ −0.8 V vs NHE	Indophenol blue		NMR	Zhou et al., 2017
FeOOH/CNTs	0.16 %H$_2$O/CH$_3$OH	262.5 ± 7.3 mg h^{-1} mg$_{cat}^{-1}$ @ −1.2 V vs Ag/AgCl	75.9 ± 4.1% @ −1.2 V vs Ag/AgCl	Indophenol blue	NH$_4^+$ ion selective electrode	NMR	Ren et al., 2021
α-Fe@Fe$_3$O$_4$ Nanorod	0.16FPEE /[C$_4$mpyr][eFAP]	~2.35 × 10^{-11} mol s^{-1} cm^{-2} @ −0.65 V vs NHE	~32% @ −0.65 V vs NHE	Indophenol blue			Suryanto et al., 2018
Single-atom boron-decorated carbon catalyst	10 M LiCl	(9.5 ± 0.4) × 10^{-10} mol s^{-1} cm^{-2} @ −0.3 V vs RHE	71 ± 1.9% @ −0.3 V vs RHE	Indophenol blue		NMR	Wang et al., 2021c
Deposited Li/Mo foil (0.6 to 0.8 mol% oxygen in 20-bar N$_2$)	0.3 M LiClO$_4$ in THF with 1.0 vol% EtOH	EE[a]: 11.7 ± 0.5% @ −4 mA cm^{-2}	78.0 ± 1.3% @ −4 mA cm^{-2}	Indophenol blue		NMR	Li et al., 2021b
Li-ion conducting glass ceramic materials	1 M LiClO$_4$/propylene carbonate (PC)	1.88 × 10^{-9} mol s^{-1} cm^{-2} @ 1.39 mAh cm^{-2}	52.3% @ 1.39 mAh cm^{-2}	Indophenol blue	NH$_4^+$ ion selective electrode		Kim et al., 2018
Deposited Li/Ni substrate	1 M LiClO$_4$/PC with 1 wt% poly(methyl me-thacrylate) (PMMA)	1.21 × 10^{-9} mol cm^{-2} s^{-1} @ 0.83 mAh cm^{-2}	57.2% @ 0.83 mAh cm^{-2}	NMR			Kim et al., 2019
Deposited Li/SSC	1 M LiBF$_4$/THF/0.11 M ethanol	30 ± 5 nmol cm^{-2} s^{-1}	35 ± 6% @ −8.8 mA cm^{-2}	Indophenol blue		NMR	Lazouski et al., 2020
Deposited Li/Cu (0.5-bar H$_2$ and 19.5-bar N$_2$)	0.2 M LiBF$_4$/0.1 M [P$_{6,6,6,14}$][eFAP] solution in THF	53 ± 1 nmol cm^{-2} s^{-1}	69 ± 1% @ −22.5 mA cm^{-2}	Indophenol blue		NMR	Suryanto et al., 2021
Deposited Li/HBTCu (20-bar N$_2$)	2 M LiClO$_4$ in 99 vol% THF and 1 vol% EtOH	46.0 ± 6.8 nmol s^{-1} cm^{-2} @ −100 mA cm^{-2}	13.3 ± 2.0% @ −100 mA cm^{-2}	Indophenol blue			Li et al., 2022
Fe$_3$Mo$_3$C (0.7 MPa pressurized)	1 M KOH	13.55 µg cm^{-2}h^{-1} @ −0.025 V vs RHE	14.74% @ −0.025 V vs RHE	Indophenol blue		NMR	Cheng et al., 2019
Rh single atom/Graphdiyne (55 atm)	5 mM H$_2$SO$_4$ and 100 mM K$_2$SO$_4$	74.15 µg h^{-1} cm^{-2} @ −0.2 V vs RHE	20.36% @ −0.2 V vs RHE	NMR			Zou et al., 2020
Ru/Carbon Black (GDE[b])	Diluted H$_2$SO$_4$/PBS	9.9 × 10^{-10} mol cm^{-2} s^{-1} @ −0.1 V vs RHE	64.8% @ −0.1 V vs RHE	Indophenol blue		NMR	Wei et al., 2021
VN$_{0.7}$O$_{0.45}$ (GDE)	0.05 M H$_2$SO$_4$	3.3 × 10^{-10} mol cm^{-2} s^{-1} @ −0.1 V vs RHE	6.0% @ −0.1 V vs RHE	Nessler's reagent		NMR	Yang et al., 2018
Ir/C and Au/C (GDE)	0.1 M KOH	Ir/C: 4.3 × 10^{-13} mol cm^{-2} s^{-1} @ −0.2 V vs RHE	Au/C: 0.55% @ −0.2 V vs RHE	Nessler's reagent			Nash et al., 2017

[a] EE: energy efficiency.
[b] GDE: gas diffusion electrode.
[c] IC: ion chromatography.
[d] NMR: nuclear magnetic resonance.

can be divided into direct and mediated bioelectrocatalysis (Fig. 8a and b). For direct bioelectrocatalysis, the enzyme is typically immobilized on the electrode surface, and the cofactor of enzyme can transfer electrons with the electrode acting as either the source or sink of electrons (Bollella and Katz, 2020). Contrastively, mediated bioelectrocatalysis involves a redox species (i.e., small molecule or redox polymer) to promote electrons shuttle between the enzyme/cofactor and electrode (Kano and Ikeda, 2000). In the case of nitrogenase, it includes a catalytic protein to reduce N_2 and an electron-transferring reductase protein to deliver electrons for N_2 fixation (Dong et al., 2020). By using methyl viologen (MV) to shuttle electrons between nitrogenase and electrode, N_2 reduction to NH_3 can be mediated at an electrode surface (Fig. 8c) (Milton et al., 2017). This MV-mediated NRR bioelectrosynthetic experiment can run for 1 h with a NH_3 yield of 2.1 ± 0.5 μmol per mg of MoFe protein at a FE of 58.8 ± 6.1%.

Nowadays, such bioelectrocatalysis concept has been extended to redox-mediated heterogeneous electrocatalysis for O_2 reduction to H_2O_2 (Murray et al., 2019), CO_2 reduction to CO (Li et al., 2021f; Ren et al., 2019a, 2019b), and N_2 reduction to NH_3 (Wang et al., 2021d). With a polyoxometalate (POM) as the redox mediator and 1 %Fe-TiO_2 as the heterogenous catalyst, electrocatalytic NRR can be shifted from the electrode surface to a separate catalyst bed, rendering huge versatility in catalyst design, loading and gas flow (Fig. 8d) (Wang et al., 2021d). The POM-mediated electrocatalytic NRR process has achieved a high current density of 100 mA cm^{-2}, a high NH_3 yield of 5.0 μg $cm^{-2}h^{-1}$ and 61.0 ppm NH_3 accumulated in the electrolyte. Redox-mediated electrocatalytic NRR can also be realized by using tris(phosphine)borane iron(I) as the molecular catalyst and decamethylcobaltocene as a metallocene mediator (up to 6.7 equiv. of NH_3 production per Fe) (Chalkley et al., 2018).

Despite unique potentials, the redox-mediated electrocatalysis is still confronted with great challenges (Chen et al., 2020b). It is difficult to choose a universal mediator with a suitable electric potential window for any system, and mediated catalysis systems are usually unstable under extremely reductive potentials for large current densities. Therefore, it is necessary to rationally design and explore effective mediators and improve their long-term/on-site stability and recyclability for electrocatalysis (Chalkley et al., 2020).

5. Conclusion and outlook

The development of green NH_3 production technologies represents a viable alternative to decarbonize and defossilize the present SMR-HB process, help close the anthropogenic nitrogen cycle, and convert intermittent renewable electricity to transportable chemicals and fuels. Recent research in the field of electrocatalysis-enabled nitrogen fixation shows both challenges and chances (Table 1). As discussed in this Review, the roadmap towards green NH_3 contains several progressive stages from (SMR-HB + CCS) through (eH_2O + HB) to electrocatalytic NRR. To enhance the electrocatalytic activity and selectivity and facilitate the development towards practical application, we critically assessed the challenges of NRR and highlighted several emerging opportunities beyond catalysts design and ambient aqueous conditions. For the (eH_2O + HB) route, additional work should be further developed to improve the energy efficiency of water splitting and innovate the HB synthesis loop to match with renewable sources in flexible scales. For the direct electrocatalytic NRR route, a combination of materials science and chemical engineering is very likely the best way to design and develop more advanced green NH_3 synthesis approaches. Specifically, the development of elec-

trocatalytic green NH_3 production can be facilitated by further efforts in the following aspects:

1) New material choices and effective interface engineering are urgently demanded to improve the electrocatalytic activity and selectivity towards NH_3 production, which can be facilitated by DFT and machine learning prediction. With the advance of *in situ* characterization tools (e.g., Raman, XRD, FTIR, DEMS), interfacial behaviours and reaction mechanism during NRR involving catalyst evolution, ions, electrolyte and key intermediates could be figured out thoroughly.

2) The investigation of some new aspects beyond materials science is believed to make breakthroughs in NRR, including the use of non-aqueous electrolytes, the regulation of ion effects, the design of Li-mediated pathway, and the operation under pressure and in flow cells. More work is required to elucidate the functional mechanism and enhance the durability of these emerging systems.

3) The exploration of other electrocatalytic nitrogen transformation reactions is beneficial for both green NH_3 synthesis and nitrogen cycle closing, such as the oxidation of nitrogen (or air) to nitrate and nitric oxide, as well as the reduction of nitrate to NH_3 with substantially greater performance. Alternative catalysis processes, such as plasma catalysis, bioelectrocatalysis, redox-mediated electrocatalysis, and photocatalysis offer new opportunities to address the challenge of N_2 activation and innovate the reaction process design.

4) Rigorous, effective, and standardized experimental protocols are prerequisite for the reliable development of green NH_3 electrosynthesis due to the present low yield and ubiquitous contaminations (Iriawan et al., 2021; Tang and Qiao, 2019). Repeated and quantified isotope-labelled test coupled with proper gas cleaning (e.g., acid trap, pre-catalysis) is the only conclusive proof of electrocatalytic production (Andersen et al., 2019).

5) More advanced ammonia separation and quantification methods are essential for the non-aqueous NRR system. The design of automatic and use-friendly separation and analysis protocol creates more chances for studying and comparing solvent effect in the NRR, and paves the way to choosing the "best" one for future industrial-scale applications.

6) The knowledge and know-how share between academia and industry is also important to inspire new concepts and strategies for enhanced electrocatalytic performance. It will help bridge the fundamental advances in materials design and mechanism understanding with the state-of-the-art technological breakthroughs in reactor engineering and system integration, leading to improved energy efficiency, economic benefits, and practical feasibility.

Hopefully, with the combination of theoretical study, *in situ* characterization, electrocatalyst design, operational condition regulation, reactor engineering, and various catalysis integration, green NH_3 synthesis and the induced "ammonia economy" will be achieved in the near future.

CRediT authorship contribution statement

Dazhi Yao: Writing – original draft, Writing – review & editing, Visualization. **Cheng Tang:** Conceptualization, Visualization, Writing – review & editing, Supervision, Funding acquisition. **Pengtang Wang:** Writing – original draft, Visualization. **Hui Cheng:** Writing – original draft. **Huanyu Jin:** Writing – original draft. **Liang-Xin

Ding: Writing – review & editing. **Shi-Zhang Qiao:** Writing – review & editing, Supervision, Funding acquisition.

Declaration of Competing Interest

The authors declare the following financial interests/personal relationships which may be considered as potential competing interests: Cheng Tang, Shizhang Qiao reports financial support was provided by Australian Research Council.

Acknowledgement

References

International Energy Agency, 2021a. An energy sector roadmap to carbon neutrality in China. https://www.iea.org/reports/an-energy-sector-roadmap-to-carbon-neutrality-in-china (accessed 2 May 2022).

International Energy Agency, 2021b. Net zero by 2050 - A roadmap for the global energy sector. https://www.iea.org/reports/net-zero-by-2050 (accessed 2 May 2022).

Anand, M., Abraham, C.S., Nørskov, J.K., 2021. Electrochemical oxidation of molecular nitrogen to nitric acid - Towards a molecular level understanding of the challenges. Chem. Sci. 12 (18), 6442–6448.

Andersen, S.Z., Čolić, V., Yang, S., Schwalbe, J.A., Nielander, A.C., McEnaney, J.M., Enemark-Rasmussen, K., Baker, J.G., Singh, A.R., Rohr, B.A., Statt, M.J., Blair, S.J., Mezzavilla, S., Kibsgaard, J., Vesborg, P.C.K., Cargnello, M., Bent, S.F., Jaramillo, T.F., Stephens, I.E.L., Nørskov, J.K., Chorkendorff, I.b., 2019. A rigorous electrochemical ammonia synthesis protocol with quantitative isotope measurements. Nature 570 (7762), 504–508.

Andersen, S.Z., Statt, M.J., Bukas, V.J., Shapel, S.G., Pedersen, J.B., Krempl, K., Saccoccio, M., Chakraborty, D., Kibsgaard, J., Vesborg, P.C.K., Nørskov, J., Chorkendorff, I.b., 2020. Increasing stability, efficiency, and fundamental understanding of lithium-mediated electrochemical nitrogen reduction. Energy Environ. Sci. 13 (11), 4291–4300.

ARPA-E, 2016. Renewable energy to fuels through utilization of energy-dense liquids (REFUEL). https://arpa-e.energy.gov/technologies/programs/refuel (accessed 2 May 2022).

Ashida, Y., Arashiba, K., Nakajima, K., Nishibayashi, Y., 2019. Molybdenum-catalysed ammonia production with samarium diiodide and alcohols or water. Nature 568 (7753), 536–540.

Atchison, J., 2021. Yara's green ammonia project YURI gets further boosts. https://www.ammoniaenergy.org/articles/yaras-green-ammonia-project-yuri-gets-further-boosts/ (accessed 2 May 2022).

Battino, R., Rettich, T.R., Tominaga, T., 1984. The solubility of nitrogen and air in liquids. J. Phys. Chem. Ref. Data 13 (2), 563–600.

Bollella, P., Katz, E., 2020. Enzyme-based biosensors: Tackling electron transfer issues. Sensors 20, 3517.

Brown, T., 2018. Green ammonia demonstration plants now operational, in Oxford and Fukushima. https://www.ammoniaenergy.org/articles/green-ammonia-demonstration-plants-now-operational-in-oxford-and-fukushima/ (accessed 2 May 2022).

Buttler, A., Spliethoff, H., 2018. Current status of water electrolysis for energy storage, grid balancing and sector coupling via power-to-gas and power-to-liquids: A review. Renew. Sustain. Energy Rev. 82, 2440–2454.

Cai, X., Fu, C., Iriawan, H., Yang, F., Wu, A., Luo, L., Shen, S., Wei, G., Shao-Horn, Y., Zhang, J., 2021. Lithium-mediated electrochemical nitrogen reduction: Mechanistic insights to enhance performance. iScience 24 (10), 103105.

Chalkley, M.J., Del Castillo, T.J., Matson, B.D., Peters, J.C., 2018. Fe-mediated nitrogen fixation with a metallocene mediator: Exploring pKa effects and demonstrating electrocatalysis. J. Am. Chem. Soc. 140 (19), 6122–6129.

Chalkley, M.J., Garrido-Barros, P., Peters, J.C., 2020. A molecular mediator for reductive concerted proton-electron transfers via electrocatalysis. Science 369 (6505), 850–854.

Chen, G.-F., Yuan, Y., Jiang, H., Ren, S.-Y., Ding, L.-X., Ma, L., Wu, T., Lu, J., Wang, H., 2020a. Electrochemical reduction of nitrate to ammonia via direct eight-electron transfer using a copper-molecular solid catalyst. Nat. Energy 5 (8), 605–613.

Chen, H., Dong, F., Minteer, S.D., 2020b. The progress and outlook of bioelectrocatalysis for the production of chemicals, fuels and materials. Nat. Catal. 3 (3), 225–244.

Chen, J.G., Crooks, R.M., Seefeldt, L.C., Bren, K.L., Bullock, R.M., Darensbourg, M.Y., Holland, P.L., Hoffman, B., Janik, M.J., Jones, A.K., Kanatzidis, M.G., King, P., Lancaster, K.M., Lymar, S.V., Pfromm, P., Schneider, W.F., Schrock, R.R., 2018. Beyond fossil fuel–driven nitrogen transformations. Science 360 (6391).

Chen, Y., Su, D., Chen, Y., Zhu, Z., Li, W., 2021. Three-phase interface-assisted advanced electrochemistry-related applications. Cell Rep. Phys. Sci. 2 (10), 100602.

Cheng, H., Cui, P., Wang, F., Ding, L.-X., Wang, H., 2019. High efficiency electrochemical nitrogen fixation achieved with a lower pressure reaction system by changing the chemical equilibrium. Angew. Chem. Int. Ed. 58 (43), 15541–15547.

Choi, J., Suryanto, B.H.R., Wang, D., Du, H.-L., Hodgetts, R.Y., Ferrero Vallana, F.M., MacFarlane, D.R., Simonov, A.N., 2020. Identification and elimination of false positives in electrochemical nitrogen reduction studies. Nat. Commun. 11, 5546.

Cui, X., Tang, C., Zhang, Q., 2018. A review of electrocatalytic reduction of dinitrogen to ammonia under ambient conditions. Adv. Energy Mater. 8 (22), 1800369.

Dai, C., Sun, Y., Chen, G., Fisher, A.C., Xu, Z.J., 2020. Electrochemical oxidation of nitrogen towards direct nitrate production on spinel oxides. Angew. Chem. Int. Ed. 59 (24), 9418–9422.

Dana, A.G., Elishav, O., Bardow, A., Shter, G.E., Grader, G.S., 2016. Nitrogen-based fuels: A power-to-fuel-to-power analysis. Angew. Chem. Int. Ed. 55 (31), 8798–8805.

Dong, F., Chen, H., Malapit, C.A., Prater, M.B., Li, M., Yuan, M., Lim, K., Minteer, S.D., 2020. Biphasic bioelectrocatalytic synthesis of chiral β-hydroxy nitriles. J. Am. Chem. Soc. 142 (18), 8374–8382.

Duca, M., Koper, M.T.M., 2012. Powering denitrification: The perspectives of electrocatalytic nitrate reduction. Energy Environ. Sci. 5, 9726–9742.

Fang, W., Du, C., Kuang, M., Chen, M., Huang, W., Ren, H., Xu, J., Feldhoff, A., Yan, Q., 2020. Boosting efficient ambient nitrogen oxidation by a well-dispersed Pd on MXene electrocatalyst. Chem. Commun. 56 (43), 5779–5782.

Foster, S.L., Bakovic, S.I.P., Duda, R.D., Maheshwari, S., Milton, R.D., Minteer, S.D., Janik, M.J., Renner, J.N., Greenlee, L.F., 2018. Catalysts for nitrogen reduction to ammonia. Nat. Catal. 1 (7), 490–500.

Furuya, N., Yoshiba, H., 1989. Electroreduction of nitrogen to ammonia on gas-diffusion electrodes modified by Fe-phthalocyanine. J. Electroanal. Chem. 263 (1), 171–174.

Gao, W.-Y., Hao, Y.-C., Su, X., Chen, L.-W., Bu, T.-A., Zhang, N., Yu, Z.-L., Zhu, Z., Yin, A.-X., 2019. Morphology-dependent electrocatalytic nitrogen reduction on Ag triangular nanoplates. Chem. Commun. 55 (72), 10705–10708.

Ghatee, M.H., Zare, M., Moosavi, F., Zolghadr, A.R., 2010. Temperature-dependent density and viscosity of the ionic liquids 1-alkyl-3-methylimidazolium iodides: Experiment and molecular dynamics simulation. J. Chem. Eng. Data 55 (9), 3084–3088.

Gnahm, M., Kolb, D.M., 2011. The purification of an ionic liquid. J. Electroanal. Chem. 651 (2), 250–252.

Greenlee, L.F., 2020. Recycling fertilizer. Nat. Energy 5 (8), 557–558.

Han, S., Wang, C., Wang, Y., Yu, Y., Zhang, B., 2021. Electrosynthesis of nitrate via the oxidation of nitrogen on tensile-strained palladium porous nanosheets. Angew. Chem. Int. Ed. 60 (9), 4474–4478.

Hanifpour, F., Sveinbjörnsson, A., Canales, C.P., Skúlason, E., Flosadóttir, H.D., 2020. Preparation of nafion membranes for reproducible ammonia quantification in nitrogen reduction reaction experiments. Angew. Chem. Int. Ed. 59 (51), 22938–22942.

Hao, Y.-C., Guo, Y.u., Chen, L.-W., Shu, M., Wang, X.-Y., Bu, T.-A., Gao, W.-Y., Zhang, N., Su, X., Feng, X., Zhou, J.-W., Wang, B.o., Hu, C.-W., Yin, A.-X., Si, R., Zhang, Y.-W., Yan, C.-H., 2019. Promoting nitrogen electroreduction to ammonia with bismuth nanocrystals and potassium cations in water. Nat. Catal. 2 (5), 448–456.

Hasnat, M.A., Karim, M.R., Machida, M., 2009. Electrocatalytic ammonia synthesis: Role of cathode materials and reactor configuration. Catal. Commun. 10 (15), 1975–1979.

Iriawan, H., Andersen, S.Z., Zhang, X., Comer, B.M., Barrio, J., Chen, P., Medford, A.J., Stephens, I.E., Chorkendorff, I., Shao-Horn, Y., 2021. Methods for nitrogen activation by reduction and oxidation. Nat. Rev. Methods Primers 1, 56.

Jia, R., Wang, Y., Wang, C., Ling, Y., Yu, Y., Zhang, B., 2020. Boosting selective nitrate electroreduction to ammonium by constructing oxygen vacancies in TiO₂. ACS Catal. 10 (6), 3533–3540.

Jia, T., Bi, S., Wu, J., 2019. Solubilities of carbon dioxide, oxygen, and nitrogen in aqueous ethylene glycol solution under low pressures. Fluid Phase Equilib. 485, 16–22.

Jiang, L., Fu, X., 2021. An ammonia–hydrogen energy roadmap for carbon neutrality: Opportunity and challenges in China. Engineering 7 (12), 1688–1691.

Kang, C.S.M., Zhang, X., MacFarlane, D.R., 2019. High nitrogen gas solubility and physicochemical properties of [C₄mpyr][eFAP]–fluorinated solvent mixtures. J. Phys. Chem. C 123 (35), 21376–21385.

Kano, K., Ikeda, T., 2000. Fundamentals and practices of mediated bioelectrocatalysis. Anal. Sci. 16 (10), 1013–1021.

Kim, K., Chen, Y., Han, J.-I., Yoon, H.C., Li, W., 2019. Lithium-mediated ammonia synthesis from water and nitrogen: A membrane-free approach enabled by an immiscible aqueous/organic hybrid electrolyte system. Green Chem. 21 (14), 3839–3845.

Kim, K., Lee, N., Yoo, C.-Y., Kim, J.-N., Yoon, H.C., Han, J.-I., 2016. Communication—electrochemical reduction of nitrogen to ammonia in 2-propanol under ambient temperature and pressure. J. Electrochem. Soc. 163 (7), F610–F612.

Kim, K., Lee, S.J., Kim, D.-Y., Yoo, C.-Y., Choi, J.W., Kim, J.-N., Woo, Y., Yoon, H.C., Han, J.-I., 2018. Electrochemical synthesis of ammonia from water and nitrogen: A lithium-mediated approach using lithium-ion conducting glass ceramics. ChemSusChem 11 (1), 120–124.

Kuang, M., Wang, Y.u., Fang, W., Tan, H., Chen, M., Yao, J., Liu, C., Xu, J., Zhou, K., Yan, Q., 2020. Efficient nitrate synthesis via ambient nitrogen oxidation with Ru-doped TiO₂/RuO₂ electrocatalysts. Adv. Mater. 32 (26), 2002189.

Kugler, K., Ohs, B., Scholz, M., Wessling, M., 2014. Towards a carbon independent and CO₂-free electrochemical membrane process for NH₃ synthesis. Phys. Chem. Chem. Phys. 16 (13), 6129–6138.

Lagadec, M.F., Grimaud, A., 2020. Water electrolysers with closed and open electrochemical systems. Nat. Mater. 19 (11), 1140–1150.

Lazouski, N., Chung, M., Williams, K., Gala, M.L., Manthiram, K., 2020. Non-aqueous gas diffusion electrodes for rapid ammonia synthesis from nitrogen and water-splitting-derived hydrogen. Nat. Catal. 3 (5), 463–469.

Lazouski, N., Schiffer, Z.J., Williams, K., Manthiram, K., 2019. Understanding continuous lithium-mediated electrochemical nitrogen reduction. Joule 3 (4), 1127–1139.

Lees, E.W., Mowbray, B.A.W., Parlane, F.G.L., Berlinguette, C.P., 2022. Gas diffusion electrodes and membranes for CO_2 reduction electrolysers. Nat. Rev. Mater. 7 (1), 55–64.

Leonard, M.E., Clarke, L.E., Forner-Cuenca, A., Brown, S.M., Brushett, F.R., 2020a. Investigating electrode flooding in a flowing electrolyte, gas-fed carbon dioxide electrolyzer. ChemSusChem 13 (2), 400–411.

Leonard, M.E., Orella, M.J., Aiello, N., Román-Leshkov, Y., Forner-Cuenca, A., Brushett, F.R., 2020b. Editors' choice—flooded by success: On the role of electrode wettability in CO_2 electrolyzers that generate liquid products. J. Electrochem. Soc. 167 (12), 124521.

Li, J., Zhan, G., Yang, J., Quan, F., Mao, C., Liu, Y., Wang, B.o., Lei, F., Li, L., Chan, A.W.M., Xu, L., Shi, Y., Du, Y.i., Hao, W., Wong, P.K., Wang, J., Dou, S.-X., Zhang, L., Yu, J.C., 2020a. Efficient ammonia electrosynthesis from nitrate on strained ruthenium nanoclusters. J. Am. Chem. Soc. 142 (15), 7036–7046.

Li, J., Kuang, Y., Meng, Y., Tian, X., Hung, W.-H., Zhang, X., Li, A., Xu, M., Zhou, W.u., Ku, C.-S., Zhang, C.-Y., Zhu, G., Guo, J., Sun, X., Dai, H., 2020b. Electroreduction of CO_2 to formate on a copper-based electrocatalyst at high pressures with high energy conversion efficiency. J. Am. Chem. Soc. 142 (16), 7276–7282.

Li, J.C., Li, M., An, N., Zhang, S., Song, Q.N., Yang, Y.L., Liu, X., 2021a. Atomically dispersed fe atoms anchored on S and N-codoped carbon for efficient electrochemical denitrification. Proc. Natl. Acad. Sci. USA 118 (33), e2105628118.

Li, K., Andersen, S.Z., Statt, M.J., Saccoccio, M., Bukas, V.J., Krempl, K., Sažinas, R., Pedersen, J.B., Shadravan, V., Zhou, Y., Chakraborty, D., Kibsgaard, J., Vesborg, P. C.K., Nørskov, J.K., Chorkendorff, I.b., 2021b. Enhancement of lithium-mediated ammonia synthesis by addition of oxygen. Science 374 (6575), 1593–1597.

Li, K., Shapel, S.G., Hochfilzer, D., Pedersen, J.B., Krempl, K., Andersen, S.Z., Sažinas, R., Saccoccio, M., Li, S., Chakraborty, D., Kibsgaard, J., Vesborg, P.C.K., Nørskov, J. K., Chorkendorff, I.b., 2022. Increasing current density of Li-mediated ammonia synthesis with high surface area copper electrodes. ACS Energy Lett. 7 (1), 36–41.

Li, L., Tang, C., Cui, X., Zheng, Y., Wang, X., Xu, H., Zhang, S., Shao, T., Davey, K., Qiao, S.-Z., 2021c. Efficient nitrogen fixation to ammonia through integration of plasma oxidation with electrocatalytic reduction. Angew. Chem. Int. Ed. 60 (25), 14131–14137.

Li, L., Tang, C., Jin, H., Davey, K., Qiao, S.-Z., 2021d. Main-group elements boost electrochemical nitrogen fixation. Chem 7 (12), 3232–3255.

Li, L., Tang, C., Xia, B., Jin, H., Zheng, Y., Qiao, S.-Z., 2019a. Two-dimensional mosaic bismuth nanosheets for highly selective ambient electrocatalytic nitrogen reduction. ACS Catal. 9 (4), 2902–2908.

Li, L., Tang, C., Yao, D., Zheng, Y., Qiao, S.-Z., 2019b. Electrochemical nitrogen reduction: Identification and elimination of contamination in electrolyte. ACS Energy Lett. 4 (9), 2111–2116.

Li, T., Han, S., Wang, C., Huang, Y., Wang, Y., Yu, Y., Zhang, B., 2021e. Ru-doped Pd nanoparticles for nitrogen electrooxidation to nitrate. ACS Catal. 11 (22), 14032–14037.

Li, Y., Hui, D., Sun, Y., Wang, Y., Wu, Z., Wang, C., Zhao, J., 2021f. Boosting thermo-photocatalytic CO_2 conversion activity by using photosynthesis-inspired electron-proton-transfer mediators. Nat. Commun. 12, 123.

Li, Y., Lan, S., Ryberg, M., Pérez-Ramírez, J., Wang, X., 2021g. A quantitative roadmap for China towards carbon neutrality in 2060 using methanol and ammonia as energy carriers. iscience 24 (6), 102513.

Liang, Y., Yan, C., Guo, Q., Xu, J., Hu, H., 2016. Spectrophotometric determination of ammonia nitrogen in water by flow injection analysis based on NH_3- o-phthalaldehyde -Na_2SO_3 reaction. Anal. Chem. Res. 10, 1–8.

Lim, J., Fernández, C.A., Lee, S.W., Hatzell, M.C., 2021. Ammonia and nitric acid demands for fertilizer use in 2050. ACS Energy Lett. 6 (10), 3676–3685.

Liu, H., Liu, Y., Li, J., 2010. Ionic liquids in surface electrochemistry. Phys. Chem. Chem. Phys. 12, 1685–1697.

Liu, R., Xu, G., 2010. Comparison of electrochemical synthesis of ammonia by using sulfonated polysulfone and nafion membrane with $Sm_{1.5}Sr_{0.5}NiO_4$. Chin. J. Chem. 28 (2), 139–142.

Liu, S., Qian, T., Wang, M., Ji, H., Shen, X., Wang, C., Yan, C., 2021. Proton-filtering covalent organic frameworks with superior nitrogen penetration flux promote ambient ammonia synthesis. Nat. Catal. 4 (4), 322–331.

Liu, S., Wang, M., Qian, T., Ji, H., Liu, J., Yan, C., 2019. Facilitating nitrogen accessibility to boron-rich covalent organic frameworks via electrochemical excitation for efficient nitrogen fixation. Nat. Commun. 10, 3898.

Long, J., Chen, S., Zhang, Y., Guo, C., Fu, X., Deng, D., Xiao, J., 2020. Direct electrochemical ammonia synthesis from nitric oxide. Angew. Chem. Int. Ed. 59 (24), 9711–9718.

MacFarlane, D.R., Cherepanov, P.V., Choi, J., Suryanto, B.H.R., Hodgetts, R.Y., Bakker, J.M., Ferrero Vallana, F.M., Simonov, A.N., 2020. A roadmap to the ammonia economy. Joule 4 (6), 1186–1205.

McEnaney, J.M., Blair, S.J., Nielander, A.C., Schwalbe, J.A., Koshy, D.M., Cargnello, M., Jaramillo, T.F., 2020. Electrolyte engineering for efficient electrochemical nitrate reduction to ammonia on a titanium electrode. ACS Sustain. Chem. Eng. 8 (7), 2672–2681.

McEnaney, J.M., Singh, A.R., Schwalbe, J.A., Kibsgaard, J., Lin, J.C., Cargnello, M., Jaramillo, T.F., Nørskov, J.K., 2017. Ammonia synthesis from N_2 and H_2O using a lithium cycling electrification strategy at atmospheric pressure. Energy Environ. Sci. 10 (7), 1621–1630.

Milton, R.D., Cai, R., Abdellaoui, S., Leech, D., De Lacey, A.L., Pita, M., Minteer, S.D., 2017. Bioelectrochemical haber-bosch process: An ammonia-producing H_2/N_2 fuel cell. Angew. Chem. Int. Ed. 56 (10), 2680–2683.

Milton, R.D., Minteer, S.D., 2019. Nitrogenase bioelectrochemistry for synthesis applications. Acc. Chem. Res. 52 (12), 3351–3360.

Murakami, T., Nishikiori, T., Nohira, T., Ito, Y., 2003. Electrolytic synthesis of ammonia in molten salts under atmospheric pressure. J. Am. Chem. Soc. 125 (2), 334–335.

Murray, A.T., Voskian, S., Schreier, M., Hatton, T.A., Surendranath, Y., 2019. Electrosynthesis of hydrogen peroxide by phase-transfer catalysis. Joule 3 (12), 2942–2954.

Musgrave, C.B., Morozov, S., Schinski, W.L., Goddard, W.A., 2021. Reduction of N_2 to ammonia by phosphate molten salt and Li electrode: Proof of concept using quantum mechanics. J. Phys. Chem. Lett. 12 (6), 1696–1701.

Nash, J., Yang, X., Anibal, J., Wang, J., Yan, Y., Xu, B., 2017. Electrochemical nitrogen reduction reaction on noble metal catalysts in proton and hydroxide exchange membrane electrolyzers. J. Electrochem. Soc. 164 (14), F1712–F1716.

Nedić, M., Wassermann, T.N., Larsen, R.W., Suhm, M.A., 2011. A combined Raman- and infrared jet study of mixed methanol–water and ethanol–water clusters. Phys. Chem. Chem. Phys. 13, 14050–14063.

Niu, Z.-Z., Chi, L.-P., Liu, R., Chen, Z., Gao, M.-R., 2021. Rigorous assessment of CO_2 electroreduction products in a flow cell. Energy Environ. Sci. 14 (8), 4169–4176.

Ong, S.P., Andreussi, O., Wu, Y., Marzari, N., Ceder, G., 2011. Electrochemical windows of room-temperature ionic liquids from molecular dynamics and density functional theory calculations. Chem. Mater. 23 (11), 2979–2986.

Pan, Z., Khalid, F., Tahir, A., Esan, O.C., Zhu, J., Chen, R., An, L., 2021. Water flooding behavior in flow cells for ammonia production via electrocatalytic nitrogen reduction. Fundam. Res. https://doi.org/10.1016/j.fmre.2021.09.001.

Peterson, D., Vickers, J., DeSantis, D., 2020. Hydrogen production cost from PEM electrolysis - 2019. https://www.hydrogen.energy.gov/pdfs/19009_h2_production_cost_pem_electrolysis_2019.pdf (accessed 2 May 2022).

Plechkova, N.V., Seddon, K.R., 2008. Applications of ionic liquids in the chemical industry. Chem. Soc. Rev. 37 (1), 123–150.

Qing, G., Ghazfar, R., Jackowski, S.T., Habibzadeh, F., Ashtiani, M.M., Chen, C.-P., Smith, M.R., Hamann, T.W., 2020. Recent advances and challenges of electrocatalytic N_2 reduction to ammonia. Chem. Rev. 120 (12), 5437–5516.

Quinn, B.M., Ding, Z., Moulton, R., Bard, A.J., 2002. Novel electrochemical studies of ionic liquids. Langmuir 18 (5), 1734–1742.

Ren, S., Joulié, D., Salvatore, D., Torbensen, K., Wang, M., Robert, M., Berlinguette, C. P., 2019a. Molecular electrocatalysts can mediate fast, selective CO_2 reduction in a flow cell. Science 365 (6451), 367–369.

Ren, Y., Yu, C., Han, X., Huang, H., Huang, H., Qiu, J., 2019b. Is it appropriate to use the nafion membrane in electrocatalytic N_2 reduction? Small Methods 3 (12), 1900474.

Ren, Y., Yu, C., Han, X., Tan, X., Wei, Q., Li, W., Han, Y., Yang, L., Qiu, J., 2021. Methanol-mediated electrosynthesis of ammonia. ACS Energy Lett. 6 (11), 3844–3850.

Rosen, B.A., Salehi-Khojin, A., Thorson, M.R., Zhu, W., Whipple, D.T., Kenis, P.J.A., Masel, R.I., 2011. Ionic liquid-mediated selective conversion of CO_2 to CO at low overpotentials. Science 334 (6056), 643–644.

Schüth, F., Palkovits, R., Schlögl, R., Su, D.S., 2012. Ammonia as a possible element in an energy infrastructure: Catalysts for ammonia decomposition. Energy Environ. Sci. 5 (4), 6278–6289.

Schwalbe, J.A., Statt, M.J., Chosy, C., Singh, A.R., Rohr, B.A., Nielander, A.C., Andersen, S.Z., McEnaney, J.M., Baker, J.G., Jaramillo, T.F., Norskov, J.K., Cargnello, M., 2020. A combined theory-experiment analysis of the surface species in lithium-mediated NH_3 electrosynthesis. ChemElectroChem 7 (7), 1542–1549.

Smith, C., Hill, A.K., Torrente-Murciano, L., 2020. Current and future role of Haber-Bosch ammonia in a carbon-free energy landscape. Energy Environ. Sci. 13 (2), 331–344.

Sun, J., Alam, D., Daiyan, R., Masood, H., Zhang, T., Zhou, R., Cullen, P.J., Lovell, E.C., Jalili, A., Amal, R., 2021. A hybrid plasma electrocatalytic process for sustainable ammonia production. Energy Environ. Sci. 14 (2), 865–872.

Suryanto, B.H.R., Du, H.-L., Wang, D., Chen, J., Simonov, A.N., MacFarlane, D.R., 2019. Challenges and prospects in the catalysis of electroreduction of nitrogen to ammonia. Nat. Catal. 2 (4), 290–296.

Suryanto, B.H.R., Kang, C.S.M., Wang, D., Xiao, C., Zhou, F., Azofra, L.M., Cavallo, L., Zhang, X., MacFarlane, D.R., 2018. Rational electrode–electrolyte design for efficient ammonia electrosynthesis under ambient conditions. ACS Energy Lett. 3 (6), 1219–1224.

Suryanto, B.H.R., Matuszek, K., Choi, J., Hodgetts, R.Y., Du, H.-L., Bakker, J.M., Kang, C. S.M., Cherepanov, P.V., Simonov, A.N., MacFarlane, D.R., 2021. Nitrogen reduction to ammonia at high efficiency and rates based on a phosphonium proton shuttle. Science 372 (6547), 1187–1191.

Tang, C., Qiao, S.-Z., 2019. How to explore ambient electrocatalytic nitrogen reduction reliably and insightfully. Chem. Soc. Rev. 48 (12), 3166–3180.

Tang, C., Zheng, Y., Jaroniec, M., Qiao, S.-Z., 2021. Electrocatalytic refinery for sustainable production of fuels and chemicals. Angew. Chem. Int. Ed. 60 (36), 19572–19590.

Tsuneto, A., Kudo, A., Sakata, T., 1993. Efficient electrochemical reduction of N_2 to NH_3 catalyzed by lithium. Chem. Lett. 22 (5), 851–854.

Tsuneto, A., Kudo, A., Sakata, T., 1994. Lithium-mediated electrochemical reduction of high-pressure N_2 to NH_3. J. Electroanal. Chem. 367 (1-2), 183–188.

van Langevelde, P.H., Katsounaros, I., Koper, M.T.M., 2021. Electrocatalytic nitrate reduction for sustainable ammonia production. Joule 5 (2), 290–294.

Wang, D., He, N., Xiao, L., Dong, F., Chen, W., Zhou, Y., Chen, C., Wang, S., 2021a. Coupling electrocatalytic nitric oxide oxidation over carbon cloth with hydrogen evolution reaction for nitrate synthesis. Angew. Chem. Int. Ed. 60 (46), 24605–24611.

Wang, L.u., Xia, M., Wang, H., Huang, K., Qian, C., Maravelias, C.T., Ozin, G.A., 2018. Greening ammonia toward the solar ammonia refinery. Joule 2 (6), 1055–1074.

Wang, M., Khan, M.A., Mohsin, I., Wicks, J., Ip, A.H., Sumon, K.Z., Dinh, C.T., Sargent, E.H., Gates, I.D., Kibria, M.G., 2021b. Can sustainable ammonia synthesis pathways compete with fossil-fuel based Haber-Bosch processes? Energy Environ Sci. 14, 2535–2548.

Wang, M., Liu, S., Ji, H., Yang, T., Qian, T., Yan, C., 2021c. Salting-out effect promoting highly efficient ambient ammonia synthesis. Nat. Commun. 12, 3198.

Wang, X., Yang, J., Salla, M., Xi, S., Yang, Y., Li, M., Zhang, F., Zhu, M.-K., Huang, S., Huang, S., Zhang, Y.-W., Wang, Q., 2021d. Redox-mediated ambient electrolytic nitrogen reduction for hydrazine and ammonia generation. Angew. Chem. Int. Ed. 60 (34), 18721–18727.

Wang, Y., Li, T., Yu, Y., Zhang, B., 2022. Electrochemical synthesis of nitric acid from nitrogen oxidation. Angew. Chem. Int. Ed. 61 (12), e202115409.

Wang, Y., Xu, A., Wang, Z., Huang, L., Li, J., Li, F., Wicks, J., Luo, M., Nam, D.-H., Tan, C.-S., Ding, Y.u., Wu, J., Lum, Y., Dinh, C.-T., Sinton, D., Zheng, G., Sargent, E.H., 2020a. Enhanced nitrate-to-ammonia activity on copper-nickel alloys via tuning of intermediate adsorption. J. Am. Chem. Soc. 142 (12), 5702–5708.

Wang, Y., Zhou, W., Jia, R., Yu, Y., Zhang, B., 2020b. Unveiling the activity origin of a copper-based electrocatalyst for selective nitrate reduction to ammonia. Angew. Chem. Int. Ed. 59 (13), 5350–5354.

Weekes, D.M., Salvatore, D.A., Reyes, A., Huang, A., Berlinguette, C.P., 2018. Electrolytic CO_2 reduction in a flow cell. Acc. Chem. Res. 51 (4), 910–918.

Wei, X., Pu, M., Jin, Y., Wessling, M., 2021. Efficient electrocatalytic N_2 reduction on three-phase interface coupled in a three-compartment flow reactor for the ambient NH_3 synthesis. ACS Appl. Mater. Interfaces 13 (18), 21411–21425.

Westhead, O., Jervis, R., Stephens, I.E.L., 2021. Is lithium the key for nitrogen electroreduction? Science 372 (6547), 1149–1150.

Wu, Z.-Y., Karamad, M., Yong, X., Huang, Q., Cullen, D.A., Zhu, P., Xia, C., Xiao, Q., Shakouri, M., Chen, F.-Y., Kim, J.Y., Xia, Y., Heck, K., Hu, Y., Wong, M.S., Li, Q.,

Gates, Siahrostami, S., Wang, H., 2021. Electrochemical ammonia synthesis via nitrate reduction on Fe single atom catalyst. Nat. Commun. 12, 2870.

Yang, K., Kas, R., Smith, W.A., Burdyny, T., 2021. Role of the carbon-based gas diffusion layer on flooding in a gas diffusion electrode cell for electrochemical CO_2 reduction. ACS Energy Lett. 6 (1), 33–40.

Yang, X., Nash, J., Anibal, J., Dunwell, M., Kattel, S., Stavitski, E., Attenkofer, K., Chen, J.G., Yan, Y., Xu, B., 2018. Mechanistic insights into electrochemical nitrogen reduction reaction on vanadium nitride nanoparticles. J. Am. Chem. Soc. 140 (41), 13387–13391.

Yao, D., Tang, C., Li, L., Xia, B., Vasileff, A., Jin, H., Zhang, Y., Qiao, S.-Z., 2020. In situ fragmented bismuth nanoparticles for electrocatalytic nitrogen reduction. Adv. Energy Mater. 10 (33), 2001289.

Zhang, L., Miyazawa, T., Kitazumi, Y., Kakiuchi, T., 2012. Ionic liquid salt bridge with low solubility of water and stable liquid junction potential based on a mixture of a potential-determining salt and a highly hydrophobic ionic liquid. Anal. Chem. 84 (7), 3461–3464.

Zhang, L., Mallikarjun Sharada, S., Singh, A.R., Rohr, B.A., Su, Y., Qiao, L., Nørskov, J.K., 2018. A theoretical study of the effect of a non-aqueous proton donor on electrochemical ammonia synthesis. Phys. Chem. Chem. Phys. 20 (7), 4982–4989.

Zhang, X.i., Wang, Y., Liu, C., Yu, Y., Lu, S., Zhang, B., 2021. Recent advances in non-noble metal electrocatalysts for nitrate reduction. Chem. Eng. J. 403, 126269.

Zhao, Y., Shi, R., Bian, X., Zhou, C., Zhao, Y., Zhang, S., Wu, F., Waterhouse, G.I.N., Wu, L.-Z., Tung, C.-H., Zhang, T., 2019. Ammonia detection methods in photocatalytic and electrocatalytic experiments: How to improve the reliability of NH_3 production rates? Adv. Sci. 6 (8), 1802109.

Zhao, X., Hu, G., Chen, G.-F., Zhang, H., Zhang, S., Wang, H., 2021. Comprehensive understanding of the thriving ambient electrochemical nitrogen reduction reaction. Adv. Mater. 33 (33), 2007650.

Zhou, F., Azofra, L.M., Ali, M., Kar, M., Simonov, A.N., McDonnell-Worth, C., Sun, C., Zhang, X., MacFarlane, D.R., 2017. Electro-synthesis of ammonia from nitrogen at ambient temperature and pressure in ionic liquids. Energy Environ. Sci. 10 (12), 2516–2520.

Zou, H., Rong, W., Wei, S., Ji, Y., Duan, L., 2020. Regulating kinetics and thermodynamics of electrochemical nitrogen reduction with metal single-atom catalysts in a pressurized electrolyser. Proc. Natl. Acad. Sci. U. S. A. 117 (47), 29462–29468.

Chapter 3

In Situ Fragmented Bismuth Nanoparticles for Electrocatalytic Nitrogen Reduction

3.1 Introduction and Significance

Electrochemical NRR provides a promising alternative to the energy-intensive H-B process for green ammonia synthesis. However, the activity and selectivity of NRR are highly limited by the large energy barrier for N_2 activation and competing hydrogen evolution reaction. Among various electrocatalyst candidates, bismuth-based materials have gained extensive attention owing to their unique electronic structures and poor hydrogen evolution. However, the identification of real active sites and reaction mechanism is still under debate due to potential-dependent variation of structure and chemical states. To address this issue, we employed Bi-based metal-organic framework (Bi-MOF) as the pre-catalyst to study the mechanism of electrochemical NRR. Our work reveals the importance of monitoring and optimizing both the electronic and geometry structures of electrocatalysts under real NRR conditions towards higher activity and selectivity. The highlights of this work include:

(1) In situ electrochemical reduction and fragmentation method was reported to synthesize densely packed Bi^0 nanoparticles (NPs) as highly active NRR electrocatalysts. In 0.10 M Na_2SO_4, the in situ synthesized Bi NPs can achieve an NH3 yield of 3.25 $\pm$ 0.08 µg cm^{-2} h^{-1} at -0.7 V vs RHE and a Faradaic efficiency of 12.11 $\pm$ 0.84 % at –0.6 V vs RHE.

(2) In situ Raman spectra was employed to investigate the structural reconstruction and chemical transformation of Bi species during NRR. The Bi-MOF pre-catalyst should be fully reduced to metallic Bi^0 species and fragmented into nanoparticles under NRR potentials more negative than –0.5 V vs RHE.

(3) Online DEMS was employed to monitor the real-time products and intermediates during NRR. NH_3 and N_2H_2 were unambiguously detected, which suggested a new NRR pathway through two-step reduction and decomposition ($N_2 \rightarrow N_2H_2 \rightarrow NH_3$).

(4) In-depth understanding of the activity origin of Bi-based NRR electrocatalysts. Combing the in situ characterizations and electrochemical evaluations, the zero-valent Bi^0 is identified as the active species, and the fragmented nanostructure is important to enhance the activity and selectivity due to enriched edge sites and space confinement effect.

3.2 In Situ Fragmented Bismuth Nanoparticles for Electrocatalytic Nitrogen Reduction

This chapter is included as it appears as a journal paper published by Dazhi Yao, Cheng Tang, Laiquan Li, Bingquan Xia, Anthony Vasileff, Huanyu Jin, Yanzhao Zhang and Shi-Zhang Qiao. In situ fragmented bismuth nanoparticles for electrocatalytic nitrogen reduction, Adv. Energy Mater. 2020, 10, 2001289.

Statement of Authorship

Title of Paper	In Situ Fragmented Bismuth Nanoparticles for Electrocatalytic Nitrogen Reduction
Publication Status	☑ Published ☐ Accepted for Publication ☐ Submitted for Publication ☐ Unpublished and Unsubmitted work written in manuscript style
Publication Details	D. Yao, C. Tang, L. Li, B. Xia, A. Vasileff, H. Jin, Y. Zhang, S. Z. Qiao, Advanced Energy Materials 2020, 10, 2001289

Principal Author

Name of Principal Author (Candidate)	Dazhi Yao
Contribution to the Paper	Designed and conducted the experiments, analysed the data, wrote the manuscript.
Overall percentage (%)	70%
Certification:	This paper reports on original research I conducted during the period of my Higher Degree by Research candidature and is not subject to any obligations or contractual agreements with a third party that would constrain its inclusion in this thesis. I am the primary author of this paper.
Signature	Date 28/09/2022

Co-Author Contributions

By signing the Statement of Authorship, each author certifies that:

i.   the candidate's stated contribution to the publication is accurate (as detailed above);

ii.   permission is granted for the candidate in include the publication in the thesis; and

iii.   the sum of all co-author contributions is equal to 100% less the candidate's stated contribution.

Name of Co-Author	Cheng Tang
Contribution to the Paper	Guided to design the whole experiment, helped data analysis, and revised the manuscript
Signature	Date 28/09/2022

Name of Co-Author	Laiquan Li
Contribution to the Paper	Guidance on the experimental setup and provided valuable insights into paper discussions
Signature	Date 28/09/2022

Name of Co-Author	Bingquan Xia		
Contribution to the Paper	Material synthesis and data analysis		
Signature		Date	28/09/2022

Name of Co-Author	Anthony Vasileff		
Contribution to the Paper	Assisted in characterization and data analysis. Provided review and comments on the manuscript.		
Signature		Date	28/09/2022

Name of Co-Author	Huanyu Jin		
Contribution to the Paper	Assisted in characterization and data analysis. Provided review and comments on the manuscript.		
Signature		Date	28/09/2022

Name of Co-Author	Yanzhao Zhang		
Contribution to the Paper	Assisted in characterization and data analysis.		
Signature		Date	28/09/2022

Name of Co-Author	Shi-Zhang Qiao		
Contribution to the Paper	Supervision of the work, discussion and conceptualization of this manuscript and manuscript evaluation and revision.		
Signature		Date	28/09/2022

In Situ Fragmented Bismuth Nanoparticles for Electrocatalytic Nitrogen Reduction

Dazhi Yao, Cheng Tang, Laiquan Li, Bingquan Xia, Anthony Vasileff, Huanyu Jin, Yanzhao Zhang, and Shi-Zhang Qiao*

The electrochemical nitrogen reduction reaction (NRR) is a promising alternative to the energy-intensive Haber–Bosch process for ammonia synthesis. Among the possible electrocatalysts, bismuth-based materials have shown unique NRR properties due to their electronic structures and poor hydrogen evolution activity. However, identification of the active sites and reaction mechanism is still difficult due to structural and chemical changes under reaction potentials. Herein, in situ Raman spectroscopy, complemented by electron microscopy, is employed to investigate the structural and chemical transformation of the Bi species during the NRR. Nanorod-like bismuth-based metal–organic frameworks are reduced in situ and fragment into densely contacted Bi^0 nanoparticles under the applied potentials. The fragmented Bi^0 nanoparticles exhibit excellent NRR performance in both neutral and acidic electrolytes, with an ammonia yield of 3.25 ± 0.08 μg cm^{-2} h^{-1} at -0.7 V versus reversible hydrogen electrode and a Faradaic efficiency of $12.11 \pm 0.84\%$ at -0.6 V in 0.10 M Na_2SO_4. Online differential electrochemical mass spectrometry detects the production of NH_3 and N_2H_2 during NRR, suggesting a possible pathway through two-step reduction and decomposition. This work highlights the importance of monitoring and optimizing the electronic and geometric structures of the electrocatalysts under NRR conditions.

Artificial nitrogen fixation to ammonia (NH_3) is one of the most fundamental technologies for the sustainable development of modern society given that NH_3 is used as a nitrogen source in agricultural fertilizers, a chemical feedstock for many industrial processes, and a high-energy-density carrier for renewable hydrogen.[1,2] Currently, the industrial production of NH_3 remains highly dependent on the capital-, energy-, and emission-intensive Haber–Bosch process. To achieve green and sustainable production of NH_3, extensive research has been devoted to investigating the electrochemical nitrogen reduction reaction

(NRR) under ambient conditions and powered by renewable electricity.[3–7] However, the electrochemical NRR suffers from poor activity and selectivity, mainly owing to: 1) a large energy barrier for activating and breaking the strong N≡N triple bond, 2) sluggish reaction kinetics and a complex reaction pathway involving six proton-coupled electron transfer steps, and; 3) the competing hydrogen evolution reaction (HER) on nearly all metal-based catalyst surfaces in aqueous systems.[8–11] Therefore, it is crucial to find potential NRR electrocatalysts with high activity and selectivity.

Among the various reported NRR electrocatalysts (e.g., noble metals, transition metal compounds, heteroatom-doped carbon, and single-atom catalysts),[10,12–21] bismuth (Bi)-based materials are very attractive for both electrochemical and photocatalytic nitrogen reduction due to their unique electronic structures.[22–24] These materials include: amorphous $Bi_4V_2O_{11}$/CeO_2 hybrid,[25] vacancy-rich $BiVO_4$,[26] Bi nanosheets,[27,28] defect-rich Bi (110) nanoplates,[29] Bi nanodendrites,[30] and ultrathin porous Bi_5O_7I nanotubes.[31] The Bi 6p band can provide localized electrons for back-donation to the π* anti-bonding orbitals of adsorbed N_2 molecules, enabling efficient activation and reduction.[10,23,31] The semiconducting Bi can also effectively suppress the HER due to the high free energy barrier for hydrogen adsorption and limited electron accessibility on its surface.[11,27,32] Both experimental evaluations and theoretical studies have shown that the oxygen vacancies in bismuth compounds and the defective edges in bismuth metal structures are the active NRR sites.[25,29] However, considering the possible reduction and reconstruction of Bi-based nanomaterials which occur during NRR conditions, a comprehensive view of the activity origin on these materials is still lacking.[27,33] This transformation could be responsible for the resultant electrochemical activity, but highly limits the accuracy and reproducibility of NRR performance tests and hinders the identification of the active sites.

Recent advances in in situ/operando studies have provided profound insight into the crucial role of the potential-driven changes to morphology, crystal structure, and chemical state during electrochemical oxidation or reduction reactions.[34,35] A

D. Yao, Dr. C. Tang, L. Li, B. Xia, A. Vasileff, H. Jin, Y. Zhang,
Prof. S.-Z. Qiao
Centre for Materials in Energy and Catalysis
School of Chemical Engineering and Advanced Materials
The University of Adelaide
Adelaide, SA 5005, Australia
E-mail: s.qiao@adelaide.edu.au

The ORCID identification number(s) for the author(s) of this article can be found under https://doi.org/10.1002/aenm.202001289.

**ADVANCED
SCIENCE NEWS**

www.advancedsciencenews.com

**ADVANCED
ENERGY
MATERIALS**

www.advenergymat.de

well-known case study is that of oxide-derived copper (OD-Cu), which shows significantly higher activity and C_{2+} selectivity in CO_2 electroreduction compared to copper itself.[35,36] Some groups have demonstrated that the presence of a small amount of subsurface oxygen or residual Cu_2O phase in OD-Cu could increase CO binding energy and favor C—C coupling.[37,38] Others have shown that the oxide precursors are fully reduced to metallic Cu^0, but fragment into densely contacted nanoparticles during reaction.[39,40] Consequently, abundant grain boundaries and high-index facets are formed which can facilitate C—C coupling.[39,40] Other oxide-derived materials like OD-Au[41] and OD-Ag[42] have also been successfully employed for CO_2 electroreduction. Compared with polycrystalline Au and Ag, OD-Au and OD-Ag could effectively increase the stabilization of $CO_2^{\cdot-}$ or $COOH^{\cdot}$ intermediates on their surfaces and thus enhance activity and selectivity. Analogously, monitoring and identifying the real surface structure and chemical state of Bi-based materials under NRR conditions is of great importance to establish a definitive correlation between structure and performance. It can accelerate the comprehensive understanding of the reaction mechanism, and provide more accurate design principles for the rational development of Bi-based NRR electrocatalysts.

In this work, we employed a Bi-based metal–organic framework (Bi-MOF) as the precursor (precatalyst) to study the mechanism of electrochemical NRR. Under the applied negative potentials, the Bi-MOF was reduced to metallic Bi^0 species and the nanorod morphology fragmented into densely packed nanoparticles (NPs). In situ Raman spectroscopy was used to investigate the chemical and structural transformation of the Bi species during the NRR, which was complemented by scanning electron microscopy (SEM) and transmission electron microscopy (TEM). The electrochemical NRR performance was evaluated in both neutral and acidic conditions. Ammonia was quantitatively determined by UV–vis spectroscopy and ion chromatography (IC), and was confirmed with $^{15}N_2$ isotope-labeling tests. In addition, online differential electrochemical mass spectrometry (DEMS) was employed for in situ mass-resolved determination of volatile electrochemical reaction intermediates and products, which confirmed the NRR activity and identified the reaction pathway on zero-valent bismuth catalysts.

The Bi-MOF was synthesized using a modified solvothermal reaction between BiOI nanosheets and trimesic acid (H_3BTC).[43,44] SEM and TEM images show that the as-synthesized Bi-MOF exhibits a nanorod-like structure with an average length of ≈4 µm and width of ≈100 nm (**Figure 1**a; and Figure S1, Supporting Information). The X-ray diffraction (XRD) patterns are indexed to CAU-17 [Bi(BTC)(H_2O)] with some characteristic diffraction peaks of residual BiOI precursors (Figure S2, Supporting Information).[44] The utilization of ultrathin BiOI nanosheets as precursors is essential for the successful synthesis of the nanosized Bi-MOF.[44] Although the Bi—O bonds in the Bi-MOF are stable in the presence of water,[43] they are likely reduced and reorganized during NRR tests due to the large cathodic potential and solvent-assisted ligand exchange effect.[27,45] Figure S3 (Supporting Information) shows the cyclic voltammograms of Bi-MOF recorded in N_2-saturated 0.10 M Na_2SO_4. The broad reduction peak in the first cathodic sweep is ascribed to the poor conductivity of the Bi-MOF and the high

energy barrier to initiate the structural disassembly. This phenomenon also coincides with the electrochemical impedance spectrum results (Figure S4, Supporting Information), where Bi-MOF exhibits a large charge-transfer resistance ($R_{ct} = 1233$ Ω). After 20 cycles, the cyclic voltammetry (CV) curves become stable with a pair of redox peaks between 0 and −1.0 V versus reversible hydrogen electrode (RHE), indicating the transformation of Bi-MOF to another steady Bi species, which is identified as metallic Bi^0 NPs by microscopy and spectroscopy characterizations. SEM images of the precatalyst-loaded electrode clearly confirm the transformation of the nanorod structure of Bi-MOF into nanoparticles after consecutive CV treatments (Figure 1b; and Figure S5a, Supporting Information). TEM images show that these nanoparticles are formed from much smaller nanoparticles with an average size of ≈5 nm (Figure 1c; and Figure S5b,c, Supporting Information). These crystalline nanoparticles exhibit clear lattice fringes with a spacing of 0.373 nm corresponding to the Bi (101) facet (inset of Figure 1c), which is consistent with the XRD patterns. All the XRD peaks assigned to the Bi-MOF disappear after electrochemical reaction, and the newly generated peaks can be indexed to rhombohedral Bi (JCPDS No.44-1246). Other peaks in the diffraction pattern are related to the carbon paper substrate (Figure S2, Supporting Information). Compared to the Bi-MOF precatalyst, the in situ obtained Bi NPs exhibit a much smaller charge-transfer resistance ($R_{ct} = 18.58$ Ω), which is beneficial for the electrocatalytic NRR process.[46–48]

To gain insight into the structural and chemical conversion of the Bi species, in situ Raman spectroscopy was used to monitor the electrochemical reduction process. A screen-printed electrode coated with Bi-MOF was studied under a thin electrolyte film (N_2-saturated 0.10 M Na_2SO_4). As displayed in Figure 1d,e, two pronounced bands can be observed at 86 and 152 cm^{-1} for the Bi-MOF sample at −0.1 V versus RHE, which are slightly shifted compared with the bulk Bi-MOF material (Figure S6a, Supporting Information). When the applied potential is stepped negatively from −0.1 to −0.3 V versus RHE, the bands at 86 and 152 cm^{-1} decrease in intensity, and two weak bands appear around 69 and 93 cm^{-1}, which can be assigned to the E_g and A_{1g} stretching modes of Bi—Bi bonds.[49,50] When potentials more negative than −0.5 V versus RHE are applied, the initial three bands disappear, and the bands around 69 and 93 cm^{-1} both increase in intensity, confirming the complete transformation of the Bi-MOF to metallic Bi^0 NPs. Note that the E_g and A_{1g} stretching modes of Bi—Bi bonds may shift with changes of morphology, such as a redshift of E_g mode from 69 cm^{-1} for nanoparticles to 71 cm^{-1} for nanosheets.[27,49] Therefore, by combining the in situ Raman spectroscopy results with the SEM, TEM, and XRD characterizations, we can conclude that the Bi-MOF nanorods undergo significant structural rearrangement and chemical change to Bi NPs during electrochemical reduction (Figure 1f). The in situ reduced metallic Bi^0 is found to be the dominant Bi species on the electrode for electrochemical NRR under potentials more negative than −0.5 V versus RHE.

The electrochemical NRR performance of the Bi NPs was evaluated using a two-compartment gas-tight H-cell under ambient temperature and pressure. The anodic and cathodic chambers were each filled with 30 mL of electrolyte, and separated by a pretreated proton-exchange membrane
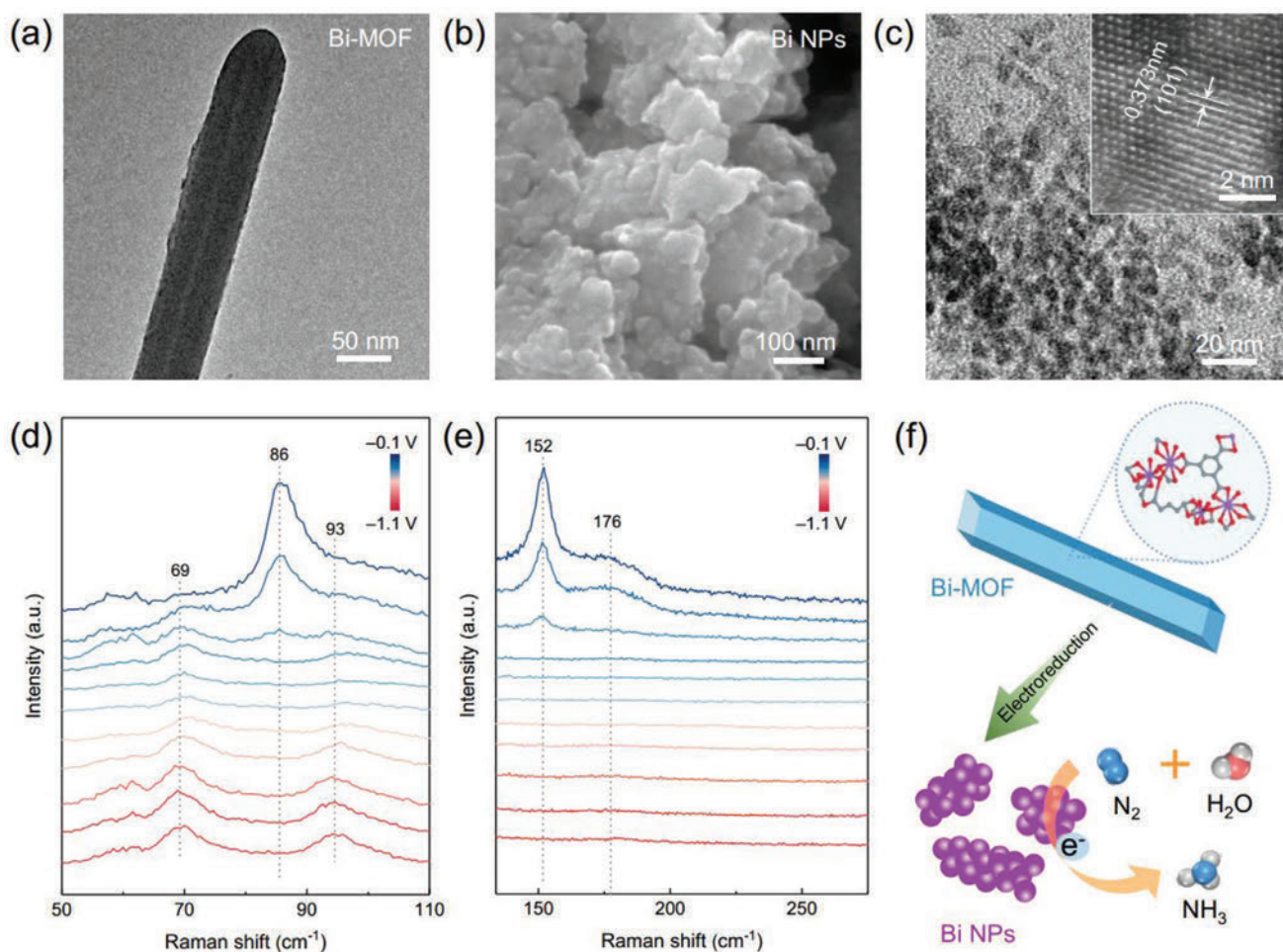
**ADVANCED
SCIENCE NEWS**

www.advancedsciencenews.com

**ADVANCED
ENERGY
MATERIALS**

www.advenergymat.de

Figure 1. Characterization of in situ transformation from Bi-MOF to Bi NPs. a) TEM image of Bi-MOF. b) High-resolution SEM image and c) TEM images of Bi NPs obtained after in situ reduction. d,e) In situ Raman spectra of the catalyst immersed into a thin electrolyte film with applied potential from −0.1 to −1.1 V versus RHE. f) Schematic diagram for the in situ electroreduction-derived transformation from nanorods to nanoparticles.

(Nafion 117). Ultrahigh-purity N_2 gas (99.999%) was first purged into the cathodic chamber for 20 min and then constantly bubbled (20 mL min^{-1}) throughout the whole electrolysis process. Magnetic stirring at 500 rpm was applied in the cathodic chamber to facilitate mass transfer. Two consecutive acid traps (5 mL of 0.05 M H_2SO_4 in each) were linked to the cathodic chamber to collect ammonia in the off-gas. The Bi-MOF precatalyst was loaded onto carbon paper at a loading of ≈0.5 mg cm^{-2}, and electrochemically reduced by a 20-cycle CV treatment in N_2-saturated 0.10 M Na_2SO_4 (Figure S3, Supporting Information). In the initial study of NRR activity, we first evaluated the polarization curves of in situ reduced Bi NPs. Linear sweep voltammetry was employed with a scan rate of 5.0 mV s^{-1} in N_2 or Ar saturated 0.10 M Na_2SO_4 (Figure S7, Supporting Information). The reduction current density below −0.6 V versus RHE in N_2 is slightly larger than that in Ar, implying that the Bi NPs may catalyze the reduction of N_2. The electrochemical NRR performance of the in situ synthesized Bi NPs was further evaluated by 1 h chronoamperometry tests under different potentials (from −0.4 to −0.9 V vs RHE) in N_2-saturated 0.10 M Na_2SO_4 aqueous solution. The electrolyte for the first cycle (20 CV

scans and 1 h electrolysis) was discarded to exclude any possible preabsorbed ammonia contamination for each newly prepared electrode. **Figure 2**a displays the chronoamperometry curves at different applied potentials. The current density increases significantly when the applied potential shifts from −0.4 to −0.9 V versus RHE. After electrolysis at a given potential, the produced ammonia in the anodic chamber, cathodic chamber, and acid traps was quantitatively determined by the indophenol blue method. The standard curves for ammonia concentration in 0.10 M Na_2SO_4 and 0.05 M H_2SO_4 are shown in Figures S8 and S9 (Supporting Information). The UV–vis absorption spectra obtained for each potential are displayed in Figure S10 (Supporting Information). As shown in Figure 2b and Figure S10d (Supporting Information), the in situ synthesized Bi NPs achieve a maximum NH_3 yield of 3.25 ± 0.08 μg cm^{-2} h^{-1} at −0.7 V versus RHE and maximum faradaic efficiency (FE) of 12.11 ± 0.84% at −0.6 V versus RHE, which are comparable with previously reported bismuth catalysts (Table S1, Supporting Information).[25–31,51–53] N_2H_4 cannot be detected in the electrolytes after 1 h electrolysis by the Watt and Chrisp method (Figures S11 and S12, Supporting Information). The

**ADVANCED
SCIENCE NEWS**

www.advancedsciencenews.com

**ADVANCED
ENERGY
MATERIALS**

www.advenergymat.de
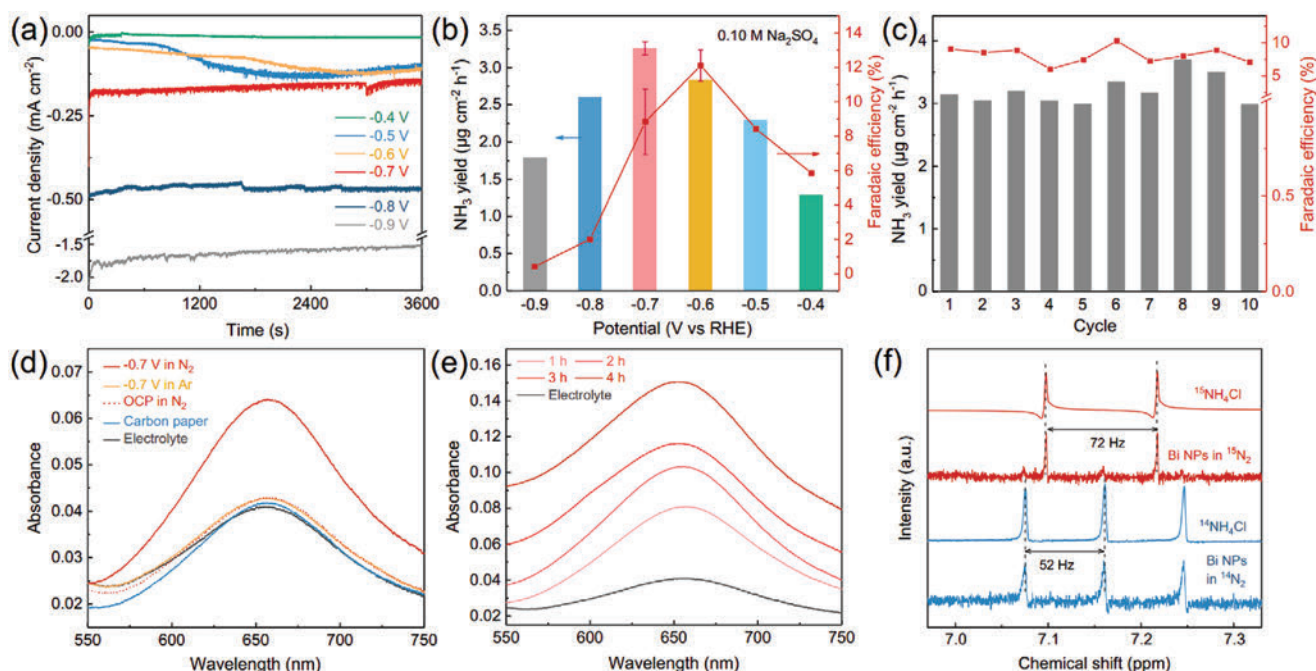
Figure 2. Electrochemical NRR performance in 0.10 M Na_2SO_4. a) Chronoamperometry responses of Bi NPs at different applied potentials in N_2-saturated 0.10 M Na_2SO_4. b) Ammonia yield and Faradaic efficiency of Bi NPs at different potentials. c) Stability test for 10 cycles at -0.7 V versus RHE. d) UV–vis spectra of cathodic electrolytes stained with indophenol indicator for control tests and e) for NRR tests with different electrolysis time. f) ^{1}H NMR spectra of both $^{14}NH_4^+$ and $^{15}NH_4^+$ produced from NRR (at -0.7 V vs RHE) using $^{14}N_2$ and $^{15}N_2$ as the nitrogen source, respectively. NMR responses (y-axis) for standard samples ($^{15}NH_4Cl$ and $^{14}NH_4Cl$) were shrunk by 20 fold numerically. Ammonia yields determined in the anodic chamber, cathodic chamber, and acid trap in panel (b) were omitted for clarity but the details can be found in Figure S10 (Supporting Information).

electrocatalytic stability of the Bi NPs was evaluated by consecutive cycling tests at -0.7 V versus RHE without changing the electrode and Nafion membrane. The NH_3 yield and FE only slightly fluctuate during 10 tests (Figure 2c; and Figures S13 and S14, Supporting Information). No obvious variations in the morphology and size of the Bi NPs is observed after long-term NRR tests (Figure S15, Supporting Information), further revealing their high stability for electrochemical NRR.

The electrochemical reduction of N_2 to NH_3 on Bi NPs was unambiguously confirmed by a series of control tests, observed product accumulation, and isotope labeling tests. As shown in Figure 2d, negligible ammonia is detected in the freshly prepared electrolyte, electrolysis at -0.7 V in Ar-saturated electrolyte (-0.7 V in Ar), Bi NPs under open circuit potential in N_2-saturated electrolyte (OCP in N_2), and electrolysis with bare carbon paper in N_2-saturated electrolyte. Further, accumulation of ammonia concentration is observed in the cathodic chamber over 4 h of electrolysis in N_2-saturated electrolyte at -0.7 V versus RHE (Figure 2e). Isotope labeling experiments and ^{1}H NMR spectroscopy demonstrate that an obvious doublet around 7.2 ppm ($J = 72$ Hz) assigned to $^{15}NH_4^+$ can be detected using $^{15}N_2$ (98 at% ^{15}N, CAS: 29817-79-6) as the feed gas (Figure 2f). A very weak but identifiable triplet ($J = 52$ Hz) assigned to $^{14}NH_4^+$ can also be observed, which is most likely due to trace contamination in the electrolyte and $^{15}N_2$ gas.[4,8,54] However, the integration of peaks for $^{15}NH_4^+$ is nearly four times that of $^{14}NH_4^+$ (Figure S16, Supporting Information), and the triplet obtained during $^{15}N_2$ tests is significantly lower than that obtained during $^{14}N_2$ tests (Figure 2f). Therefore, we

confirm that the ammonia product originates from the electrochemical reduction of N_2 on the Bi NPs.

To study the pH effect on NRR performance, we also evaluated the Bi NPs in 0.05 M H_2SO_4 (Figure S17, Supporting Information). In this case, both the indophenol blue method with UV–vis spectroscopy and IC were performed to quantify the ammonia concentration (Figures S18–S20, Supporting Information). IC technique is very attractive for the quantitative detection of ammonia due to its high sensitivity, low detection limit, fast response, and low-cost in operation,[55,56] but the NH_4^+ signal can be interfered by the high Li^+ and Na^+ signals in common neutral electrolytes. In 0.05 M H_2SO_4, the peak with a retention time of 9.7 min is assigned to NH_4^+, and its peak area is linearly correlated with the concentration of NH_4^+ (Figure S19, Supporting Information). As shown in **Figure 3**a, results from these two quantitative methods have an acceptable relative error (<10%). It meets the requirement of instrumental analysis and confirms the reliability of the indophenol blue method. When compared with that in the neutral electrolyte, a similar trend of NH_3 yield in the potential range from -0.4 to -0.9 V versus RHE is achieved, with the highest NH_3 yield of 3.03 ± 0.03 µg cm^{-2} h^{-1} occurring at -0.7 V versus RHE (Figure 3a). However, the FE in acid decreases dramatically when the potential is more negative than -0.4 V versus RHE (Figure 3b), and the value at -0.7 V versus RHE is only $1.42 \pm 0.21\%$, which is nearly one magnitude lower than that in neutral. Nørskov and co-workers revealed that the rate of NRR is zeroth order in electron and proton concentrations, while the rate of HER is first order in both.[11] Thus, the HER activity

ADVANCED
SCIENCE NEWS
www.advancedsciencenews.com

ADVANCED
ENERGY
MATERIALS
www.advenergymat.de
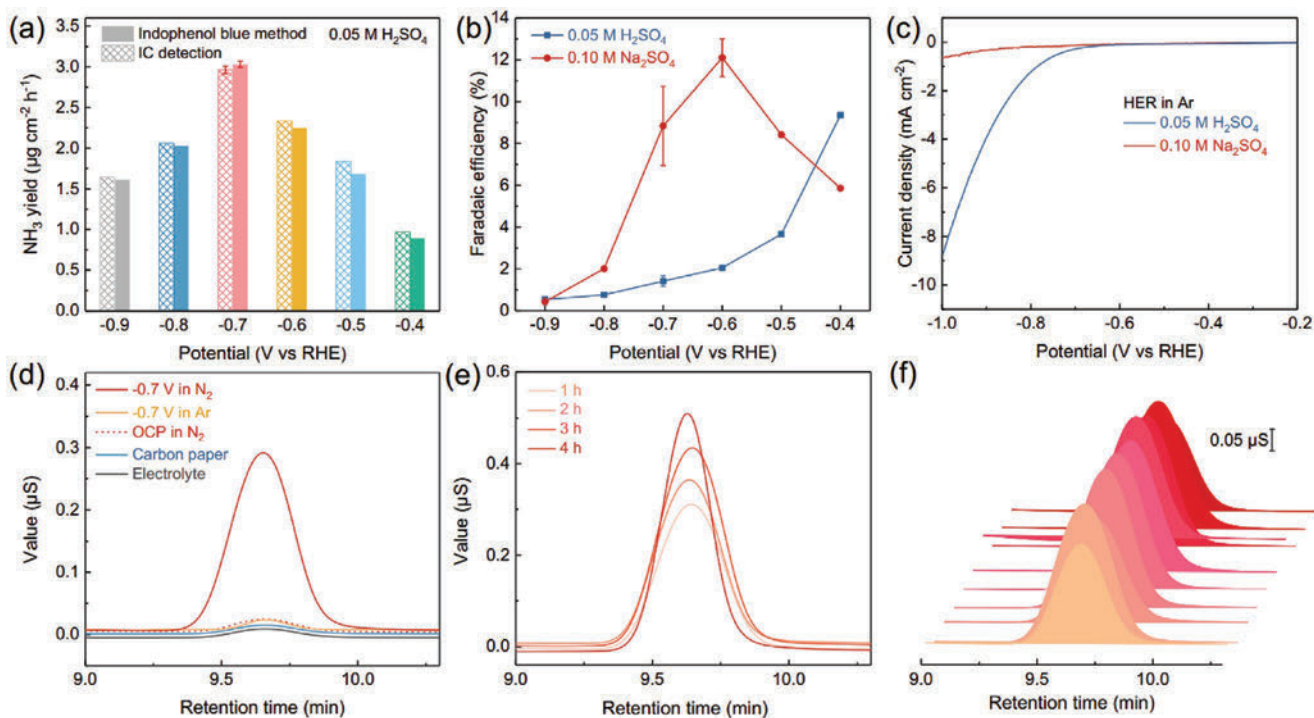
Figure 3. Electrochemical NRR performance in 0.05 M H_2SO_4. a) Ammonia yield at different potentials determined by indophenol blue method and IC technique, respectively. b) Faradaic efficiency comparison for Bi NPs at different potentials in 0.05 M H_2SO_4 and 0.10 M Na_2SO_4, respectively. c) HER current density of Bi NPs in Ar-saturated 0.10 M Na_2SO_4 and 0.05 M H_2SO_4 at the scan rate of 50 mV s^{-1}. d) IC responses of cathodic electrolytes for control tests and e) for NRR tests with different electrolysis time. f) IC responses of cathodic electrolytes for 10-cycle NRR tests at −0.7 V versus RHE in 0.05 M H_2SO_4.

will be significantly enhanced due to the abundant electrons and protons in acid, as confirmed by the cathodic polarization curves of Bi NPs in Ar-saturated 0.10 M Na_2SO_4 and 0.05 M H_2SO_4 (Figure 3c). Rigorous control tests, product accumulation, and stability were also investigated in the acidic electrolyte, and the obtained ammonia was quantified by IC. Only trace amounts of ammonia is detected in the freshly prepared electrolyte, and no obvious increase is observed in all of the control experiments (Figure 3d). It is consistent with results in the neutral electrolyte determined by the indophenol blue method (Figure 2d). The peak area generally increases with electrolysis time (Figure 3e), and remains nearly constant for 10 cycling tests at −0.7 V versus RHE (Figure 3f; and Figure S21, Supporting Information). Therefore, the in situ synthesized Bi NPs are also stable and active for electrochemical NRR in acidic conditions. However, the pH of the electrolytes should be carefully selected to optimize selectivity.

The electrochemical NRR process was further investigated by online DEMS to monitor the volatile intermediates and products (**Figure 4**a, see the Experimental Details in the Supporting Information).[57–59] The DEMS measurements were carried out in a thin layer flow cell without separation between the cathodic and anodic chambers. To rigorously identify the mass-to-charge ratio (m/z) signals, the standard mass spectra of all possible species (NH_3, O_2, N_2, H_2O, N_2H_4) are provided in Figures S22–S26 (Supporting Information). As summarized in Table S2 (Supporting Information), the existence of m/z signals at 27, 30, 31, and 33 can be attributed exclusively to the formation of N_2H_4,

and the signal at 15 can be assigned to either NH_3 or N_2H_4. Figure 4b and Figure S27 (Supporting Information) record the typical online DEMS results of Bi NPs under −0.7 V versus RHE in N_2-saturated 0.10 M Na_2SO_4. The absence of m/z signals at 27, 31, and 33 indicates that no featured fragments from N_2H_4 are detected, which is also supported by the Watt and Chrisp method (Figure S12, Supporting Information). Thus, the obvious m/z signal at 15 confirms the formation of NH_3 in the products. In contrast, no ammonia-related fragments can be detected when Ar is used as the feed gas, and all the signals are assigned to H_2O in the electrolyte and O_2 generated on the anode (Figure S28, Supporting Information). Figure 4c shows that the intensity (colored area) of the m/z signal at 17 (NH_3) varies with the applied voltage, and the highest value is achieved at −0.7 V versus RHE, in good accordance with the electrochemical results obtained in the H-cell (Figure 2b). Although m/z at 17 may arise from evaporated water, the fragment from water does not vary with potential. Therefore, we reasonably assume that the NRR process can be tracked using an m/z of 17. Further, the ion current shows a time-dependence when a negative potential is applied to the catalyst in N_2-saturated electrolyte. As shown in Figure 4d, the integrated ion current increases with electrolysis time, while there is an absence of signal when the potential was not applied. Also note that the m/z signal at 30 during the NRR is weak but recognizable (2×10^{-11}, Figure S27, Supporting Information), indicating the presence of N_2H_2.[59] Recently, Shao and co-workers detected a N_2H_x ($0 \leq x \leq 2$) intermediate of the NRR on Rh by surface-enhanced
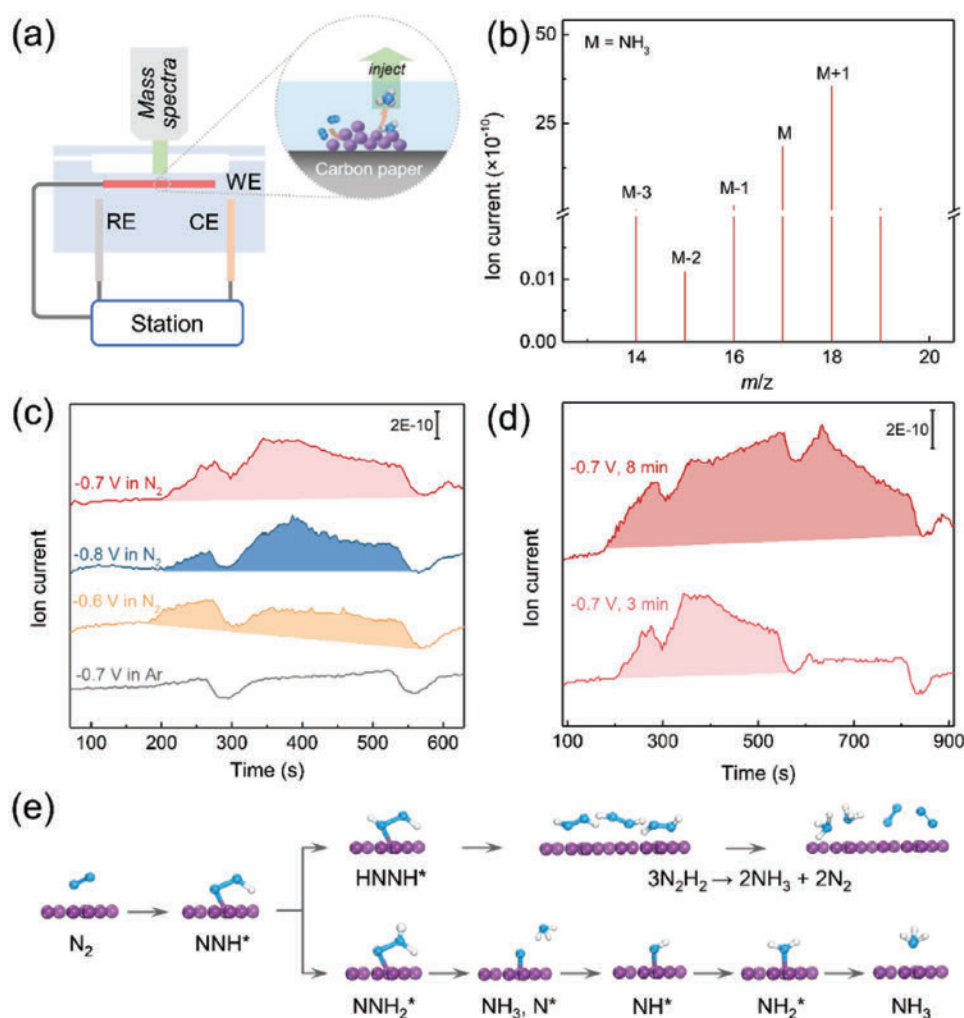
Figure 4. Online DEMS investigation. a) Schematic illustration of the DEMS technique for the real-time detection of volatile intermediates and products during NRR. b) Mass spectra obtained during NRR tests with Bi NPs at -0.7 V versus RHE in N_2-saturated 0.10 M Na_2SO_4. c) Ion current responses of the m/z signal at 17 at different reaction potentials and conditions. d) Ion current responses of the m/z signal at 17 for different NRR test time at -0.7 V versus RHE in N_2-saturated 0.10 M Na_2SO_4. e) Possible reaction pathways of NRR on the surface of Bi NPs.

infrared absorption spectrometry (SEIRAS) and DEMS, and proposed a new two-step reaction pathway for NRR.[59] Analogously, the possible reaction pathway for NRR on the Bi surface is proposed and illustrated in Figure 4e. In this pathway, the absorbed N_2 molecule on edge or defective sites first reduces to N_2H_2* by a two-electron transfer process. This is then followed by its desorption and decomposition in the electrolyte to form NH_3 ($3N_2H_2 \rightarrow 2NH_3 + 2N_2$).[59,60] However, the possibility of the distal associative pathway cannot be completely ruled out, which involves the sequential hydrogenation on the outer N atom, release of one NH_3, and continuing hydrogenation for another NH_3 molecule.[29]

In conclusion, we utilized electrochemical reduction to fabricate zero-valent metallic bismuth nanoparticles (Bi NPs) in situ from a Bi-MOF for electrochemical NRR under ambient conditions. The structural reconstruction and chemical transformation of the bismuth species during electroreduction was investigated by in situ Raman spectroscopy for the first time. The MOF-derived Bi NPs are densely assembled from

nanosized crystalline nanoparticles ($\approx$5 nm) and achieve significant activity and stability for the electrochemical NRR in both neutral and acidic conditions. In 0.10 M Na_2SO_4, the in situ synthesized Bi NPs achieve an NH_3 yield of 3.25 ± 0.08 µg cm^{-2} h^{-1} at -0.7 V versus RHE and a FE of $12.11 \pm 0.84\%$ at -0.6 V versus RHE. In 0.05 M H_2SO_4, the NH_3 yield achieved is similar, but the FE decreases by an order of magnitude due to the much higher HER activity in acid. The online DEMS study detects the production of NH_3 and N_2H_2 during the NRR, which suggests an associative pathway is a possible NRR mechanism on the bismuth surface. The in situ investigation of both the material and reaction products in this work confirms that metallic bismuth (Bi^0) is active for electrochemical NRR. This work demonstrates the importance of studying the potential-dependent transformations of precatalysts, either intentionally via pretreatment processes or incidentally during in situ reactions, which may affect the reproducibility of electrochemical tests and alter the resulting performance. It is anticipated that this work will provide new insight and strategies for material

**ADVANCED
SCIENCE NEWS**

www.advancedsciencenews.com

**ADVANCED
ENERGY
MATERIALS**

www.advenergymat.de

design, catalyst monitoring, and reaction pathway study in this field, and ultimately benefit the development of electrochemical ammonia synthesis.

Supporting Information

Supporting Information is available from the Wiley Online Library or from the author.

Conflict of Interest

The authors declare no conflict of interest.

Keywords

[1] J. G. Chen, R. M. Crooks, L. C. Seefeldt, K. L. Bren, R. M. Bullock, M. Y. Darensbourg, P. L. Holland, B. Hoffman, M. J. Janik, A. K. Jones, M. G. Kanatzidis, P. King, K. M. Lancaster, S. V. Lymar, P. Pfromm, W. F. Schneider, R. R. Schrock, *Science* **2018**, *360*, 7.

[2] S. L. Foster, S. I. P. Bakovic, R. D. Duda, S. Maheshwari, R. D. Milton, S. D. Minteer, M. J. Janik, J. N. Renner, L. F. Greenlee, *Nat. Catal.* **2018**, *1*, 490.

[3] X. Y. Cui, C. Tang, Q. Zhang, *Adv. Energy Mater.* **2018**, *8*, 25.

[4] B. H. R. Suryanto, H. L. Du, D. B. Wang, J. Chen, A. N. Simonov, D. R. MacFarlane, *Nat. Catal.* **2019**, *2*, 290.

[5] G. F. Chen, S. Y. Ren, L. L. Zhang, H. Cheng, Y. R. Luo, K. H. Zhu, L. X. Ding, H. H. Wang, *Small Methods* **2019**, *3*, 1800337.

[6] X. Zhu, S. Mou, Q. Peng, Q. Liu, Y. Luo, G. Chen, S. Gao, X. Sun, *J. Mater. Chem. A* **2020**, *8*, 1545.

[7] S. Z. Andersen, V. Čolić, S. Yang, J. A. Schwalbe, A. C. Nielander, J. M. McEnaney, K. Enemark-Rasmussen, J. G. Baker, A. R. Singh, B. A. Rohr, M. J. Statt, S. J. Blair, S. Mezzavilla, J. Kibsgaard, P. C. K. Vesborg, M. Cargnello, S. F. Bent, T. F. Jaramillo, I. E. L. Stephens, J. K. Nørskov, I. Chorkendorff, *Nature* **2019**, *570*, 504.

[8] C. Tang, S. Z. Qiao, *Chem. Soc. Rev.* **2019**, *48*, 3166.

[9] C. J. M. van der Ham, M. T. M. Koper, D. G. H. Hetterscheid, *Chem. Soc. Rev.* **2014**, *43*, 5183.

[10] S. Y. Wang, F. Ichihara, H. Pang, H. Chen, J. H. Ye, *Adv. Funct. Mater.* **2018**, *28*, 1803309.

[11] A. R. Singh, B. A. Rohr, J. A. Schwalbe, M. Cargnello, K. Chan, T. F. Jaramillo, I. Chorkendorff, J. K. Nørskov, *ACS Catal.* **2017**, *7*, 706.

[12] X. Guo, H. Du, F. Qu, J. Li, *J. Mater. Chem. A* **2019**, *7*, 3531.

[13] H. Y. Jin, L. Q. Li, X. Liu, C. Tang, W. J. Xu, S. M. Chen, L. Song, Y. Zheng, S. Z. Qiao, *Adv. Mater.* **2019**, *31*, 1902709.

[14] X. Yang, J. Nash, J. Anibal, M. Dunwel, S. Kattel, E. Stavitski, K. Attenkofer, J. G. G. Chen, Y. S. Yan, B. J. Xu, *J. Am. Chem. Soc.* **2018**, *140*, 13387.

[15] N. Cao, Z. Chen, K. T. Zang, J. Xu, J. Zhong, J. Luo, X. Xu, G. F. Zheng, *Nat. Commun.* **2019**, *10*, 2877.

[16] W. Qiu, X. Xie, J. Qiu, W. Fang, R. Liang, X. Ren, X. Ji, G. Cui, A. M. Asiri, G. Cui, B. Tang, X. Sun, *Nat. Commun.* **2018**, *9*, 3485.

[17] J. Zhang, Y. J. Ji, P. T. Wang, Q. Shao, Y. Y. Li, X. Huang, *Adv. Funct. Mater.* **2020**, *30*, 1906579.

[18] L. L. Zhang, G. F. Chen, L. X. Ding, H. H. Wang, *Chem. Eur. J.* **2019**, *25*, 12464.

[19] X. Liu, Y. Jiao, Y. Zheng, M. Jaroniec, S. Z. Qiao, *J. Am. Chem. Soc.* **2019**, *141*, 9664.

[20] S. S. Liu, M. F. Wang, T. Qian, H. Q. Ji, J. Liu, C. L. Yan, *Nat. Commun.* **2019**, *10*, 3898.

[21] L. L. Zhang, L. X. Ding, G. F. Chen, X. F. Yang, H. H. Wang, *Angew. Chem. Int., Ed.* **2019**, *58*, 2612.

[22] Q. Hao, C. Liu, G. Jia, Y. Wang, H. randiyan, W. Wei, B.-J. Ni, *Mater. Horiz.* **2020**, *7*, 1014.

[23] J. Li, H. Li, G. M. Zhan, L. Z. Zhang, *Acc. Chem. Res.* **2017**, *50*, 112.

[24] Y. C. Hao, Y. Guo, L. W. Chen, M. Shu, X. Y. Wang, T. A. Bu, W. Y. Gao, N. Zhang, X. Su, X. Feng, J. W. Zhou, B. Wang, C. W. Hu, A. X. Yin, R. Si, Y. W. Zhang, C. H. Yan, *Nat. Catal.* **2019**, *2*, 448.

[25] C. Lv, C. Yan, G. Chen, Y. Ding, J. Sun, Y. Zhou, G. Yu, *Angew. Chem. Int., Ed.* **2018**, *57*, 6073.

[26] J. X. Yao, D. Bao, Q. Zhang, M. M. Shi, Y. Wang, R. Gao, J. M. Yan, Q. Jiang, *Small Methods* **2019**, *3*, 1800333.

[27] L. Q. Li, C. Tang, B. Q. Xia, H. Y. Jin, Y. Zheng, S.-Z. Qiao, *ACS Catal.* **2019**, *9*, 2902.

[28] R. Zhang, L. Ji, W. Kong, H. Wang, R. Zhao, H. Chen, T. Li, B. Li, Y. Luo, X. Sun, *Chem. Commun.* **2019**, *55*, 5263.

[29] Y. Wang, M. M. Shi, D. Bao, F. L. Meng, Q. Zhang, Y. T. Zhou, K. H. Liu, Y. Zhang, J. Z. Wang, Z. W. Chen, D. P. Liu, Z. Jiang, M. Luo, L. Gu, Q. H. Zhang, X. Z. Cao, Y. Yao, M. H. Shao, Y. Zhang, X. B. Zhang, J. G. Chen, J. M. Yan, Q. Jiang, *Angew. Chem. Int., Ed.* **2019**, *58*, 9464.

[30] F. Wang, X. Lv, X. Zhu, J. Du, S. Lu, A. A. Alshehri, K. A. Alzahrani, B. Zheng, X. Sun, *Chem. Commun.* **2020**, *56*, 2107.

[31] Y. Liu, B. Huang, X. Chen, Z. Tian, X. Zhang, P. Tsiakaras, P. K. Shen, *Appl. Catal. B: Environ.* **2020**, *271*, 118919.

[32] J. Greeley, T. F. Jaramillo, J. Bonde, I. Chorkendorff, J. K. Nørskov, *Nat. Mater.* **2006**, *5*, 909.

[33] N. Han, Y. Wang, H. Yang, J. Deng, J. Wu, Y. Li, Y. Li, *Nat. Commun.* **2018**, *9*, 1320.

[34] Y. Zhu, J. Wang, H. Chu, Y.-C. Chu, H. M. Chen, *ACS Energy Lett.* **2020**, *5*, 1281.

[35] A. D. Handoko, F. X. Wei, B. S. Y. Jenndy, Z. W. Seh, *Nat. Catal.* **2018**, *1*, 922.

[36] R. M. Arán-Ais, F. Scholten, S. Kunze, R. Rizo, B. Roldan Cuenya, *Nat. Energy* **2020**, *5*, 317.

[37] H. Mistry, A. S. Varela, C. S. Bonifacio, I. Zegkinoglou, I. Sinev, Y. W. Choi, K. Kisslinger, E. A. Stach, J. C. Yang, P. Strasser, B. Roldan Cuenya, *Nat. Commun.* **2016**, *7*, 12123.

[38] A. Eilert, F. Cavalca, F. S. Roberts, J. Osterwalder, C. Liu, M. Favaro, E. J. Crumlin, H. Ogasawara, D. Friebel, L. G. M. Pettersson, A. Nilsson, *J. Phys. Chem. Lett.* **2017**, *8*, 285.

[39] H. Jung, S. Y. Lee, C. W. Lee, M. K. Cho, D. H. Won, C. Kim, H.-S. Oh, B. K. Min, Y. J. Hwang, *J. Am. Chem. Soc.* **2019**, *141*, 4624.

**ADVANCED
SCIENCE NEWS**

www.advancedsciencenews.com

**ADVANCED
ENERGY
MATERIALS**

www.advenergymat.de

[40] Q. Lei, H. Zhu, K. Song, N. Wei, L. Liu, D. Zhang, J. Yin, X. Dong, K. Yao, N. Wang, X. Li, B. Davaasuren, J. Wang, Y. Han, *J. Am. Chem. Soc.* **2020**, *142*, 4213.

[41] Y. Chen, C. W. Li, M. W. Kanan, *J. Am. Chem. Soc.* **2012**, *134*, 19969.

[42] M. Ma, B. J. Trześniewski, J. Xie, W. A. Smith, *Angew. Chem. Int., Ed.* **2016**, *55*, 9748.

[43] H. Ouyang, N. Chen, G. Chang, X. Zhao, Y. Sun, S. Chen, H. Zhang, D. Yang, *Angew. Chem. Int., Ed.* **2018**, *57*, 13197.

[44] L. Xu, Y. Xu, X. Li, Z. Wang, T. Sun, X. Zhang, *Dalton Trans.* **2018**, *47*, 16696.

[45] P. Lamagni, M. Miola, J. Catalano, M. S. Hvid, M. A. H. Mamakhel, M. Christensen, M. R. Madsen, H. S. Jeppesen, X.-M. Hu, K. Daasbjerg, T. Skrydstrup, N. Lock, *Adv. Funct. Mater.* **2020**, *30*, 1910408.

[46] C. S. Cao, D. D. Ma, J. F. Gu, X. Y. Xie, G. Zeng, X. F. Li, S. G. Han, Q. L. Zhu, X. T. Wu, Q. Xu, *Angew. Chem. Int., Ed.* **2020**, https://doi.org/10.1002/ange.202005577.

[47] G. Qing, R. Ghazfar, S. T. Jackowski, F. Habibzadeh, M. M. Ashtiani, C. P. Chen, M. R. Smith, T. W. Hamann, *Chem. Rev.* **2020**, *120*, 5437.

[48] J. Hou, M. Yang, J. Zhang, *Nanoscale* **2020**, *12*, 6900.

[49] L. Kumari, J. H. Lin, Y. R. Ma, *J. Phys. D. Appl. Phys.* **2008**, *41*, 025405.

[50] A. Reyes-Contreras, M. Camacho-López, S. Camacho-López, O. Olea-Mejía, A. Esparza-García, J. G. Bañuelos-Muñetón, M. A. Camacho-López, *Opt. Mater. Express* **2017**, *7*, 1777.

[51] L. Xia, W. Fu, P. Zhuang, Y. Cao, M. O. L. Chee, P. Dong, M. Ye, J. Shen, *ACS Sustainable Chem. Eng.* **2020**, *8*, 2735.

[52] B. Chang, Q. Liu, N. Chen, Y. Yang, *ChemCatChem* **2019**, *11*, 1884.

[53] Y. Qiu, S. Zhao, M. Qin, J. Diao, S. Liu, L. Dai, W. Zhang, X. Guo, *Inorg. Chem. Front.* **2020**, *7*, 2006.

[54] L. Q. Li, C. Tang, D. Z. Yao, Y. Zheng, S. Z. Qiao, *ACS Energy Lett.* **2019**, *4*, 2111.

[55] Y. X. Zhao, R. Shi, X. A. N. Bian, C. Zhou, Y. F. Zhao, S. Zhang, F. Wu, G. I. N. Waterhouse, L. Z. Wu, C. H. Tung, T. R. Zhang, *Adv. Sci.* **2019**, *6*, 1802109.

[56] G. Y. Duan, Y. Ren, Y. Tang, Y. Z. Sun, Y. M. Chen, P. Y. Wan, X. J. Yang, *ChemSusChem* **2020**, *13*, 88.

[57] R. Manjunatha, A. Schechter, *Electrochem. Commun.* **2018**, *90*, 96.

[58] K. J. P. Schouten, E. Pérez Gallent, M. T. M. Koper, *J. Electroanal. Chem.* **2014**, *716*, 53.

[59] Y. Yao, S. Zhu, H. Wang, H. Li, M. Shao, *Angew. Chem. Int., Ed.* **2020**, *59*, 10479.

[60] B. M. Barney, J. McClead, D. Lukoyanov, M. Laryukhin, T.-C. Yang, D. R. Dean, B. M. Hoffman, L. C. Seefeldt, *Biochemistry* **2007**, *46*, 6784.

**ADVANCED
ENERGY
MATERIALS**

Supporting Information

In Situ Fragmented Bismuth Nanoparticles for Electrocatalytic Nitrogen Reduction

Dazhi Yao, Cheng Tang, Laiquan Li, Bingquan Xia, Anthony Vasileff, Huanyu Jin, Yanzhao Zhang, and Shi-Zhang Qiao*

Supporting Information

In situ Fragmented Bismuth Nanoparticles for Electrocatalytic Nitrogen Reduction

Dazhi Yao,[†] Cheng Tang,[†] Laiquan Li,[†] Bingquan Xia, Anthony Vasileff, Huanyu Jin, Yanzhao Zhang, Shi-Zhang Qiao*

[†]These authors contributed equally to this work.

D. Yao, Dr. C. Tang, L. Li, B. Xia, A. Vasileff, H. Jin, Y. Zhang, Prof. S. Z. Qiao
Centre for Materials in Energy and Catalysis
School of Chemical Engineering and Advanced Materials
The University of Adelaide
Adelaide, SA 5005, Australia
Email: s.qiao@adelaide.edu.au

1. Experimental Section

Materials and chemicals. Acetic acid (CH₃COOH), ammonia chloride (NH₄Cl, 99.998%), ammonium-^{15}N chloride (^{15}NH₄Cl, ≥98 at. % ^{15}N, ≥99% CP), bismuth (III) chloride (BiCl₃, ≥98%), dimethylformamide (DMF, anhydrous, 99.8%), dimethyl sulfoxide-d₆ (d₆-DMSO), methanol (anhydrous, 99.8%), deuterium oxide (D₂O, SKU-293040, 99.9 at. % D, contains 0.75 wt. % 3-(trimethylsilyl)propionic-2,2,3,3-d₄ acid, sodium salt), ^{15}N₂ (98 at. % ^{15}N, CAS: 29817-79-6), potassium sodium tartrate (NaKC₄H₄O₆·4H₂O), para-(dimethylamino) benzaldehyde ((CH₃)₂NC₆H₄CHO, 99%), potassium iodide (KI, ≥ 99.5%), sodium hydroxide (NaOH, anhydrous pellets, ≥98%), sodium nitroferricyanide (C₅FeN6Na₂O, ≥ 99%), sodium hypochlorite (available chlorine 10–15 %), sulfuric acid (H₂SO₄, ACS reagent, 95.0–98.0%), trimesic acid (Benzene-1,3,5-tricarboxylic acid, H₃BTC), and sodium salicylate (S3007, ≥ 99.5%) were purchased from Sigma-Aldrich Chemical Reagent Co. Ltd. Isopropanol, sodium hydroxide and sodium sulfate (AR, Anhydrous Powder) were ordered from Chem-Supply Pty. Ltd. Carbon paper and Nafion 117 membrane (Dupont) were purchased from Fuelcell store. Ultra-high purity Nitrogen (99.999%) and Argon (99.999%) were supplied from BOC gas, Australia.

Synthesis of bismuth oxyiodide (BiOI) nanosheets. BiCl₃ (0.2 mmol) was firstly dissolved in 20 mL of 1.2 M acetic acid and stirred for 30 min, followed by addition of 5 mL of 0.04 M KI solution. Then, the pH of the above mixture solution was adjusted to 6 using 1 M NaOH. After stirring for another 30 min, the solution was then transferred to a 50 mL Teflon-lined autoclave and heated at 160 ℃ for 2 h. The final product (BiOI nanosheets) was collected by centrifugation, washing by deionized water and freezing drying.

Synthesis of bismuth-based metal-organic frameworks (Bi-MOF). In a typical procedure, 0.339 g BiOI nanosheets and 0.6 g H₃BTC were dissolved in 15 mL of DMF and 5 mL of methanol at room temperature and stirred for 30 min. Then, the dispersion was transferred into the 50 mL Teflon-lined autoclave and heated at 120 ℃ for 3 h. The obtained salmon pink powder was collected by centrifugation and washing with methanol several times to remove the solvent. Finally, the product was dried in an oven at 60 ℃ for 12 h.

Pretreatment of Nafion 117. The Nafion 117 membrane was preconditioned by boiling in 5% H₂O₂ solution and ultrapure deionized water at 80 ℃ for 1 h, respectively, followed by treatment in 0.05 M H₂SO₄ for 3 h and deionized water for another 1h.

In situ *formation of Bi NPs from Bi-MOF precatalysts.* 10 mg of Bi-MOF was dispersed in 960 μL of mixed solvent ($V_{isoproponal}$:V_{water} = 1:2) with the addition of 40 μL of 5 wt% Nafion. The dispersion was vigorously sonicated for 6 h to form a homogenous ink. The ink was drop-casted onto a 1 × 1 cm² polytetrafluoroethylene (PTFE)-coated carbon paper to reach a precatalyst loading of 0.5 mg$_{Bi-}$

$_\text{MOF}$ cm^{-2}. The *in situ* electroreduction of Bi-MOF to Bi NPs was achieved by 20-cycle consecutive cyclic voltammetry (CV) scans from 0 to –1.0 V vs reversible hydrogen electrode (RHE) in 0.10 M Na$_2$SO$_4$ with a scan rate of 50 mV s^{-1}.

Characterization. Field-emission scanning electron microscopy (SEM) images were collected on a FEI QUANTA 450 electron microscope. The transmission electron microscopy (TEM) images were collected on a Philips CM 200 transmission electron microscope operated at 200 kV. X-ray powder diffraction (XRD) patterns were obtained using a Rigaku MiniFlex 600 X-Ray Diffractometer with Co Kα radiation. The absorbance data of spectrophotometer were collected on SHIMADZU UV-2600 ultraviolet-visible (UV-Vis) spectrophotometer. Raman data were collected on a HORIBA LabRAM HR Evolution spectroscopy using a 100 X objective lens and 532 nm laser as the excitation wavelength. For *in situ* Raman test, a screen-printed electrode coated with Bi-MOF was immersed into a thin electrolyte film (N$_2$-saturated 0.10 M Na$_2$SO$_4$). Each spectrum was collected for 60 s (20 s for each exposure time and 3 times for accumulation) with the potential applied from −0.1 to −1.1 V vs RHE.

Electrochemical experiment. Electrochemical NRR performance was evaluated in a gas-tight standard three-electrode H-cell with the cathodic and anodic compartments separated by a Nafion 117 membrane. A graphite rod and saturated Ag/AgCl electrode served as the counter and reference electrodes, respectively. All experiments were carried out at room temperature (25 °C). Potentials (E) in this study were calibrated to the RHE reference scale by E (V vs RHE) = E (V vs saturated Ag/AgCl) + 0.0591 × pH + 0.197. Before electrolysis, the electrolyte was purged with ultrahigh-purity N$_2$ (99.999%) for 20 min to ensure the removal of residual air in the reaction system. During electrolysis, high-purity N$_2$ was continuously fed into the cathodic compartment with magnetic stirring (500 rpm). An acid trap was connected with the cathodic chamber with two 10 mL clean PP tubes with 5 mL of 0.05 M H$_2$SO$_4$ in each tube. The electrolyte of the first cycle (20 CV scans and 1 h electrolysis) was discarded to exclude any possible pre-absorbed ammonia contamination for each newly prepared electrode. For comparison, electrolysis tests were also conducted in high-purity (99.999%) Ar-saturated electrolyte under the same experimental conditions. Current densities were normalized to the geometrical area of the electrodes. AC Impedance technique was employed to study the electrochemical impedance spectra of Bi-MOF and Bi NPs. The range of frequency was set from 100 mHz to 1000 Hz. The stability test was performed by replacing the electrolyte every 1 h without changing the electrode and Nafion membrane.

^{15}N$_2$ isotope-labelled experiments. Isotope labelling tests were conducted using ^{15}N$_2$ as the feed gas. After electrolysis for 2 h at –0.7 V vs RHE in 0.10 M Na$_2$SO$_4$ solution with a flow rate of 5 sccm, the obtained ^{15}NH$_4^+$ electrolyte was acidified to a pH of 1–2. Then, 125 μL of the acidified electrolyte

was mixed with 125 µL of D_2O and 750 µL of d_6-DMSO and then determined by ^1H nuclear magnetic on a Bruker Ascend 600 MHz system with water suppression.

Quantification of NH$_3$ by indophenol blue method. All test solutions (electrolytes in cathodic and anodic compartments, acid trap, standard solutions) were incubated with indophenol blue indicator at 25 °C for 1 h before UV-Vis tests. The absorbance at 650 nm for each solution was collected with a UV-vis spectrophotometer (SHIMADZU, UV-2600). A series of standard solutions with suitable NH_4Cl concentration diluted with 0.10 M Na_2SO_4 or 0.05 M H_2SO_4 were prepared and tested to plot a calibration curve. The concentrations of ammonia in the test solutions were calculated directly from the calibration curve for each pH value, respectively.

Indophenol blue indicator is prepared by mixing three reagents. *Chromogenic reagent (A)*: 5 g of sodium salicylate and 5 g of potassium sodium tartrate were dissolved in 100 mL of 1 M NaOH; *Oxidizing solution (B)*: 3.5 mL of sodium hypochlorite (available chlorine 10–15 %) was added into 100 mL of deionized water; *Catalysing reagent (C)*: 0.2 g of sodium nitroferricyanide was dissolved in 20 mL of deionized water. For UV-Vis absorbance measurement, 2 mL of chromogenic reagent (A), 1 mL of oxidizing solution (B) and 0.2 mL of catalysing reagent (C) was added to the vial which contained 2 mL of the test solutions. After mixed it up and incubation for 1 h, the concentration of the produced indophenol blue was measured using UV-Vis absorbance spectrophotometer.

Quantification of hydrazine. Watt and Chrisp method were employed to quantify the possible hydrazine. 2.0 g of para-(dimethylamino)benzaldehyde was dissolved in a mixture of 10 mL of concentrated HCl and 100 mL of ethanol. After mixing with the chromogenic reagent in the resulting electrolyte, concentration of hydrazine was determined according to the absorbance at 460 nm.

Quantification of NH$_3$ with ion chromatograph. The amount of ammonia produced in acid electrolytes was also measured by ion chromatograph (Thermo-Fisher DIONEX Integrion HPIC). The test procedure followed the standard operation procedure provided by the vendor. Briefly, 25 µL of the resultant electrolyte was injected into the chamber for separation. Dilution factor was set as 1.0000 and average step was 0.2 s. Delivery speed was 4.0 mL min^{-1} and running time for each sample was 30 min. The peak appeared at a retention time of 9.7 min was assigned to NH_4^+, and the peak area was calculated for calibration with a series of standard solutions.

Calculation of NH$_3$ yield and Faradaic efficiency. The ammonia formation rate was determined using the following equation: $r(NH_3) = (c \times V) / (t \times A)$, where c is the measured NH_3 concentration, V is the volume of the electrolyte or acid trap, t is the reaction time, and A is the geometric area of the working electrode. The Faradaic efficiency was calculated as follows: $FE = (3F \times c \times V) / (17 \times Q)$, where F is the Faraday constant (96485 C mol^{-1}), c is the measured NH_3 concentration, V is the volume of the electrolyte or acid trap, and Q is the total charge used for the electrodes. The total

ammonia production was calculated as the summary of the ammonia products in cathodic chamber, anodic chamber, and also in-line acid traps.

Online differential electrochemical mass spectra (DEMS). The DEMS data were collected on the QAS 100 by Linglu Instruments (Shanghai) Co. Ltd. to perform online analysis of gas. The measurements were carried out using a thin layer flow cell, which permitted experiments under controlled and continuous mass transport conditions. The volatile or the dissolved gaseous products were evaporated in the high vacuum of a prechamber, and the remaining species were directed to a main chamber, where the sample was analyzed by a commercial quadrupole mass spectrometer (Pfeiffer Prisma). The working electrode was prepared by depositing the electrocatalyst ink on a carbon paper with a loading around 0.5 mg cm^{-2}. The electrode was separated from the porous PTFE membrane (Gore-Tex) by a 100 μm thick PTFE spacer. The saturated Ag/AgCl electrode was positioned in the electrolyte inlet as the reference electrode. The Pt wire was positioned in the electrolyte outlet as the counter electrode. Amperometry method was employed and potential applied was between −0.7 and −0.9 V vs RHE. N_2 and Ar were continuously purged during the experiment and 0.10 M Na_2SO_4 was chosen as the electrolyte. There was no separation between the cathodic and anodic chambers in the three-electrode system for DEMS determination. The flow rate of electrolyte was 10.0 μL s^{-1}. The volatile products of the electrochemical reactions were monitored at different values of *m/z* ionic signals. All original data in the mass spectra are reported at 1 PPAmu.

2. Supplementary Figures
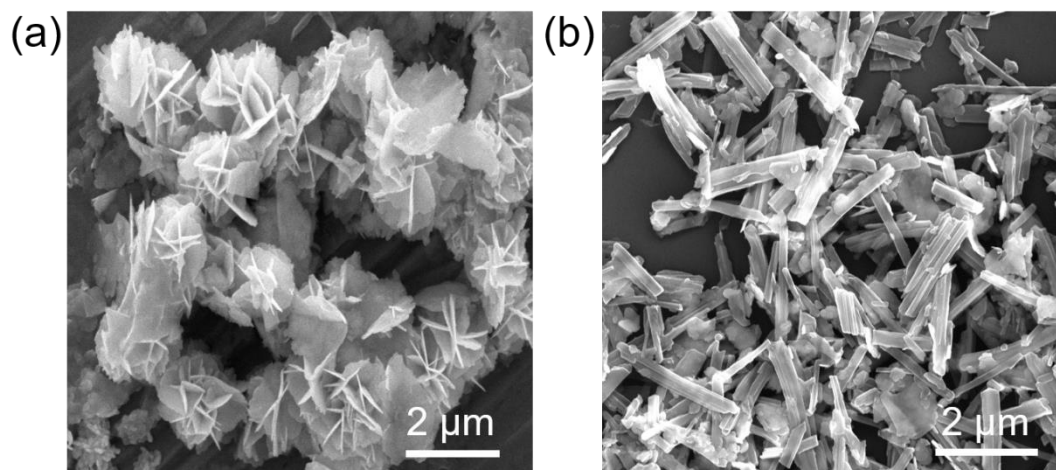
Figure S1. Typical SEM images for a) BiOI nanosheets and b) Bi-MOF nanorods. As shown in Figure S1b, there are some residual BiOI nanosheets in the Bi-MOF products, which are also illustrated by XRD results.
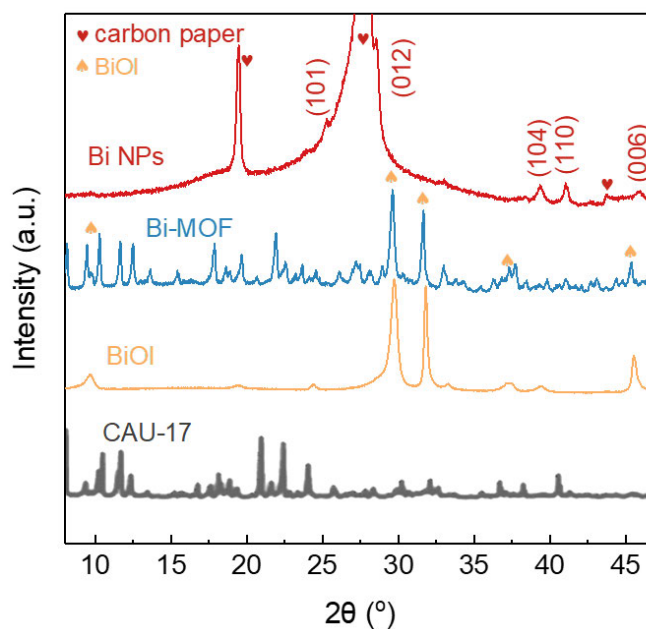
Figure S2. XRD patterns of synthesized Bi-MOF and *in situ* reduced Bi NPs, compared with BiOI and CAU-17.[1]
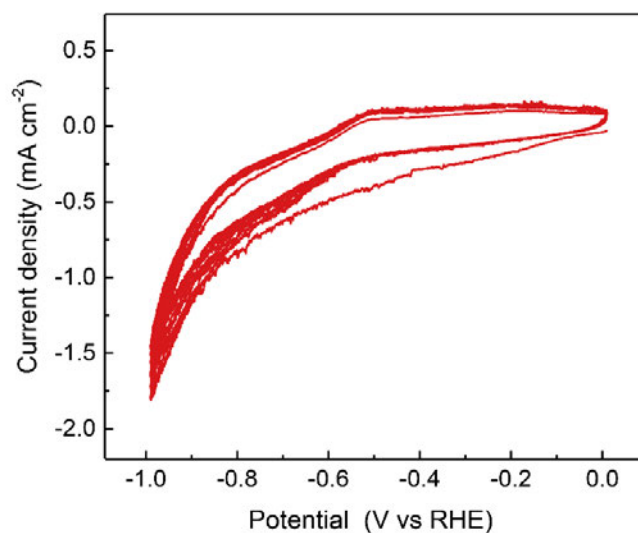
Figure S3. 20 cycles of CV treatments for the *in situ* electrochemical reduction of Bi-MOF to Bi NPs (scan rate = 50 mV s^{-1}).
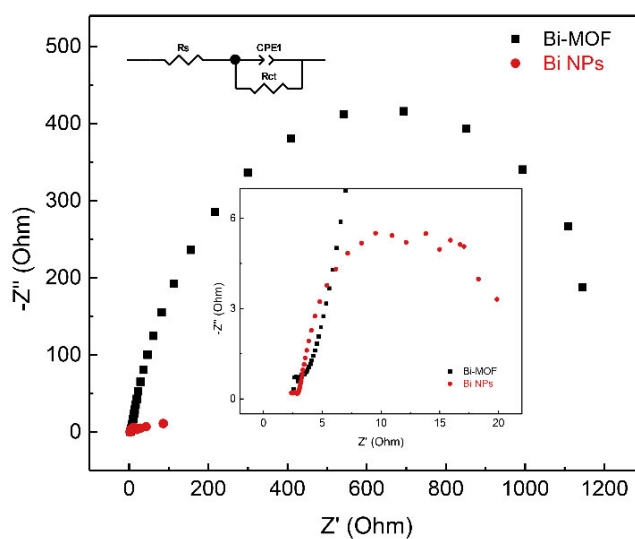
Figure S4. Electrochemical impedance spectra for the Bi-MOF and *in situ* synthesized Bi NPs on carbon paper under open circuit potential. The circuit elements R_s, R_{ct} and CPE1 in the circuit diagram refer to solution resistance, charge-transfer resistance and the Constant Phase Element, respectively.
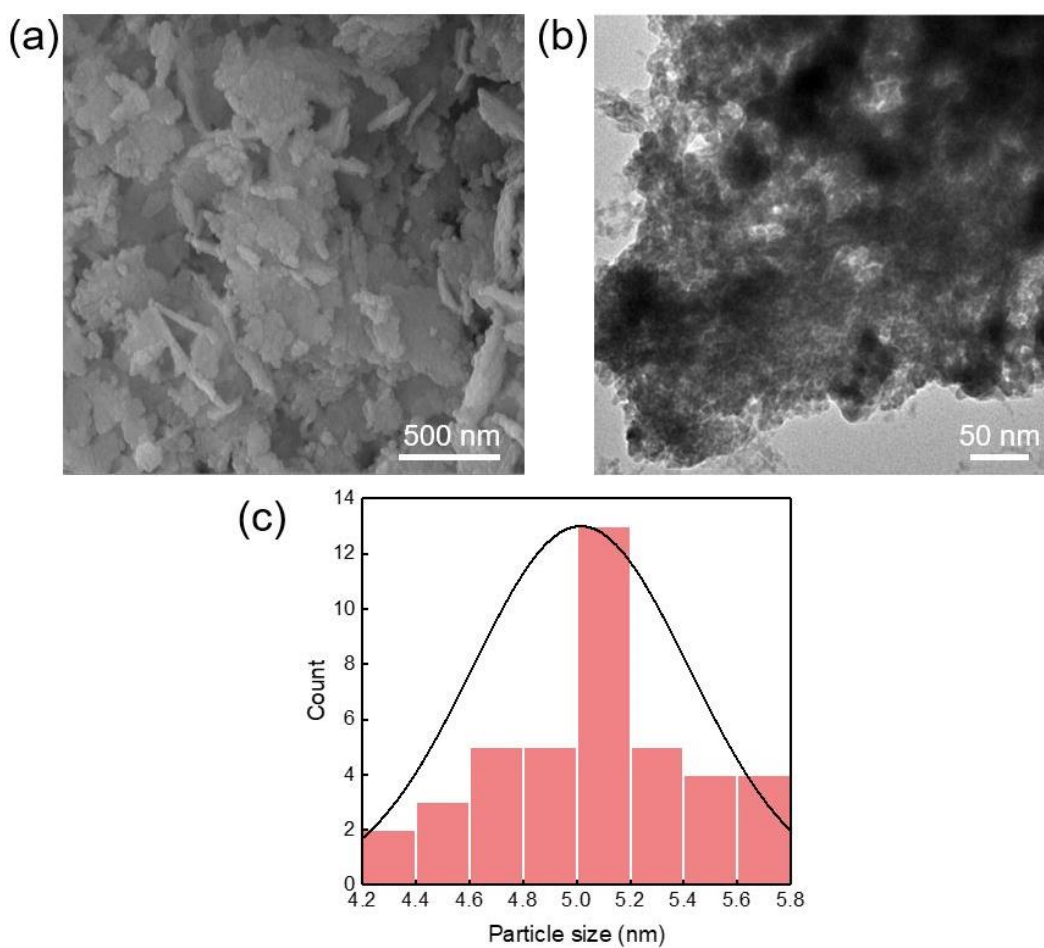
Figure S5. a) SEM and b) TEM images for Bi NPs after the *in situ* electrochemical reduction. c) Particle size distribution of the crystalline nanoparticles based on a statistic analysis.
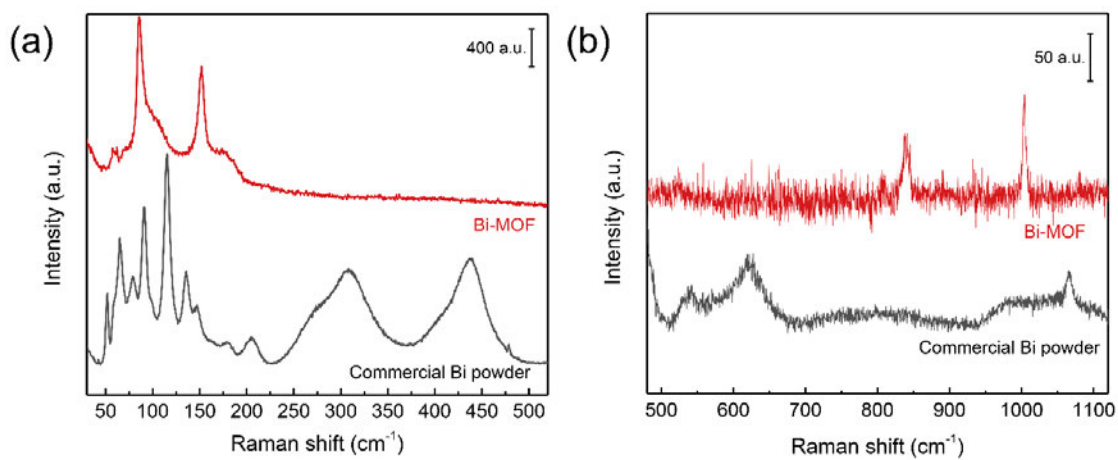
Figure S6. Raman spectra of the synthesized Bi-MOF and commercial Bi powder for comparison. (λ = 532 nm, 50x objective, 10 mW lase power).
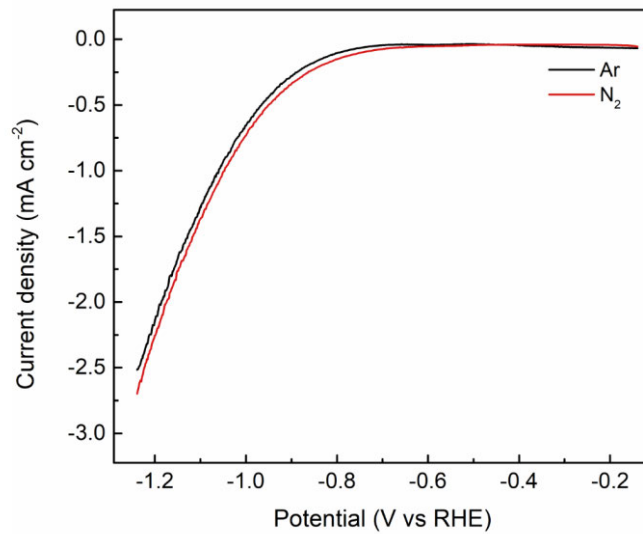
Figure S7. LSV curves for Bi NPs in N_2-saturated 0.10 M Na_2SO_4 (red line) and Ar-saturated 0.10 M Na_2SO_4 (black line).
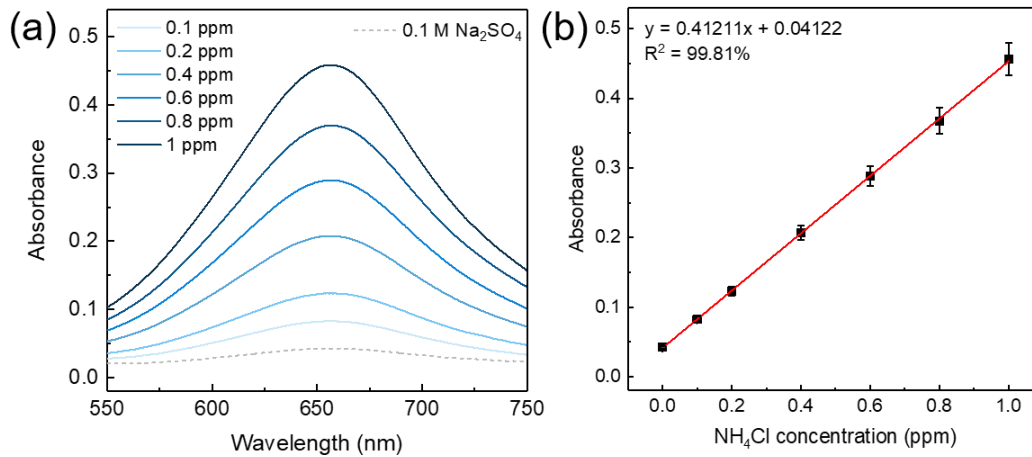
Figure S8. Standard curves for NH_4Cl solution with different concentrations in 0.10 M Na_2SO_4 by indophenol blue colorimetric method. a) UV-Vis spectra of different solutions after stained with indophenol indicator for 1 hour and b) corresponding linear fitting between absorbance and NH_4Cl concentration. The error bars were calculated by determination of three times.
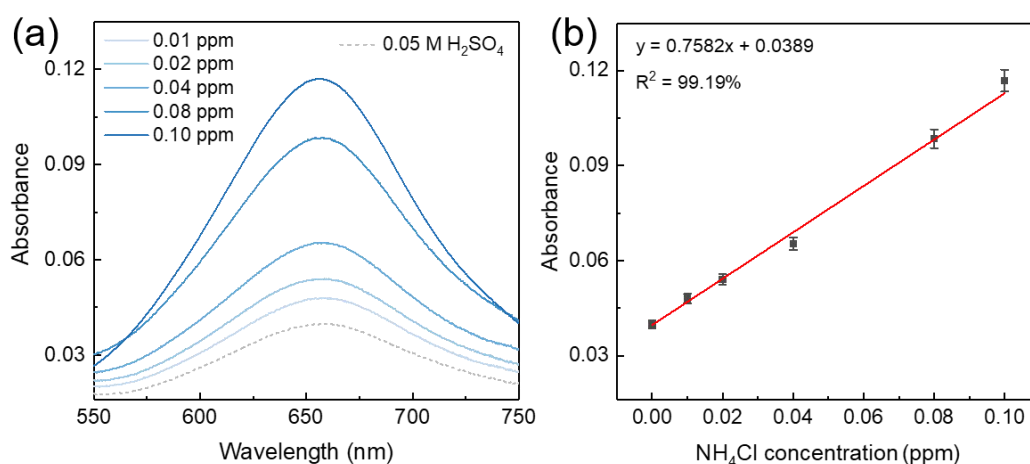
Figure S9. Standard curves for NH₄Cl solution with different concentrations in 0.05 M H₂SO₄ by indophenol blue colorimetric method. a) UV-Vis spectra of different solutions after stained with indophenol indicator for 1 hour and b) corresponding linear fitting between absorbance and NH₄Cl concentration. The error bars were calculated by determination of three times.
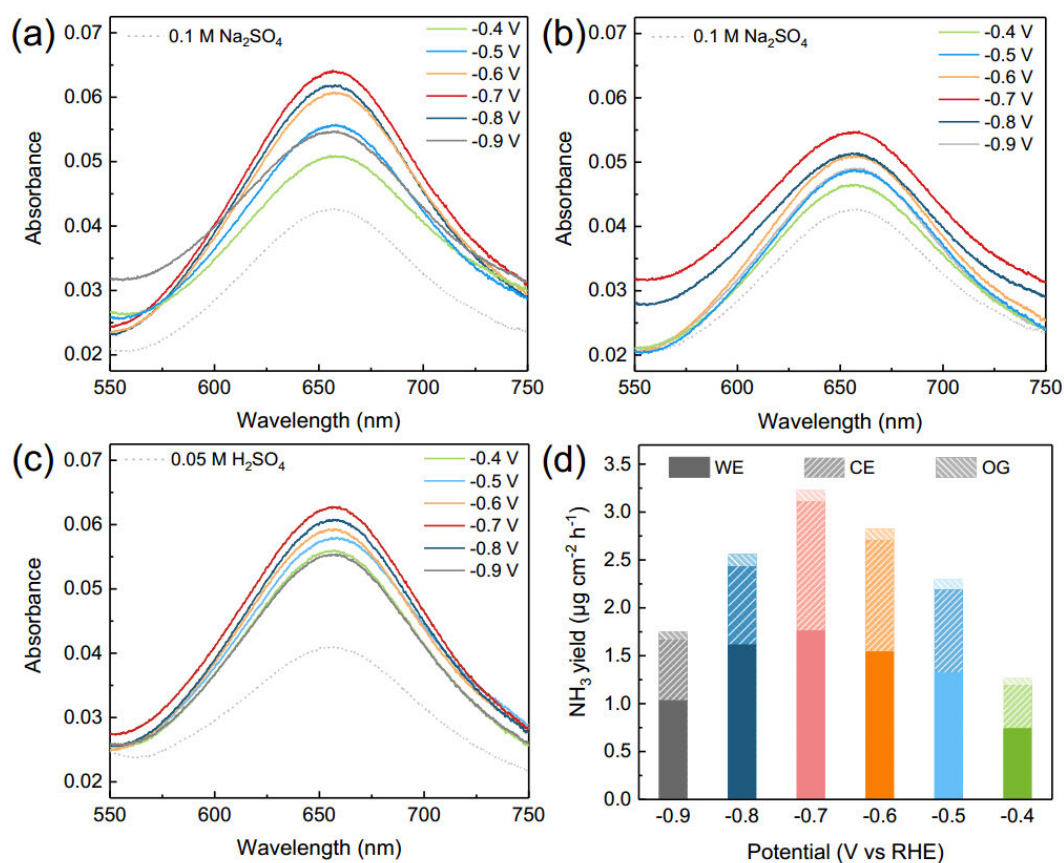
Figure S10. Typical UV-Vis spectra of the solution stained with indophenol indicator after NRR in 0.10 M Na₂SO₄ at different potentials for a) cathodic chamber (WE), b) anodic chamber (CE), and c) acid trap solutions (OG). d) Corresponding NH₃ yield.
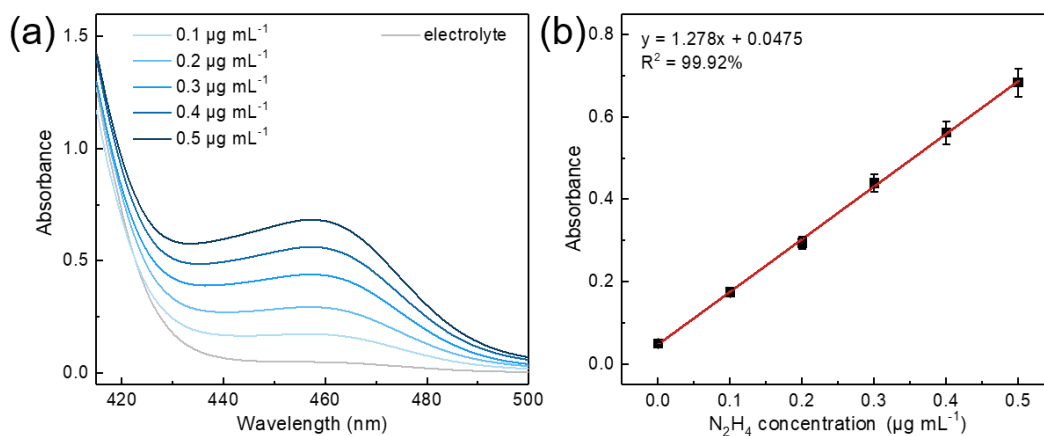
Figure S11. Standard curves for hydrazine with different concentrations in 0.10 M Na$_2$SO$_4$ by the Watt and Chrisp method. a) UV-Vis spectra and b) corresponding linear fitting between absorbance at 460 nm and hydrazine concentration. The error bars were calculated by determination of three times.
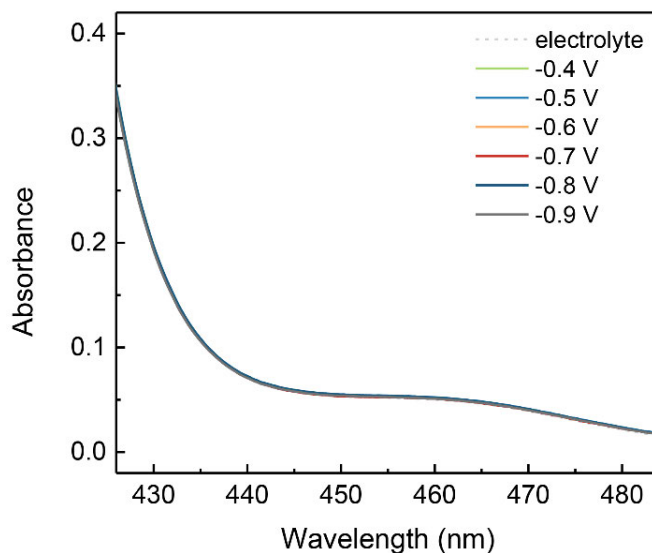
Figure S12. Typical UV-Vis spectra for detecting hydrazine in the cathodic chamber after electrolysis at different potentials in 0.10 M Na$_2$SO$_4$.
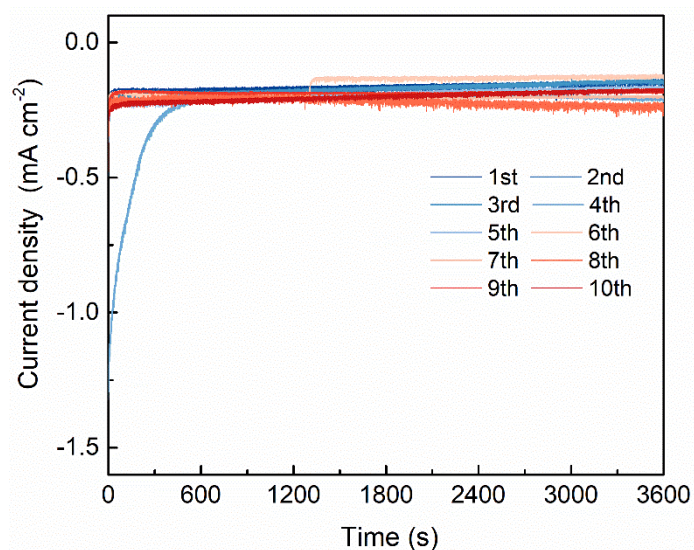
Figure S13. Chronoamperometry responses of *in situ* synthesized Bi NPs for NRR at −0.7 V vs RHE in N$_2$-saturated 0.10 M Na$_2$SO$_4$ for 10 cycles.
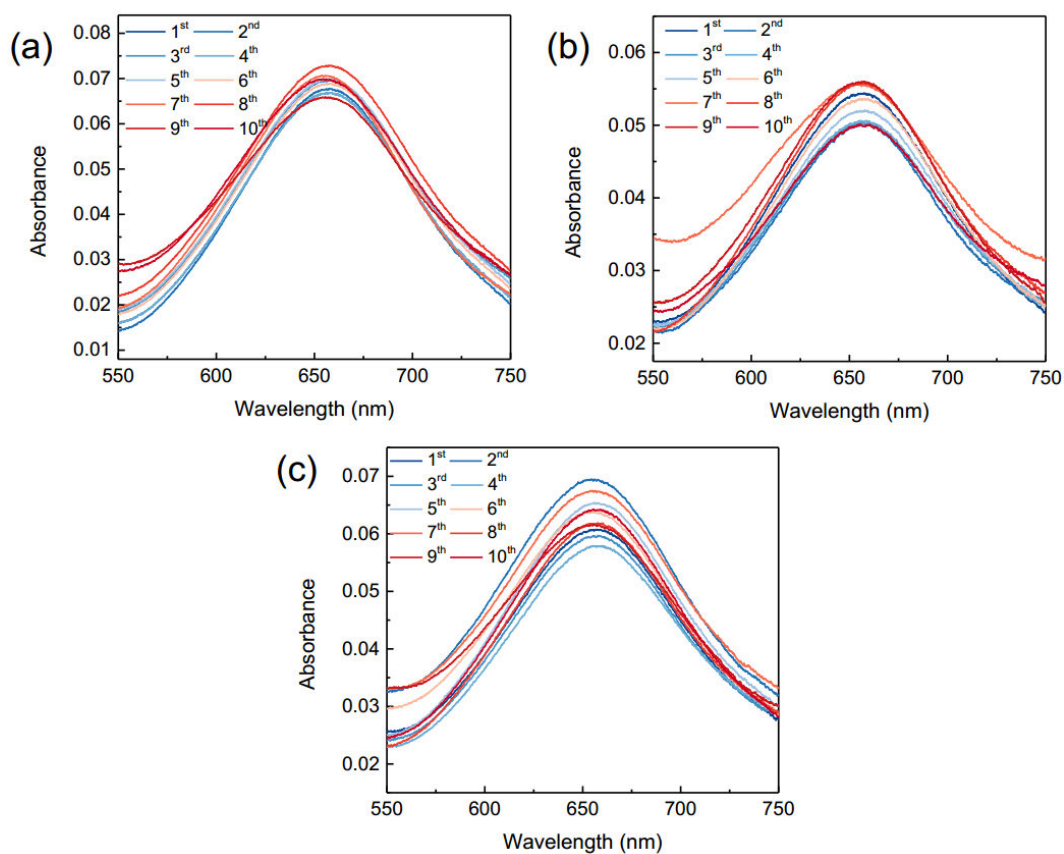
Figure S14. UV-Vis absorption spectra of the solution stained with indophenol indicator after NRR in 0.10 M Na$_2$SO$_4$ at different potentials in consecutive cycling tests. a) Cathodic chamber (WE), b) anodic chamber (CE), and c) acid trap solutions (OG).
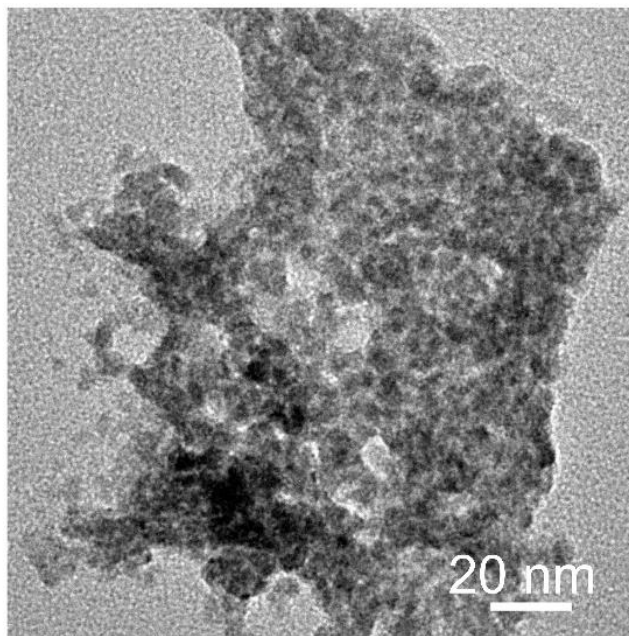
Figure S15. High-resolution TEM image of Bi NPs after long-term tests.
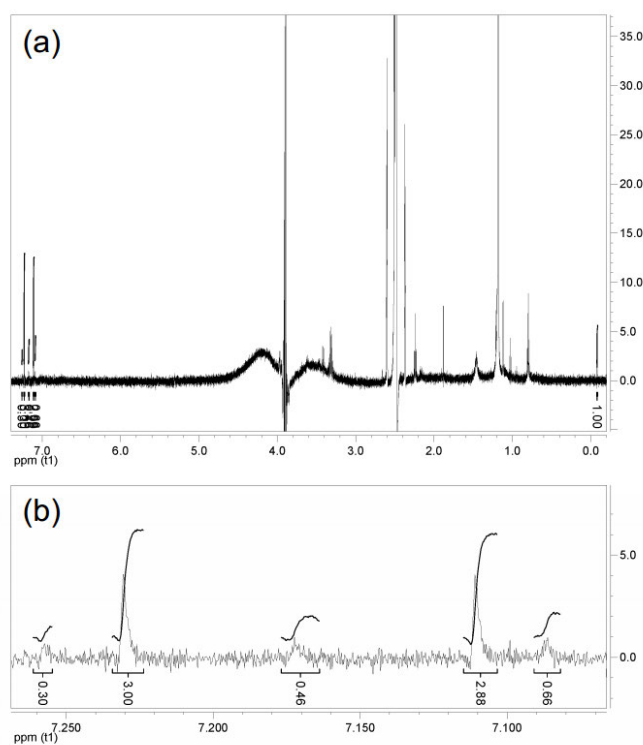
Figure S16. Integrals of peaks in ^{1}H NMR for a) the whole range and b) $^{15}NH_4^+$ obtained from the NRR (at −0.7 V vs RHE) using $^{15}N_2$ as the feed gas.
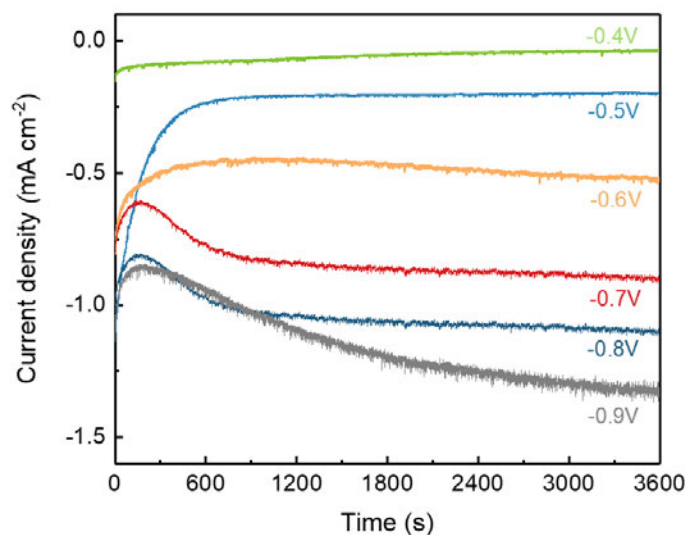
Figure S17. Chronoamperometry responses of Bi NPs for NRR at different potentials in N_2-saturated 0.05 M H_2SO_4.
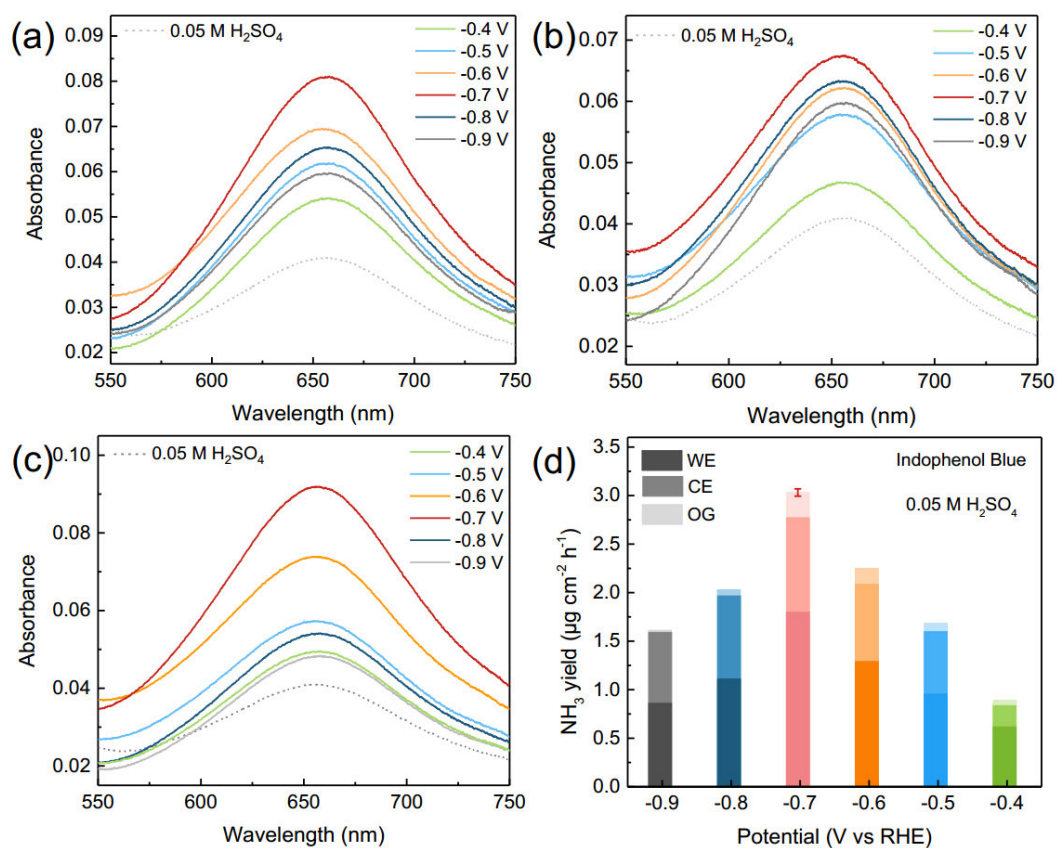
Figure S18. Typical UV-Vis spectra of the solution stained with indophenol indicator after NRR in 0.05 M H_2SO_4 at different potentials for a) cathodic chamber (WE), b) anodic chamber (CE), and c) acid trap solutions (OG). d) Corresponding NH_3 yield.
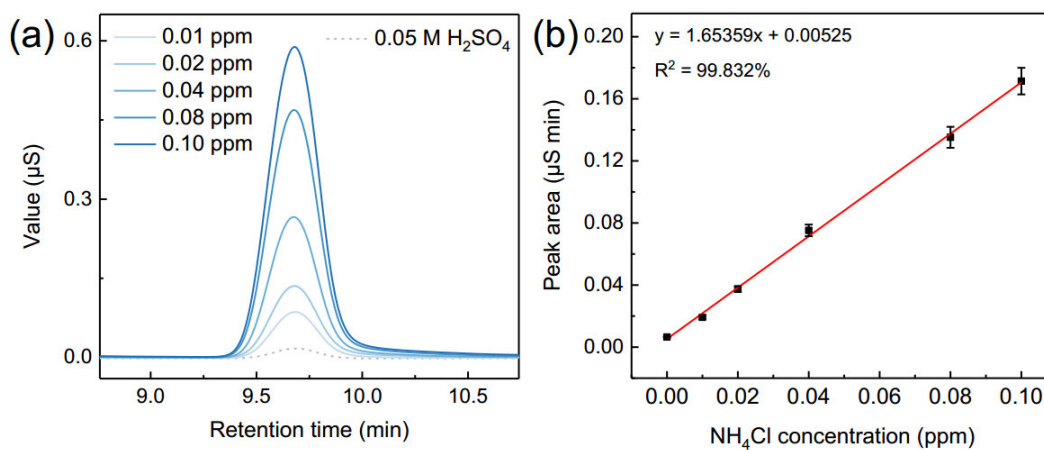
Figure S19. Standard curves for NH4Cl solution with different concentrations in 0.05 M H2SO4 detected by ion chromatograph. a) Responses of NH4Cl solution with different concentrations in ion chromatograph and b) corresponding linear fitting between the NH_4^+ peak area (retention time ~9.7 min) and NH4Cl concentration. The error bars were calculated by determination of three times.
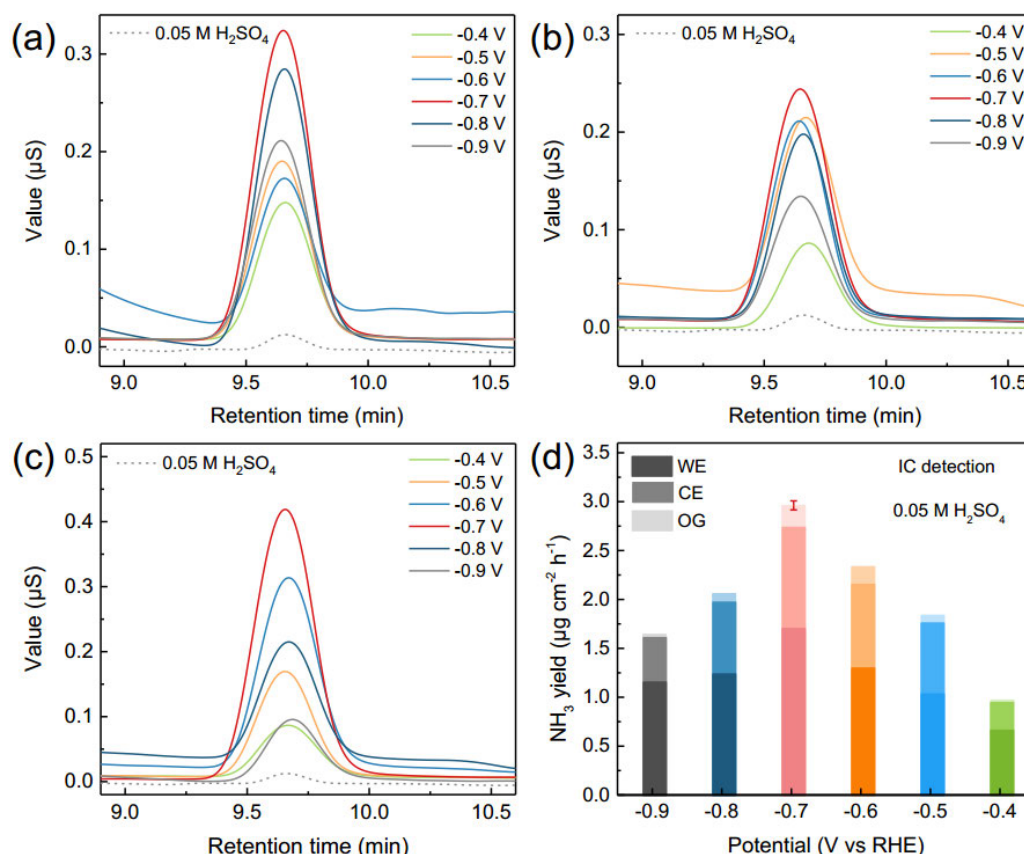
Figure S20. Typical ion chromatographic responses of acid electrolytes (0.05 M H2SO4) after electrolysis at different potentials in the a) cathodic chamber (WE), b) anodic chamber (CE), and c) acid trap solutions (OG). d) Corresponding ammonia yield.
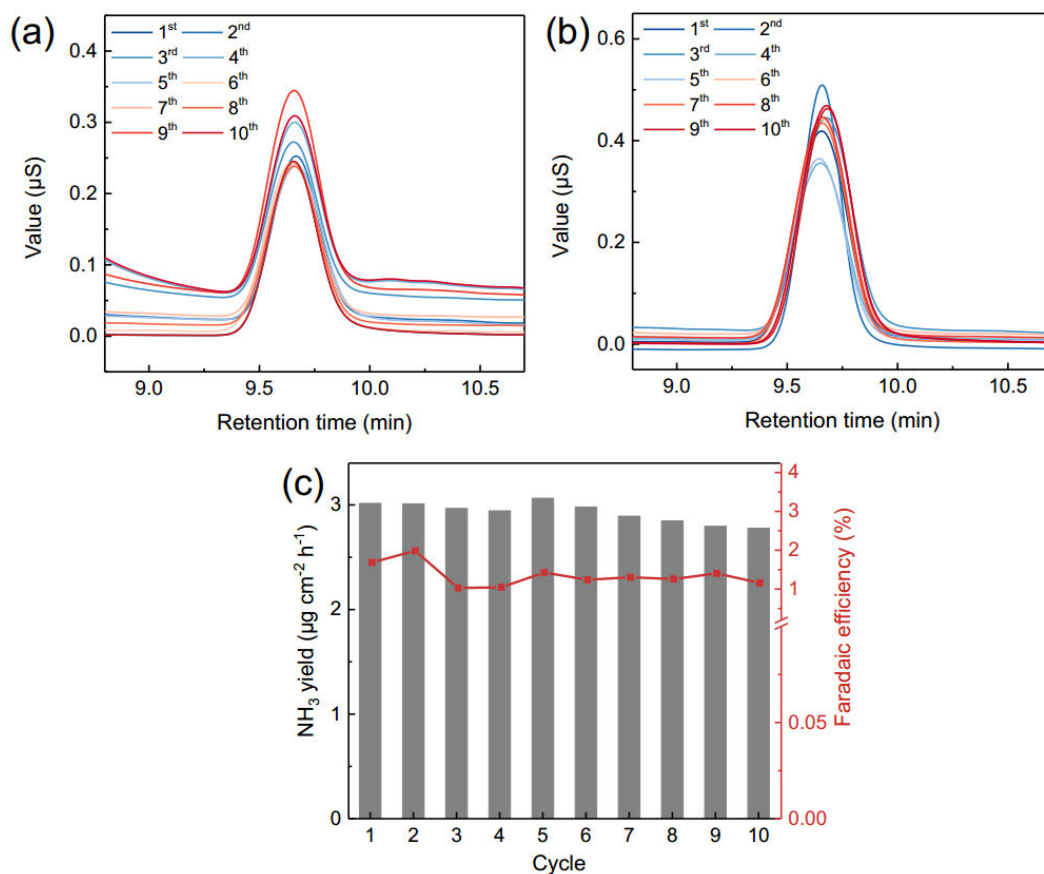
Figure S21. Ion chromatographic responses in different electrolytes for a) anodic chamber (CE), and b) acid trap (OG). c) Statistic columns for ammonia yield and Faradaic efficiency determined by IC method for 10 cycles in 0.05 M H_2SO_4 at -0.7 V vs RHE.
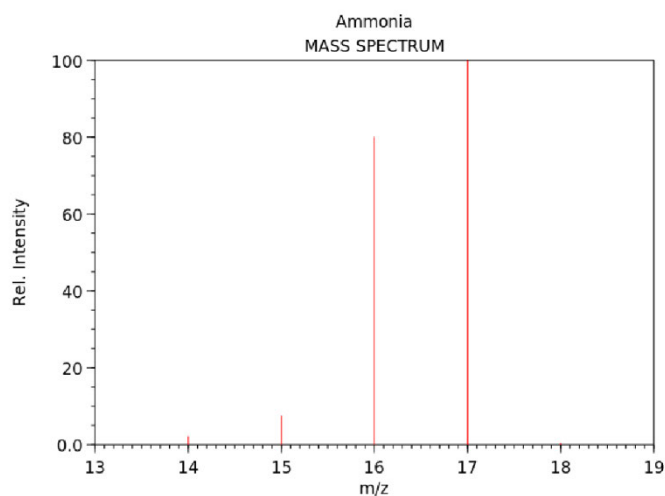
Figure S22. Standard mass spectra of NH_3 gas in NIST database.

(https://webbook.nist.gov/cgi/cbook.cgi?ID=C7664417&Mask=200)
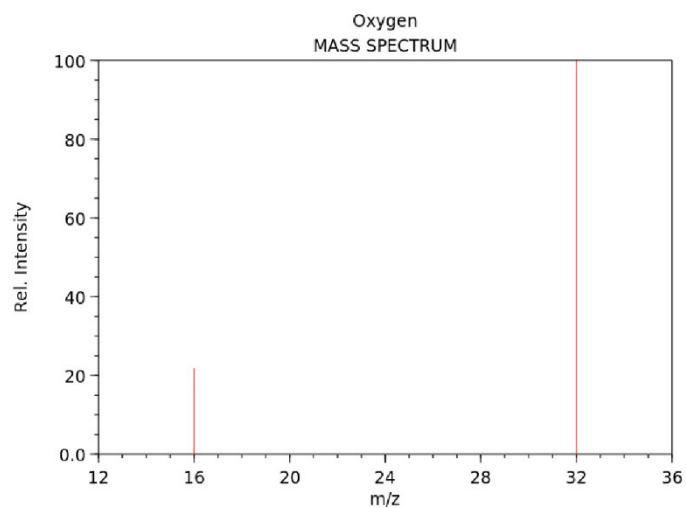
Figure S23. Standard mass spectra of O_2 in NIST database. (https://webbook.nist.gov/cgi/cbook.cgi?ID=C7782447&Mask=200)
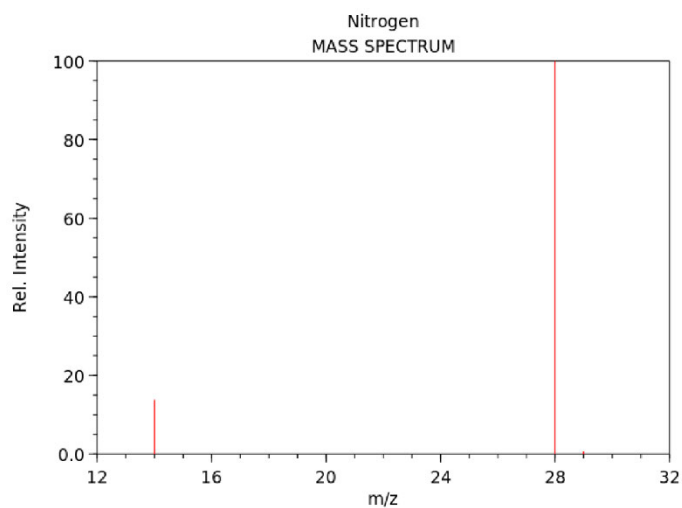
Figure S24. Standard mass spectra of N_2 in NIST database. (https://webbook.nist.gov/cgi/cbook.cgi?ID=C7727379&Mask=200)
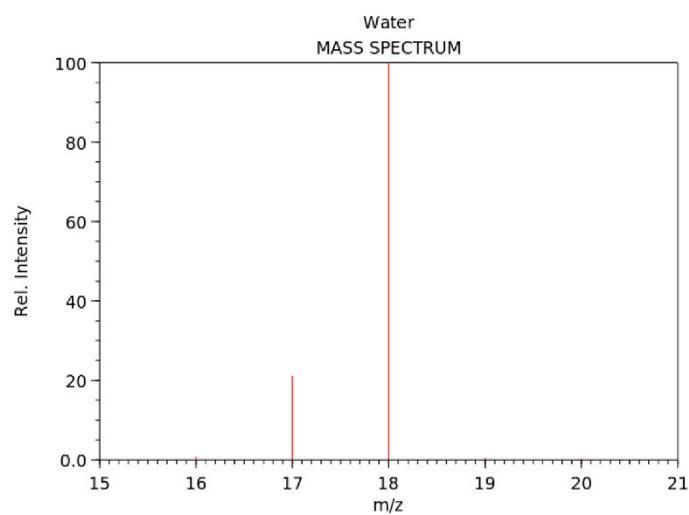
Figure S25. Standard mass spectra of H_2O in NIST database.
(https://webbook.nist.gov/cgi/cbook.cgi?ID=C7732185&Mask=200)
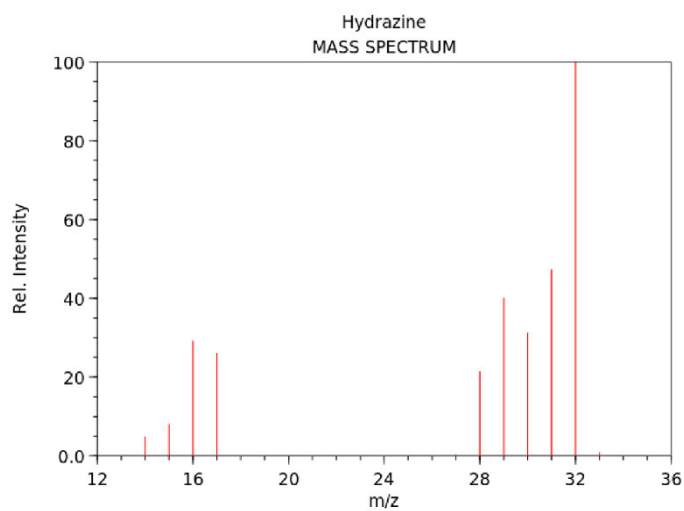
Figure S26. Standard mass spectra of N_2H_4 in NIST database.
(https://webbook.nist.gov/cgi/cbook.cgi?ID=C302012&Mask=200)
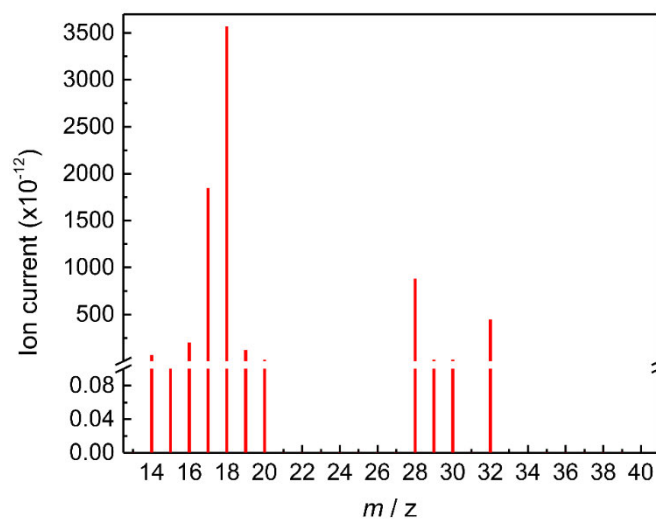
Figure S27. Extended range of DEMS results obtained during NRR tests with Bi NPs at –0.7 V vs RHE in N$_2$-saturated 0.10 M Na$_2$SO$_4$.
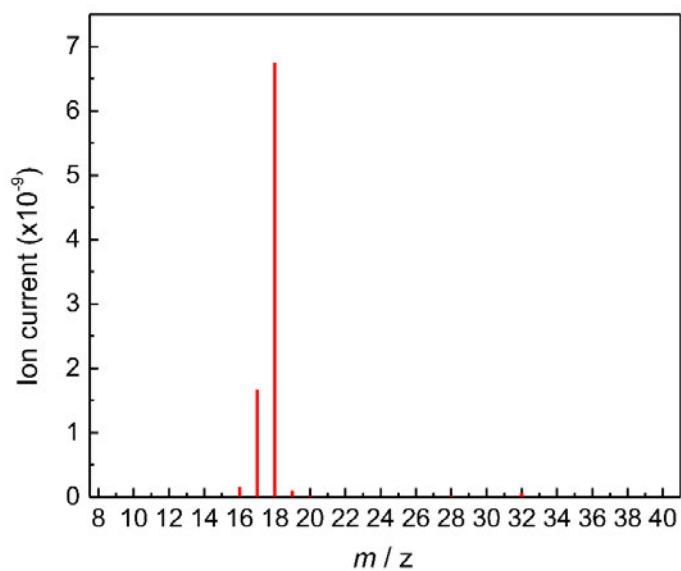
Figure S28. Extended range of DEMS results obtained during electrochemical tests with Bi NPs at –0.7 V vs RHE in Ar-saturated 0.10 M Na$_2$SO$_4$.

3. Supplementary Tables

Table S1. Summary of the representative reports on bismuth-based NRR electrocatalysts.

Catalyst	Electrolyte	NH$_3$ yield	Potential	Faradaic efficiency	Ref.
Bi NPs	0.10 M Na$_2$SO$_4$	3.25 μg cm^{-2} h^{-1}	−0.7 V	12.11% at −0.6 V	This work
Bi NPs	0.05 M H$_2$SO$_4$	3.03 μg cm^{-2} h^{-1}	−0.7 V	1.42%	This work
BiVO$_4$	0.2 M Na$_2$SO$_4$	8.6 μg h^{-1} mg$^{-1}_{cat.}$	−0.5 V	10.04%	2
Bi$_4$V$_2$O$_{11}$/ CeO$_2$	0.10 M HCl	23.21 μg h^{-1} mg$^{-1}_{cat.}$	−0.2 V	10.16%	3
β-Bi$_2$O$_3$ nanoflower	0.10 M Na$_2$SO$_4$	19.92 μg h^{-1} mg$^{-1}_{cat.}$	−0.8 V	4.3 %	4
Bismuth nanocrystals	0.5 M K$_2$SO$_4$ (pH = 3.5)	884 μg cm^{-2} h^{-1}	−0.6 V	66%	5
2D mosaic Bi NSs	0.10 M Na$_2$SO$_4$	2.54 μg cm^{-2} h^{-1}	−0.8 V	10.46%	6
defect-rich Bi nanoplates	0.2 M Na$_2$SO$_4$	5.453 μg h^{-1} mg$^{-1}_{Bi}$	−0.9 V	11.68% at −0.6 V	7
Bi nanodendrite	0.10 M HCl	25.86 μg h^{-1} mg$^{-1}_{cat.}$	−0.6 V	10.8% at −0.55 V	8
edge-rich Bi NSs	0.10 M NaHCO$_3$	12.49 μg h^{-1} mg$^{-1}_{cat.}$	−0.3 V	7.09%	9
Bi NSs array	0.10 M HCl	4.22 μg cm^{-2} h^{-1}	−0.5 V	10.26%	10
yolk-shell Bi@porous C	0.10 M HCl	28.63 μg h^{-1} mg$^{-1}_{cat.}$	−0.5 V	10.58%	11
porous Bi$_5$O$_7$I nanotubes	0.1 M Na$_2$SO$_4$	3.146 μg cm^{-2} h^{-1}	−0.4 V	13.42%	12

Table S2. Distribution of *m*/*z* signals of related molecules obtained from the standard mass spectra (Figure S22-S26).

m/*z*	NH$_3$	O$_2$	N$_2$	H$_2$O	N$_2$H$_4$
14	√		√		√
15	√				√
16	√	√		√	√
17	√			√	√
18	√			√	
19				√	
20				√	
27					√
28			√		√
29			√		√
30					√
31					√
32		√			√
33					√

4. Supplementary References

[1]   L. Xu, Y. Xu, X. Li, Z. Wang, T. Sun, X. Zhang, *Dalton Trans.* **2018**, *47*, 16696.

[2]   J. X. Yao, D. Bao, Q. Zhang, M. M. Shi, Y. Wang, R. Gao, J. M. Yan, Q. Jiang, *Small Methods* **2019**, *3*, 1800333.

[3]   C. Lv, C. Yan, G. Chen, Y. Ding, J. Sun, Y. Zhou, G. Yu, *Angew. Chem. Int. Ed.* **2018**, *57*, 6073.

[4]   B. Chang, Q. Liu, N. Chen, Y. Yang, *ChemCatChem* **2019**, *11*, 1884.

[5]   Y. C. Hao, Y. Guo, L. W. Chen, M. Shu, X. Y. Wang, T. A. Bu, W. Y. Gao, N. Zhang, X. Su, X. Feng, J. W. Zhou, B. Wang, C. W. Hu, A. X. Yin, R. Si, Y. W. Zhang, C. H. Yan, *Nat. Catal.* **2019**, *2*, 448.

[6]   L. Li, C. Tang, B. Xia, H. Jin, Y. Zheng, S. Z. Qiao, *ACS Catal.* **2019**, *9*, 2902.

[7]   Y. Wang, M. M. Shi, D. Bao, F. L. Meng, Q. Zhang, Y. T. Zhou, K. H. Liu, Y. Zhang, J. Z. Wang, Z. W. Chen, D. P. Liu, Z. Jiang, M. Luo, L. Gu, Q. H. Zhang, X. Z. Cao, Y. Yao, M. H. Shao, Y. Zhang, X. B. Zhang, J. G. Chen, J. M. Yan, Q. Jiang, *Angew. Chem. Int. Ed.* **2019**, *58*, 9464.

[8]   F. Wang, X. Lv, X. Zhu, J. Du, S. Lu, A. A. Alshehri, K. A. Alzahrani, B. Zheng, X. Sun, *Chem. Commun.* **2020**, *56*, 2107.

[9]   L. Xia, W. Fu, P. Zhuang, Y. Cao, M. O. L. Chee, P. Dong, M. Ye, J. Shen, *ACS Sustainable Chem. Eng.* **2020**, *8*, 2735.

[10]   R. Zhang, L. Ji, W. Kong, H. Wang, R. Zhao, H. Chen, T. Li, B. Li, Y. Luo, X. Sun, *Chem. Commun.* **2019**, *55*, 5263.

[11]   Y. Qiu, S. Zhao, M. Qin, J. Diao, S. Liu, L. Dai, W. Zhang, X. Guo, *Inorg. Chem. Front.* **2020**, *7*, 2006.

[12]   Y. Liu, B. Huang, X. Chen, Z. Tian, X. Zhang, P. Tsiakaras, P. K. Shen, *Appl. Catal. B* **2020**, *271*, 118919.

Chapter 4

The Controllable Reconstruction of Bi-MOFs for Electrochemical CO_2 Reduction through Electrolyte and Potential Mediation

4.1 Introduction and Significance

The reconstruction of catalyst materials is widely observed under operating conditions. However, this process usually results in uncontrollable and detrimental deviation from target active sites and expected catalytic performance. Therefore, it is highly desirable to understand and modulate these processes toward stable and well-defined surface chemistry. To address this issue, we employed Bi-based metal-organic frameworks (Bi-MOFs) as a case study to investigate and control the reconstruction process during electrochemical CO_2 reduction reaction (CRR). The Highlights of this work include:

(1) A comprehensive understanding of the two-step reconstruction of Bi-MOFs under CRR conditions. In situ Raman spectra combined with ex situ electron microscopy revealed the two-step reconstruction: a) electrolyte-mediated conversion of Bi-MOFs to $Bi_2O_2CO_3$, and; b) potential-mediated reduction of $Bi_2O_2CO_3$ to Bi.

(2) A controllable reconstruction was proposed to synthesize well-defined electrocatalysts in situ. Intentional pre-treatment of Bi-MOFs achieved a highly active, selective (Faradaic efficiency ~ 92%), and stable (>10 h for reaction, and > 1 week in electrolyte) Bi electrocatalyst for formate production.

(3) Understanding of active sites and reaction mechanism on Bi-based CRR electrocatalysts. Theoretical computations, kinetics analyses, and in situ infrared spectroscopy confirmed that surface unsaturated Bi atoms formed during the controlled reconstruction serve as the active sites, and bicarbonate functions as the proton donor for *OCHO formation in the first hydrogeneration step.

4.2 The Controllable Reconstruction of Bi-MOFs for Electrochemical CO_2 Reduction through Electrolyte and Potential Mediation

This chapter is included as it appears as a journal paper published by Dazhi Yao, Cheng Tang, Anthony Vasileff, Xing Zhi, Yan Jiao and Shi-Zhang Qiao. The controllable reconstruction of Bi-MOFs for electrochemical CO_2 reduction through electrolyte and potential mediation. Angew. Chem. Int. Ed. 2021, 60, 18178– 18184.

Statement of Authorship

Title of Paper	The Controllable Reconstruction of Bi-MOFs for Electrochemical CO2 Reduction through Electrolyte and Potential Mediation
Publication Status	☑ Published ☐ Accepted for Publication ☐ Submitted for Publication ☐ Unpublished and Unsubmitted work written in manuscript style
Publication Details	D. Yao, C. Tang, A. Vasileff, X. Zhi, Y. Jiao, S. Z. Qiao, Angewandte Chemie International Edition, 2021, 60, 18178-18184

Principal Author

Name of Principal Author (Candidate)	Dazhi Yao		
Contribution to the Paper	Designed and conducted the experiments, analysed the data, wrote the manuscript.		
Overall percentage (%)	70%		
Certification:	This paper reports on original research I conducted during the period of my Higher Degree by Research candidature and is not subject to any obligations or contractual agreements with a third party that would constrain its inclusion in this thesis. I am the primary author of this paper.		
Signature		Date	28/09/2022

Co-Author Contributions

By signing the Statement of Authorship, each author certifies that:

i. the candidate's stated contribution to the publication is accurate (as detailed above);

ii. permission is granted for the candidate in include the publication in the thesis; and

iii. the sum of all co-author contributions is equal to 100% less the candidate's stated contribution.

Name of Co-Author	Cheng Tang		
Contribution to the Paper	Guided to design the whole experiment, helped data analysis, and revised the manuscript		
Signature		Date	28/09/2022

Name of Co-Author	Anthony Vasileff		
Contribution to the Paper	Assisted in experimental design and setup, sample characterization and data analysis. Provided review and comments on the manuscript.		
Signature		Date	28/09/2022

Name of Co-Author	Xing Zhi		
Contribution to the Paper	Helped with DFT calculations and data analysis. Discussion and revision of manuscript		
Signature		Date	28/09/2022

Name of Co-Author	Yan Jiao		
Contribution to the Paper	Guided the DFT calculations and data analysis. Discussion of manuscript		
Signature		Date	28/09/2022

Name of Co-Author	Shi-Zhang Qiao		
Contribution to the Paper	Supervision of the work, discussion and conceptualization of this manuscript and manuscript evaluation and revision.		
Signature		Date	28-09-2022

Electrocatalysis

The Controllable Reconstruction of Bi-MOFs for Electrochemical CO$_2$ Reduction through Electrolyte and Potential Mediation

Dazhi Yao$^+$, Cheng Tang$^+$, Anthony Vasileff, Xing Zhi, Yan Jiao, and Shi-Zhang Qiao*

Abstract: Monitoring and controlling the reconstruction of materials under working conditions is crucial for the precise identification of active sites, elucidation of reaction mechanisms, and rational design of advanced catalysts. Herein, a Bi-based metal–organic framework (Bi-MOF) for electrochemical CO$_2$ reduction is selected as a case study. In situ Raman spectra combined with ex situ electron microscopy reveal that the intricate reconstruction of the Bi-MOF can be controlled using two steps: 1) electrolyte-mediated dissociation and conversion of Bi-MOF to Bi$_2$O$_2$CO$_3$, and 2) potential-mediated reduction of Bi$_2$O$_2$CO$_3$ to Bi. The intentionally reconstructed Bi catalyst exhibits excellent activity, selectivity, and durability for formate production, and the unsaturated surface Bi atoms formed during reconstruction become the active sites. This work emphasizes the significant impact of pre-catalyst reconstruction under working conditions and provides insight into the design of highly active and stable electrocatalysts through the regulation of these processes.

Introduction

Electrochemical CO$_2$ reduction (CRR) is a promising strategy for carbon capture, storage, and utilization,[1] as it can convert greenhouse CO$_2$ into useful carbon feedstocks (e.g., CO[2] and HCOOH[3]) and value-added C$_{2+}$ products (e.g., hydrocarbons[4] and alcohols[5]) for fuels and chemicals manufacturing.[6] Recent studies have focused on tuning the intrinsic catalytic activity and selectivity of a catalyst by changing composition, morphology, and atomic arrangement.[7] However, the catalyst design, performance evaluation, and structure–property correlation are always conducted empirically and ambiguously. This is generally because of a limited identification and understanding of the actual active sites and reaction pathway under working conditions.[8] Specifically, the catalyst materials may undergo dynamic changes, such as phase transformation,[9] nanoclustering,[10] degradation,[11] and reduction,[3a,12] under operating conditions. This reconstruction will result in uncontrollable and

detrimental deviation from the target active sites and expected catalytic performance.[8c,11b]

Reconstruction of an electrocatalyst is any change of chemical composition and/or structure at the surface or in the bulk and is widely observed.[8a,b,11b,13] The reconstruction is usually triggered and mediated by the interaction with surrounding reactants/products under working conditions,[8b,c,14] and by external stimuli like electric potential.[8b,11b] For instance, during the CRR and nitrogen reduction reaction (NRR), negative reduction potentials led to the surface reconstruction of Bi-based metal–organic frameworks (MOFs) into metallic Bi^0, which then serves as the active phase.[15] Interestingly, in a similar potential region, the reconstruction of Bi-MOFs generated various morphologies that were different from the precursors, such as Bi nanoparticles,[15b,d] nanosheets,[15a] and nanoleaves.[15c] However, the reconstruction process and its causal factors are not well understood, resulting in poor control of the final morphology, chemical valence states and active sites. Consequently, this leads to an inaccurate understanding of structure–property relationships and limited means to optimize catalytic performance.[3d,13g,15b] Therefore, it is highly desirable to fully understand the reconstruction behavior of electrocatalysts under working conditions, and controllably regulate the inevitable reconstruction toward higher activity and stability. This is crucial for refining reaction mechanisms and designing optimal catalysts.

Herein, we report a comprehensive investigation into the favorable control of the reconstruction of Bi-MOFs for the CRR. With a combination of ex situ electron microscopy and infrared spectroscopy, and in situ Raman spectra, we reveal that the reconstruction can be controllably tailored by two steps (Figure 1 a): 1) electrolyte-mediated dissociation and conversion of Bi-MOFs to Bi$_2$O$_2$CO$_3$, and 2) potential-mediated reduction of Bi$_2$O$_2$CO$_3$ to Bi. The intentional pre-treatment of the Bi-MOFs achieves a highly active, selective, and stable Bi catalyst for CO$_2$ electroreduction to formate. Density functional theory (DFT) computations, kinetics analyses, and in situ infrared spectroscopy tests are performed to explain the underlying reaction mechanism.

Results and Discussion

Bi-MOF nanorods (NR) were first prepared according to previous reports with some modifications.[15d,16] Scanning electron microscopy (SEM) and transmission electron microscopy (TEM) images show that they are typically 4 μm in length and 100 nm in width (Figure 1 b, Figure S1). The X-ray diffraction (XRD) pattern confirms the crystal phase indexed

[*] D. Yao,[+] Dr. C. Tang,[+] Dr. A. Vasileff, Dr. X. Zhi, Dr. Y. Jiao,
Prof. S. Z. Qiao
Centre for Materials in Energy and Catalysis
School of Chemical Engineering and Advanced Materials
The University of Adelaide
Adelaide, SA 5005 (Australia)
E-mail: s.qiao@adelaide.edu.au

[+] These authors contributed equally to this work.

Supporting information and the ORCID identification number(s) for the author(s) of this article can be found under:
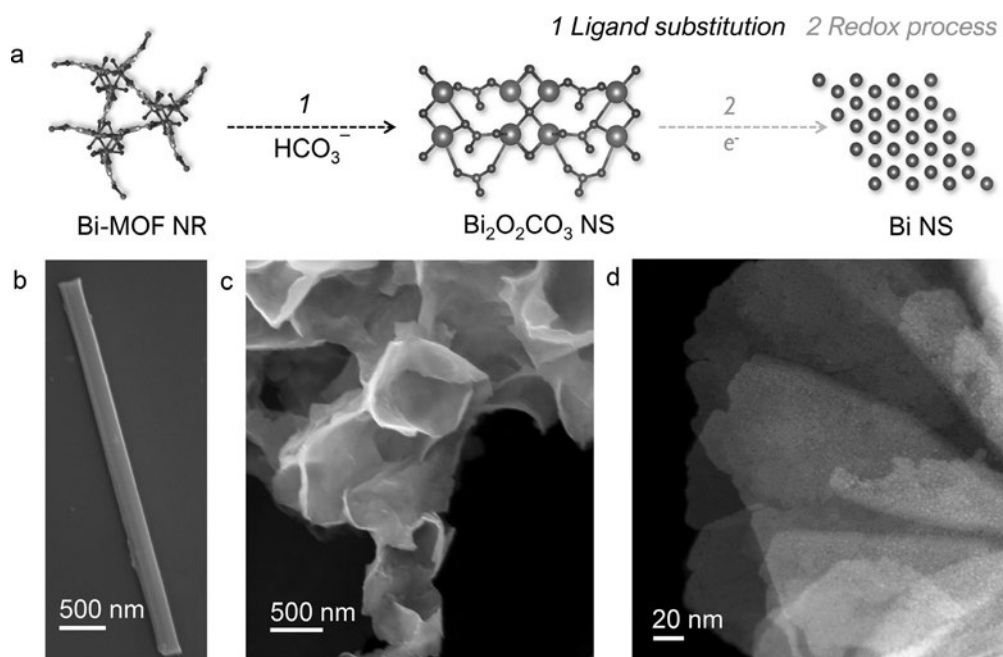https://doi.org/10.1002/anie.202104747.

Angew. Chem. Int. Ed. **2021**, *60*, 18178–18184

73

Figure 1. In situ surface reconstruction of the Bi-MOF NR to Bi NS for the CRR. a) Schematic of the two-step reconstruction process, including 1) the electrolyte-mediated chemical and structural transformation from Bi-MOF NR to $Bi_2O_2CO_3$ NS, and 2) electrochemical reduction of $Bi_2O_2CO_3$ NS to Bi NS. b) SEM image for Bi-MOF NR and c) $Bi_2O_2CO_3$ NS. d) TEM image for the final Bi NS.

to CAU-17 (Figure S2).[16a] When the Bi-MOF is used as a pre-catalyst for the CRR, it will be exposed simultaneously to the electrolyte and applied potential. Therefore, the electrolyte-mediated and potential-mediated reconstruction were investigated separately to understand the reconstruction process and distinguish influential factors.

Once contacted with the CRR electrolyte (0.1 M or 1.0 M $KHCO_3$ aqueous solution), the Bi-MOF NR was converted into nanosheets, as shown by SEM images (Figure 1c, Figure S3 and S4). XRD patterns confirm that the nanosheets are $Bi_2O_2CO_3$ (Figure S5), showing two characteristic peaks around 30° and 33° (JCPDS No. 44-1488). To resolve the atomic-scale structure of the $Bi_2O_2CO_3$, bright field and high-angle annular dark field (HAADF) imaging was performed on an aberration-corrected scanning transmission electron microscope (STEM). As shown in Figure S6a–d, the tetragonal structure of $Bi_2O_2CO_3$ exhibits an interplanar distance of 0.273 nm for (110) facets, consistent with the XRD analysis. Figure S6b shows a vertical $Bi_2O_2CO_3$ NS with a thickness of about 4 nm. The crystallographic orientation of $Bi_2O_2CO_3$ NS was confirmed by analyzing the fast Fourier transform (FFT) pattern of the STEM images, and shows that growth occurred along the ⟨002⟩ direction (Figure S6d,e). It is worth noting that bismuth vacancies and in-plane defects are contained on $Bi_2O_2CO_3$ NS, presumably derived from strain and CO_2 release during atomic reorganization. Importantly, these nanosheets retain their morphology under CRR working conditions (Figure 1d), indicating that the final structure and morphology of electrocatalysts is determined by the formation of $Bi_2O_2CO_3$.

To better understand the electrolyte-mediated formation of $Bi_2O_2CO_3$, Fourier-transform infrared spectroscopy (FT-IR) and Raman spectra were employed to monitor the conversion. Compared to the Bi-MOF NR precursor, the $Bi_2O_2CO_3$ NS showed none of the characteristic FT-IR bands for carboxylate groups in the trimesic acid (H_3BTC) ligands, whilst several new bands at 1477, 1385, 1053, and 845 cm^{-1} assigned to the carbonate groups in $Bi_2O_2CO_3$ arose (Figure 2a, Figure S7, Table S1).[17] Ex situ Raman spectra of the Bi-MOF NR and $Bi_2O_2CO_3$ NS revealed an obvious shift in the Bi−O vibrational band from 85 to 77 cm^{-1} and from 150 to 162 cm^{-1} (Figure 2b). In situ Raman tests showed this dynamic transformation from Bi-MOF to $Bi_2O_2CO_3$ more clearly (Figure 2c). As the immersion time increases, the bands at 820 cm^{-1} and 1002 cm^{-1} gradually weaken, which is attributed to the loss of C−H in the BTC^{3-} ligands (Table S2). After immersing in 0.1 M $KHCO_3$ for 20 min, the band at 820 cm^{-1} disappeared, whilst a new band appeared at 1069 cm^{-1}, which was assigned to the stretching vibration of C−O in $Bi_2O_2CO_3$. These findings imply that the reconstruction involves a change of Bi coordination from Bi←O_{BTC} to Bi←$O_{bicarbonate}$ due to ligand exchange in 0.1 M $KHCO_3$ solution.

We note that no change in morphology or crystal structure was observed after immersing the Bi-MOF NR in water (Figure S8), 0.1 M NaCl aqueous solution (Figure S9), 0.1 M HCl, and 0.1 M NaOH (Figure S10), consistent with previous studies.[18] In addition, the thickness of the $Bi_2O_2CO_3$ NS in $KHCO_3$ aqueous solution is dependent on the bicarbonate concentration. Specifically, 3.8 nm and 11.5 nm thick sheet were obtained in 0.1 M and 1 M $KHCO_3$ solution, respectively (Figure S11 and S12). These observations indicate that the Bi←O_{BTC} coordination in the Bi-MOF NR is stable against water, Cl^-, OH^-, and Na^+,[16a] but is sensitive to HCO_3^-. Due to the similarity in bite angle with BTC^{3-}, HCO_3^- is likely to replace the BTC^{3-} linkers by solvent-assisted ligand ex-
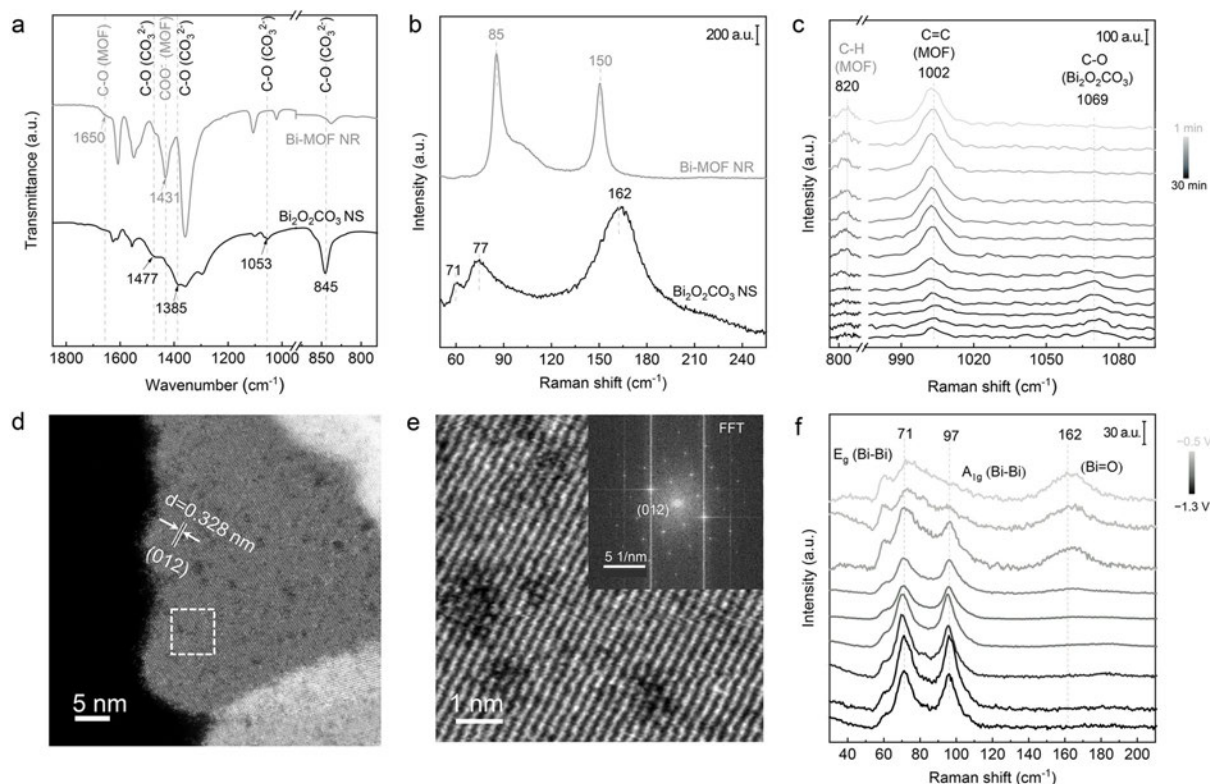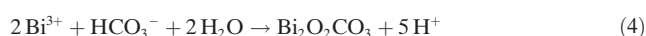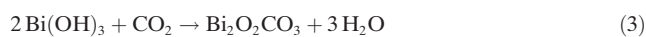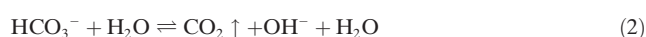
Figure 2. Spectroscopic and morphological characterizations for reconstruction process from Bi-MOF NR to $Bi_2O_2CO_3$ NS and in situ electro-reduction to Bi NS prior to CRR. a) FT-IR spectra and b) Raman spectra of Bi-MOF NR and resultant $Bi_2O_2CO_3$ NS. c) In situ Raman spectra to reveal the conversion from Bi-MOF NR to $Bi_2O_2CO_3$ NS on exposure to 0.1 M $KHCO_3$. d) HAADF-STEM image of Bi NS. e) Magnified HAADF-STEM image of the marked area from Figure 2d (inserted FFT image). f) In situ Raman spectra to characterize the transformation from $Bi_2O_2CO_3$ NS to Bi NS under CRR conditions.

change, thereby accelerating the dissociation of Bi^{3+} and triggering chemical and structural transformation.[15b,18] In this reaction scheme, the hydrolysis of HCO_3^- and dissociation of Bi^{3+} could occur at the same time and contribute to each other. Therefore, the electrolyte-mediated reconstruction can be described by Equations (1)–(3).[19] The whole reaction can be written as Equation (4).

$$Bi^{3+} + 3H_2O \rightleftharpoons Bi(OH)_3 \downarrow + 3H^+ \tag{1}$$

$$HCO_3^- + H_2O \rightleftharpoons CO_2 \uparrow + OH^- + H_2O \tag{2}$$

$$2Bi(OH)_3 + CO_2 \rightarrow Bi_2O_2CO_3 + 3H_2O \tag{3}$$

$$2Bi^{3+} + HCO_3^- + 2H_2O \rightarrow Bi_2O_2CO_3 + 5H^+ \tag{4}$$

The electrochemical stability of the $Bi_2O_2CO_3$ NS during the CRR was assessed using cyclic voltammetry (CV) in CO_2-staturated 0.1 M $KHCO_3$ solution. As shown in Figure S13, the current density in the first scan is smaller than the following segments, and finally becomes stable after 10 segments. This indicates the potential-mediated conversion of $Bi_2O_2CO_3$ NS to another electrochemically stable Bi species, identified as Bi NS by spectroscopy and microscopy characterizations. As shown in Figure S14, all the XRD peaks assigned to $Bi_2O_2CO_3$ disappeared after the electroreduction, whilst new peaks indexed to rhombohedral Bi (JCPDS No. 44-1246) were

formed. Compared to the $Bi_2O_2CO_3$ NS, the in situ reduced Bi NS showed no noticeable morphological change after CV treatment or amperometry *i–t* testing (Figure S15 and S16). The resultant nanosheets were also ultrathin and contained abundant in-plane defects (Figure 1d and 2d). As shown in Figure 2e, the clear lattice fringes and corresponding FFT pattern matched well into the Bi (012) facet. The thickness of in situ converted Bi NS is similar to that of the $Bi_2O_2CO_3$ NS (Figure S17), which is determined to be 3.5 nm and 11 nm, respectively.

The potential-mediated reconstruction of $Bi_2O_2CO_3$ NS to Bi NS was also investigated by in situ Raman spectroscopy (Figure 2f and S18). When the applied potential was scanned from −0.5 to −1.3 V versus the reversible hydrogen electrode (vs. RHE), the characteristic vibrations of C−O (1069 cm^{-1}) and Bi=O (162 cm^{-1}) from $Bi_2O_2CO_3$ weakened gradually, whilst two new bands appeared at 71 and 97 cm^{-1}. These bands likely correspond to the E_g and A_{1g} stretching modes of Bi−Bi bonds, respectively.[15d] This confirmed the complete transformation of $Bi_2O_2CO_3$ NS to Bi NS.

By combining in situ Raman spectroscopy with ex situ electron microscopy, we can conclude that the bicarbonate anion plays a key role in triggering the surface reconstruction, and the applied negative potential is crucial for the formation of the stable and active Bi phase. Based on these findings, we propose a two-step intentional pre-treatment of Bi-MOFs
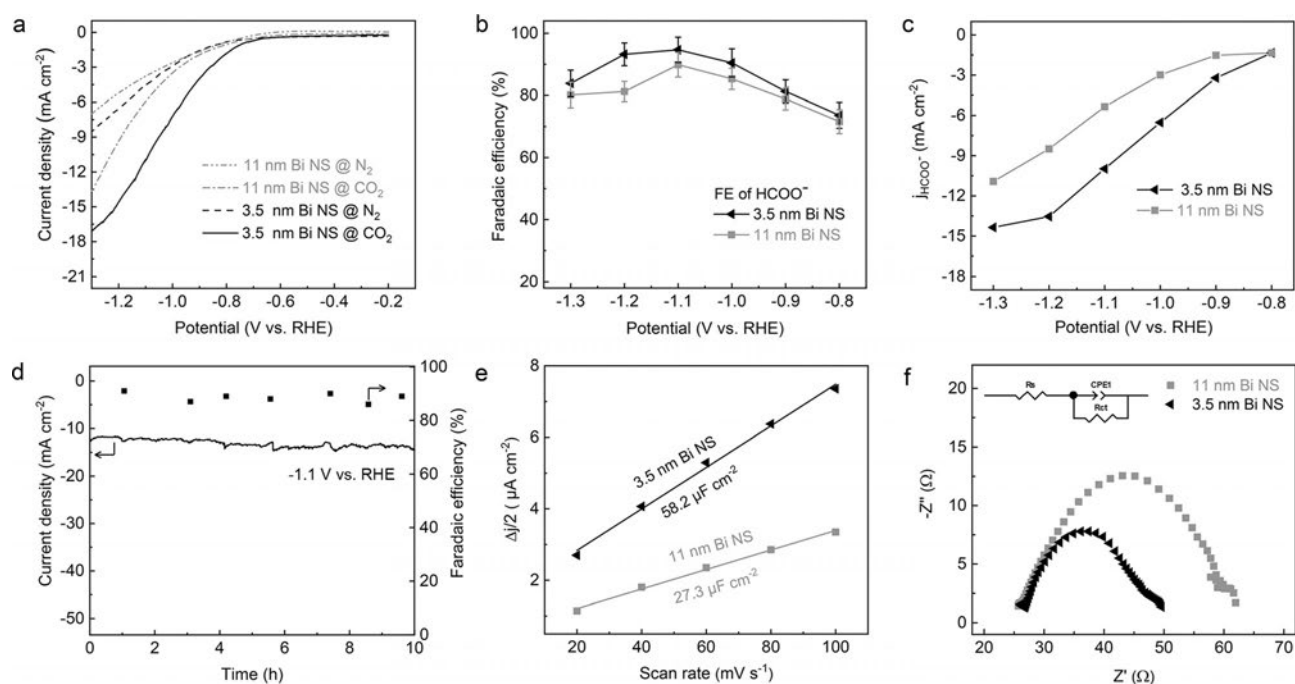
Figure 3. Electrochemical performance of the Bi NS for the CRR. a) LSV curves of the two Bi NS in N_2- and CO_2-saturated 0.1 M KHCO$_3$. b) Potential-dependent Faradaic efficiencies of HCOO$^-$ for the Bi NS in CO_2-saturated 0.1 M KHCO$_3$. c) Potential-dependent HCOO$^-$ partial current densities of the Bi NS. d) Amperometric $i–t$ stability of the 3.5 nm Bi NS in 0.1 M KHCO$_3$ at -1.1 V vs. RHE. e) Electrochemically active surface area measurement. Half of charging current density differences ($\Delta j/2$) are plotted against scan rates. f) Nyquist plots for the two Bi NS with fitted circuit shown.

before CRR operation to achieve controllable reconstruction. This includes 1) immersing the Bi-MOF electrode in KHCO$_3$ electrolyte for 30 min, and 2) reducing the electrode by 10 segments of cyclic voltammetry.

Electrocatalytic CRR performance of the in situ reconstructed Bi NS samples (3.5 nm and 11 nm thick) was then investigated in a two-compartment gas-tight H-cell. Figure 3a shows linear scan voltammograms (LSV) of the Bi NS in CO_2- and N_2-saturated 0.1 M KHCO$_3$. Both Bi NS samples exhibited higher current densities in the CO_2-saturated electrolyte, showing obvious activity for the CRR. The cathodic current density of the 3.5 nm Bi NS increases significantly below -0.8 V, reaching -17 mA cm^{-2} at -1.3 V vs. RHE. To further evaluate CRR activity and selectivity, chronoamperometry tests were conducted at different potentials in CO_2-saturated 0.1 M KHCO$_3$ solution (Figure S19). The resultant gaseous and liquid products after one-hour electrolysis were collected and analyzed by gas chromatography (GC) and nuclear magnetic resonance (NMR), respectively. As shown in Figure 3b and S20, formate (HCOO$^-$) was the primary product over the whole potential range, and CO and H$_2$ were minor products. The 3.5 nm Bi NS achieves a maximum Faradaic efficiency (FE) for formate production of 92% at -1.1 V vs. RHE, and a maximum formate partial current density (j_{HCOO^-}) of -15 mA cm^{-2} at -1.3 V vs. RHE (Figure 3c). All these parameters are superior to the 11 nm Bi NS, and among the best results for Bi-based CRR catalysts (Table S3).[15b,c,19b] Furthermore, the 3.5 nm Bi NS exhibits stable CRR performance at -1.1 V for 10 h with negligible change in current density and FE for formate (around 90%; Fig-

ure 3d). The catalytic performance was also retained after the electrodes were stored in N_2-saturated water for one week (Figure S21). Postmortem analysis after long-term electrolysis reveals that the morphology of the Bi NS was preserved (Figure S22). The excellent stability of the Bi NS in both electrocatalytic conditions and storage in water is attributed to the controlled morphological reconstruction from the pre-treatment process.

To understand the thickness-dependent performance of these Bi NS, the electrochemically active surface area (EC-SA) and electrochemical impedance spectra (EIS) were investigated. As shown in Figure 3e and S23, the 3.5 nm Bi NS possessed nearly twice the ECSA of the 11 nm Bi NS. Further, the Nyquist plots in Figure 3f show a smaller charge-transfer resistance for the 3.5 nm NS compared with the thicker counterpart (21.99 Ω vs. 35.13 Ω). Therefore, the thinner Bi NS provides more accessible active sites and exhibits faster electron transfer. This can be easily optimized by changing the bicarbonate concentration in the first electrolyte-mediated reconstruction step.

DFT computations were conducted to understand the activity origins of the Bi NS for the CRR. As shown in Figure 2d,e, the Bi NS possessed abundant defects in the crystalline planes. Therefore, we studied the Bi (012) surface with a complete lattice (pristine Bi) and with one vacant Bi atom in the top layer (defective Bi), as shown in Figure S24. Electronic structure analysis reveals that the p-orbital density of states (DOS) position of defective Bi moves toward the Fermi level (Figure S25), indicating stronger adsorption of CO_2 and intermediates.[20] As illustrated in previous studies,

the electrochemical reduction of CO_2 to HCOOH on Bi generally occurs through the *OCHO intermediate, with oxygen atom(s) binding to the Bi surface.[6a] Therefore, *OCHO was selected as the key intermediate to be studied for CO_2 electroreduction. Figure S26 presents the computed free energy diagrams for CO_2 electro-reduction to HCOOH via the *OCHO pathway on both pristine and defective Bi models. The Gibbs free energy change (ΔG) for the first electron/proton transfer to *OCHO is much higher than the second one, denoting that the first hydrogenation step on both Bi NS is the rate-determining step (RDS). However, on defective Bi, ΔG for the first electron transfer (0.29 eV) is lower than that on pristine Bi (0.33 eV). It implies that this step is thermodynamically more favorable on defective Bi. Furthermore, charge difference analysis reveals electron depletion on the Bi atoms during *OCHO adsorption (Figure S27). The active Bi site (the most negatively charged) in defective Bi loses 0.23 more electrons for OCHO* adsorption than that in pristine Bi (Figure S28). Taken together, the computation results show that vacancy-adjacent (or unsaturated) Bi sites in the Bi NS are the active sites and have enhanced adsorption of *OCHO intermediates.[20a,c]

The reaction mechanism was further studied by investigating the kinetics and intermediates. As displayed in Figure 4a, a comparison of Tafel plots between 3.5 nm and 11 nm Bi NS shows that the thinner Bi NS exhibited improved reaction kinetics by virtue of the smaller Tafel slope (170.1 vs. 213.2 mV dec^{-1}) in a similar potential region. Although the Tafel slope is much higher than 118 mV dec^{-1}, it is likely the first electron transfer step is the RDS on 3.5 nm Bi NS,[21] and

is consistent with the DFT analysis (Figure S26). Reaction order study reveals a quasi-first order (0.80) dependency of formate partial current density on bicarbonate concentration (Figure 4b, Figure S29). This suggests that the bicarbonate will participate directly in the formate pathway.[15a,21]

To determine the role of bicarbonate in the formate pathway, in situ attenuated total reflectance surface-enhanced infrared absorption spectroscopy (ATR-SEIRAS) measurements were performed in both CO_2- and N_2-saturated 0.1 M KHCO$_3$. As the applied potential was stepped from −0.6 V to −1.3 V vs. RHE, an increase of a band around 2936 cm^{-1} was observed (Figure 4c). This is ascribed to the C−H stretching vibration of *OCHO intermediates,[22] rationalizing the selection of *OCHO as the key reaction intermediate for DFT computation. Interestingly, a weak C−H stretching vibration band was also observed in N_2-saturated electrolyte (Figure 4d), suggesting a possible CRR pathway without direct CO_2 feed.[15a] This can be rationalized by the generation of CO_2 from HCO$_3^-$ decomposition [Eq. (2)].[19a] However, the CRR activity contributed solely by HCO$_3^-$ is less than 5% (based on FE$_{formate}$) after one-hour electrolysis, compared with that in CO_2-saturated electrolyte (Figure S30). Consequently, we infer that bicarbonate serves predominantly as a proton donor for *OCHO formation in the first hydrogenation step according to Equations (5)–(7) (Figure 4e, θ depicts an active site on which species can adsorb).[15a,21,23]

$$\theta_{Bi} + CO_2(aq) + e^- + HCO_3^- \rightleftharpoons \theta_{Bi-OCHO} + CO_3^{2-} \quad (5)$$

$$\theta_{Bi-OCHO} + e^- + H^+ \rightarrow \theta_{Bi-HCOOH} \quad (6)$$

$$\theta_{Bi-HCOOH} \rightarrow \theta_{Bi} + HCOOH \quad (7)$$
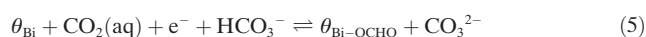
Conclusion

We definitively revealed the reconstruction process of Bi-MOFs under CRR conditions, which guided the synthesis of a highly active, selective, and stable Bi catalyst for CRR. The intricate reconstruction process of Bi-MOFs prior to CRR can be decoupled into two steps: 1) electrolyte-mediated conversion of Bi-MOF NR to $Bi_2O_2CO_3$ NS by bicarbonate-initiated ligand substitution, and 2) potential-mediated reduction of $Bi_2O_2CO_3$ NS to Bi NS. The first step controls the final morphology and defects, whilst the second step determines the final composition and valence states. For example, tuning the bicarbonate concentration can produce $Bi_2O_2CO_3$ NS and Bi NS with different thickness and catalytic performance. In situ reconstructed Bi NS with thickness of 3.5 nm achieved a FE of 92% towards formate production and was stable under operating conditions. Abundant unsaturated Bi atoms were formed adjacent to the surface vacancies during the two-step reconstruction, contributing to more favorable adsorption of *OCHO intermediates and ultimately benefiting the reaction process. This work emphasizes the necessity and importance of thoroughly understanding the surface reconstruction process under working conditions. It also highlights the controllable manipulation of such reconstruc-
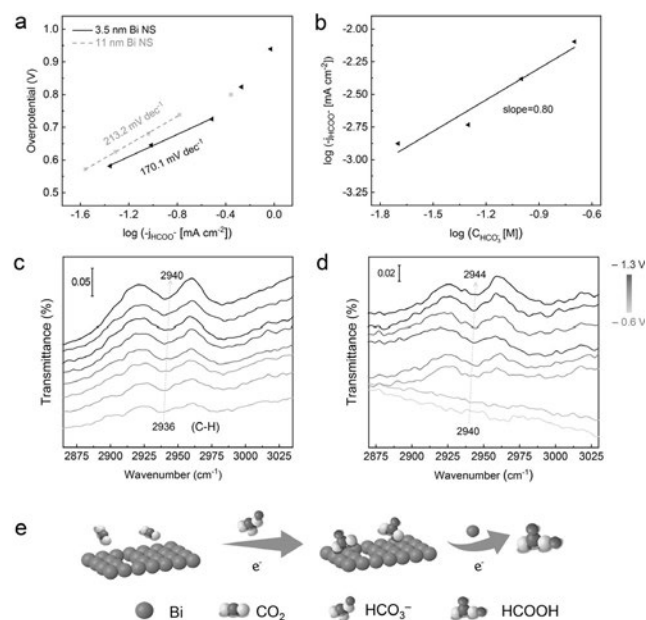

Figure 4. CRR catalytic mechanism and pathway study on the Bi NS. a) Tafel plots for the two Bi NS. b) Rate dependency on the concentration of bicarbonate ([HCO$_3^-$]) for 3.5 nm Bi NS at −0.9 V vs. RHE. c) In situ ATR-SEIRAS of 3.5 nm Bi NS in CO_2-saturated 0.1 M KHCO$_3$ and d) N_2-saturated 0.1 M KHCO$_3$ between −0.6 V and −1.3 V vs. RHE. e) Proposed CRR pathway on the defective Bi NS surface with HCO$_3^-$ participation.

tion processes to rationally design highly active and stable electrocatalysts.

Conflict of Interest

The authors declare no conflict of interest.

[1] a) C. T. Dinh, T. Burdyny, M. G. Kibria, A. Seifitokaldani, C. M. Gabardo, F. P. G. de Arquer, A. Kiani, J. P. Edwards, P. De Luna, O. S. Bushuyev, C. Q. Zou, R. Quintero-Bermudez, Y. J. Pang, D. Sinton, E. H. Sargent, *Science* **2018**, *360*, 783–787; b) C. Xia, P. Zhu, Q. Jiang, Y. Pan, W. T. Liang, E. Stavitski, H. N. Alshareef, H. T. Wang, *Nat. Energy* **2019**, *4*, 776–785; c) S. Hernández, M. A. Farkhondehfal, F. Sastre, M. Makkee, G. Saracco, N. Russo, *Green Chem.* **2017**, *19*, 2326–2346; d) D. D. Zhu, J. L. Liu, S. Z. Qiao, *Adv. Mater.* **2016**, *28*, 3423–3452.

[2] a) T. Zheng, K. Jiang, N. Ta, Y. Hu, J. Zeng, J. Liu, H. Wang, *Joule* **2019**, *3*, 265–278; b) C. Xu, X. Zhi, A. Vasileff, D. Wang, B. Jin, Y. Jiao, Y. Zheng, S. Z. Qiao, *Small Struct.* **2021**, *2*, 2000058.

[3] a) H. Yang, N. Han, J. Deng, J. Wu, Y. Wang, Y. Hu, P. Ding, Y. Li, Y. Li, J. Lu, *Adv. Energy Mater.* **2018**, *8*, 1801536; b) F. Yang, A. O. Elnabawy, R. Schimmenti, P. Song, J. Wang, Z. Peng, S. Yao, R. Deng, S. Song, Y. Lin, M. Mavrikakis, W. Xu, *Nat. Commun.* **2020**, *11*, 1088; c) A. S. Agarwal, Y. Zhai, D. Hill, N. Sridhar, *ChemSusChem* **2011**, *4*, 1301–1310; d) X. Zhang, T. Lei, Y. Liu, J. Qiao, *Appl. Catal. B* **2017**, *218*, 46–50.

[4] a) M. G. Kibria, C. T. Dinh, A. Seifitokaldani, P. De Luna, T. Burdyny, R. Quintero-Bermudez, M. B. Ross, O. S. Bushuyev, F. P. G. de Arguer, P. D. Yang, D. Sinton, E. H. Sargent, *Adv. Mater.* **2018**, *30*, 1804867; b) A. Vasileff, Y. P. Zhu, X. Zhi, Y. Q. Zhao, L. Ge, H. M. Chen, Y. Zheng, S. Z. Qiao, *Angew. Chem. Int. Ed.* **2020**, *59*, 19649–19653; *Angew. Chem.* **2020**, *132*, 19817–19821.

[5] a) X. Lv, L. Shang, S. Zhou, S. Li, Y. Wang, Z. Wang, T.-K. Sham, C. Peng, G. Zheng, *Adv. Energy Mater.* **2020**, *10*, 2001987; b) T. T. Zhuang, Z. Q. Liang, A. Seifitokaldani, Y. Li, P. De Luna, T. Burdyny, F. Che, F. Meng, Y. Min, R. Quintero-Bermudez, C. T. Dinh, Y. Pang, M. Zhong, B. Zhang, J. Li, P. N. Chen, X. L.

Zheng, H. Liang, W. N. Ge, B. J. Ye, D. Sinton, S. H. Yu, E. H. Sargent, *Nat. Catal.* **2018**, *1*, 421–428; c) D. Karapinar, N. T. Huan, N. Ranjbar Sahraie, J. Li, D. Wakerley, N. Touati, S. Zanna, D. Taverna, L. H. Galvão Tizei, A. Zitolo, F. Jaouen, V. Mougel, M. Fontecave, *Angew. Chem. Int. Ed.* **2019**, *58*, 15098–15103; *Angew. Chem.* **2019**, *131*, 15242–15247.

[6] a) L. R. L. Ting, B. S. Yeo, *Curr. Opin. Electrochem.* **2018**, *8*, 126–134; b) L. Fan, C. Xia, F. Yang, J. Wang, H. Wang, Y. Lu, *Sci. Adv.* **2020**, *6*, eaay3111; c) S. Nitopi, E. Bertheussen, S. B. Scott, X. Liu, A. K. Engstfeld, S. Horch, B. Seger, I. E. L. Stephens, K. Chan, C. Hahn, J. K. Nørskov, T. F. Jaramillo, I. Chorkendorff, *Chem. Rev.* **2019**, *119*, 7610–7672; d) C. Tang, Y. Zheng, M. Jaroniec, S. Z. Qiao, *Angew. Chem. Int. Ed.* **2021**, https://doi.org/10.1002/anie.202101522; *Angew. Chem.* **2021**, https://doi.org/10.1002/ange.202101522.

[7] a) A. Vasileff, C. Xu, Y. Jiao, Y. Zheng, S. Z. Qiao, *Chem* **2018**, *4*, 1809–1831; b) Y. Zheng, A. Vasileff, X. Zhou, Y. Jiao, M. Jaroniec, S. Z. Qiao, *J. Am. Chem. Soc.* **2019**, *141*, 7646–7659.

[8] a) P. Chen, Y. Tong, C. Wu, Y. Xie, *Acc. Chem. Res.* **2018**, *51*, 2857–2866; b) H. Jiang, Q. He, Y. Zhang, L. Song, *Acc. Chem. Res.* **2018**, *51*, 2968–2977; c) Y. Huang, A. G. A. Mohamed, J. Xie, Y. Wang, *Nano Energy* **2021**, *82*, 105745.

[9] W. R. Zheng, M. J. Liu, L. Y. S. Lee, *ACS Catal.* **2020**, *10*, 81–92.

[10] Y. F. Li, F. Cui, M. B. Ross, D. Kim, Y. Sun, P. D. Yang, *Nano Lett.* **2017**, *17*, 1312–1317.

[11] a) S. Popović, M. Smiljanić, P. Jovanovič, J. Vavra, R. Buonsanti, N. Hodnik, *Angew. Chem. Int. Ed.* **2020**, *59*, 14736–14746; *Angew. Chem.* **2020**, *132*, 14844–14854; b) J. Huang, N. Hörmann, E. Oveisi, A. Loiudice, G. L. De Gregorio, O. Andreussi, N. Marzari, R. Buonsanti, *Nat. Commun.* **2018**, *9*, 3117.

[12] a) N. Han, Y. Wang, H. Yang, J. Deng, J. Wu, Y. Li, Y. Li, *Nat. Commun.* **2018**, *9*, 1320; b) Q. Lei, H. Zhu, K. Song, N. Wei, L. Liu, D. Zhang, J. Yin, X. Dong, K. Yao, N. Wang, X. Li, B. Davaasuren, J. Wang, Y. Han, *J. Am. Chem. Soc.* **2020**, *142*, 4213–4222; c) S. H. Lee, J. C. Lin, M. Farmand, A. T. Landers, J. T. Feaster, J. E. Avilés Acosta, J. W. Beeman, Y. Ye, J. Yano, A. Mehta, R. C. Davis, T. F. Jaramillo, C. Hahn, W. S. Drisdell, *J. Am. Chem. Soc.* **2021**, *143*, 588–592; d) Q. Gong, P. Ding, M. Xu, X. Zhu, M. Wang, J. Deng, Q. Ma, N. Han, Y. Zhu, J. Lu, Z. Feng, Y. Li, W. Zhou, Y. Li, *Nat. Commun.* **2019**, *10*, 2807.

[13] a) S. L. Zhao, C. H. Tan, C. T. He, P. F. An, F. Xie, S. Jiang, Y. F. Zhu, K. H. Wu, B. W. Zhang, H. J. Li, J. Zhang, Y. Chen, S. Q. Liu, J. C. Dong, Z. Y. Tang, *Nat. Energy* **2020**, *5*, 881–890; b) T. Wu, S. Sun, J. Song, S. Xi, Y. Du, B. Chen, W. A. Sasangka, H. Liao, C. L. Gan, G. G. Scherer, L. Zeng, H. Wang, H. Li, A. Grimaud, Z. J. Xu, *Nat. Catal.* **2019**, *2*, 763–772; c) A. Zhang, Y. Liang, H. Li, B. Zhang, Z. Liu, Q. Chang, H. Zhang, C. F. Zhu, Z. Geng, W. Zhu, J. Zeng, *Nano Lett.* **2020**, *20*, 8229–8235; d) Y. Wang, Y. L. Zhu, S. L. Zhao, S. X. She, F. F. Zhang, Y. Chen, T. Williams, T. Gengenbach, L. H. Zu, H. Y. Mao, W. Zhou, Z. P. Shao, H. T. Wang, J. Tang, D. Y. Zhao, C. Selomulya, *Matter* **2020**, *3*, 2124–2137; e) Y. Zhao, X. Tan, W. Yang, C. Jia, X. Chen, W. Ren, S. C. Smith, C. Zhao, *Angew. Chem. Int. Ed.* **2020**, *59*, 21493–21498; *Angew. Chem.* **2020**, *132*, 21677–21682; f) Q. He, H. Xie, Z. u. Rehman, C. Wang, P. Wan, H. Jiang, W. Chu, L. Song, *ACS Energy Lett.* **2018**, *3*, 861–868; g) X. H. Zhao, Q. S. Chen, D. H. Zhuo, J. Lu, Z. N. Xu, C. M. Wang, J. X. Tang, S. G. Sun, G. C. Guo, *Electrochim. Acta* **2021**, *367*, 137478.

[14] F. Tao, P. A. Crozier, *Chem. Rev.* **2016**, *116*, 3487–3539.

[15] a) C. S. Cao, D. D. Ma, J. F. Gu, X. Y. Xie, G. Zeng, X. F. Li, S. G. Han, Q. L. Zhu, X. T. Wu, Q. Xu, *Angew. Chem. Int. Ed.* **2020**, *59*, 15014–15020; *Angew. Chem.* **2020**, *132*, 15124–15130; b) P. Lamagni, M. Miola, J. Catalano, M. S. Hvid, M. A. H. Mamakhel, M. Christensen, M. R. Madsen, H. S. Jeppesen, X. M. Hu, K. Daasbjerg, T. Skrydstrup, N. Lock, *Adv. Funct. Mater.* **2020**, *30*, 1910408; c) J. Yang, X. L. Wang, Y. T. Qu, X. Wang, H. Huo, Q. K. Fan, J. Wang, L. M. Yang, Y. E. Wu, *Adv. Energy Mater.*

2020, *10*, 2001709; d) D. Yao, C. Tang, L. Li, B. Xia, A. Vasileff, H. Jin, Y. Zhang, S. Z. Qiao, *Adv. Energy Mater.* **2020**, *10*, 2001289.

[16] a) M. Köppen, A. Dhakshinamoorthy, A. K. Inge, O. Cheung, J. Angstrom, P. Mayer, N. Stock, *Eur. J. Inorg. Chem.* **2018**, 3496–3503; b) L. Xu, Y. Xu, X. Li, Z. Wang, T. Sun, X. Zhang, *Dalton Trans.* **2018**, *47*, 16696–16703.

[17] P. Taylor, S. Sunder, V. J. Lopata, *Can. J. Chem.* **1984**, *62*, 2863–2873.

[18] W. W. Yuan, J. X. Wu, X. D. Zhang, S. Z. Hou, M. Xu, Z. Y. Gu, *J. Mater. Chem. A* **2020**, *8*, 24486–24492.

[19] a) S. Zhu, B. Jiang, W.-B. Cai, M. Shao, *J. Am. Chem. Soc.* **2017**, *139*, 15664–15667; b) X. An, S. Li, X. Hao, X. Du, T. Yu, Z. Wang, X. Hao, A. Abudula, G. Guan, *Sustainable Energy Fuels* **2020**, *4*, 2831–2840; c) T. Fan, W. Ma, M. Xie, H. Liu, J. Zhang, S. Yang, P. Huang, Y. Dong, Z. Chen, X. Yi, *Cell Rep. Phys. Sci.* **2021**, *2*, 100353; d) Y. Zhang, X. Zhang, Y. Ling, F. Li, A. M.

Bond, J. Zhang, *Angew. Chem. Int. Ed.* **2018**, *57*, 13283–13287; *Angew. Chem.* **2018**, *130*, 13467–13471.

[20] a) X. Zhi, Y. Jiao, Y. Zheng, S. Z. Qiao, *Small* **2019**, *15*, 1804224; b) Y. Jiao, Y. Zheng, K. Davey, S. Z. Qiao, *Nat. Energy* **2016**, *1*, 16130; c) A. Vasileff, X. Zhi, C. Xu, L. Ge, Y. Jiao, Y. Zheng, S. Z. Qiao, *ACS Catal.* **2019**, *9*, 9411–9417.

[21] A. Wuttig, Y. Yoon, J. Ryu, Y. Surendranath, *J. Am. Chem. Soc.* **2017**, *139*, 17109–17113.

[22] a) G. Socrates, *Infrared and Raman characteristic group frequencies: tables and charts*, Wiley, Hoboken, **2004**; b) Y. Ichinohe, T. Wadayama, A. Hatta, *J. Raman Spectrosc.* **1995**, *26*, 335–340.

[23] K. Fan, Y. Jia, Y. Ji, P. Kuang, B. Zhu, X. Liu, J. Yu, *ACS Catal.* **2020**, *10*, 358–364.

The Controllable Reconstruction of Bi-MOFs for Electrochemical CO$_2$ Reduction through Electrolyte and Potential Mediation

Dazhi Yao$^+$, Cheng Tang$^+$, Anthony Vasileff, Xing Zhi, Yan Jiao, and Shi-Zhang Qiao*

anie_202104747_sm_miscellaneous_information.pdf

Experimental Procedures

Chemicals and materials: Acetic acid (CH_3COOH), bismuth (III) chloride ($BiCl_3$, ≥ 98%), concentrated hydrochloric acid (HCl, 36%), dimethylformamide (DMF, anhydrous, 99.8%), dimethyl sulfoxide-d_6 (DMSO, SKU-151874, 99.9 at.% D), deuterium oxide (D_2O, SKU-293040, 99.9 at.% D, contains 0.75 wt.% 3-(trimethylsilyl)propionic-2,2,3,3-d_4 acid, sodium salt), formate standard for ion chromatography (1000 mg/L in water), methanol (anhydrous, 99.8%), phenol, potassium iodide (KI, ≥ 99.5%), potassium chloride (KCl, ACS reagent, 99.0-100.5%), potassium bicarbonate ($KHCO_3$, BioUltra, ≥ 99.5%), sodium chloride (NaCl, ACS reagent, ≥99.0%), sulfuric acid (H_2SO_4, ACS reagent, 95.0–98.0%), and trimesic acid (Benzene-1,3,5-tricarboxylic acid, H_3BTC, 95%) were purchased from Sigma-Aldrich Chemical Reagent Co. Ltd. Isopropanol (≥ 99.8%), sodium hydroxide (NaOH, anhydrous pellets, ≥ 98%), ethanol (denatured, 100% AR), and concentrated nitric acid (HNO_3, 70%) were ordered from Chem-Supply Pty. Ltd. Carbon paper and Nafion 117 membrane (Dupont) were purchased from Fuelcell store. Ultra-high purity N_2 (99.999%), laser-grade CO_2 (99.995%), and ultra-high purity Ar (99.999%) were supplied by BOC gas, Australia. Ultrapure water (18.2 MΩ·cm, PURELAB OptionQ) was used in all experiments. All chemicals were used in this work without further purification.

Synthesis of bismuth oxyiodide (BiOI) nanosheets: $BiCl_3$ (0.2 mmol) was firstly dissolved in 20 mL of 1.2 M acetic acid and stirred for 30 min, followed by addition of 5 mL of 0.04 M KI solution. Then, the pH of the above mixture solution was adjusted to 6.0 using 1 M NaOH. After stirring for another 30 min, the solution was transferred to a 50 mL Teflon-lined autoclave and heated at 160 ºC for 2 h. The final product (BiOI nanosheets) was collected by centrifugation, washing with deionized water and freezing drying.

Synthesis of bismuth-based metal-organic framework nanorods (Bi-MOF NR): In a typical procedure, 0.339 g of BiOI nanosheets and 0.6 g of H_3BTC were dissolved in 15 mL of DMF

and 5 mL of methanol at room temperature and stirred for 30 min. Then, the dispersion was transferred into a 50 mL Teflon-lined autoclave and heated at 120 °C for 3 h. The obtained salmon pink powder was collected by centrifugation and washed with methanol several times to remove the solvent. Finally, the product was dried in an oven at 60 °C for 12 h.

Pretreatment of Nafion 117: The Nafion 117 (proton exchange membrane) was preconditioned by boiling in 5% H_2O_2 solution and ultrapure deionized water at 80 °C for 1 h, respectively, followed by treatment in 0.05 M H_2SO_4 for 3 h and in deionized water for another hour.

Electrode preparation: 10 mg of Bi-MOFs was dispersed in 960 µL of mixed solvent ($V_{isoproponal}$: V_{water} = 1 : 2) with the addition of 40 µL of 5 wt% Nafion. The dispersion was vigorously sonicated for 6 h to form a homogenous ink. The ink was drop-cast onto a 1 × 1 cm^2 carbon paper to reach a loading of 0.5 $mg_{Bi-MOFs}$ cm^{-2}.

***In situ* reconstruction of Bi-MOFs to $Bi_2O_2CO_3$ nanosheets (NS):** The prepared electrode modified with Bi-MOFs was directly immersed into fresh 0.1 M $KHCO_3$ or 1.0 M $KHCO_3$. After 30 minutes, this electrode was taken out and rinsed with deionized water and ethanol several times and finally kept in N_2-saturated ethanol for further use.

***In situ* electrochemical reduction of $Bi_2O_2CO_3$ to Bi NS:** The as-obtained $Bi_2O_2CO_3$ electrode was electro-reduced by 10-segment consecutive cyclic voltammetry (CV) scans from –0.3 V to –1.4 V versus the reversible hydrogen electrode (vs RHE) in CO_2-saturated 0.1 M $KHCO_3$ with a scan rate of 50 mV s^{-1}.

Material characterizations: The crystal structure and chemical structure of the samples was characterized by powder X-ray diffraction spectroscopy (Rigaku MiniFlex 600 X-ray Diffractometer). The morphology of the materials was characterized by a field emission scanning electron microscope (SEM, FEI Quatum 450, 3.0 kV) and transmission electron microscope (TEM, FEI Tecnai G2 spirit TEM, 120 kV). High-angle annular dark-field scanning transmission electron microscopy (HADDF-STEM) imaging and energy-dispersive X-ray spectroscopy (EDX) mapping were taken on an FEI Titan Themis 80-200 (200 kV voltage) equipped with a Super-X high sensitivity windowless EDX detector for rapid compositional analysis. Atomic force microscopy (AFM) images were collected on NT-MDT Ntegra Solaris instrument. Fourier-transform infrared (FT-IR) spectroscopy was performed with a Thermo-Fisher Nicolet iS10.

Electrochemical measurements: Electrochemical measurements were performed on a 760E potentiostat (CH Instruments, USA) using a gas-tight H-cell with anode and cathode compartments separated by a Nafion 117. The *in situ* reconstructed Bi NS electrode was used

directly as the working electrode. An Ag/AgCl electrode and RuO$_2$-coated titanium mesh electrode were used as the reference and counter electrode, respectively. All electrochemical measurements were conducted in CO$_2$-saturated (pH = 6.8) or N$_2$-saturated (pH = 8.3) 0.1 M KHCO$_3$ electrolyte. Amperometric *i-t* technique was utilized to evaluate electrocatalytic performance for CO$_2$ reduction. Electrolysis was carried out at potentials between −0.8 V and −1.3 V vs RHE in 100 mV intervals for 1 hour testing. *iR* compensation was included in all electrochemical measurements. The conversion for the potential in Ag/AgCl to RHE was calculated as following (Correction under hydrogen saturated electrolyte):

$$E_{RHE} = E_{Ag/AgCl} + 0.224 + 0.059 \times pH \qquad (1)$$

Determination of products and calculation of Faradaic efficiency (FE): Briefly, 100 µL of headspace gas in the cathode compartment was automatically injected into a gas chromatograph (GC, Agilent 8890B configured with thermal conductivity detector and methanizer/flame ionization detector) for gas product quantification. The liquid products (formic acid/formate) were determined using nuclear magnetic resonance spectroscopy (NMR, Agilent 500/600 MHz ^{1}H NMR) and were quantified with internal standards (DMSO and phenol in D$_2$O).

The Faradaic efficiency for gaseous product was calculated as follows:

$$FE_{gas} = \frac{Q_{gas}}{Q_{total}} \times 100\% = \frac{\left(\frac{v}{60\ s/min}\right) \times \left(\frac{x}{24000\ cm^{-3}/mol}\right) \times N \times F}{j} \times 100\% \qquad (2)$$

where v = 10 mL min^{-1} is the volume flow rate of CO$_2$; x is the measured CO/H$_2$ concentration in sample loop referring to standard curve; N is the number of transferred electrons for production of CO/H$_2$ (here is 2); F = 96,485 C mol^{-1}; and j is the recorded current (A).

The Faradaic efficiency for liquid product was determined as follows:

$$FE_{liquid} = \frac{Q_{liquid}}{Q_{total}} \times 100\% = \frac{n \times N \times F}{Q_{total}} \times 100\% \qquad (3)$$

where n is the moles of liquid product; N is the number of transferred electrons for formic acid/formate (here is 2); F = 96,485 C mol^{-1}.

Tafel analysis and kinetic study: Overpotentials for HCOO$^-$ production were determined using the following equation:

$$\eta = E_{RHE} - E^0 \qquad (4)$$

where E^0 is the equilibrium potential for formate production.[2] For the analysis of electrochemical kinetics, Tafel slopes were derived from the Tafel equation:

$$\eta = b \lg \left(\frac{j_{HCOO^-}}{j^0} \right) \qquad (5)$$

where η (V) is an overpotential between the applied potential and the standard $CO_2/HCOO^-$ reduction potential E^0; b is the Tafel slope (mV dec^{-1}); j_{HCOO^-} is the partial current density (mA cm^{-2}) for $HCOO^-$ formation; j^0 is the total exchange current density (mA cm^{-2}).

Electrochemically active surface area (ECSA) measurement: ECSA $= R_f \times s$, in which s stands for the geometric area of carbon paper electrode (in this work, $s = 1.0$ cm^2). The roughness factor (R_f) was estimated from the ratio of double-layer capacitance (C_{dl}) for the working electrode and an ideal smooth metal electrode. Assuming that the average double-layer capacitance is 20 μF cm^{-2} for a smooth metal surface, $R_f = C_{dl}/20$.[1] The C_{dl} was determined by measuring the capacitive current associated with double-layer charging from the scan-rate dependence of cyclic voltammetric stripping. For this, the potential window of cyclic voltammetric stripping was 0.05 V−0.15 V vs Ag/AgCl (electrolyte: 0.1 M KHCO$_3$ solution). The scan rates were 20, 40, 60, 80 and 100 mV s^{-1}. The C_{dl} was estimated by plotting the $\Delta j/2 = (j_a - j_c)/2$ at 0.10 V vs Ag/AgCl against the scan rate, where j_c and j_a are the cathodic and anodic current densities, respectively.

In situ **Raman measurements:** The catalyst inks used for *in situ* Raman spectroscopy measurements were the same as those for electrochemical measurements. 40 μL of catalyst ink was uniformly deposited on a 5 mm × 4 mm screen-printed working electrode (Pine Research Instrumentation, RRPE1002C). The fully dried electrode was connected to the 760E electrochemical workstation via a cell grip and USB connector and was then attached to a microscope slide on the sample stage. 100 μL of CO_2-saturated 0.1 M KHCO$_3$ electrolyte was added dropwise to the electrode. A coverslip was then placed on the top of the electrode. *In situ* Raman spectra were collected using a Raman spectroscope (HORIBA LabRAM HR Evolution) configured with an MPLN50x objective len (Olympus), 1800 l mm^{-1} grating, and a 785-nm Raman laser. Baseline correction was applied in all *in situ* Raman spectra. All applied potentials were converted to RHE.

In situ **attenuated total reflectance surface-enhanced infrared absorption spectroscopy (ATR-SEIRAS) measurements:** *In situ* ATR-SEIRAS was performed with a Thermo-Fisher Nicolet iS20 equipped with a liquid nitrogen-cooled HgCdTe (MCT) detector and purged with dry air (grade 1). A PIKE electrochemical cell was mounted on a VeeMax III ATR accessory, with 60° Au-coated silicon prism (PIKE Technologies). A CHI 760E electrochemical workstation (CH Instruments, USA) was connected for chronoamperometric tests. All ATR-SEIRAS measurements were collected with a spectral resolution of 4 cm^{-1}, optical velocity of 1.8988,

and gain of 1.0. 100 µL of the catalyst ink suspension (0.5 mg mL^{-1}) was dropped onto the prism and left to dry slowly. The silicon prism was then assembled into electrochemical cell fitted with an Ag/AgCl electrode (Pine Research) and Pt wire as the reference and counter electrodes, respectively. The cell was filled with 5.5 mL of 0.1 M $KHCO_3$ solution and the defective Bi NS were *in situ* obtained after purging CO_2 for 30 min and following a similar electrochemical reduction discussed above.

Theoretical calculations: All calculations were performed using density functional theory (DFT). The Perdew-Burke Ernzerhof (PBE) functional was employed for electron exchange-correlation within the generalized gradient approximation (GGA), as implemented in the VASP code.[3] The ionic cores were described by the projector-augmented wave (PAW) method. Van der Waals (vdW) interactions between atoms were considered in all the energy calculations[4] with the plane-wave cutoff energy value of 450 eV. During geometry optimization, the structures were relaxed to forces on the atoms smaller than 0.01 eV Å^{-1}. Gamma k-point was used for all calculation. A ($3 \times 3 \times 1$) k-point grid was applied for bulk lattice constants optimization and studying the CO_2 electroreduction mechanism on Bi surface slabs. For density of state (DOS) analysis, more k-point grid ($8 \times 8 \times 8$) was utilized to increase the accuracy of plot.[5] The pristine Bi (012) surface was modelled with a five slab by cleaving a ($2 \times 2 \times 1$) supercell with 20 Å of vacuum space,[6] according to the HAADF-STEM image. The optimized lattice constants are $a = 4.609$ Å, $b = 14.393$ Å, and $c = 30.193$ Å. The defective Bi models were built by removing one Bi atom in the top layer.

The Gibbs free energy (G) of adsorbed and gas-phase species was calculated as:

$$G = E_{DFT} + ZPE - TS \qquad (6)$$

where E_{DFT} is the total energy of the system calculated from DFT; ZPE is the calculated zero-point energy, S is the calculated entropy, and T is the standard temperature of 298.15 K (Table S4). For the construction of free energy diagrams, all the species are referred to the Bi + CO_2 (g) + 2(H$^+$ + e$^-$) state, where Bi is the energy of the pristine or defective Bi slab models and CO_2 (g) is the gas-phase Gibbs free energy of CO_2. pH correction was also included and thus the free energy of H$^+$ was derived as $G_{H+} = 1/2 G_{H2} - k_B T \ln 10 \times pH$ (k_B is Boltzmann's constant).

The vibrational frequencies were computed by treating all 3N degrees of the adsorbates as vibrational within the harmonic oscillator approximation, and assuming that any changes in the vibrations of the nanocomposite surface were minimal, in concert with earlier studies.[7] Gas-phase free energies were also obtained by standard methods.[6] The standard state pressure of 101,325 Pa was used for the fugacity of gaseous CO_2 species, while a fugacity of 3534 Pa and

19 Pa were used for H_2O and HCOOH respectively, corresponding to vapour pressure of water, 1 M HCOOH.[8] The adsorbate solvation effects were included approximately in the same manner as in previous studies: intermediates containing adsorbed *OCHO was stabilized by 0.10 eV.[7a] Gas phase energetics of species containing a CO backbone were compensated to match experimental values. Specifically, 0.19 eV of compensation was used for CO_2.[4, 7a, 9] *OCHO was selected as the intermediate for formate production. This is supported by previous reports,[8b, 9] and more convincingly, by the C–H vibration signal detected in the *in situ* ATR-SEIRAS measurements.

The computational hydrogen electrode (CHE) model was applied to include the electrode potential correction to the free energy of each state, by considering the electrochemical proton-electron transfer being a function of the applied electrical potential.[7a, 10] In this model, the free energy of a proton-electron pair at 0 V vs RHE is defined to be equal to 1/2 of the H_2 free energy at 101,325 Pa. Spin−orbit coupling (SOC) was not included in the calculations.[1, 9a, 11]

Charge difference (ρ_{diff}) is calculated according to the following equation:

$$\rho_{diff} = \rho_{total} - \rho_{CO2^*} - \rho_{substrate} \qquad (7)$$

where ρ_{total} is the total charge density of Bi model with one CO_2 molecule adsorbed; ρ_{CO2^*} and $\rho_{substrate}$ are the charge densities of a gaseous CO_2 molecule and the initial system (Bi model), respectively.

Supplementary Figures
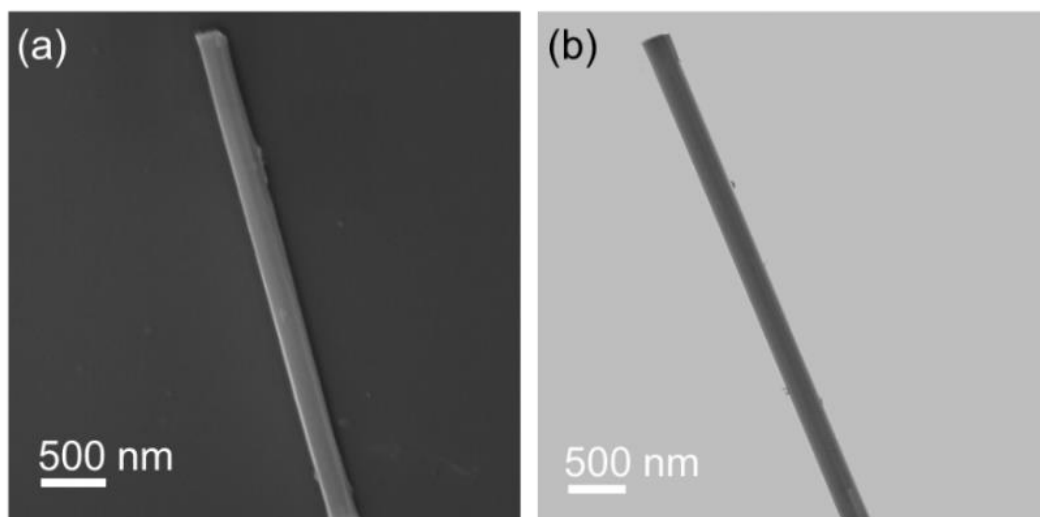
Figure S1. a) SEM image and b) TEM image of Bi-MOF NR.
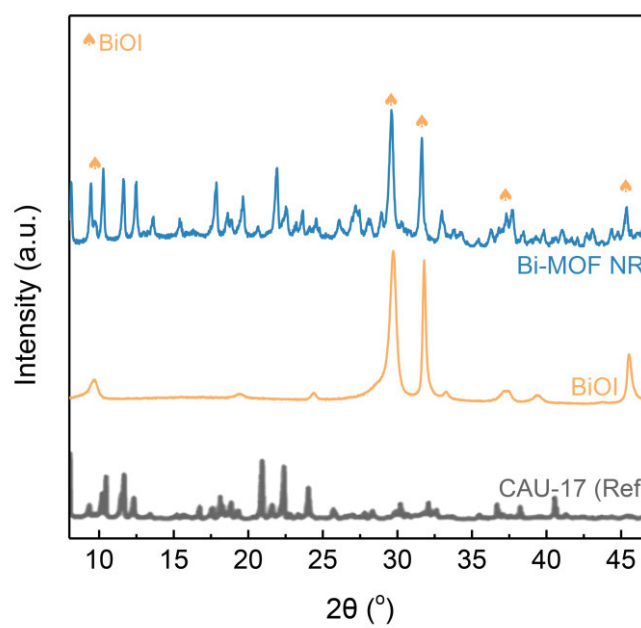
Figure S2. XRD pattern of Bi-MOF NR, with some precursor (BiOI) remaining.
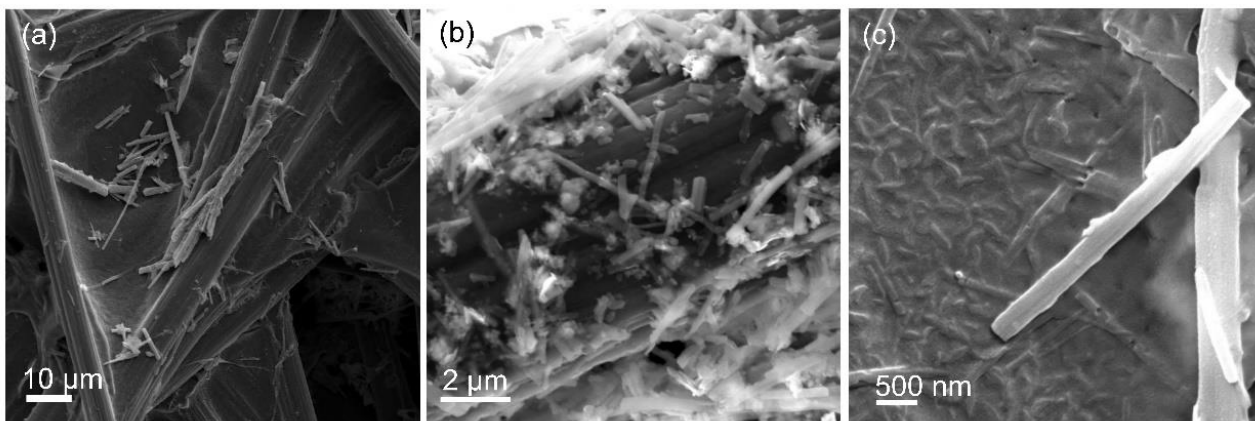
Figure S3. SEM images of different magnifications for Bi-MOF NR on carbon paper.
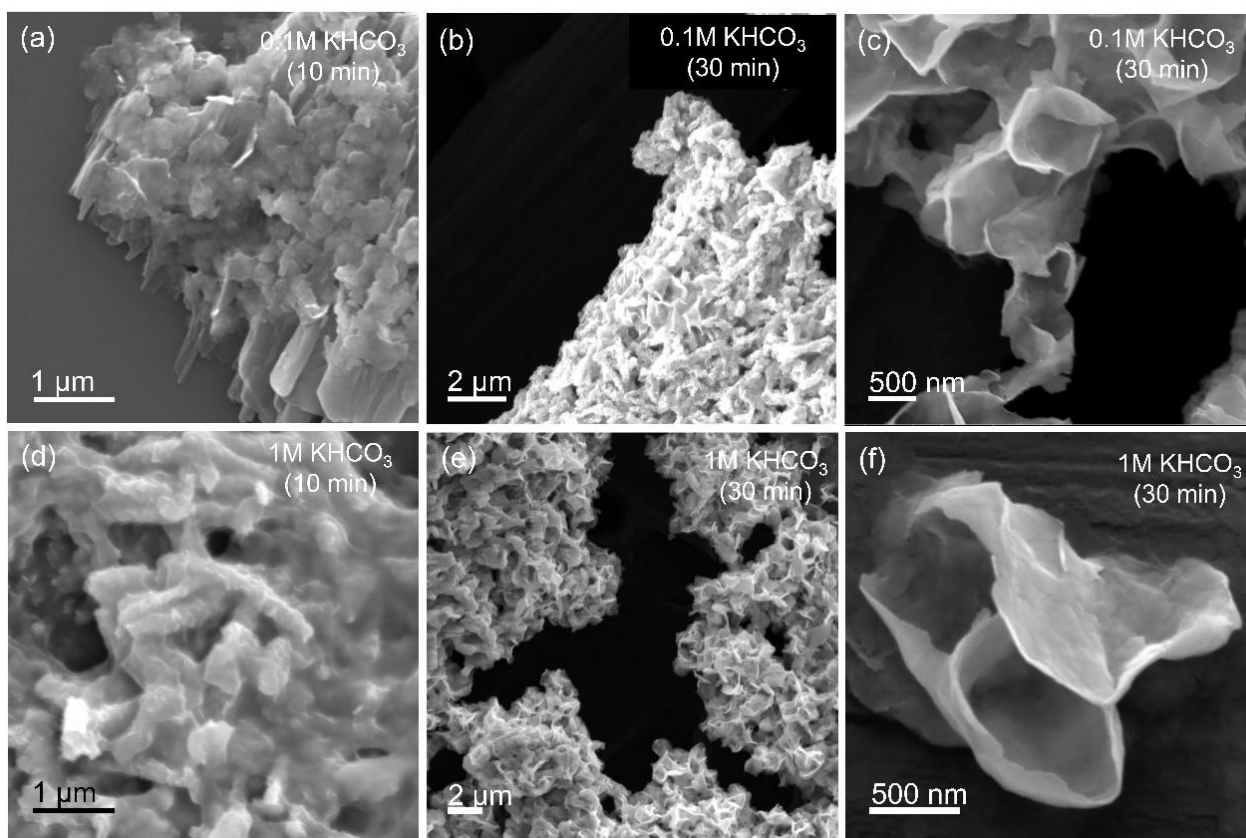
Figure S4. Typical SEM images of Bi-MOF NR soaked in KHCO$_3$ aqueous solution with different concentrations, showing drastic morphological transformation from Bi-MOF NR to Bi$_2$O$_2$CO$_3$ NS.
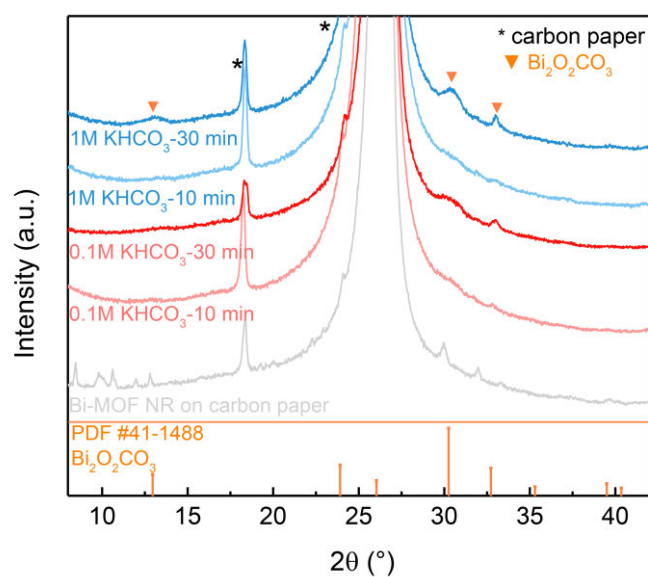
Figure S5. XRD patterns of Bi-MOF NR soaked in KHCO$_3$ aqueous solution for different lengths of time, generating a new phase corresponding to Bi$_2$O$_2$CO$_3$.
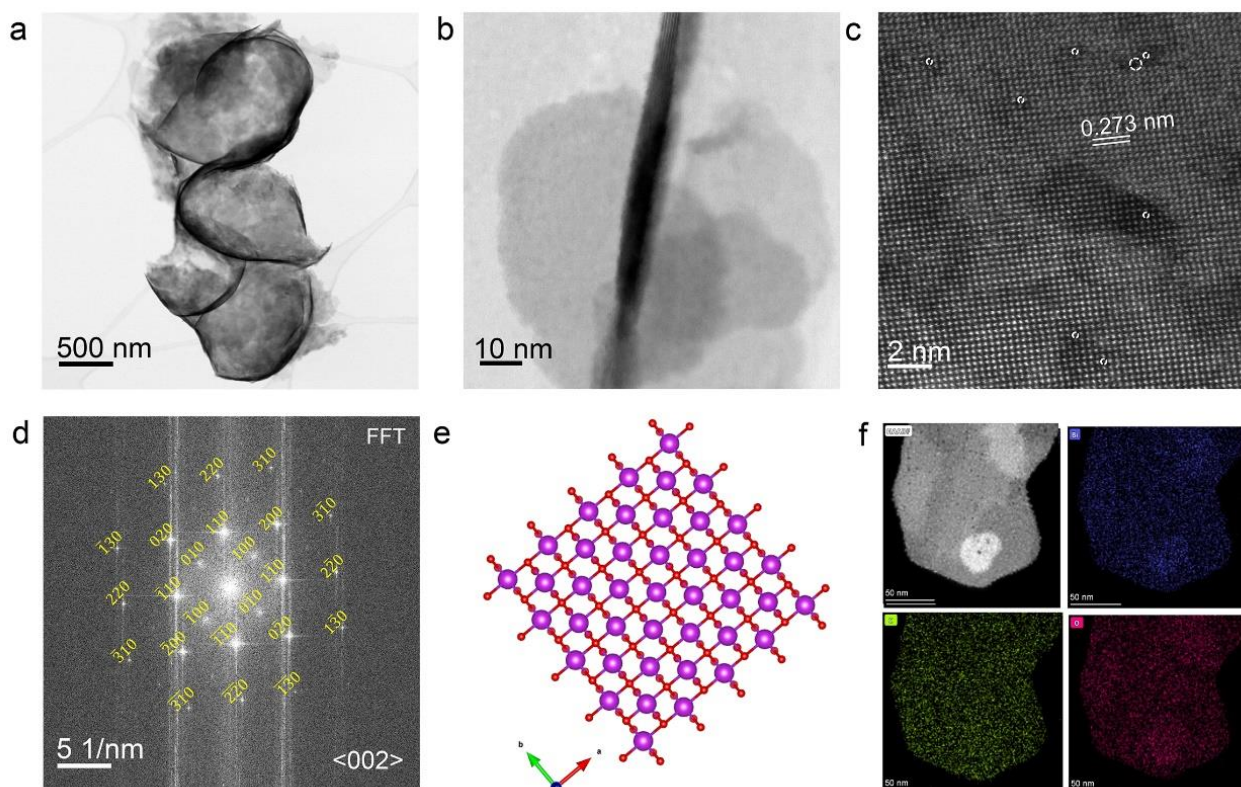
Figure S6. a-b) Bright field STEM images for Bi$_2$O$_2$CO$_3$ NS. c) HADDF-STEM image, d) corresponding fast Fourier transform (FFT) pattern, and e) visualized crystal structure for Bi$_2$O$_2$CO$_3$ NS. f) STEM-EDX mapping for Bi$_2$O$_2$CO$_3$ NS.
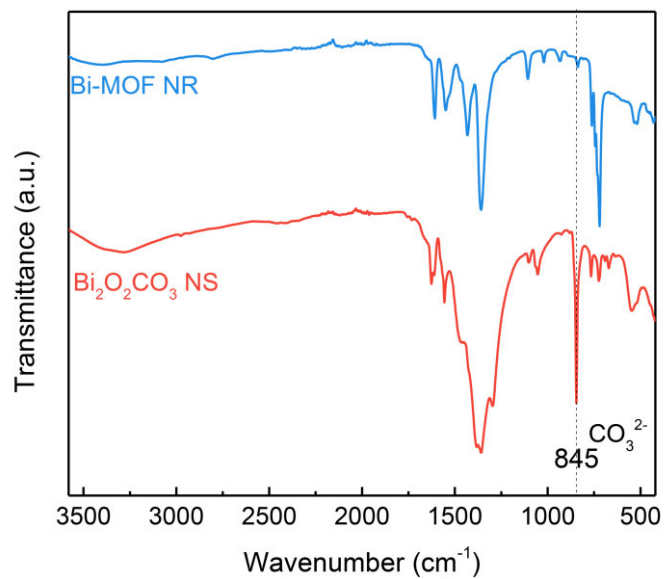
Figure S7. FT-IR spectra of Bi-MOF NR and Bi$_2$O$_2$CO$_3$ NS.
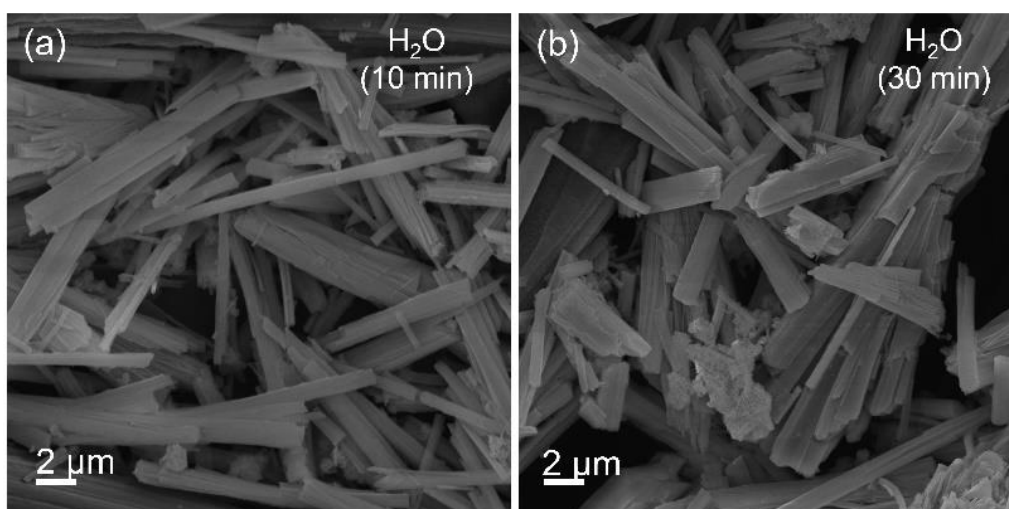
Figure S8. SEM images of Bi-MOF NR soaked in pure water for a) 10 min and b) 30 min.
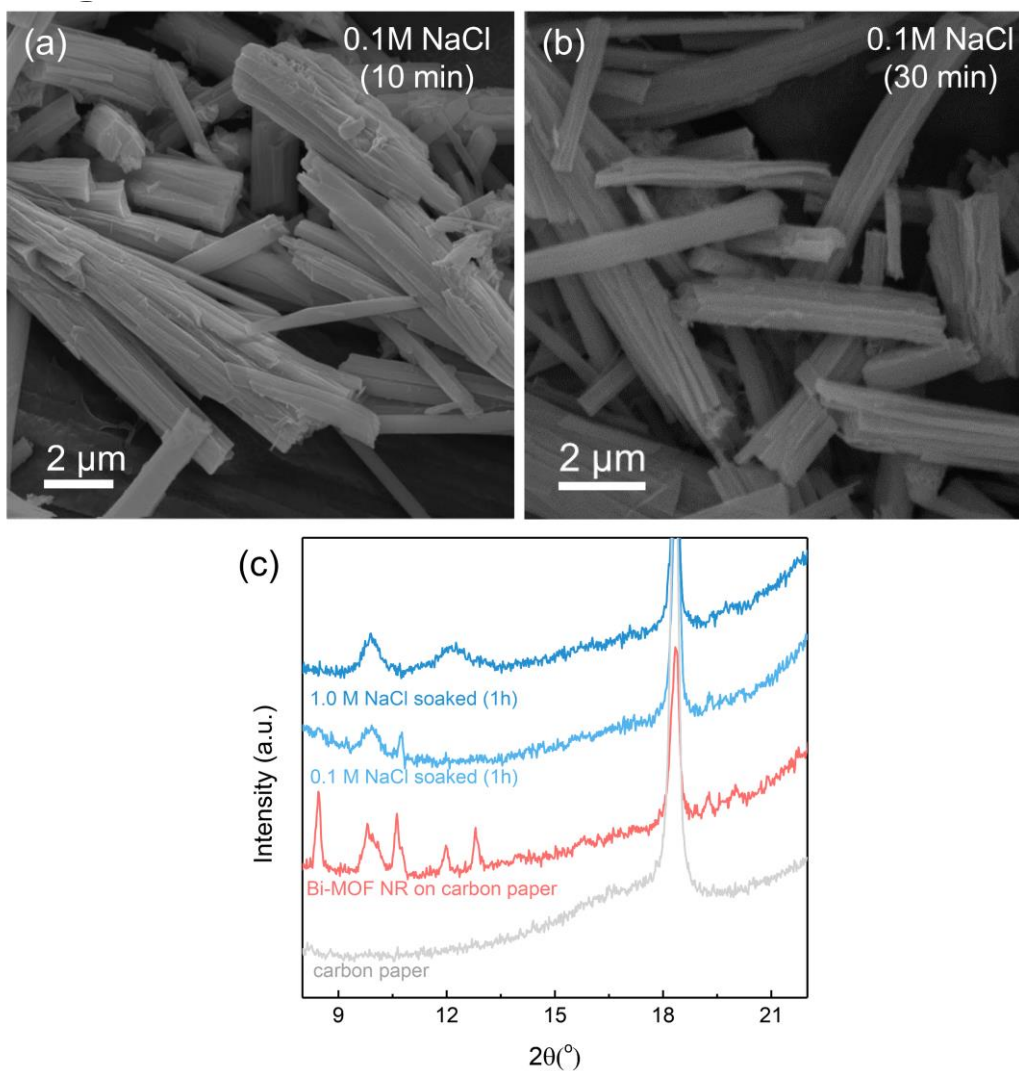
Figure S9. Typical SEM images of Bi-MOF NR soaked in 0.1 M NaCl aqueous solution for a) 10 min and b) 30 min. c) XRD patterns to characterize any compositional or phase change of the Bi-MOF NR after soaking in 0.1 M NaCl aqueous solution for 1 h.
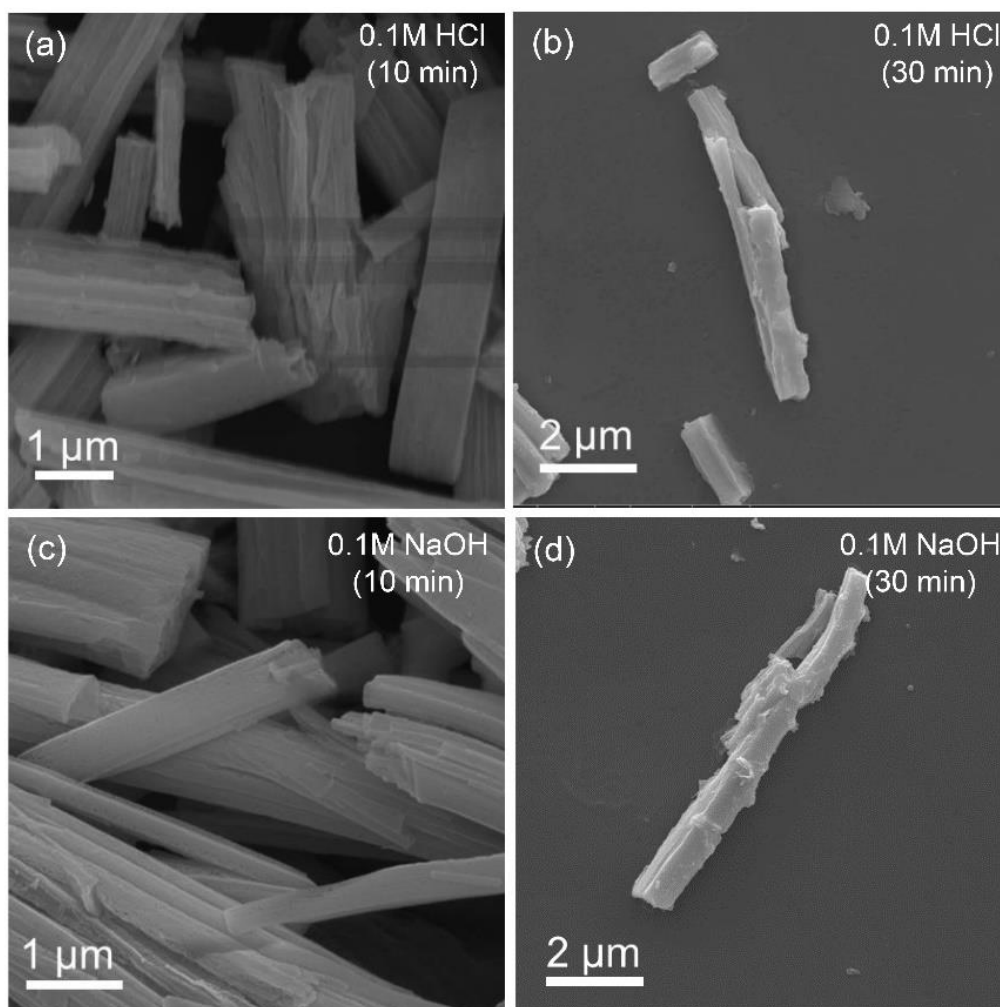
Figure S10. SEM images to characterize morphological changes of Bi-MOF NR soaked in a, b) 0.1 M HCl and c, d) 0.1 M NaOH aqueous solution.
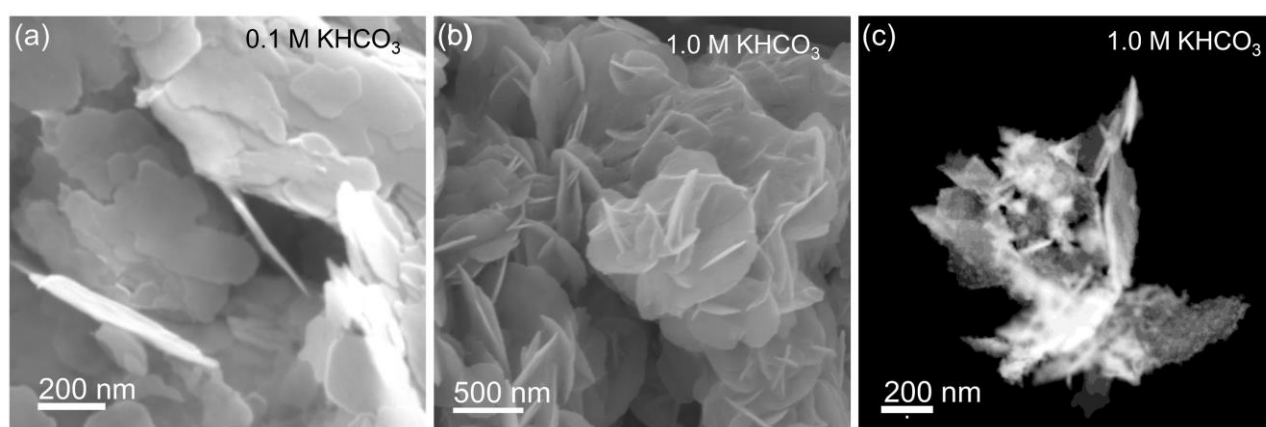
Figure S11. a, b) Typical SEM images and c) HADDF-STEM image of $Bi_2O_2CO_3$ NS derived from Bi-MOF NR soaked in different concentrations of $KHCO_3$ solution. The lateral size of $Bi_2O_2CO_3$ NS in c) is measured to be about 12.2 nm.
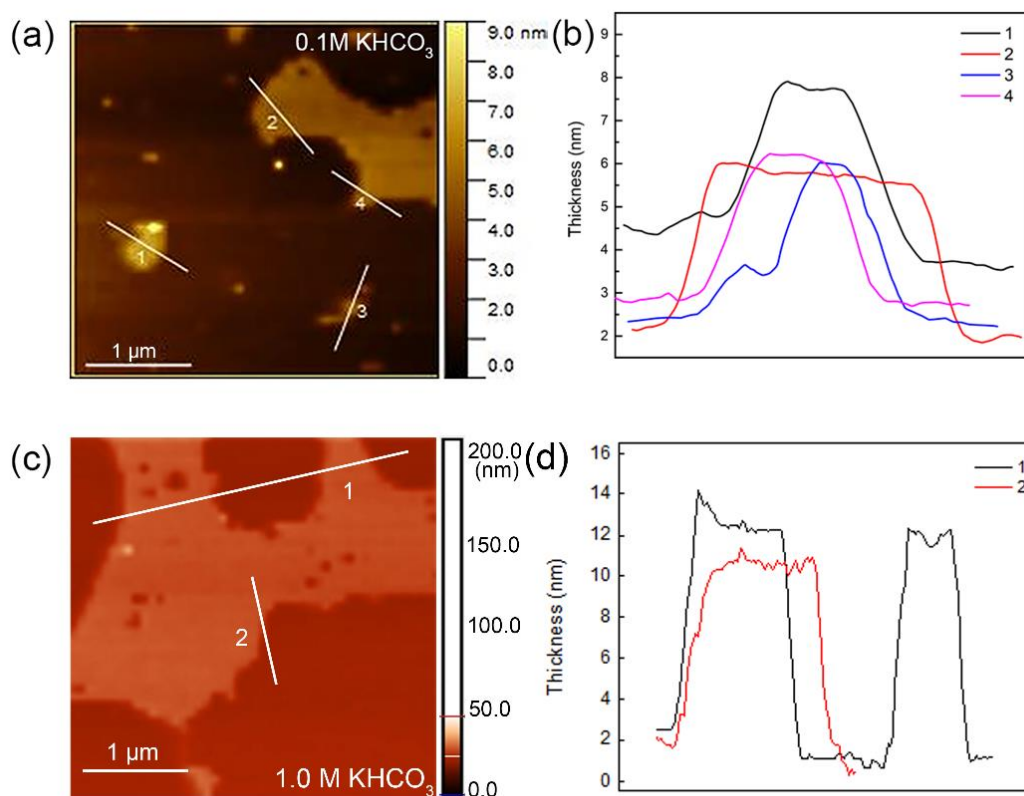
Figure S12. Typical AFM images of $Bi_2O_2CO_3$ NS after soaking Bi-MOF NR in a) 0.1 M $KHCO_3$ and c) 1.0 M $KHCO_3$. b) and d) are the height profiles corresponding to the marked lines in (a) and (c), respectively. The average thickness of the $Bi_2O_2CO_3$ NS is a) 3.8 nm and c) 11.5 nm, respectively, consistent with the measurement from lateral HAADF-STEM images (Figure S6b and S11c).
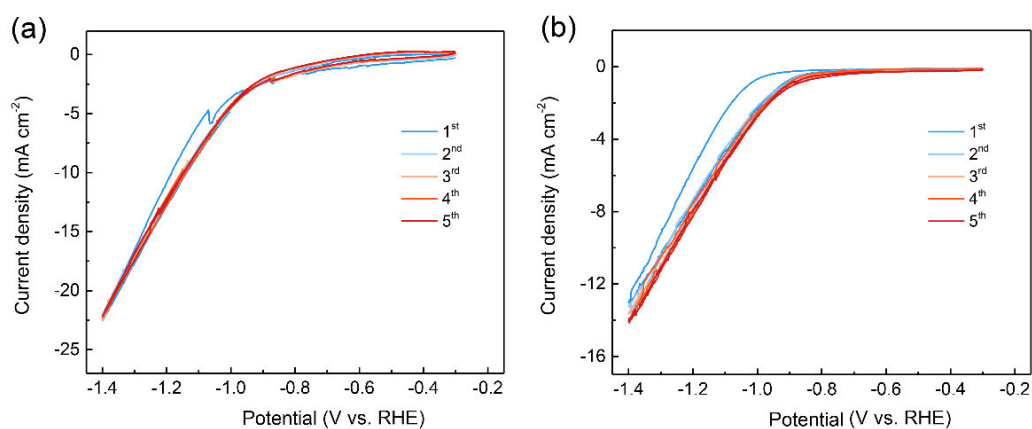
Figure S13. CV treatments used for the *in situ* electrochemical reduction of a) 3.8 nm $Bi_2O_2CO_3$ and b) 11.5 nm $Bi_2O_2CO_3$ NS to Bi NS under CO_2 atmosphere.
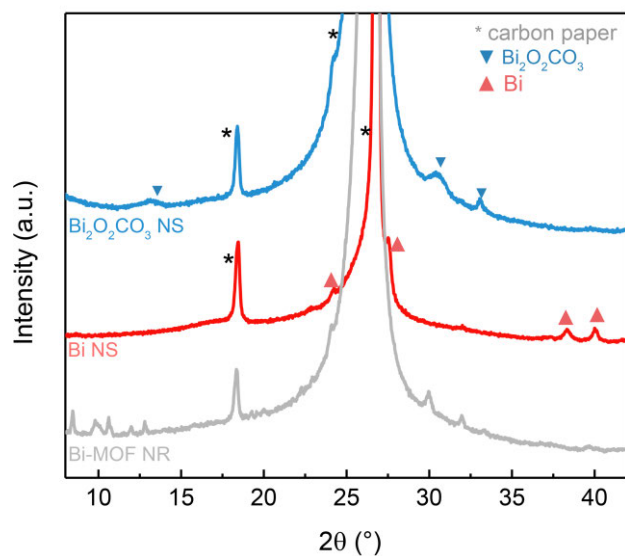
Figure S14. XRD patterns of Bi-MOF NR, and derived $Bi_2O_2CO_3$ NS and Bi NS.
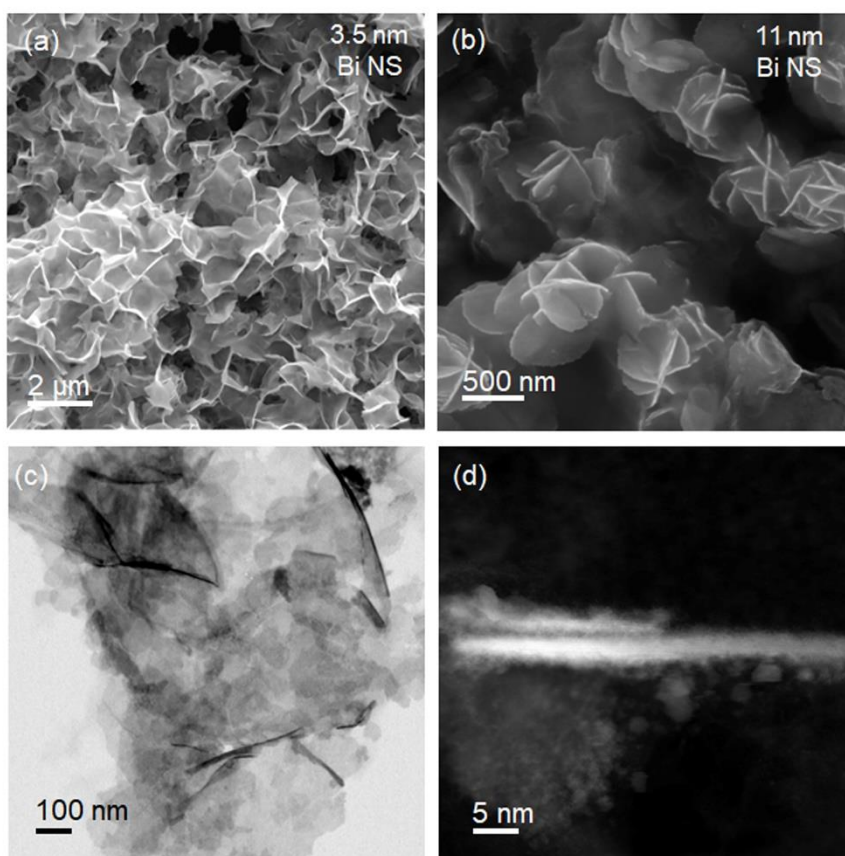
Figure S15. Morphological characterization of resultant Bi NS from *in situ* electroreduction of different $Bi_2O_2CO_3$ NS via CV technique in CO_2-staturated 0.1 M $KHCO_3$ solution. a, b) SEM images of Bi NS derived from 3.8 nm and 11.5 nm $Bi_2O_2CO_3$ NS, respectively. c, d) TEM images of Bi NS derived from 3.8 nm $Bi_2O_2CO_3$ NS.
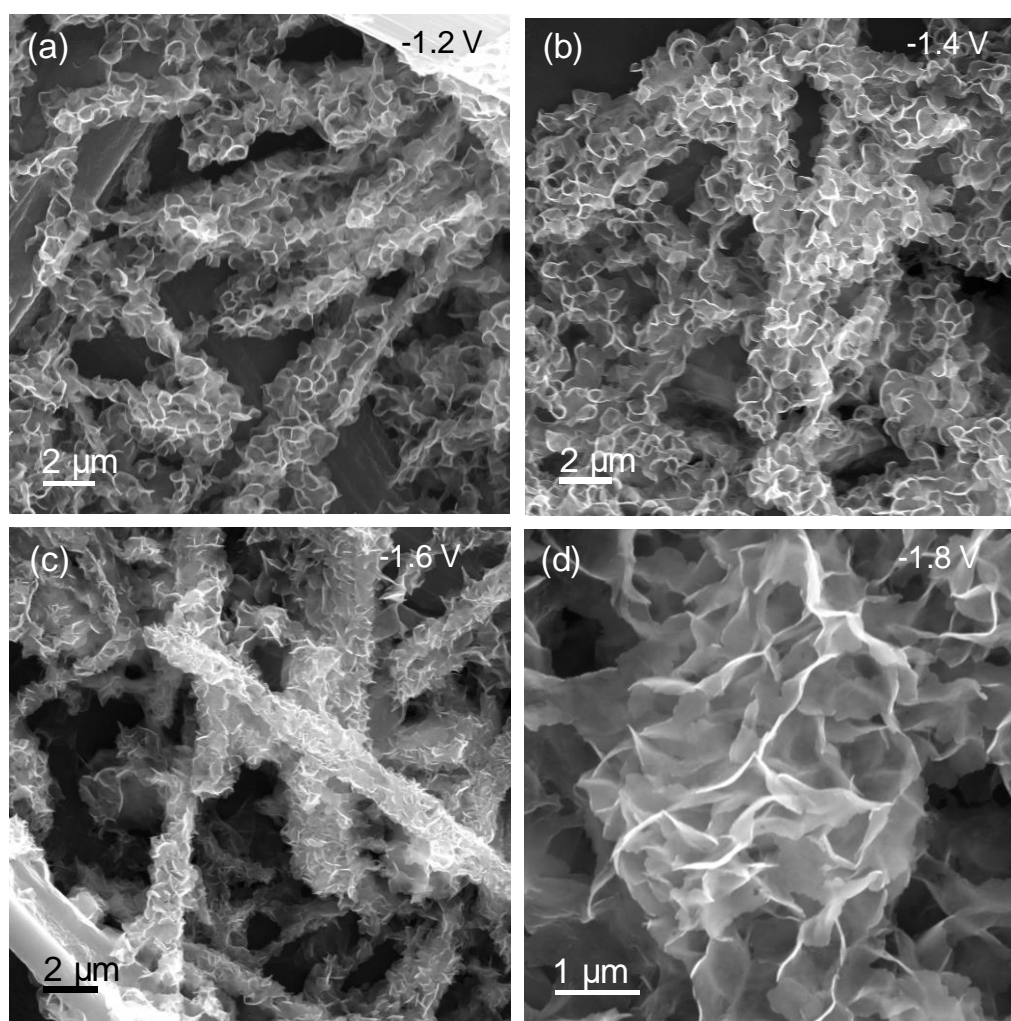
Figure S16. Morphological characterization of resultant Bi NS from *in situ* electroreduction of different $Bi_2O_2CO_3$ NS via amperometric i-t technique in CO_2-staturated 0.1 M $KHCO_3$ solution. Typical SEM images of Bi NS derived from 3.8 nm $Bi_2O_2CO_3$ NS under a) –1.2 V, b) –1.4 V, c) –1.6 V and d) –1.8 V (vs Ag/AgCl) for 30 min.
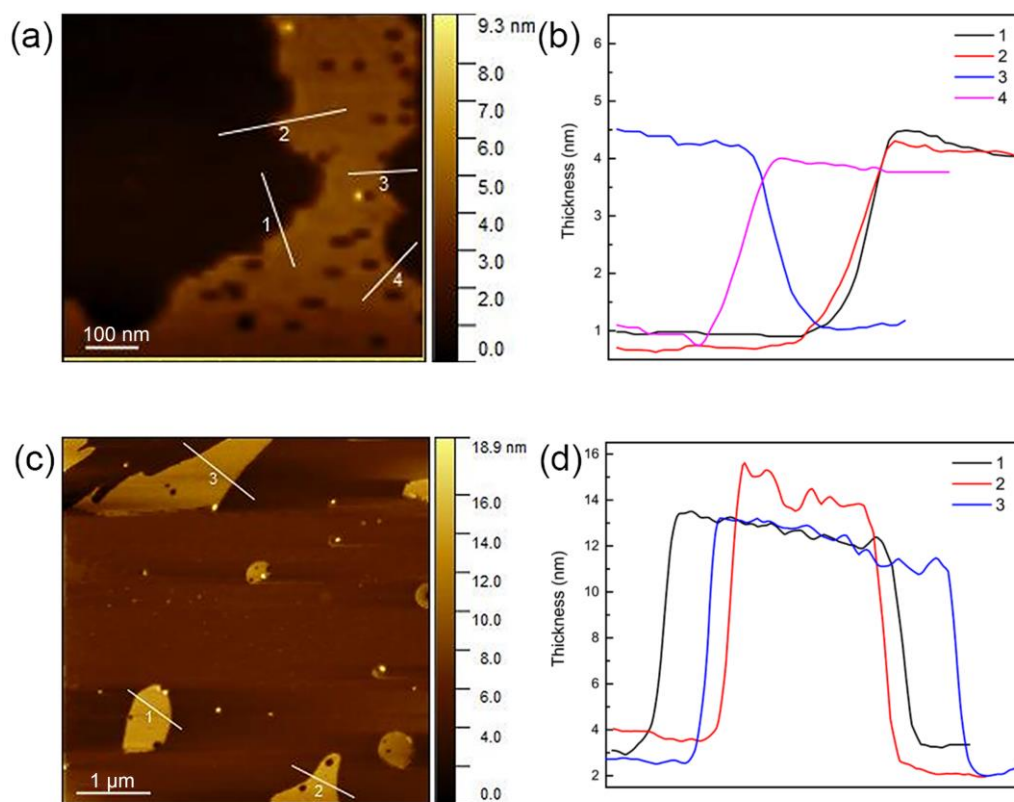
Figure S17. Typical AFM images of as-obtained Bi NS from *in situ* electroreduction of a) 3.8 nm and c) 11.5 nm $Bi_2O_2CO_3$ NS. b) and d) are the height profiles corresponding to the marked lines in (a) and (c), respectively. The average thickness of the Bi NS is a) 3.5 nm and c) 11 nm respectively.
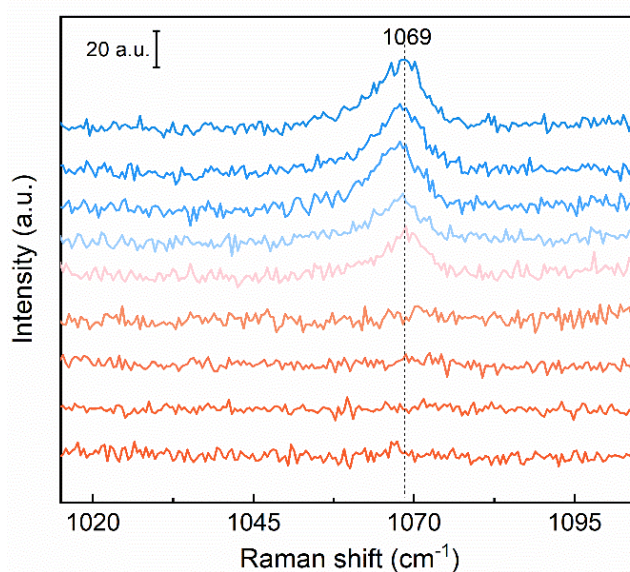
Figure S18. *In situ* Raman spectra to characterize the loss of the carbonate vibrational band during the electroreduction of $Bi_2O_2CO_3$ NS to Bi NS under CRR conditions.
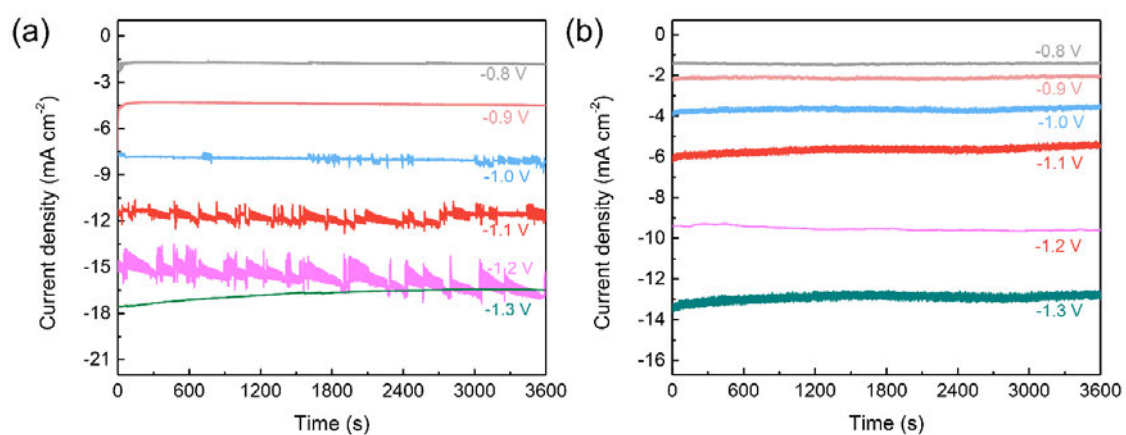
Figure S19. Chronoamperometry responses for a) 3.5 nm Bi NS and b) 11 nm Bi NS at different potentials in CO_2-saturated 0.1 M $KHCO_3$ (Potentials marked in the Figure are vs RHE).
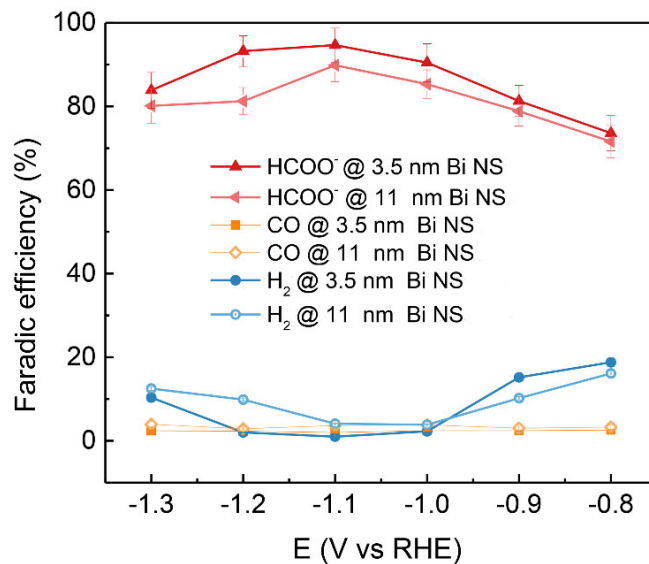
Figure S20. Potential-dependent Faradaic efficiencies toward $HCOO^-$, CO, and H_2 on 3.5 nm Bi NS (dark line) and 11 nm Bi NS (light line) in 0.1 M $KHCO_3$.
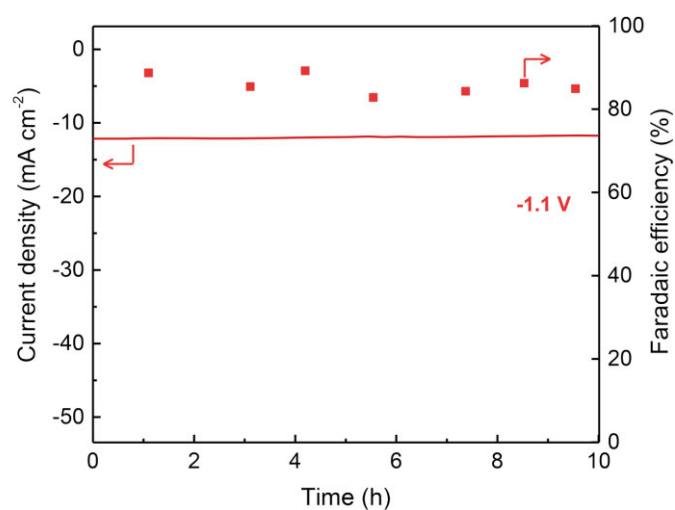
Figure S21. Chronoamperometry response of stored 3.5 nm Bi NS at −1.1 V vs RHE in CO_2-saturated 0.1 M $KHCO_3$. The working electrode was stored in N_2-saturated water for one week since initial testing.
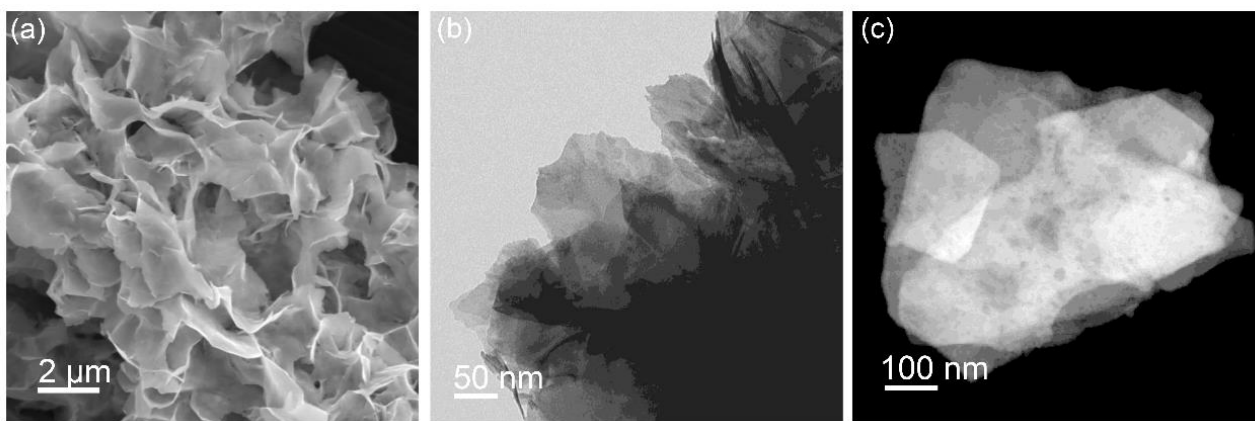
Figure S22. Typical a) SEM image, b) TEM image, and c) HADDF-STEM image of 3.5 nm Bi NS after long-term testing.
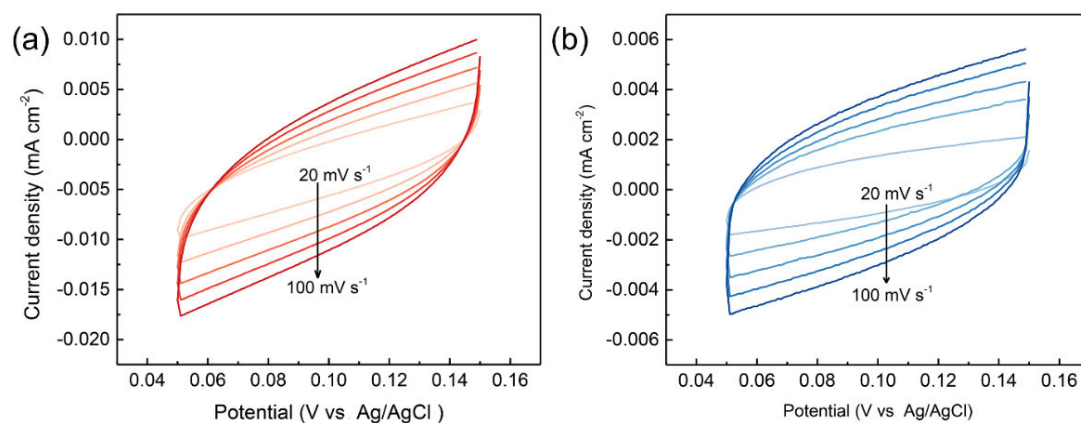
Figure S23. ECSA measurements. Cyclic voltammograms of a) 3.5 nm Bi NS and b) 11 nm Bi NS at various scan rates (20 to 100 mV s^{-1}) in the region of 0.05 to 0.15 V vs Ag/AgCl.
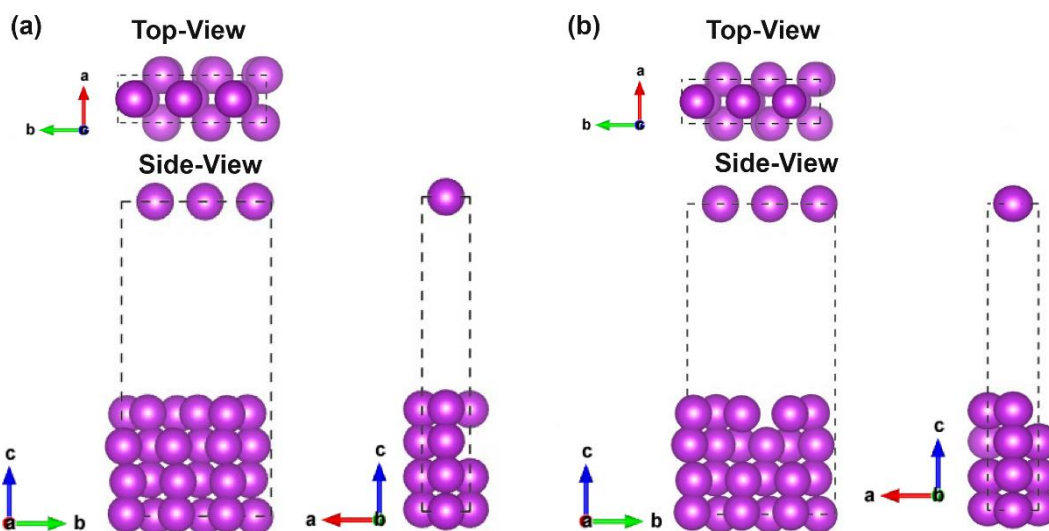
Figure S24. Optimized configurations of a) the pristine Bi model and b) the defective Bi model. Models are presented from both top and side directions. Purple spheres represent Bi atoms.
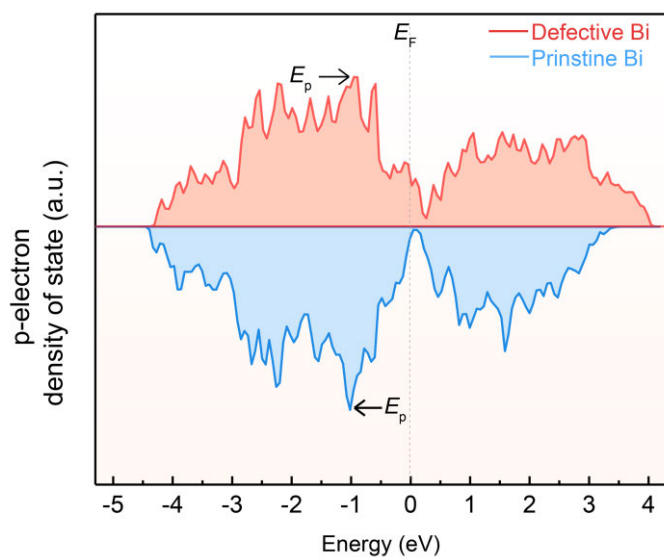
Figure S25. p-Electron DOS of pristine Bi and defective Bi models. The dashed line indicates the Fermi level (E_F), and the arrow labels indicate the p-DOS descriptor (the highest peak near the Fermi level).[4b]
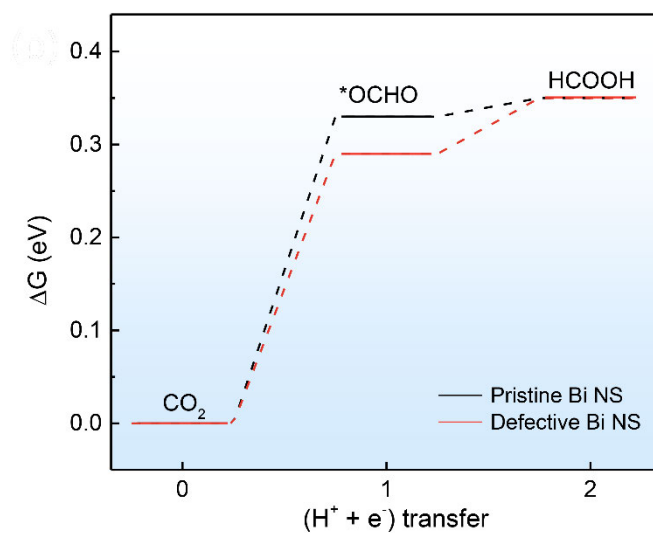
Figure S26. Free energy diagrams of CO_2 reduction pathways to HCOOH on the pristine Bi model (black line) and the defective Bi model (red line). (U = 0 vs RHE, pH corrected at 6.8)
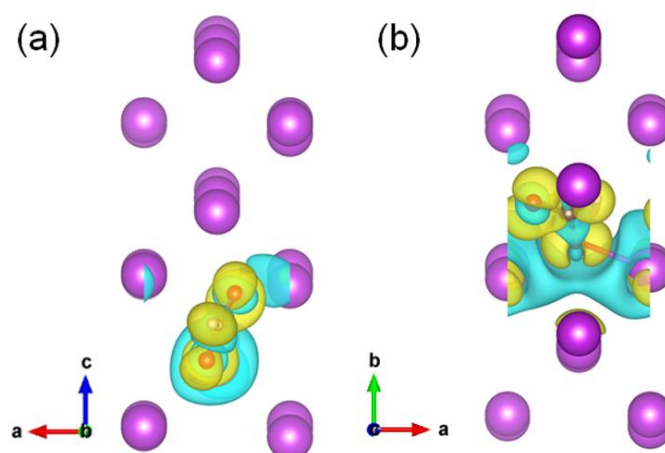
Figure S27. Electron charge difference for *OCHO adsorption on a) the pristine Bi model and b) the defective Bi model. Cyan regions show electron depletion, and yellow regions show electron accumulation. The isosurface value is 0.003 e$^-$ Å^{-3}. White, brown, red and purple spheres represent H, C, O and Bi atoms, respectively.
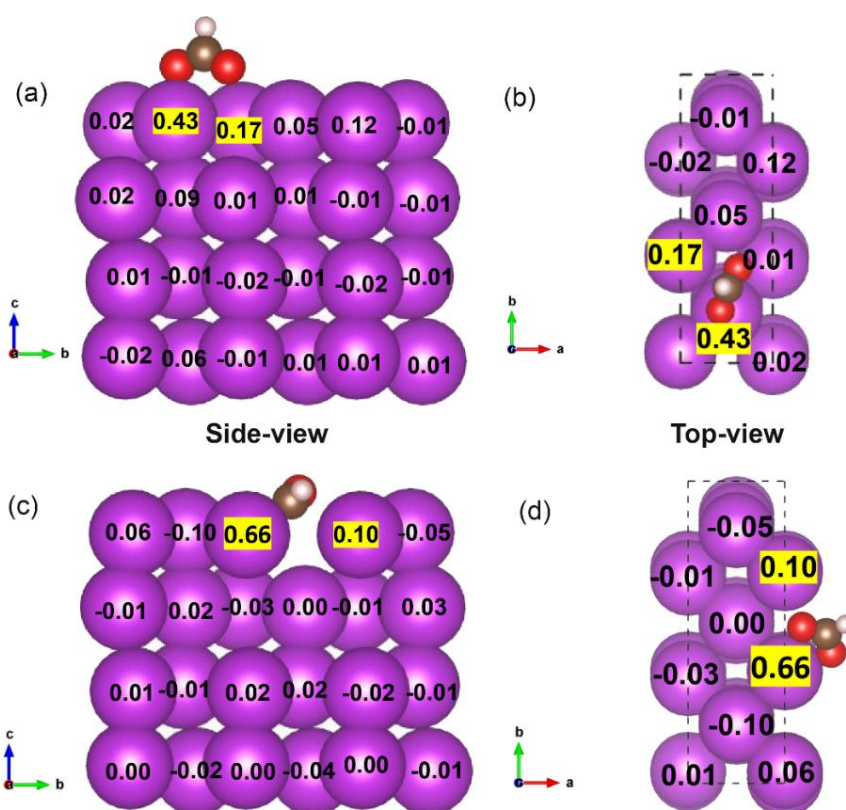

Figure S28. Bader charge analysis of a, b) the pristine Bi model and c, d) the defective Bi model with *OCHO intermediate adsorbed. Models are presented from both top and side directions. Positive values represent a positive charge on the atom. White, brown, red and purple spheres represent H, C, O and Bi atoms, respectively.
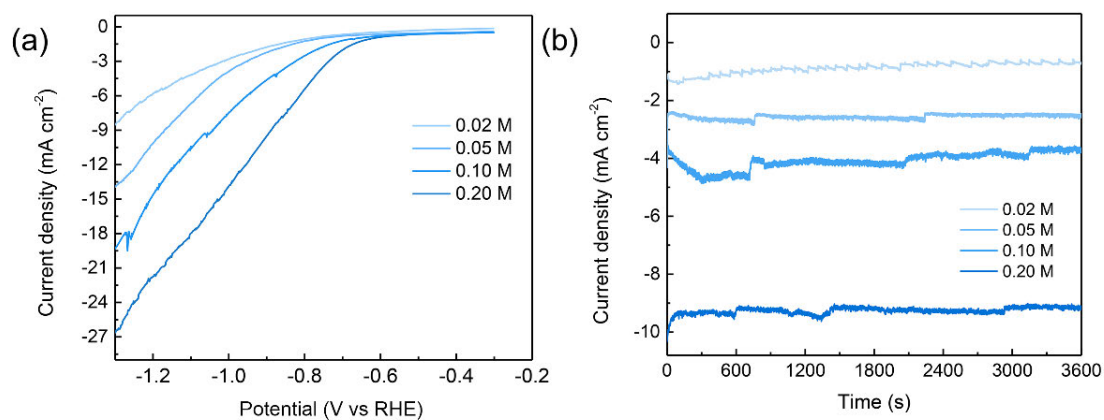
Figure S29. a) Linear sweep voltammetry responses of 3.5 nm Bi NS in CO_2-saturated $KHCO_3$ solution with different concentrations (0.02 to 0.20 mol L^{-1}). b) Chronoamperometry responses of 3.5 nm Bi NS at –0.9 V vs RHE in CO_2-saturated $KHCO_3$ aqueous solution with different concentrations.
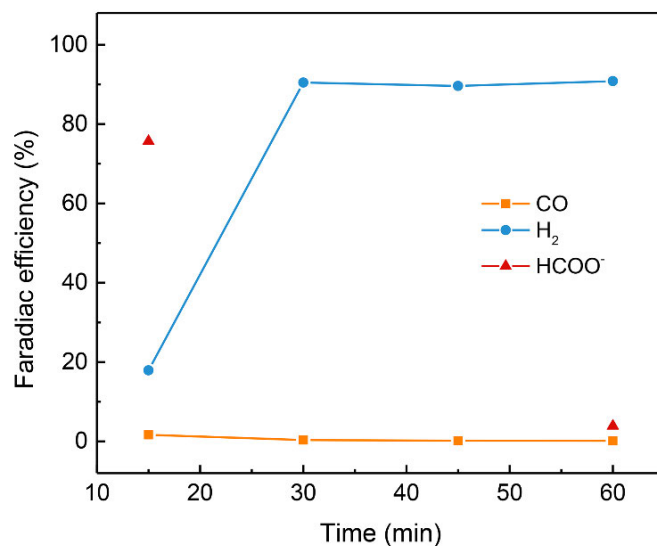

Figure S30. Faradiac efficiency of CO, H_2, and $HCOO^-$ for 1-h electrolysis in the N_2-saturated 0.1 M $KHCO_3$ on the 3.5 nm Bi NS. During initial 15 min, some formate was produced; however, no more formate was detected after 1-h electrolysis.

Supplementary Tables

Table S1. Assignment of selected vibrations in the FT-IR spectra.[12]

Wavelength number (cm⁻¹)	Assignment		Origin
2936	v(C–H)	stretching vibration o C–H in Aldehydes	Formate
1716	v_{as}(COO)	asymmetric stretching vibration of the carboxylate groups	H_3BTC
1650	v_{as}(C–O)	asymmetric stretching vibration of C–O	Bi-MOF
1609	v_s(C–C)	symmetric stretching vibration of C–C	H_3BTC
1524	v_{as}(C–O)	asymmetric stretching vibrations of C–O	Bi-MOF
1477	$í_3$(CO_3^{2-})	anti-symmetric vibration stretching of CO_3^{2-}	$Bi_2O_2CO_3$
1450	v_s(COO)	symmetric stretching vibration of the carboxylate groups	H_3BTC
1431	v_s(C–O)	symmetric stretching vibration of C–O	Bi-MOF
1385	$í_3$(CO_3^{2-})	anti-symmetric vibration stretching of CO_3^{2-}	$Bi_2O_2CO_3$
1355	v_s(C–O)	symmetric stretching vibration of C–O	Bi-MOF
1053	$í_1$(CO_3^{2-})	symmetric stretching vibration of CO_3^{2-}	$Bi_2O_2CO_3$
845	$í_2$(CO_3^{2-})	out-of-plane bending of CO_3^{2-}	$Bi_2O_2CO_3$
738	γ(aryl–H)	out-of-plane bending of aryl–H	H_3BTC
690	$í_4$(CO_3^{2-})	in-plane deformation of CO_3^{2-}	$Bi_2O_2CO_3$

Table S2. Assignment of selected vibrations in the Raman spectra.[12b, 12d, 13]

Raman shift (cm^{-1})		Assignment	Origin
1069	v(C–O)$_{CO_3^{2-}}$	symmetric stretching vibration of C–O (carbonate)	$Bi_2O_2CO_3$
1002	v(C=C)$_{Ar}$	out-of-plane bending of the ring double bond and a carboxylic group	Bi-MOF
820	δ(C–H)$_{Ar}$	C–H out-of-plane deformation band	Bi-MOF
162	--	external vibration mode of Bi=O	$Bi_2O_2CO_3$
150	--	external vibration mode of Bi=O	Bi-MOF
97	A_{1g}	lattice vibration mode of Bi–Bi	Bi
85	--	vibration mode of Bi=O	Bi-MOF
77	--	external vibration mode of Bi=O	$Bi_2O_2CO_3$
71	E_g	lattice vibration mode of Bi–Bi	Bi

Table S3. Summary and comparison of CRR performance on Bi-based electrocatalysts.

Catalyst	Electrolyte	Potential	FE$_{formate}$	Potential ranges (mV) for FE$_{formate}$ > 80%	Ref
3.5 nm Bi NSs	0.1 M KHCO$_3$	−1.1 V vs RHE	92%	~450	This work
11 nm Bi NSs	0.1 M KHCO$_3$	−1.1 V vs RHE	87%	400	This work
nano-Bi/Cu	0.1 M KHCO$_3$	−1.5 V vs Ag/AgCl	91%	300	[14]
elongated Bismuth oxides	0.5 M KHCO$_3$	−0.9 V vs RHE	91%	300	[15]
HSA-Bi	0.5 M KHCO$_3$	−1.5 V vs SCE	92%	300	[16]
Bi$_2$O$_2$CO$_3$ reduced Bi NS	0.1 M KHCO$_3$	−1.2 V vs Ag/AgCl	83%	100	[17]
Oxide-derived Bi	0.5 M KHCO$_3$	−0.82 V vs RHE	82%	100	[18]
Bi nanodendrite	0.5 M NaHCO$_3$	−1.8 V vs SCE	96%	200	[19]
nano-Bi	0.5 M KHCO$_3$	−1.6 V vs SCE	98%	200	[20]
exfoliated Bi nanosheets	0.1 M KHCO$_3$	-1.1 V vs RHE	86%	100	[21]
Bi dendrite	0.5 M KHCO$_3$	−0.74 V vs RHE	89%	200	[22]
Bi nanoflakes	0.1 M KHCO$_3$	−0.8 V vs RHE	90%	100	[23]
Bi$_{45}$/GDE	0.5 M KHCO$_3$	−1.45 V vs SCE	90%	300	[24]
Bi nanostructure	0.5 M KHCO$_3$	−0.9 V vs RHE	92%	400	[25]
MOF-derived Bi$_2$O$_2$CO$_3$	0.5 M KHCO$_3$	−0.67 V vs RHE	96%	300	[26]
MOF-derived Bi NPs	0.5 M KHCO$_3$	−0.97 V vs RHE	95%	400	[27]
MOL-derived Bi NSs	0.5 M KHCO$_3$	−0.9 V vs RHE	~100%	500	[9b]

Catalyst	Electrolyte	Potential	$FE_{formate}$	Potential ranges (mV) for $FE_{formate} > 80\%$	Ref
3.5 nm Bi NSs	0.1 M $KHCO_3$	−1.1 V vs RHE	92%	~450	This work
11 nm Bi NSs	0.1 M $KHCO_3$	−1.1 V vs RHE	87%	400	This work
Bi_2S_3-derived defect-rich Bi	0.5 M $NaHCO_3$	−0.75 V vs RHE	84%	100	[28]
AgBi-500	0.1 M $KHCO_3$	−0.7 V vs RHE	94%	500	[29]
Bismuthene	0.5 M $KHCO_3$	−0.58 V vs RHE	98%	300	[1]
topotactic transformed Bi NS	0.5 M $NaHCO_3$	−1.7 V vs SCE	~100%	400	[9a]
Curved Bi nanotubes	0.5 M $KHCO_3$	−1.0 V vs RHE	92%	600	[30]
Bi@C	0.5 M $KHCO_3$	−0.9 V vs RHE	92 %	400	[31]
Cu foam@BiNW	0.5 M $NaHCO_3$	−0.69 V vs RHE	95%	600	[32]
Bi_2O_3 -NGQD	0.5 M $KHCO_3$	−0.9 V vs RHE	100%	600	[33]
Bi_2O_3 NS@MCCM	0.1 M $KHCO_3$	−1.256 V vs RHE	93%	600	[34]
2D Mesoporous Bi NS	0.5 M $NaHCO_3$	−0.9 V vs RHE	~99%	500	[35]
POD-Bi	0.5 M $KHCO_3$	−1.16 V vs RHE	95%	500	[36]

Table S4. Computed gas phase properties and thermodynamic energy correction for *OCHO.

	E_{DFT} (eV)	ZPE (eV)	$T*S$ (eV)
H_2	−22.96	0.27	−0.40
CO_2	−6.68	0.31	−0.66
H_2O (g)	−14.22	0.57	−0.54
HCOOH	−29.88	0.77	−0.17
*OCHO	—	0.62	−0.19

Supporting References

[1] F. Yang, A. O. Elnabawy, R. Schimmenti, P. Song, J. Wang, Z. Peng, S. Yao, R. Deng, S. Song, Y. Lin, M. Mavrikakis, W. Xu, *Nat. Commun.* **2020**, *11*, 1088.

[2] a) A. Vasileff, C. Xu, L. Ge, Y. Zheng, S. Z. Qiao. *Chem. Commun.* **2018**, *54*, 13965-13958; b) J. Qiao, Y. Liu, F. Hong, J. Zhang, *Chem. Soc. Rev.* **2014**, *43*, 631-675.

[3] G. Kresse, J. Furthmüller, *Phys. Rev. B* **1996**, *54*, 11169-11186.

[4] S. Grimme, *J. Comput. Chem.* **2006**, *27*, 1787-1799.

[5] a) X. Zhi, Y. Jiao, Y. Zheng, S. Z. Qiao, *Small* **2019**, *15*, 1804224; b) Y. Jiao, Y. Zheng, K. Davey, S. Z. Qiao, *Nat. Energy* **2016**, *1*, 16130.

[6] J. K. Nørskov, F. Studt, F. Abild-Pedersen, T. Bligaard, *Fundamental concepts in heterogeneous catalysis*, John Wiley & Sons, **2014**.

[7] a) A. A. Peterson, F. Abild-Pedersen, F. Studt, J. Rossmeisl, J. K. Nørskov, *Energy Environ. Sci.* **2010**, *3*, 1311-1315; b) Y. Jiao, Y. Zheng, P. Chen, M. Jaroniec, S. Z. Qiao, *J. Am. Chem. Soc.* **2017**, *139*, 18093-1810.

[8] a) W. J. Durand, A. A. Peterson, F. Studt, F. Abild-Pedersen, J. K. Nørskov, *Surf. Sci.* **2011**, *605*, 1354-1359; b) L. R. L. Ting, B. S. Yeo, *Curr. Opin. Electrochem.* **2018**, *8*, 126-134.

[9] a) N. Han, Y. Wang, H. Yang, J. Deng, J. Wu, Y. Li, Y. Li, *Nat. Commun.* **2018**, *9*, 1320; b) C. S. Cao, D. D. Ma, J. F. Gu, X. Y. Xie, G. Zeng, X. F. Li, S. G. Han, Q. L. Zhu, X. T. Wu, Q. Xu, *Angew. Chem. Int. Ed.* **2020**, *59*, 15014-15020; *Angew. Chem.* **2020**, *132*, 15124-15130.

[10] J. K. Nørskov, J. Rossmeisl, A. Logadottir, L. Lindqvist, J. R. Kitchin, T. Bligaard, H. Jónsson, *J. Phys. Chem. B* **2004**, *108*, 17886-17892.

[11] a) Y. Wang, X. Zhu, Y. Li, *J. Phys. Chem. Lett.* **2019**, *10*, 4663-4667; b) W. Oh, C. K. Rhee, J. W. Han, B. Shong, *J. Phys. Chem. C* **2018**, *122*, 23084-23090.

[12] a) G. Socrates, *Infrared and Raman characteristic group frequencies: tables and charts*, John Wiley & Sons, **2004**; b) G. Wang, Y. Liu, B. Huang, X. Qin, X. Zhang, Y. Dai, *Dalton Trans.* **2015**, *44*, 16238-16241; c) M. Koppen, A. Dhakshinamoorthy, A. K. Inge, O. Cheung, J. Angstrom, P. Mayer, N. Stock, *Eur. J. Inorg. Chem.* **2018**, 3496-3503; d) K. Ito, H. J. Bernstein, *Can. J. Chem.* **1956**, *34*, 170-178.

[13] a) W. W. Rudolph, G. Irmer, E. Königsberger, *Dalton Trans.* **2008**, 900-908; b) V. H. Nguyen, T. D. Nguyen, T. Van Nguyen, *Top. Catal.* **2020**, *63*, 1109-1120; c) Y. Wang; W. Cao, L. Wang, Q. Zhuang, Y. Ni, *Microchim. Acta* **2018**, *185*, 315; d) J. D. Frantz, Chem. Geo. **1998**, *152*, 211-225.

[14] W. Lv, J. Zhou, J. Bei, R. Zhang, L. Wang, Q. Xu, W. Wang, *Appl. Surf. Sci.* **2017**, *393*, 191-196.

[15] P. Deng, H. Wang, R. Qi, J. Zhu, S. Chen, F. Yang, L. Zhou, K. Qi, H. Liu, B. Y. Xia, *ACS Catal.* **2020**, *10*, 743-750.

[16] H. Zhang, Y. Ma, F. Quan, J. Huang, F. Jia, L. Zhang, *Electrochem. Commun.* **2014**, *46*, 63-66.

[17] W. Lv, J. Bei, R. Zhang, W. Wang, F. Kong, L. Wang, W. Wang, *ACS Omega* **2017**, *2*, 2561-2567.

[18] E. Bertin, S. Garbarino, C. Roy, S. Kazemi, D. Guay, *J. CO$_2$ Util.* **2017**, *19*, 276-283.

[19] H. Zhong, Y. Qiu, T. Zhang, X. Li, H. Zhang, X. Chen, *J. Mater. Chem. A* **2016**, *4*, 13746-13753.

[20] Y. Qiu, J. Du, W. Dong, C. Dai, C. Tao, *J. CO$_2$ Util.* **2017**, *20*, 328-335.

[21] W. Zhang, Y. Hu, L. Ma, G. Zhu, P. Zhao, X. Xue, R. Chen, S. Yang, J. Ma, J. Liu, Z. Jin, *Nano Energy* **2018**, *53*, 808-816.

[22] J. H. Koh, D. H. Won, T. Eom, N.K. Kim, K. D. Jung, H. Kim, Y. J. Hwang, B. K. Min, *ACS Catal.* **2017**, *7*, 5071-5077.

[23] S. Kim, W. J. Dong, S. Gim, W. Sohn, J. Y. Park, C. J. Yoo, H. W. Jang, J.L. Lee, *Nano Energy* **2017**, *39*, 44-52.

[24] X. Zhang, T. Lei, Y. Liu, J. Qiao, *Appl. Catal. B-Environ.* **2017**, *218*, 46-50.

[25] P. Lu, D. Gao, H. He, Q. Wang, Z. Liu, S. Dipazir, M. Yuan, W. Zu, G. Zhang, *Nanoscale* **2019**, *11*, 7805-7812.

[26] W.W. Yuan, J.X. Wu, X.D. Zhang, S.Z. Hou, M. Xu, Z.Y. Gu, *J. Mater. Chem. A* **2020**, *8*, 24486-24492.

[27] P. Lamagni, M. Miola, J. Catalano, M. S. Hvid, M. A. H. Mamakhel, M. Christensen, M. R. Madsen, H. S. Jeppesen, X.-M. Hu, K. Daasbjerg, T. Skrydstrup, N. Lock, *Adv. Funct. Mater.* **2020**, *30*, 1910408.

[28] Y. Zhang, F. Li, X. Zhang, T. Williams, C. D. Easton, A. M. Bond, J. Zhang, *J. Mater. Chem. A* **2018**, *6*, 4714-4720.

[29] J.H. Zhou, K. Yuan, L. Zhou, Y. Guo, M.Y. Luo, X.Y. Guo, Q.Y. Meng, Y.W. Zhang, *Angew. Chem. Int. Ed.* **2019**, *58*, 14197-14201; *Angew. Chem.* **2019,** *131*, 14335-14339.

[30] K. Fan, Y. Jia, Y. Ji, P. Kuang, B. Zhu, X. Liu, J. Yu, *ACS Catal.* **2020**, *10*, 358-364.

[31] P. Deng, F. Yang, Z. Wang, S. Chen, Y. Zhou, S. Zaman, B. Y. Xia, *Angew. Chem. Int. Ed.* **2020**, *59*, 10807-10813; *Angew. Chem.* **2020**, *132*, 10899-10905.

[32] X. Zhang, X. Sun, S.X. Guo, A. M. Bond, J. Zhang, *Energy Environ. Sci.* **2019**, *12*, 1334-1340.

[33] Z. Chen, K. Mou, X. Wang, L. Liu, *Angew. Chem. Int. Ed.* **2018**, *57*, 12790-12794; *Angew. Chem.* **2018**, *130*, 12972-12976.

[34] S. Liu, X. F. Lu, J. Xiao, X. Wang, X. W. Lou, *Angew. Chem. Int. Ed.* **2019**, *58*, 13828-13833; A*ngew. Chem.* **2019**, *131*, 13966-13971.

[35] H. Yang, N. Han, J. Deng, J. Wu, Y. Wang, Y. Hu, P. Ding, Y. Li, Y. Li, J. Lu, *Adv. Energy Mater.* **2018**, *8*, 1801536.

[36] S. He, F. Ni, Y. Ji, L. Wang, Y. Wen, H. Bai, G. Liu, Y. Zhang, Y. Li, B. Zhang, H. Peng, *Angew. Chem. Int. Ed.* **2018**, *57*, 16114-16119; *Angew. Chem.* **2018**, *130*, 16346-16351.

Chapter 5

Inter-metal Interaction with a Threshold Effect in NiCu Dual-atom Catalysts for CO_2 Electroreduction

5.1 Introduction and Significance

Dual-atom catalysts (DACs) have become an emerging platform to provide more reactivity and active sites for the multi-electron/proton concerning electrocatalytic reaction, such as CO_2 reduction (CRR). However, the introduction of the asymmetric dual-atom site causes complexity in its structure, leaving incomprehensive understanding of the catalytic mechanism. Particularly, the role and mechanism of inter-metal interaction has yet to be understood. Therefore, it is urgent and crucial to investigate the inter-metal site distance effect of DACs, which can not only promote the full potential of DACs, but also guide the design of advanced atomically-dispersed single-atom catalysts. To address this issue, we employed a peripherally distributed NiCu dual-atom catalyst supported on the nitrogen-doped carbon (NiCu-NC) as a case study. The distance (d)-dependent inter-metal interaction was investigated, and thus a newly-proposed macro-descriptor as the guidance for future design of DACs was also provided. The highlights of this work include:

(1) First report of d-dependent inter-metal interaction features in DACs. We propose a rational and universal model ("M_1, M_2") to study the "structure-to-property" of DACs and theoretically reveal that the electronic structures, CRR activity and selectivity can be effectively altered by the inter-metal interaction, which is determined by the inter-metal distance.

(2) Mutually confirmed threshold effect for inter-metal interaction in DACs. We experimentally confirm a distance threshold around 5.3 Å between adjacent Ni and Cu moieties to trigger effective electronic regulation. On this threshold distance distribution, both selectivity and activity of the CRR are boosted, evidenced by high-angle annular dark-field scanning transmission electron microscopy (HAADF-STEM), X-ray synchrotron-based measurements, and electrochemical measurements.

(3) Universal macro-descriptor to guide DACs design. We rigorously establish an effective and universal macro-descriptor to correlate the inter-metal distance and intrinsic material features, i.e. $d \propto (thickness \times metal\ loading)^{-0.5}$, by Monte Carlo experiments using both algorithm modelling simulation and mathematical derivation. It closely aligns with experiments and previous reports, and will serve as a practical guide for designing atomically-dispersed catalysts.

In short, this work offers new insights into the understanding and design of atomically-dispersed catalysts in the future. The optimized synergistic effect and reactivity can be readily achieved by just reaching their diatomic threshold distance, which can be realistically obtained by controlling the amount of the added metal precursors.

5.2 Inter-metal Interaction with a Threshold Effect in NiCu Dual-atom Catalysts for CO_2 Electroreduction

This chapter is presented as a submitted research paper by Dazhi Yao, Cheng Tang, Xing Zhi, Bernt Johannessen, Ashley Slattery, Shane Chern and Shi-Zhang Qiao. Inter-metal interaction with a threshold effect in NiCu dual-atom catalysts for CO_2 electroreduction, Adv. Mater., 2022, 2209386. https://doi.org/adma.202209386.

Statement of Authorship

Title of Paper	Inter-metal interaction with a threshold effect in NiCu dual-atom catalysts for CO_2 electroreduction
Publication Status	☐ Published ☑ Accepted for Publication ☐ Submitted for Publication ☐ Unpublished and Unsubmitted work written in manuscript style
Publication Details	D. Yao, C. Tang, X. Zhi, B Johannessen, A. Slattery, S. Chern, S. Z. Qiao, Advanced Materials, 2022, DOI: 10.1002/adma.202209386

Principal Author

Name of Principal Author (Candidate)	Dazhi Yao	
Contribution to the Paper	Design and conducted the experiments, analysed the data, wrote the manuscript.	
Overall percentage (%)	70%	
Certification:	This paper reports on original research I conducted during the period of my Higher Degree by Research candidature and is not subject to any obligations or contractual agreements with a third party that would constrain its inclusion in this thesis. I am the primary author of this paper.	
Signature		Date 28/09/2022

Co-Author Contributions

By signing the Statement of Authorship, each author certifies that:

     i.   the candidate's stated contribution to the publication is accurate (as detailed above);

     ii.   permission is granted for the candidate in include the publication in the thesis; and

     iii.   the sum of all co-author contributions is equal to 100% less the candidate's stated contribution.

Name of Co-Author	Cheng Tang	
Contribution to the Paper	Guided to design the whole experiment, helped data analysis, and revised the manuscript	
Signature		Date 28/09/2022

Name of Co-Author	Xing Zhi	
Contribution to the Paper	Conducted DFT calculations and analysed the data. Wrote the manuscript	
Signature		Date 28/Sep/2022

Name of Co-Author	Bernt Johannessen
Contribution to the Paper	Collected XAS data and assisted in the analysis thereof. Revised the manuscript.
Signature	Date	28/Sep/2022

Name of Co-Author	Ashley Slattery
Contribution to the Paper	Conducted STEM imaging and assisted in the analysis. Revised the manuscript.
Signature	Date	28-09-2022

Name of Co-Author	Shane Chern
Contribution to the Paper	Conducted mathematic modelling and equation derivation. Assisted in the analysis. Revised the manuscript.
Signature	Date	09/28/2022

Name of Co-Author	Shi-Zhang Qiao
Contribution to the Paper	Supervision of the work, discussion and conceptualization of this manuscript and manuscript evaluation and revision.
Signature	Date	28/09/2022

Inter-Metal Interaction with a Threshold Effect in NiCu Dual-Atom Catalysts for CO$_2$ Electroreduction

Dazhi Yao, Cheng Tang, Xing Zhi, Bernt Johannessen, Ashley Slattery, Shane Chern, and Shi-Zhang Qiao*

D. Yao. C. Tang, X. Zhi, S.-Z. Qiao

Centre for Materials in Energy and Catalysis, School of Chemical Engineering and Advanced Materials, The University of Adelaide, Adelaide, SA 5005, Australia

E-mail: s.qiao@adelaide.edu.au (S.-Z. Q.)

B. Johannessen

Australian Synchrotron, 800 Blackburn Rd, Clayton, VIC 3168, Australia

A. Slattery

Adelaide Microscopy, The University of Adelaide, Adelaide, SA 5005, Australia

S. Chern

Department of Mathematics and Statistics, Dalhousie University, Halifax, Nova Scotia, B3H 4R2, Canada

Abstract: Dual-atom catalysts (DACs) have become an emerging platform to provide more flexible active sites for electrocatalytic reactions with multi-electron/proton transfer, such as CO$_2$ reduction reaction (CRR). However, the introduction of asymmetric dual-atom sites causes complexity in structure, leaving an incomprehensive understanding of inter-metal interaction and catalytic mechanism. Taking NiCu DACs as an example, herein, we propose a more rational structural model, and investigate the distance-dependent inter-metal interaction by combining theoretical simulations and experiments, including density functional theory computation, aberration-corrected transmission electron microscopy, synchrotron-based X-ray absorption fine structure, and Monte Carlo experiments. A distance threshold around 5.3 Å between adjacent Ni–N$_4$ and Cu–N$_4$ moieties is revealed to trigger effective electronic regulation and boost CRR performance on both selectivity and activity. A universal macro-descriptor rigorously correlating the inter-metal distance and intrinsic material features (e.g., metal loading, thickness) is established to guide the rational design and synthesis of advanced

DACs. This study highlights the significance of identifying the inter-metal interaction in DACs, and helps bridge the gap between theoretical study and experimental synthesis of atomically dispersed catalysts with highly correlated active sites.

Keywords: dual-atom catalysts, inter-metal interaction, atomic distance, threshold effect, electrocatalysis, CO_2 reduction

1. Introduction

Single-atom catalysts (SACs), i.e., isolated metal atoms coordinated by neighbouring sites on the host support, have attracted significant attention in heterogeneous catalysis owing to unique structure and maximized atomic utilization of them [1]. Generally, SACs feature homonuclear metal sites and manifest enhanced electrocatalytic activity for various reactions, especially oxygen reduction reaction (ORR) [2]. However, such site homogeneity with a single kind of active centre significantly hinders their performance in complex reactions where the adsorption of multiple intermediates demands independent regulation [3]. Taking CO_2 reduction reaction (CRR) as an example, the adsorption energy scaling relationship between *CO and other carbon-bound species reveals that the key reduction intermediates, *COOH and *CHO, cannot be stabilized independently of *CO [3a, 4]. Such scaling relations generally result in high overpotential and low catalytic efficiency, thus leaving unsatisfactory CRR reactivity and selectivity in practice [3c, 4b, 5]. Aiming at higher flexibility in optimizing active centres and intermediate adsorption, dual-atom catalysts (DACs) have been proposed to construct asymmetric bimetallic sites [6]. The incorporation of second heteronuclear metal sites induces more top/bridge sites, diverse absorption strength and modes, and synergistic effects via inter-metal interaction, enabling a new degree of freedom to break the linear scaling relations of different intermediates and thus improve the reaction activity and selectivity [6c, 7]. Recent reports including NiFe [8], ZnLn [9], IrNi [10], and IrFe [11] moieties highlight the unique advantages and effective applications of DACs in lowering the reaction barrier (overpotential)

and accelerating the reaction kinetics for multi-step electrocatalytic reactions including ORR and CRR [7a, 12].

With the promising development of SACs from monometallic to multi-metallic systems, the chemical interaction between individual atoms has been revealed as a crucial factor to alter electronic structures and catalytic reactivity [13]. However, the role and mechanism of inter-metal interaction have yet to be understood. The crucial challenges include: 1) bottleneck in the precise and controllable synthesis of DACs with well-defined configurations, 2) difficulty in characterizing the adjacent and uniform distribution of heteronuclear atoms, and 3) knowledge gap between experimental observation and theoretical interpretation [3a, 14]. Ideally, the heteronuclear metal sites in DACs are connected by linking or bridging atoms (e.g., O/N/S atoms) with a well-defined configuration on the host support (e.g., N-doped graphene), which is denoted as "M_1-M_2" in **Figure 1**a [6b]. However, such adjacent and specific moieties cannot be strictly and uniformly constructed by prevailing synthetic methods [14-15]. The simplified "M_1-M_2" model and corresponding atomic bonding/orbital coupling theory cannot rationalize the experimentally observed performance of DACs [8b, 15-16]. As comparison, a new model of "M_1, M_2" for DACs which considers two crucial features – random distribution of heteronuclear metal sites and proximity effect between each other, is seldom studied [3a, 13a]. The characteristics of "M_1, M_2" configuration can effectively bridge the research from isolated SACs (M_1) through correlated SACs (M_1, M_1) to ideal DACs (M_1-M_2) (Figure 1a), rendering a more justified and universal structure model to unravel the fundamental mechanism of inter-metal interaction [6b]. Therefore, it is urgent and crucial to first investigate the inter-metal distance effect of DACs based on the "M_1, M_2" configuration, which can not only promote the full potential of DACs, but also guide the design of advanced SACs with more flexibility in concentration, composition, structure, and property.

Herein, NiCu dual-atom dispersed on nitrogen-doped carbon (NiCu-NC) was selected as a case to investigate the inter-metal distance effect on its CRR performance. We first conducted

theoretical predictions with various SACs and DACs models to evaluate the effect of inter-metal interaction on the electronic structure, and CRR activity and selectivity of DACs, revealing a distance threshold for effective inter-metal interaction. Further experimental synthesis, atomic characterization and electrocatalytic measurement confirmed the superior CRR activity and selectivity of DACs over SACs, especially on the onset potential and CO selectivity. The non-bonding inter-metal interaction and synergistic effect were further elucidated by analysing the electronic structure. Aiming at a more efficient and practicable design principle for DACs, we conducted random computational simulation and mathematical analysis to correlate the inter-metal distance with intrinsic material properties, such as the metal loading and substrate thickness. These findings offer some fresh and qualitative insights into the structural understanding, activity origin, and rational design of DACs by regulating the inter-metal distance and synergistic effect.

2. Result and Discussion

2.1. Theoretical Investigation of Inter-Metal Interaction Effect

We first evaluated the inter-metal interaction of DACs and its effect on CRR performance by changing the inter-metal distance (d) between adjacent Cu and Ni atoms. As shown in Figure 1b, four DACs models were built with the same first coordination sphere configuration (metal–N$_4$) but varied d values for density functional theory (DFT) computation. The models are denoted as dNiCu-d, where d is calculated to be 2.6, 4.1, 4.9, and 5.3 Å, respectively. Two monometallic counterparts, donated as sNi and sCu, were also considered to simulate the DACs without inter-metal interaction by increasing d to infinity. All these DACs models are confirmed to be thermodynamically stable with lower formation energies than those of SACs (Figure 1b).

To investigate the effect of inter-metal interaction on electronic structures, we introduce the "net electron difference" ($|\Delta e|$) to reflect the d-dependent electron redistribution on both Ni and Cu sites. The $|\Delta e|$ value is set as zero for both sNi and sCu models as the baseline. As shown
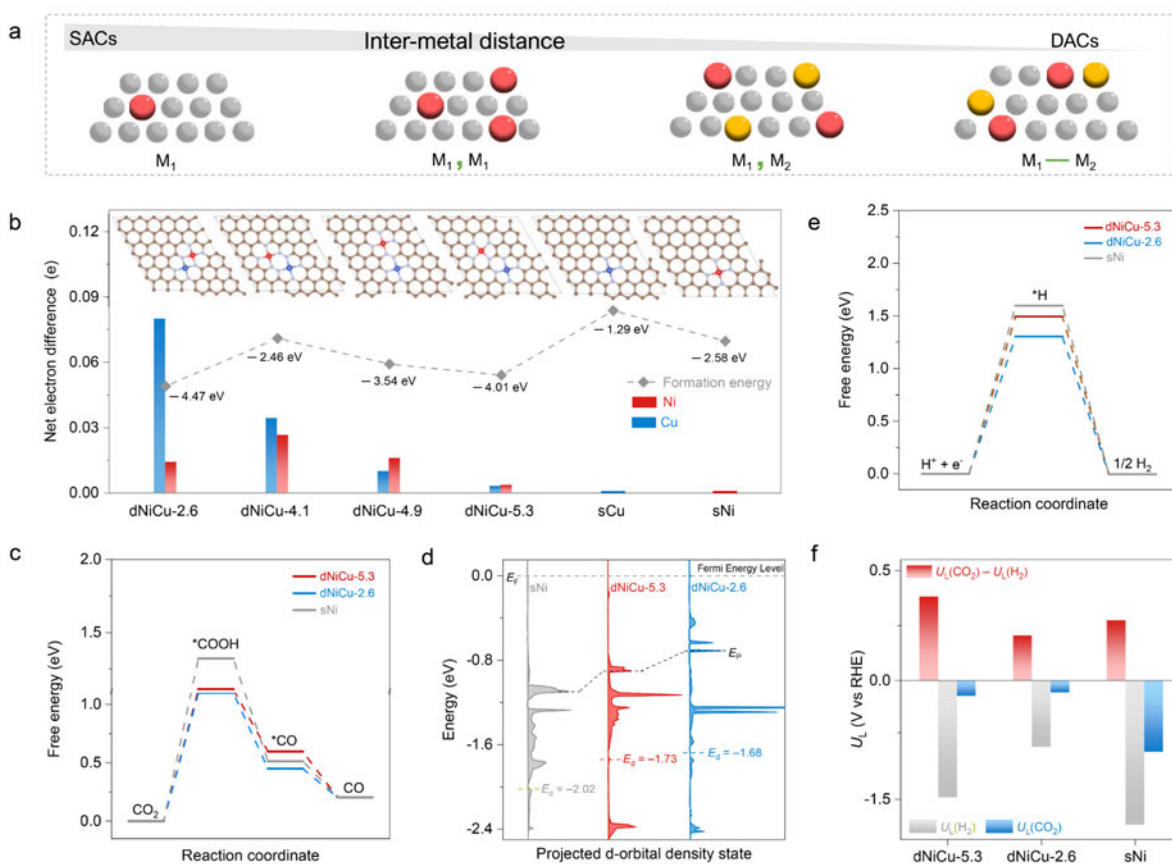
Figure 1. Theoretical calculations to study the inter-metal interaction effect on the dNiCu model. (a) Schematic of SACs and DACs showing the change in site proximity with different models. (b) Net electron difference of Ni and Cu sites in different dNiCu models using sNi and sCu models as the baseline, respectively. (c) Free energy diagrams of CO_2 electroreduction to CO on the Ni sites for dNiCu-5.3, dNiCu-2.6 and sNi models (U = 0 eV; pH = 6.8). (d) Computed pDOS of the Ni d-orbital for dNiCu-5.3, dNiCu-2.6 and sNi models. (e) Free energy diagrams of HER on the Ni sites for dNiCu-5.3, dNiCu-2.6 and sNi models (U = 0 eV; pH = 6.8). (f) Calculated limiting potentials difference for CO_2 reduction over H_2 evolution on Ni sites.

in Figure 1b, the DFT computation reveals a negative correlation between $|\Delta e|$ and d values for both sNi and sCu. The dNiCu-2.6 structure exhibits the most electron depletion on Cu (~0.08 e) and some on Ni (~0.02 e), and such electron redistribution effect is continuously weakened as the distance elongated. When d is larger than ~5.0 Å, the electron difference is becoming negligible (<0.003 e) compared to that of sNi and sCu. Therefore, there is a distance threshold (here 5.3 Å) to trigger effective inter-metal interaction in terms of the electronic structures for

DACs, which is consistent with the findings in densely populated Fe SACs [13a]. When d is closer than the threshold, the electronic structure of metal centres will be substantially altered by decreasing the inter-metal distance; however, the d-dependent effect will be negligible for the distance above the threshold. This two-stage d-dependent electronic interaction is believed to play a vital role in regulating the CRR activity and selectivity for DACs.

The influence of inter-metal interaction on CRR activity and selectivity was further studied by computing the free energy diagrams and limiting potentials (U_L) for different structures. We investigated the CO_2 reduction to CO through *COOH on both DACs (i.e., dNiCu-2.6, dNiCu-5.3) and SACs (sNi, sCu). As shown in Figure 1c and Figure S1, the formation of *COOH from CO_2 is the potential-limiting step for all cases, and the Gibbs free energy change of this step (ΔG_{COOH}) is used as the activity descriptor (Table S1 and S2). For all studied models, Ni sites are revealed to serve as the catalytic active centres with theoretical overpotentials relatively lower than those on Cu sites (Figure 1c and Figure S1). Additionally, the formation of DACs facilitates the adsorption of *COOH, evidenced by the lower ΔG_{COOH} on the dNiNi-2.6 comparing with sNi (Figure S1). Compared to the SACs without inter-metal interaction, the dNiCu-5.3 moiety exhibits obviously decreased energy barrier (ΔG_{COOH}) and thus higher CRR activity on the Ni sites. Such enhancement effect by introducing a neighbouring Cu site to Ni sites is further elucidated by investigating Ni 3d electronic configuration (Figure 1d and Figure S2). As shown in Figure 1d, the computed partial density of states (pDOS) reveal an obvious upshift of the peak location (E_p, first maximum near Fermi energy) and d-band centre (E_d) upon the incorporation of heterogeneous Cu sites and a decrease of the inter-metal distance. This regulated electronic structure is responsible for accelerated adsorption of reaction intermediates [13b, 17]. Notably, the closer d will simultaneously strengthen the adsorption of *H for competing hydrogen evolution reaction (HER) on Ni sites (Figure 1e), resulting in a trade-off between CRR activity and selectivity. The limiting potentials for CRR over HER, i.e., ($U_L(CO_2)$–$U_L(H_2)$), were applied as a reasonable descriptor to clearly figure out the CRR selectivity on

the d-dependent Ni sites [18]. As compared in Figure 1f and Figure S3, dNiCu-5.3 exhibits both high activity and selectivity for CRR, while dNiCu-2.6 is unfavourable due to the significantly decreased selectivity, even lower than that of Ni SACs.

The theoretical study well reveals that the electronic structure, CRR activity and selectivity of DACs can be effectively altered by the inter-metal interaction, which is determined by the inter-metal distance. It is noteworthy that the d-dependence features a novel threshold effect. Specifically, for dNiCu-5.3 DACs featuring the threshold d, the inter-metal interaction-derived electronic structure regulation (<0.003 e) significantly promotes the *COOH adsorption for CRR (Figure 1c) while slightly improves the *H adsorption for HER on Ni sites (Figure 1e), thus rendering a highly active and selective catalyst for CO_2 reduction to CO. By further decreasing d, however, the strong electronic interaction (e.g., one order of magnitude higher for dNiCu-2.6) leads to unfavourable enhancement of HER and lower selectivity towards CRR (Figure 1e and 1f). Therefore, these theoretical findings highlight the crucial importance to refine the fundamental mechanism understanding of d-dependent synergistic effects to guide the design of DACs with optimal structures and properties.

2.2. Synthesis and Characterization of NiCu DACs

Guided by theoretical predictions, we synthesized peripherally dispersed NiCu DACs on the nitrogen-doped graphene (denoted as NiCu-NC) by pyrolyzing a mixture of dicyandiamide, glucose, nickel, and copper salts in the argon atmosphere (Figure S4). Ni and Cu SACs, denoted as Ni-NC and Cu-NC, were also fabricated via similar approaches with the only addition of one corresponding salt precursor. Transmission electron microscopy (TEM) images show that the as-obtained NiCu-NC sample exhibits corrugated nanosheets with a multi-layer thickness (Figure 2a and 2b). Such nanosheet morphology is attributed to the added dicyandiamide as a sacrificial template, which initially assembles into the layered graphitic carbon nitride (g- C_3N_4), and binds aromatic carbon intermediates from the glucose. Finally, graphene nanosheet is
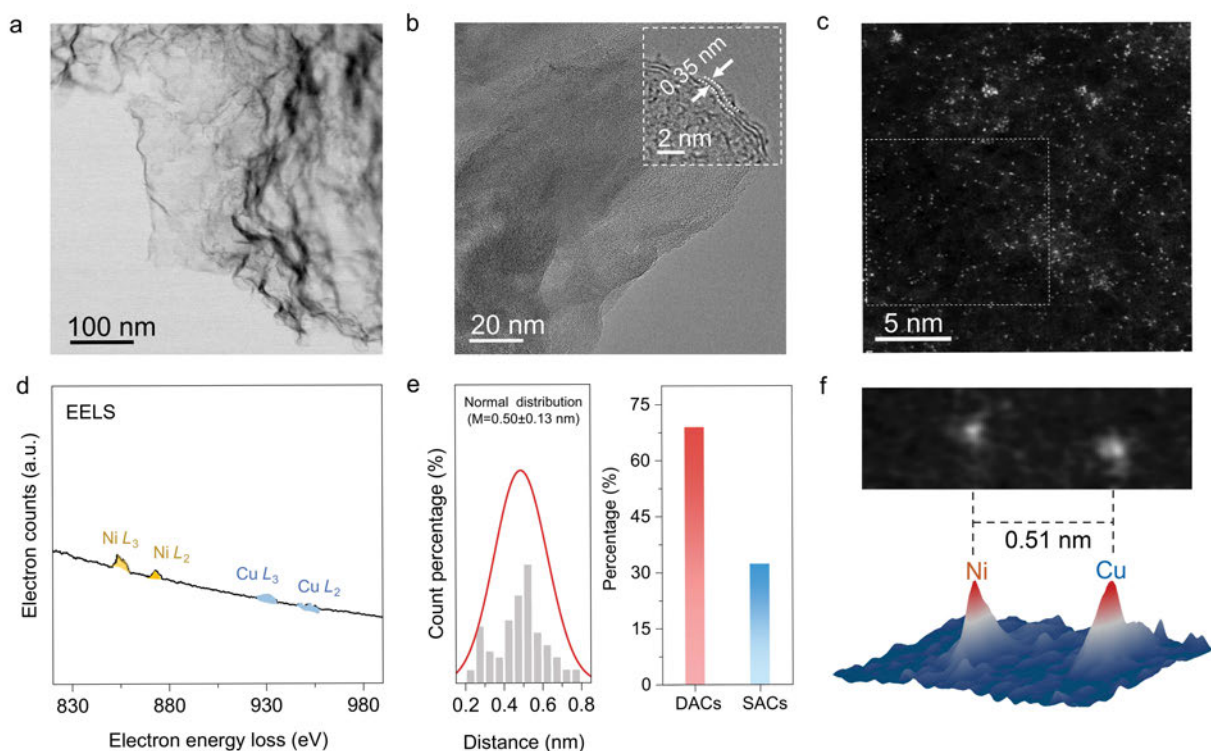
Figure 2. Atomic characterization of the obtained NiCu-NC DACs. (a) TEM image and (b) high-resolution TEM images of the as-obtained NiCu-NC. The insert in Figure 2b shows the edge thickness of the N-doped carbon nanosheet. (c) Representative atomic-resolution HAADF-STEM image and (d) EELS of NiCu-NC. (e) Histogram of the observed inter-metal distance (left) and percentage of DACs versus SACs with 5.3 Å as the threshold (right). (f) Magnified HAADF-STEM image of a NiCu atomic pair and the corresponding 3D intensity profile.

formed at higher temperatures (900°C) after the complete pyrolysis of g-C$_3$N$_4$ [19]. The interplanar spacing (0.35 nm) is slightly larger than that of pristine multi-layer graphene (0.335 nm), which might ascribe to the corrugation-derived lattice distortion and heteroatom-doped defects [19b]. Raman spectra further confirm the defective structure of nitrogen-doped graphene substrates, showing a large intensity ratio of D and G bands around 1.0 (Figure S5). Such defective laminated morphology is beneficial for the uniform anchoring and dispersion of atomic metal species. Powder X-ray diffraction (XRD) analysis of as-obtained samples reveals two broad peaks centred around 28° and 44°, assigned to the (002) and (101) facets of graphitic carbon (Figure S6) [20]. The absence of diffraction peaks for metallic nanoparticles, as well as no pronounced agglomeration in high-resolution TEM images, suggests the formation of

isolated Ni and Cu sites. As comparison, Ni-NC and Cu-NC samples were also characterized by Raman spectra, XRD spectra, and TEM images (Figure S5–S7), both of which display identical features as NiCu-NC.

The atomic dispersion and inter-metal distance were further investigated by aberration-corrected high-angle annular dark-field scanning transmission electron microscopy (HAADF-STEM). The HAADF-STEM image of NiCu-NC DACs displays a large amount of well-dispersed, bright dots with different brightness and size below 2 Å on the carbon matrix (Figure 2c, Figure S8). They are assigned to isolated Ni and Cu metal atoms due to the atomic number-dependent contrast variation. Electron energy loss spectroscopy (EELS) and energy-dispersive X-ray spectroscopy (EDX) mapping validate the uniform dispersion of Ni and Cu elements on the N-doped carbon matrix (Figure 2d and Figure S9). CO adsorption measurement via *in situ* Diffuse Reflectance Infrared Fourier Transform (DRIFT) Spectroscopy also verifies the formation of single-atom catalysts [21]. As shown in Figure S10, time-dependent DRIFT spectra reveal that CO absorption bands on NiCu-NC are centred at $2120\,cm^{-1}$. As the time of CO purging increases, the intensity of CO adsorption bands also increases. The uniform and isolated dispersion of metal atoms is also confirmed for Ni-NC and Cu-NC SACs samples (Figure S7). The Ni and Cu metal loadings in NiCu-NC are quantified by inductively coupled plasma mass spectrometer (ICP-MS) to be ~0.67 wt.% and 0.88 wt.%, respectively. All the as-obtained DACs and SACs samples exhibit a similar total metal loading, ranging from 1.14 to 1.55 wt.% (Figure S11, Table S3). These results further validate the atomic-resolution HAADF-STEM analyses, demonstrating the successful preparation of atomically dispersed NiCu-NC catalysts.

To gain more insights into the adjacent distribution of Ni and Cu atoms, we conducted statistical analysis by considering more than 300 atoms in HAADF-STEM images (Figure 2c, Figure S8, Figure S12). For one specific single-atom site, its inter-metal distance was determined by measuring the distance from its nearest metal site (Figure S12b). As shown in Figure 2e, the statistic histogram of inter-metal distance satisfies a normal distribution, with a

fitted average value of 0.50 ± 0.13 nm. If we take the theoretically predicted *d* value with effective inter-metal interaction (i.e., < 5.3 Å) as the threshold between SACs and DACs, more than 60% of the bright single-atom dots can be regarded as bimetallic pairs (Figure 2e), which is comparable with and even higher than previous reports [6d]. Considering the great challenge to identify each metal atom by HAADF-STEM, this statistical analysis provides an effective, reasonable and qualitative approach to investigating the inter-metal distance and interaction in both DACs and densely populated SACs. Figure 2f exhibits the HAADF-STEM image and corresponding intensity profile for a typical NiCu bimetallic pair with different contrast and *d* of 0.51 nm. The atomic-resolution elemental analysis via electron energy-loss spectroscopy (EELS) line-scan [8a, c] further corroborates the dual-atom element composition, i.e., one Ni atom and one Cu atom with a diatomic distance of 5.1 Å (Figure S13), which accounts for the largest proportion (Figure 2e) and matches well with the dNiCu-5.3 moiety.

2.3. Electronic and Coordination Structure Analysis of NiCu DACs

To identify the atomic structure and inter-metal interaction of as-obtained NiCu-NC DACs, we performed the synchrotron-based X-ray absorption fine structure (XAFS) spectroscopy characterization. As shown in Figure 3a, the Ni *K*-edge X-ray absorption near edge structure (XANES) spectra of NiCu-NC and Ni-NC locate between those of nickel (II) phthalocyanine (NiPc) and Ni Foil. It implies that the average valence state of isolated Ni atoms is between 0 and +2 in both SACs and DACs, which is the same for isolated Cu atoms (Figure 3b). The subtle difference in valence states between SACs and DACs is then investigated by the first-derivative XANES spectra (Figure 3c and 3d). Notably, the adsorption edges corresponding to the 1s → 4p transition [10, 13b, 22a] are almost identical (shift within 0.2 eV) for Ni *K*-edge between NiCu-NC (8338.3 eV) and Ni-NC (8338.1 eV) and for Cu *K*-edge between NiCu-NC (8981.6 eV) and Cu-NC (8981.5 eV), respectively. To further clarify the electronic states of Ni and Cu, we investigated the near-edge X-ray absorption fine structure (NEXAFS) spectrum for NiCu-NC. As shown in Figure S14, the NEXAFS spectrum of N *K*-edge for NiCu-NC suggests an
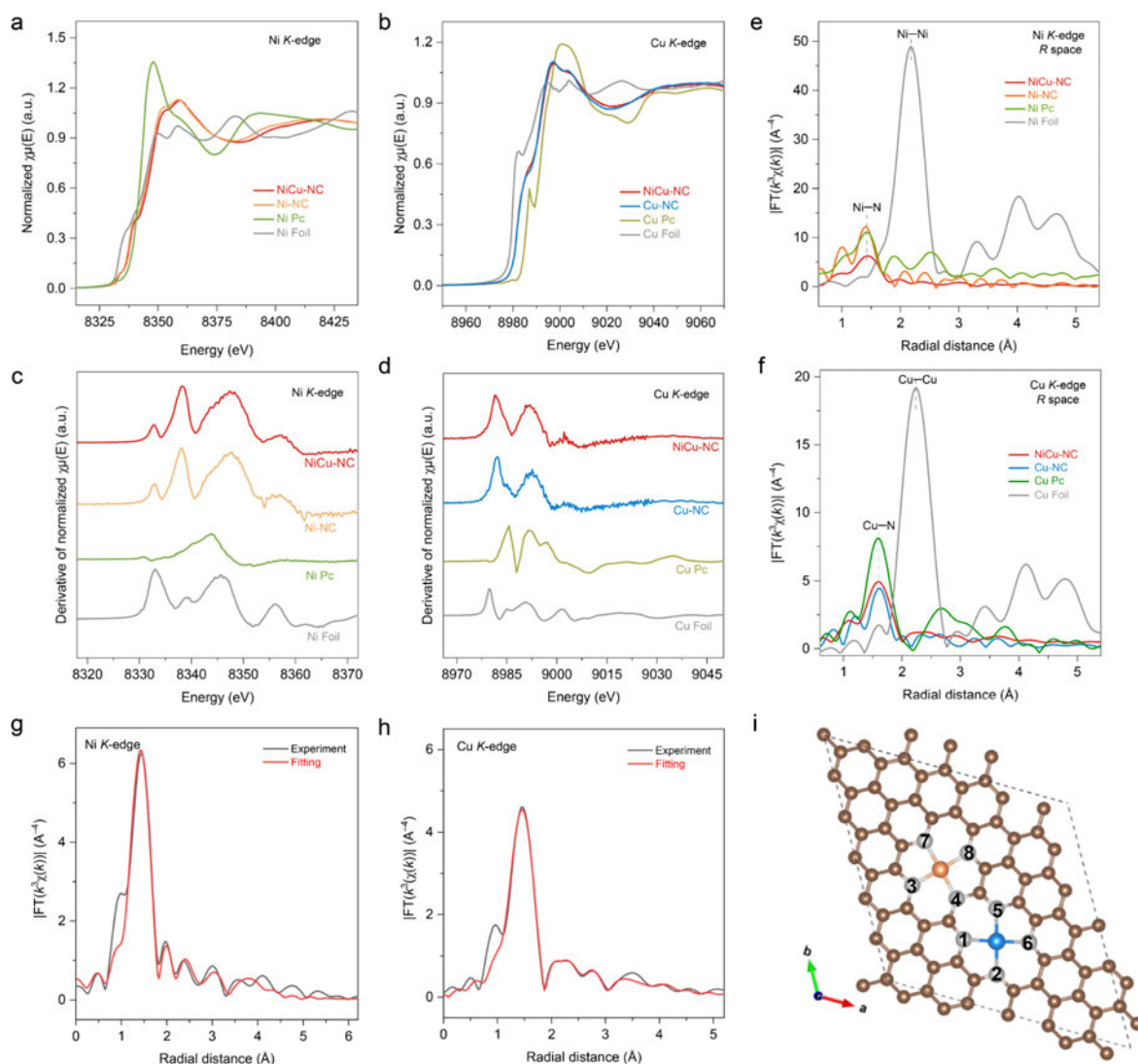
Figure 3. Coordination structure analysis of the obtained NiCu-NC DACs. (a) Ni *K*-edge and (b) Cu *K*-edge XANES spectra. (c) The derivative of the normalized Ni *K*-edge and (d) Cu *K*-edge XANES spectra of NiCu-NC, Ni-NC, Ni/Cu Pc and Ni/Cu foil. (e) Ni *K*-edge and (f) Cu *K*-edge FT-EXAFS spectra of different samples in *R*-space. (g) The *R*-space EXAFS-fitting curves of the as-obtained NiCu-NC sample at Ni *K*-edge and (h) Cu *K*-edge using the dNiCu-5.3 model. (i)The most likely structural model of the as-obtained NiCu-NC. The brown, grey, orange and blue balls represent C, N, Ni and Cu atoms, respectively.

evident absorption at ~399.5 eV, further proving the formation of metal–nitrogen bonding [8a, 22]. The Ni *L*-edge of both NiCu-NC and Ni-NC shows a shoulder peak around 853.6 eV at the *L*₃ region, implying that Ni is partially oxidized state in both samples (Figure S14b) [8a, 10a]. Also, no pronounced peak shift between NiCu-NC and Ni-NC further denotes the subtle interaction between atomical Ni and Cu sites, which is similar to that in the Cu *L*-edge of both NiCu-NC

and Cu-NC (Figure S14c). These findings reveal a subtle electronic structure change between as-obtained DACs and SACs, which is in line with the computation results of dNiCu-5.3 (Figure 1b) but different from previous reports [13b, 22].

To further investigate the coordination configuration of Ni and Cu atoms in NiCu-NC DACs and SACs counterparts, the extended X-ray absorption fine structure (EXAFS) was analysed. Figure 3e and 3f display the Fourier transform (FT) of k^3-weighted EXAFS spectra for Ni and Cu K-edge in the R-space, respectively. The Ni K-edge spectra exhibit a predominant peak around 1.45 Å for NiCu-NC and Ni-NC samples, similar to that for NiPc, which is assigned to the scattering of the first shell Ni–N path. The Cu K-edge spectra also feature the main peak around 1.5 Å originating from the Cu–N scattering for NiCu-NC and Cu-NC samples, in line with that for CuPc. Compared to Ni and Cu foils, the absence of metal–metal coordination (~2.2 Å) for as-obtained DACs and SACs samples further corroborates the isolated dispersion of each metal and suggests a moderate distance without direct bonding between metal atoms. We also introduced wavelet-transform (WT) analysis for EXAFS spectra to identify the surrounding coordination of Ni and Cu centers in the radial distance and the k space [23, 24]. As shown in Figure S15, the maximum intensity of Ni K-edge and Cu K-edge spectra is found at ~3.5 Å^{-1} for both NiCu-NC, Ni-NC and Cu-NC, which is attributed to the Ni–N or Cu–N scattering paths in the first coordination shell, consistent with FT-EXAFS results. At high radial magnitude (>2.5 Å), the WT-EXAFS intensity for NiCu-NC is comparable to these of Ni-NC and Cu-NC, but different from that of Ni/Cu metal foil [10, 22-23]. Furthermore, the local coordination structure of NiCu-NC DACs was quantitatively analysed by the least-squares EXAFS curve fitting using structure models with varied d values [8b, 23, 24]. The detailed fitting results, including metal−N/metal−metal path length and coordination numbers, are shown in Table S4. If the sCu/sNi models with an infinitely large d or the dNiCu-2.6 model with a very small d are applied, the fitting curves exhibit significant deviation in the region of the second shell (Figure S16 and S17). In contrast, the EXAFS curve fitting using the dNiCu-

5.3 model achieves the best fitting coefficient and matches well with the experimental spectra for NiCu-NC (Figure 3g–i, Figure S18 and S19). On one hand, the fitting results confirm an average coordination number of 4 for both Ni and Cu centres to form the Ni$-$N$_4$ and Cu$-$N$_4$ moieties in the first shell and eliminate the existence of Ni$-$Cu coordination bonds. On the other hand, additional metal–C/N bonds with longer lengths (> 2.5 Å) have been found (i.e., Ni–C(16)/C(31) and Ni–N(1)/N(5) bonds in Table S4), corroborating the non-bonding diatomic entity without direct metal–metal or metal–C/N–metal bonds. Taken together, the above-mentioned characterizations of as-obtained NiCu-NC DACs, especially the HAADF-STEM and EXAFS results, match well with the proposed dNiCu-5.3 model in terms of the electronic structure change, local coordination configuration, and inter-metal distance.

2.4. CRR Activity and Selectivity of NiCu DACs

To investigate the electrocatalytic performance enhancement of DACs by inter-metal interaction, we conducted CRR measurements in CO_2-saturated 0.10 M $KHCO_3$ using a gas-tight H-cell, which could provide much smaller biases and interference on the catalysts, thus leading to the slightest change in the structure of catalysts and benefit the clear mechanistic studies [25]. As shown in Figure 4a, the linear scan voltammogram (LSV) tests reveal that NiCu-NC DACs deliver higher current responses than Ni-NC and Cu-NC SACs below −0.40 V vs reversible hydrogen electrode (RHE) in the CO_2-saturated electrolyte, implying its superior CRR activity. CRR selectivity was evaluated by chronoamperometry tests at different potentials (Figure S20), and gaseous products were quantitatively analysed by online gas chromatography. Carbon monoxide (CO) and hydrogen (H_2) are identified as the predominant products over the whole potential range, with a total Faradaic efficiency (FE) close to 100% (Figure 4b,c). At an applied potential as positive as −0.32 V vs RHE, CO product can be obviously detected for NiCu-NC but is not evident for Ni-NC and Cu-NC samples, suggesting a smaller onset overpotential (η) of converting CO_2 to CO (Figure 4b). NiCu-NC sample can achieve a

maximum FE for CO production (FE$_{CO}$) as high as ~98%, much better than that of Ni-NC and Cu-NC SACs. Furthermore, NiCu-NC exhibits a significantly wide potential window for FE$_{CO}$ > 80% (from −0.47 V to −1.27 V vs RHE; 800 mV), which is ~200 mV wider than that of Ni-NC. Given the boosted activity and selectivity, NiCu-NC exhibits much higher CO partial current density (j_{CO}) over the entire potential window. Specifically, NiCu-NC can deliver a high j_{CO} of −18.2 mA cm^{-2} at −1.27 V vs RHE, which is ~1.5 and ~9 times greater than those of Ni-NC and Cu-NC, respectively (Figure 4d). Such CO$_2$-to-CO activity and selectivity of NiCu-NC are among the best results for state-of-the-art DACs and SACs evaluated in H-cells (Table S5).
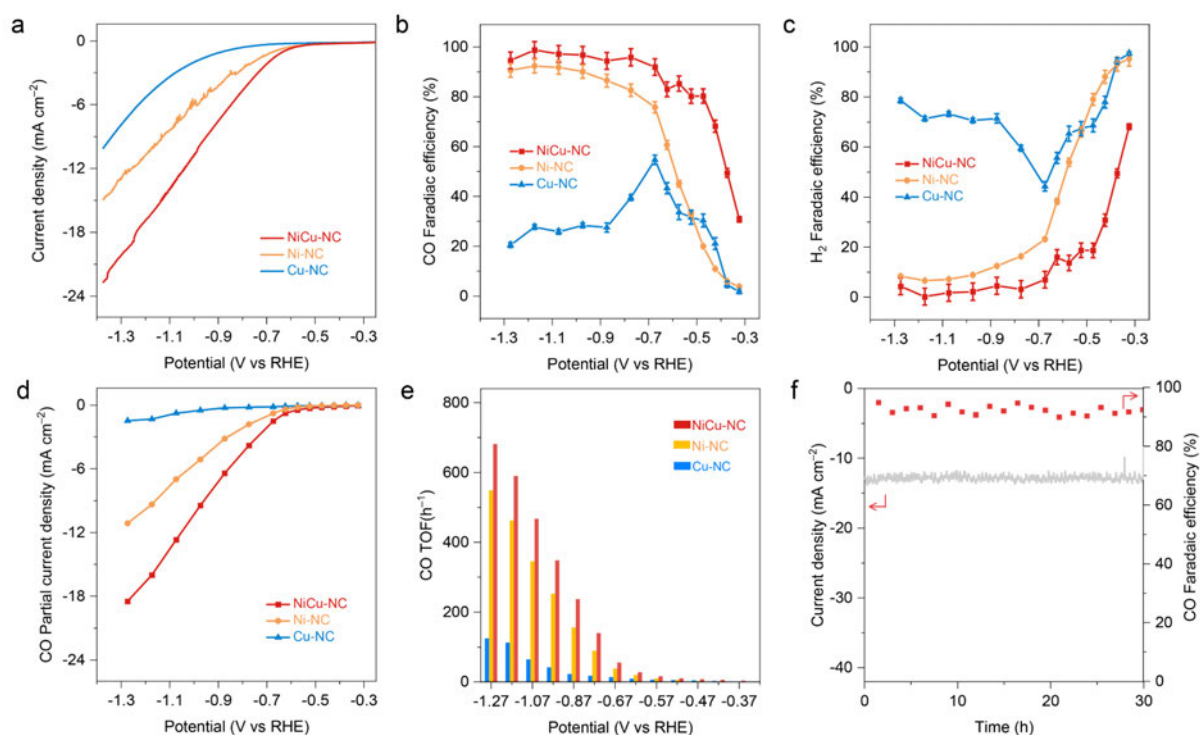
Figure 4. Catalytic performance of CO$_2$ electroreduction to CO. (a) LSV polarization curves for NiCu-NC, Ni-NC, and Cu-NC in CO$_2$-saturated 0.1 M KHCO$_3$ electrolyte. Potential-dependent Faradaic efficiencies of (b) CO and (c) H$_2$ for NiCu-NC, Ni-NC, and Cu-NC in CO$_2$-saturated 0.1 M KHCO$_3$. The error bars were calculated by three independent tests. (d) Potential-dependent CO partial current densities for different samples. (e) Calculated TOF for NiCu-NC, Ni-NC, and Cu-NC on different applied potentials. (f) Stability evaluation of NiCu-NC by chronoamperometric test at −1.07 V vs RHE for continuous 30 hours.

The superior intrinsic activity of NiCu-NC DACs is further illustrated by calculating the turnover frequency (TOF) for CO production based on the number of all metal sites (Ni and/or

Cu), as well as the kinetics studies. As shown in Figure 4e, NiCu-NC exhibits a maximum TOF of 681 h^{-1} at -1.27 V vs RHE, which is ~1.2 and ~5.5 times higher than those of Ni-NC and Cu-NC, respectively. Moreover, NiCu-NC shows excellent durability for CRR electrocatalysis, demonstrated by the stable current density and FE$_{CO}$ over 30 h during the continuous electrolysis at a constant potential of -1.07 V vs RHE (Figure 4f). Post-mortem microscopy characterization of NiCu-NC after long-term electrolysis indicates no formation of nanoparticles or nanoclusters by potential-induced agglomeration (Figure S21). Additionally, we conducted Tafel analysis to understand the reaction kinetics of the dual-atom sample for the boosted catalytic performance. As shown in Figure S22, the Tafel slope for CO evolution on NiCu-NC is 138 mV dec^{-1}, where the first electron transfer can be attributed to a rate-determining step (RDS), i.e., CO$_2$ activation with proton-coupled electron transfer (PCET) [26]. The reaction order analysis elaborates more on the RDS (Figure S22b). The approximate zero-order dependency on [HCO$_3^-$] suggests that the source of the proton in PCET step was mainly from water dissociation rather than directly from bicarbonate, i.e., $* + CO_2 + H_2O + e^- = {}^*COOH + OH^-$ [26]. Compared with Ni-NC (257 mV dec^{-1}) and Cu-NC (289 mV dec^{-1}), NiCu-NC has the smallest Tafel slope, confirming its improved kinetics for the CO$_2$ to CO conversion, benefiting from the synergistic Ni/Cu dual sites. Such results are also consistent with the findings and rationality in the DFT computations, where sCu exhibited higher ΔG_{COOH} while the sNi or Ni site of the dNiCu-5.3 lowered the energy barrier (Figure S2). These results manifest the crucial role of inter-metal interaction and synergistic effect between Ni and Cu atoms on enhancing the electrocatalytic performance of DACs, which will be elucidated further by theoretical studies. Since Ni sites are identified as the catalytic active centres (Figure 1 and Figure S2), we analysed the electron state change of Ni sites with *COOH bonded to investigate the synergistic mechanism in DACs. As compared in Figure S23 and S24, upon *COOH adsorption on the Ni sites of dNiCu-5.3 and sNi, different electron transfer behaviours are observed. For dNiCu-5.3, more electron depletion is observed on both Ni (from

+1.03 to +1.16) and Cu sites (from +0.91 to +1.05). This synergistic interaction leads to 0.33e accumulation on the *COOH adsorbed onto the Ni site in the dNiCu-5.3, while COOH on the sNi can just receive 0.26e (Figure S23), which can rationalize the similar net electron change but counterintuitively lowered *COOH adsorption energy between dNiCu-5.3 and sNi. Given the large inter-metal distance exceeding the metal–metal bond length, the electron contribution from Cu sites should be shuttled through the NC substrate to Ni sites, and finally to the *COOH intermediate. Therefore, such through-structure electron transfer is likely to be the active origin of the non-bonding synergistic interaction between neighbouring DACs.

2.5. Macro-Descriptor for Rational Design of DACs

Although theoretical and experimental studies mutually verify the effect of inter-metal interaction and d-dependent electrocatalytic performance for DACs, it remains difficult to rationally design and synthesize DACs with favourable inter-metal interaction. Based on current technological advances on DACs synthesis, it is very reasonable to assume that the experimentally obtained DACs feature random distribution of metal atoms for most cases. The atomic distribution and inter-metal distance of metal sites can be mathematically analysed by Monte Carlo experiments. Specifically, we built a 20 nm × 20 nm grid to stand for the N-doped graphene substrate, and randomly spread a certain amount of orange and blue spheres (radius: 0.15 nm, in equal numbers) inside to represent Ni atoms and Cu atoms in the NiCu-NC DACs. The distance between any given orange sphere and its nearest blue sphere was defined as the inter-sphere (i.e., inter-metal) distance (Figure 5a; Experiment Section). The random algorithm programming logic and details can be found in the Experimental Section. Figure 5a and Figure S25 display the typical position distribution after randomly dispatching spheres with number ranging from 100 to 1200. It is noticeable that the range of inter-sphere distance decreases as the surface density of spheres (i.e., n = sphere number/grid area) grows (Figure 5b). When n increases from 0.25 nm^{-2} to 3.0 nm^{-2}, the most probable inter-sphere distance will decrease from 1.11 nm to 0.29 nm (Figure 5c), which matches well with the d range for dNiCu-2.6 and
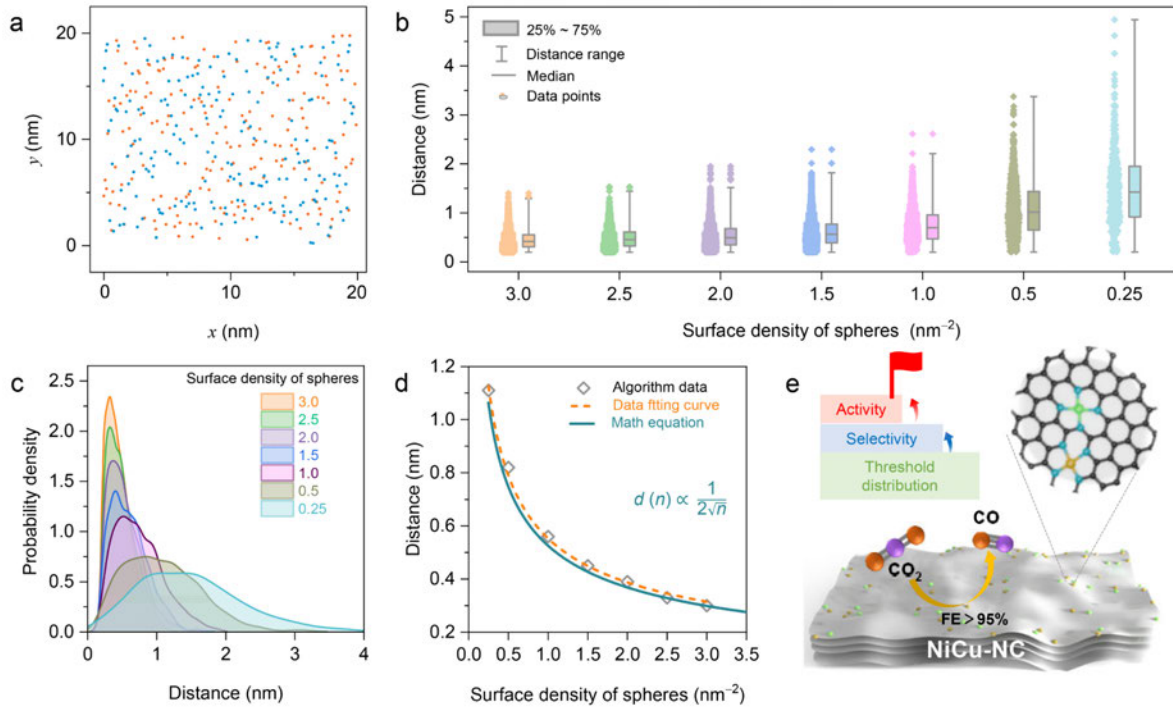
Figure 5. Macro-descriptor of the inter-metal distance for DACs via random distribution analysis. (a) The typical position of 400 spheres in two different colours after random distribution on the 20 × 20 nm grid. (b) The Box-line plot for the statistical illustration of the inter-distance of varied numbers of randomly distributed spheres. (c) The probability density curves converted from Figure 5b. (d) The fitting curve correlating the inter-site distance and the surface density of spheres, based on the mode of distance (peak value) from Figure 5c. (e) Schematic of Ni and Cu atoms dispersed on multilayered graphene nanosheets within the threshold distance, showing the synergistic effect to boost CRR activity and selectivity.

dNiCu-5.3 moieties. Furthermore, by referring to a previously reported mathematical model investigating the distance between two random uniform points in a unit square [27], the expected value of inter-sphere distance (d) can be rigorously correlated with the surface density of spheres (n) (Equation 1). The step-by-step mathematical derivation is presented in the Supplementary Text.

$$d \propto \frac{1}{2\sqrt{n}} \qquad\qquad (1)$$

It is notable that the fitting curve (orange dash line in Figure 5d) of simulation results shows almost the same coefficient (–0.51) as that from mathematical derivation (–0.5). Considering the experimentally obtained DACs supported on a two-dimensional (2D) host substrate (i.e., N-

doped graphene, Figure S26), the d can be further correlated with the intrinsic material parameters (Equation 2).

$$d \propto (F \times T \times r_a)^{-0.5} \qquad (2)$$

where F is a material-dependent factor showing the total atom number of monolayer substrate per unit square, T is the thickness of the 2D substrate, and r_a is the atomic ratio of metal atoms.

Promisingly, such d–r_a correlation can serve as a universal and practicable macro-descriptor to guide the design and synthesis of DACs and SACs with targeted inter-metal distance and favourable performance enhancement by regulating the substrate thickness and metal loading. It has been validated in Fe–N$_4$ SACs for ORR application [13a]. The increase of metal loading will decrease the inter-metal distance of adjacent Fe atoms and optimize the ORR activity. Given the most recent advance of the SACs formation mechanism [28] and present insight into the d–r_a correlation, the fabrication of well-defined carbonaceous DACs or SACs can be rationally achieved by regulating the carbon precursor amount and type, carbonization method, the vaporization-dependent metal precursor amount, and other related factors. Meanwhile, it is more economic and feasible to synthesize high-performance DACs/SACs with moderate metal loading and threshold inter-metal effect, rather than to pursue ultrahigh metal loading amount (Figure 5e).

3. Conclusion

We unravelled a critical and qualitative effect of threshold distance between neighbouring metals of DACs on the electronic structure and electrocatalytic performance. It has been mutually confirmed by theoretical simulation and experiments, including microscopic, spectroscopic and electrochemical techniques, as well as computational modellings. By taking NiCu-NC as an example, Ni and Cu atoms featuring a threshold distance of 5.3 Å exhibited non-bonding interaction but the synergistic effect to regulate the electronic structure and promote intermediate adsorption, thus boosting the activity and selectivity of CO_2 electroreduction. The threshold-distributed NiCu-NC DACs exhibited a low onset potential

(300 mV) and a wide potential window of ~ 800 mV for selective CO_2 reduction to CO (> 80%), with a maximum FE of ~98% at −1.07 V vs RHE in 0.1 M $KHCO_3$. The random distribution simulation and mathematical analysis also revealed an effective macro-descriptor to correlate the inter-metal distance with structure features, such as the substrate thickness and metal loading. This work stresses the importance of a thorough structural investigation of DACs and paves the way for a deeper understanding of inter-metal interaction with more rational and realistic principles, which will benefit the design, characterization, and mechanism elucidation of atomically dispersed catalysts in the future.

4. Experimental Section

Experimental details can be found in the Supporting Information.

Supporting Information

Supporting Information is available from the Wiley Online Library or from the author.

Conflict of Interest

The authors declare no conflict of interest.

Data Availability Statement

The data that support the findings of this study are available from the corresponding author upon reasonable request.

References

[1]   a) X. F. Yang, A. Wang, B. Qiao, J. Li, J. Liu, T. Zhang, *Acc. Chem. Res.* **2013**, *46*, 1740; b) Y. Chen, S. Ji, C. Chen, Q. Peng, D. Wang, Y. Li, *Joule* **2018**, *2*, 1242; c) C. Tang, Y. Jiao, B. Shi, J. N. Liu, Z. Xie, X. Chen, Q. Zhang, S. Z. Qiao, *Angew. Chem. Int. Ed.* **2020**, *59*, 9171.

[2]   a) K. Liu, J. Fu, Y. Lin, T. Luo, G. Ni, H. Li, Z. Lin, M. Liu, *Nat. Commun.* **2022**, *13*, 2075; b) F. Wu, C. Pan, C.-T. He, Y. Han, W. Ma, H. Wei, W. Ji, W. Chen, J. Mao, P. Yu, D. Wang, L. Mao, Y. Li, *J. Am. Chem. Soc.* **2020**, *142*, 16861; c) Y. Chen, S. Ji, S. Zhao, W. Chen, J. Dong, W.-C. Cheong, R. Shen, X. Wen, L. Zheng, A. I. Rykov, S. Cai, H. Tang, Z. Zhuang, C. Chen, Q. Peng, D. Wang, Y. Li, *Nat. Commun.* **2018**, *9*, 5422; d) F. Zhang, Y. Zhu, C. Tang, Y. Chen, B. Qian, Z. Hu, Y. C. Chang, C. W. Pao, Q. Lin, S. A. Kazemi, Y. Wang, L. Zhang, X. Zhang, H. Wang, *Adv. Funct. Mater.* **2022**, *32*, 2110224.

[3]   a) W. Zhang, Y. Chao, W. Zhang, J. Zhou, F. Lv, K. Wang, F. Lin, H. Luo, J. Li, M. Tong, E. Wang, S. Guo, *Adv. Mater.* **2021**, *33*, 2102576; b) J. Zhang, Q.-A. Huang, J. Wang, J. Wang, J. Zhang, Y. Zhao, *Chin. J. Catal.* **2020**, *41*, 783; c) G. Sun, Z. J. Zhao, R. Mu, S. Zha, L. Li, S. Chen, K. Zang, J. Luo, Z. Li, S. C. Purdy, A. J. Kropf, J. T. Miller, L. Zeng, J. Gong, *Nat. Commun.* **2018**, *9*, 4454.

[4]   a) F. Calle-Vallejo, D. Loffreda, M. T. M. Koper, P. Sautet, *Nat. Chem.* **2015**, *7*, 403; b) X. Hong, K. Chan, C. Tsai, J. K. Nørskov, *ACS Catal.* **2016**, *6*, 4428; c) Q. Wang, X. Zheng, J. Wu, Y. Wang, D. Wang, Y. Li, *Small Struct.* **2022**, *3*, 2200059.

[5]   a) K. P. Kuhl, T. Hatsukade, E. R. Cave, D. N. Abram, J. Kibsgaard, T. F. Jaramillo, *J. Am. Chem. Soc.* **2014**, *136*, 14107; b) H. A. Hansen, J. B. Varley, A. A. Peterson, J. K. Nørskov, *J. Phys. Chem. Lett.* **2013**, *4*, 388.

[6]   a) Z. W. Chen, L. X. Chen, C. C. Yang, Q. Jiang, *J. Mater. Chem. A* **2019**, *7*, 3492; b) A. Pedersen, J. Barrio, A. Li, R. Jervis, D. J. L. Brett, M. M. Titirici, I. E. L. Stephens, *Adv. Energy Mater.* **2022**, *12*, 2102715; c) L. Li, K. Yuan, Y. Chen, *Acc. Mater. Res.* **2022**, *3*, 584; d) L. Zhang, R. Si, H. Liu, N. Chen, Q. Wang, K. Adair, Z. Wang, J. Chen, Z. Song, J. Li, M.

N. Banis, R. Li, T.-K. Sham, M. Gu, L.-M. Liu, G. A. Botton, X. Sun, Nat. Commun. **2019**, *10*, 4936.

[7]   a) C. Liu, T. Li, X. Dai, J. Zhao, D. He, G. Li, B. Wang, X. Cui, *J. Am. Chem. Soc.* **2022**, *144*, 4913; b) J. Shan, C. Ye, Y. Jiang, M. Jaroniec, Y. Zheng, S.-Z. Qiao, *Sci. Adv.* **2022**, *8*, eabo0762.

[8]   a) L. Jiao, J. Zhu, Y. Zhang, W. Yang, S. Zhou, A. Li, C. Xie, X. Zheng, W. Zhou, S.-H. Yu, H. L. Jiang, *J. Am. Chem. Soc.* **2021**, *143*, 19417; b) Y. Li, W. Shan, M. J. Zachman, M. Wang, S. Hwang, H. Tabassum, J. Yang, X. Yang, S. Karakalos, Z. Feng, G. Wang, G. Wu, *Angew. Chem. Int. Ed.* **2022**, *61*, e202205632; c) X. Zhang, X. Zhu, S. Bo, C. Chen, M. Qiu, X. Wei, N. He, C. Xie, W. Chen, J. Zheng, P. Chen, S. P. Jiang, Y. Li, Q. Liu, S. Wang, *Nat. Commun.* **2022**, *13*, 5337.

[9]   Z. Liang, L. Song, M. Sun, B. Huang, Y. Du, *Sci. Adv.* **2021**, *7*, eabl4915.

[10]   D. Liu, Y. Zhao, C. Wu, W. Xu, S. Xi, M. Chen, L. Yang, Y. Zhou, Q. He, X. Li, B. Ge, L. Song, J. Jiang, Q. Yan, *Nano Energy* **2022**, *98*, 107296.

[11]   Z. Yu, C. Si, A. P. LaGrow, Z. Tai, W. A. Caliebe, A. Tayal, M. J. Sampaio, J. P. S. Sousa, I. Amorim, A. Araujo, L. Meng, J. L. Faria, J. Xu, B. Li, L. Liu, *ACS Catal.* **2022**, 9397.

[12]   Y. Yang, Y. Qian, H. Li, Z. Zhang, Y. Mu, D. Do, B. Zhou, J. Dong, W. Yan, Y. Qin, L. Fang, R. Feng, J. Zhou, P. Zhang, J. Dong, G. Yu, Y. Liu, X. Zhang, X. Fan, *Sci. Adv.* **2020**, *6*, eaba6586.

[13]   a) Z. Jin, P. Li, Y. Meng, Z. Fang, D. Xiao, G. Yu, *Nat. Catal.* **2021**, *4*, 615; b) J. Zhu, M. Xiao, D. Ren, R. Gao, X. Liu, Z. Zhang, D. Luo, W. Xing, D. Su, A. Yu, Z. Chen, *J. Am. Chem. Soc.* **2022**, *144*, 9661; c) H. Li, L. Wang, Y. Dai, Z. Pu, Z. Lao, Y. Chen, M. Wang, X. Zheng, J. Zhu, W. Zhang, R. Si, C. Ma, J. Zeng, *Nat. Nanotechnol.* **2018**, *13*, 411; d) M. O. Cichocka, Z. Liang, D. Feng, S. Back, S. Siahrostami, X. Wang, L. Samperisi, Y. Sun, H. Xu, N. Hedin, H. Zheng, X. Zou, H. C. Zhou, Z. Huang, *J. Am. Chem. Soc.* **2020**, *142*, 15386.

[14]   a) T. He, A. R. P. Santiago, Y. Kong, M. A. Ahsan, R. Luque, A. Du, H. Pan, *Small* **2022**, *18*, 2106091; b) W. Li, J. Yang, and D. Wang, *Angew. Chem. Int. Ed.* **2022**, *61*, e202213318, https://doi.org/10.1002/anie.202213318.

[15]   J. Leverett, R. Daiyan, L. Gong, K. Iputera, Z. Tong, J. Qu, Z. Ma, Q. Zhang, S. Cheong, J. Cairney, R. S. Liu, X. Lu, Z. Xia, L. Dai, R. Amal, *ACS Nano* **2021**, *15*, 12006.

[16]   Z. Zeng, L. Y. Gan, H. Bin Yang, X. Su, J. Gao, W. Liu, H. Matsumoto, J. Gong, J. Zhang, W. Cai, Z. Zhang, Y. Yan, B. Liu, P. Chen, *Nat. Commun.* **2021**, *12*, 4088.

[17]   X. Zhi, Y. Jiao, Y. Zheng, A. Vasileff, S.-Z. Qiao, *Nano Energy* **2020**, *71*, 104601.

[18]   a) C. Shi, H. A. Hansen, A. C. Lausche, J. K. Nørskov, *Phys. Chem. Chem. Phys.* **2014**, *16*, 4720; b) A. Vasileff, X. Zhi, C. Xu, L. Ge, Y. Jiao, Y. Zheng, S. Z. Qiao, *ACS Catal.* **2019**, *9*, 9411.

[19]   a) X. H. Li, S. Kurasch, U. Kaiser, M. Antonietti, *Angew. Chem. Int. Ed.* **2012**, *51*, 9689; b) D. Liu, C. Wu, S. Chen, S. Ding, Y. Xie, C. Wang, T. Wang, Y. A. Haleem, Z. ur Rehman, Y. Sang, Q. Liu, X. Zheng, Y. Wang, B. Ge, H. Xu, L. Song, *Nano Res.* **2018**, *11*, 2217.

[20]   C. Xu, A. Vasileff, D. Wang, B. Jin, Y. Zheng, S. Z. Qiao, *Nanoscale Horiz.* **2019**, *4*, 1411.

[21]   a) X. Hai, S. Xi, S. Mitchell, K. Harrath, H. Xu, D. F. Akl, D. Kong, J. Li, Z. Li, T. Sun, H. Yang, Y. Cui, C. Su, X. Zhao, J. Li, J. Pérez-Ramírez, J. Lu, *Nat. Nanotechnol.* **2022**, *17*, 174; b) P. Hollins, J. Pritchard, *Surf. Sci.* **1979**, *89*, 486; c) K. S. Smirnov, G. Raseev, *Surf. Sci.* **1997**, *384*, L875.

[22]   a) H. Cheng, X. Wu, M. Feng, X. Li, G. Lei, Z. Fan, D. Pan, F. Cui, G. He, *ACS Catal.* **2021**, *11*, 12673; b) L. Jiao, W. Yang, G. Wan, R. Zhang, X. Zheng, H. Zhou, S. H. Yu, H. L. Jiang, *Angew. Chem. Int. Ed.* **2020**, *59*, 20589.

[23]   H. Funke, M. Chukalina, A. C. Scheinost, *J. Synchrotron. Radiat.* **2007**, *14*, 426.

[24]   B. Ravel, M. Newville, *J. Synchrotron. Radiat.* **2005**, *12*, 537.

[25]   a) K. Krause, C. Lee, J. K. Lee, K. F. Fahy, H. W. Shafaque, P. J. Kim, P. Shrestha, A. Bazylak, *ACS Sustain. Chem. Eng.* **2021**, *9*, 5570; b) Z. Z. Niu, L. P. Chi, R. Liu, Z. Chen, M. R. Gao, *Energy Environ. Sci.* **2021**, *14*, 4169; c) D. M. Weekes, D. A. Salvatore, A. Reyes, A. Huang, C. P. Berlinguette, *Acc. Chem. Res.* **2018**, *51*, 910; d) J. Yang, H. Qi, A. Li, X. Liu, X. Yang, S. Zhang, Q. Zhao, Q. Jiang, Y. Su, L. Zhang, J. F. Li, Z. Q. Tian, W. Liu, A. Wang, T. Zhang, *J. Am. Chem. Soc.* **2022**, *144*, 12062.

[26]   a) M. Dunwell, W. Luc, Y. Yan, F. Jiao, B. Xu, *ACS Catal.* **2018**, *8*, 8121; b) C. Xu, X. Zhi, A. Vasileff, D. Wang, B. Jin, Y. Jiao, Y. Zheng, S. Z. Qiao, *Small Struct.* **2021**, *2*, 2000058; c) M. Ma, B. J. Trześniewski, J. Xie, W. A. Smith, *Angew. Chem. Int. Ed.* **2016**, *55*, 9748; d) D. Yao, C. Tang, A. Vasileff, X. Zhi, Y. Jiao, S. Z. Qiao, *Angew. Chem. Int. Ed.* **2021**, *60*, 18178.

[27] G. Marsaglia, B. Narasimhan, A. Zaman, *Commun. Stat. - Theory Methods* **1990**, *19*, 4199.

[28]   L. Han, H. Cheng, W. Liu, H. Li, P. Ou, R. Lin, H. T. Wang, C. W. Pao, A. R. Head, C. H. Wang, X. Tong, C. J. Sun, W. F. Pong, J. Luo, J. C. Zheng, H. L. Xin, *Nat. Mater.* **2022**, *21*, 681.

The table of contents entry

Investigating the inter-metal site distance effect of dual-atom catalysts (DACs) can not only promote the full potential of DACs, but guide the design of advanced atomically-dispersed catalysts. Herein, we employ a peripherally distributed NiCu dual-atom catalyst as a case study to investigate the distance (d)-dependent inter-metal interaction, and provide a newly-proposed macro-descriptor as the guidance for the future design of DACs.

Dazhi Yao, Cheng Tang, Xing Zhi, Bernt Johannessen, Ashley Slattery, Shane Chern, Shi-Zhang Qiao*

Inter-Metal Interaction with a Threshold Effect in NiCu Dual-Atom Catalysts for CO_2 Electroreduction

ToC figure (55 mm broad × 50 mm high)
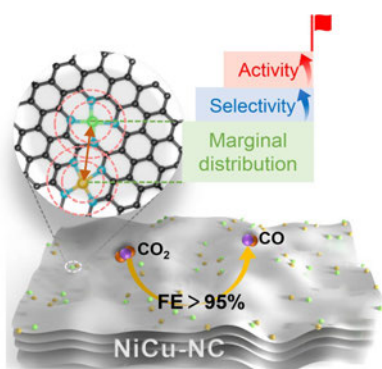
Supporting Information

Inter-Metal Interaction with a Threshold Effect in NiCu Dual-Atom Catalysts for CO$_2$ Electroreduction

Dazhi Yao, Cheng Tang, Xing Zhi, Bernt Johannessen, Ashley Slattery, Shane Chern, and Shi-Zhang Qiao*

D. Yao. C. Tang, X. Zhi, S.-Z. Qiao

Centre for Materials in Energy and Catalysis, School of Chemical Engineering and Advanced Materials, The University of Adelaide, Adelaide, SA 5005, Australia

E-mail: s.qiao@adelaide.edu.au (S.-Z. Q.)

B. Johannessen

Australian Synchrotron, 800 Blackburn Rd, Clayton, VIC 3168, Australia

A. Slattery

Adelaide Microscopy, The University of Adelaide, Adelaide, SA 5005, Australia

S. Chern

Department of Mathematics and Statistics, Dalhousie University, Halifax, Nova Scotia, B3H 4R2, Canada

1. Experimental Section

1.1. Theoretical calculations

All calculations were performed using DFT. The Perdew−Burke Ernzerhof (PBE) functional was employed for electron exchange-correlation within the generalized gradient approximation (GGA), as implemented in the VASP code [S1]. The ionic cores were described by the projector-augmented wave (PAW) method. Van der Waals (vdW) interactions between atoms were considered in all the energy calculations with a plane-wave cut-off energy value of 500 eV. During geometry optimization, the structures were relaxed to forces on the atoms smaller than 0.02 eV Å^{-1}. A Monkhorst-Pack k-point grid of ($2 \times 2 \times 1$) was applied. The DFT-D3 method of Grimme was employed to address vdW interactions between atoms. For DOS calculation, Gamma k-point grid with a condense number ($9 \times 9 \times 9$) was applied. The sCu, sNi, and various dCuNi models were built on a 6×6 graphene supercell with 15 Å of vacuum space. The Cu and Ni atoms were bonded to N atoms. The computational hydrogen electrode (CHE) model was employed for free energy calculations [S2, S3]. The free energies (G) of intermediates were obtained by $G = E + ZPE - TS$. The zero-point energy (ZPE) and entropy correction (TS) were calculated from vibration analysis and used to convert electronic energy (E) into G at 298.15 K. The solvation effects were included for *COOH and *CO stabilized by 0.25 eV and 0.1 eV, respectively [S3, S4]. The calculation of formation energy ($E_{formation}$) is referenced from previous reports [S4]. For single-atom catalysts model (sNi/sCu), $E_{formation}$ was calculated as $E_{formation} = E_{sNi/Cu} - E_{Ni/Cu-V} - \mu_{Ni/Cu}$, where $E_{sNi/Cu}$ is the energy of the sNi/sCu model, $E_{Ni/Cu-V}$ is the energy of nitrogen-doped carbon matrix without the incorporation of metal atom (Ni/Cu), and $\mu_{Ni/Cu}$ denotes the chemical potential of Ni/Cu species (i.e., one Ni/Cu atom of bulk Ni/Cu). For dual-atom catalyst model (dNiCu), $E_{formation}$ is derived from the following equation: $E_{formation} = E_{dNiCu} - E_{dNiCu-V} - \mu_{Ni} - \mu_{Cu}$, where E_{dNiCu} represents the energy of dNiCu model, and $E_{dNiCu-V}$ is the energy of nitrogen-doped carbon matrix without the incorporation of both Ni and Cu metal atoms. The d-band center was determined according to the following equation $\varepsilon_d = \frac{\int_{-\infty}^{\infty} n_d(\varepsilon)\varepsilon \, d\varepsilon}{\int_{-\infty}^{\infty} n_d(\varepsilon) \, d\varepsilon}$, where ε is the energy of electrons, and $n_d(\varepsilon)$ is the density of electron. The free energy of H$^+$ was derived as $G_{H+} = 1/2G_{H2} - k_B T \ln 10 \times pH$ (k_B is Boltzmann's constant)[S4]. The electron transfer was studied through Bader charge and charge density difference analyses.

1.2. Materials synthesis

Nickle (II) chloride hexahydrate (NiCl$_2$·6H$_2$O), copper (II) chloride dihydrate (CuCl$_2$·2H$_2$O), dicyandiamide, dimethyl sulfoxide-d$_6$ (DMSO, SKU-151874, 99.9 at.% D), deuterium oxide (D2O, SKU-293040, 99.9 at.% D, contains 0.75 wt.% 3-(trimethylsilyl)propionic-2,2,3,3-d$_4$

acid, sodium salt), glucose, copper (II) phthalocyanine (CuPc, $C_{32}H_{16}N_8Cu$), nickel (II) phthalocyanine (NiPc, $C_{32}H_{16}N_8Ni$), potassium bicarbonate ($KHCO_3$), phenol, hydrochloric acid (HCl, 37%), and nitric acid (HNO_3, 65%) were purchased from Sigma-Aldrich. Carbon paper and Nafion 117 membrane (Dupont) were purchased from the Fuel-cell store. Laser-grade CO_2 (99.995%) and ultra-high purity Argon (99.999%) were supplied by BOC gas, Australia. Ultrapure water (18.2 MΩ·cm, PURELAB Option Q) was used in all experiments. All chemicals were used in this work without further purification.

NiCu DACs sample was prepared using a modified method according to previous reports [S5, S6]. In detail, 2.0 g of dicyandiamide and 0.1 g of glucose were dissolved in deionized water, followed by the dropwise addition of an equivalent volume (0.5 mL) of freshly made $NiCl_2$ and $CuCl_2$ aqueous solution (0.01 M). After vigorous stirring, the solution was dried by rotary evaporation at 80°C. The as-obtained powder was ground and then transferred into lidded crucibles in a tube furnace under Argon atmosphere. The powder was annealed at 900°C for one hour with a heating rate of 3°C min^{-1}. Once cooled to room temperature, the product was washed with water and 1 M HCl and centrifuged at 10,000 rpm three times. The purified sample was dried in an oven under vacuum at 60°C overnight. Ni SACs and Cu SACs were prepared using a similar method but with the only addition of 1 mL of either 0.01 M $NiCl_2$ or 0.01 M $CuCl_2$ aqueous solution.

1.3. Materials characterization

The crystal structure of the samples was characterized by powder X-ray diffraction spectroscopy (Rigaku MiniFlex 600 X-ray Diffractometer). The morphology was characterized by the transmission electron microscope (TEM, FEI Tecnai G2 spirit TEM, 120 kV). HADDF-STEM imaging and EDX mapping were taken on the FEI Titan Themis 80-200 (200 kV voltage) equipped with a Super-X high-sensitivity windowless EDX detector for rapid compositional analysis. EELS spectra of Ni L-edge and Cu L-edge were collected with a probe current of ~110 pA, sampling with a dwell time of 5 s per pixel and a pixel size of ~6.3 nm. The metal loading amount was determined by an inductively-coupled plasma mass spectrometer (Agilent 8900x QQQ-ICP-MS, Agilent, USA). Raman spectra were collected using a Raman spectroscope (HORIBA LabRAM HR Evolution) configured with a 100 × objective lens (Olympus), 1800 l mm^{-1} grating, and a 532-nm Raman laser. In situ Diffuse Reflectance Infrared Fourier Transform Spectroscopy (DRIFTS) measurements on CO adsorption were performed using a Thermo Nicolet IS20 spectrometer. A Pike Technologies DRIFTS cell was used. Before each of the following IR experiments, the sample was pretreated in the DRIFTS cell in flowing Argon (20 mL min^{-1}) at room temperature for 20 minutes. In CO

adsorption experiments, the pretreated sample was purged with Argon at room temperature before switching to CO (5 mL min^{-1}) flow for 30 min. IR spectra were recorded continuously throughout these processes. All reported IR spectra are referenced to a background spectrum collected after pretreatment but prior to CO adsorption.

1.4. XAS characterization

All X-ray absorption spectra (XAS) were performed on Australia Synchrotron, Clayton, Victoria, Australia. The NEXAFS spectroscopy measurements for N, Ni, and Cu were performed with Drain Current detector. The XANES and EXAFS of the samples at Ni K-edge (8333 eV) and Cu K-edge (8979 eV) were collected from 1.9 T Wiggler XAS beamline using liquid nitrogen cooled Si (111) crystal at Hutch B experimental station (8−19 keV). Samples were mounted using standard sample holders and analyzed at room temperature. Ni Foil and Cu foil were used as references. All data of metal foils were obtained via transmission mode, while other samples were tested using fluorescence mode. The acquired EXAFS data were extracted and processed according to the standard procedures via the ATHENA and ARTEMIS modules implemented in the FEFIT software packages [S7]. The position of the absorption edge was determined from the first maximum of the first derivatives of $\mu(E)$. The k^3-weighted FT of $\chi(k)$ in R space was obtained over the range of 3 to 12.0 Å by applying a Hanning window function. Energy calibration was performed based on Ni and Cu metal foils. For EXAFS modelling, the amplitude reduction factor (S_0^2) was determined according to the EXAFS of the corresponding metal foil.

1.5. Electrochemical measurement

Electrochemical measurements were performed on a 760E electrochemical workstation (CH Instruments, USA) using a gas-tight H-cell with anode and cathode compartments separated by a proton exchange membrane (Nafion 117). An Ag/AgCl electrode (3.0 M KCl) and RuO$_2$-coated titanium mesh electrode were used as the reference and counter electrode, respectively. All electrochemical measurements were conducted in CO$_2$-saturated (pH = 6.8) or Ar-saturated (pH = 8.3) 0.1 M KHCO$_3$ electrolyte. The amperometry i-t technique was utilized to evaluate electrocatalytic performance for CO$_2$ reduction. Electrolysis was carried out at potentials between −0.32 V and −1.27 V vs RHE for 1-hour testing. The tested potential (vs Ag/AgCl) was converted to that vs RHE as follows: $E_{RHE} = E_{Ag/AgCl} + 0.224 + 0.059 \times pH$. For electrochemical kinetic analysis, Tafel slopes were derived from the Tafel equation: $\eta = b \lg (j_{CO})$, where η is the overpotential (V) between the applied potential to the standard CO$_2$-to-CO

reduction potential (−0.11 V vs RHE), b is the Tafel slope (mV dec^{-1}), and j$_{co}$ is the partial current density for CO (mA cm^{-2}).

1.6. Qualification of CO and H$_2$

The CRR products were determined using similar procedures as previous works [S8]. Briefly, the headspace gas in the cathode compartment was automatically injected into Agilent 8890 gas chromatography (GC) configured with a thermal conductivity detector (TCD) and methanizer/flame ionization detector (FID). The liquid products were determined using a nuclear magnetic resonance (NMR, Agilent 500/600 MHz ^{1}H NMR) and quantified with internal standards (DMSO and phenol in D$_2$O). No notable liquid products were found.

1.7. Determination of products and calculation of Faradaic efficiency (FE) [S9, S10]

Briefly, 100 μL of headspace gas in the cathode compartment was automatically injected into a gas chromatograph (GC, Agilent 8890B configured with a thermal conductivity detector and methanizer/flame ionization detector) for gas product quantification. The FE for the gaseous product was calculated as the following Equation:

$$\text{FE}_{\text{gas}} = \frac{Q_{gas}}{Q_{total}} \times 100\% = \frac{\left(\frac{v}{60\ s/min}\right) \times \left(\frac{x}{Vm}\right) \times N \times F}{I} \times 100\%$$

where v = 10 mL min^{-1} is the volume flow rate of CO$_2$; x is the measured concentration of gas product in sample loop referring to standard curve (part per million, ppm); V_m is the gaseous molar volume (24000 mL mol^{-1} at 25°C, 101 kPa). N is the number of transferred electrons for one molecule product (here is 2); F is the Faradaic constant, 96485 C mol^{-1}; and I is the recorded current (A).

1.8. Calculation of Turnover Frequency (TOF, h^{-1}) [S9, S10]

The TOF for CO was calculated as the following Equation:

$$\text{TOF}\ (h^{-1}) = \frac{\frac{I_{CO}}{N \times F}}{m_{cat} \times \frac{\omega}{M_{metal}}} \times 3600$$

where I_{CO} is the partial current (A) of CO formation; N is the number of transferred electrons for one molecule product (here is 2); F is the Faradaic constant, 96485 C mol^{-1}; m_{cat} is the catalyst mass (g) on the electrode; ω is the mass fraction (wt.%) of metal obtained from the ICP-MS analysis; M_{metal} is the atomic mass of Ni (58.6 g mol^{-1}) or Cu (63.5 g mol^{-1}).

1.9. Programming for random distribution simulation

Program codes were established and run on the environment of the Python 3.10 version. To

simply visualize the distribution of DACs on the N-doped graphene, spheres in different colours were selected to represent Ni and Cu atoms. The random number function, together with one 'while' loop, was employed for the generation of spheres on a 20 nm × 20 nm grid. We defined the total number of spheres as N, and two kinds of spheres were generated in equal numbers but in different colours (O for the orange spheres while B for blue spheres; O equals B). The 'while' loop will terminate when $N = O + B$. The radius of every sphere was defined as 0.15 nm, while the distance between spheres was set to larger than 0.20 nm. In each iteration, two random numbers (x and y) were generated, representing the coordinate of the randomly generated position. By changing the input value of N from 100 to 1200, the random distribution of different surface density of spheres on a 20 nm × 20 nm grid was obtained. Later on, the Euclidean distance between a given orange sphere and its nearest blue one was counted, and the corresponding distance histograms were plotted after counting all inter-sphere distances. For a more statistically average result, 12 stochastic simulations were conducted following the aforementioned procedures.

1.10. Programming boundary condition setting

To obtain chemically meaningful results from the simulation, reasonable boundary conditions were considered during the random distribution simulation: (1) the radius of the sphere was set to 0.15 nm; (2) the distance between any two spheres must be greater than 0.2 nm; and (3) all spheres need to be randomly distributed on a 20 nm × 20 nm grid. These limitations were proposed due to the following factors: (1) the atomic radius of Ni atoms and Cu atoms is calculated as 0.135 nm [S11] and (2) the inter-metal distance observed in the reported DACs is generally larger than 0.2 nm. In each iteration, two random numbers (x and y) were generated. (x, y) stood for the coordinate of the randomly generated position. If the distance between this position and every other occupied position was larger than 0.2 nm, one sphere will be placed on this (x, y) position. At odd iterations, orange spheres were placed onto the grid according to this algorithm. At even iterations, blue spheres were placed on the grid.

1.11. Mathematical model and derivation

The aforementioned Monte Carlo experiment can be mathematically formalized as follows. Symbols shown in this part are just for mathematical discussions and not associated with those shown in the Main Text.

Setup: Let n be a positive integer. Let $X_1, \ldots, X_n$ and $Y_1, \ldots, Y_n$ be random points that are uniformly sampled in a unit square. Given two points X and Y, we denote by $\| X - Y \|$ the Euclidean distance between X and Y. For each X_i with $1 \leq i \leq n$, we compute $\min_{1 \leq j \leq n} \| X_i - Y_j \|$.

To investigate the distribution of $\min_{1 \leq j \leq n} \| X_i - Y_j \|$, it suffices to calculate the probability density function of $\min_{1 \leq j \leq n} \| X - Y_j \|$ for X and $Y_1, \ldots, Y_n$ random uniform points in a unit square. Notice that

$$0 \leq \min_{1 \leq j \leq n} \| X - Y_j \| \leq \sqrt{2}.$$

First, we know from Theorem 1 [S12] that for two random uniform points X and Y in a unit square, the density of their squared distance $\| X - Y \|^2$ is given by $h(z) = 0$ for $z < 0$ and $z > 2$, and for $0 \leq z \leq 2$,

$$h(z) = g\,(\min\,(z, 1), z, 1, 1) - g\,(\max\,(z - 1, 0), z, 1, 1)$$

where $g(x, z, r, s)$ is Equation 2 (S6) (corrected):

$$g(x,z,r,s) = \int \left(1 - \frac{r}{\sqrt{z-x}} \right)\left(1 - \frac{s}{\sqrt{x}} \right) dx$$

$$= x + 2r\sqrt{z-x} - 2s\sqrt{x} + rs \arcsin(2xz^{-1} - 1).$$

Therefore,

$$h(z) = \begin{cases} \pi - 4\sqrt{z} + z, & (0 \leq z \leq 1), \\ -2 + 4\sqrt{z-1} - z + 2\arcsin(2z^{-1} - 1), & (1 < z \leq 2). \end{cases}$$

We then compute that the probability of $\| X - Y \| \leq t$ is

$$\mathbf{Pr}(\| X - Y \| \leq t)$$

$$= \mathbf{Pr}(\| X - Y \|^2 \leq t^2) = \int_0^{t^2} h(z)\,dz$$

$$= \begin{cases} \pi t^2 - \frac{8}{3}t^3 + \frac{1}{2}t^4, & (0 \leq t \leq 1), \\ \frac{1}{3} + \frac{4}{3}\sqrt{t^2 - 1} + \frac{8}{3}t^2\sqrt{t^2 - 1} \\ \quad - 2t^2 - \frac{1}{2}t^4 - 2t^2\arcsin(1 - 2t^{-2}), & (1 < t \leq \sqrt{2}). \end{cases}$$

Also, $\mathbf{Pr}(\| X - Y \| \leq t)$ equals 0 if $t < 0$ and equals 1 if $t > \sqrt{2}$. It follows that the probability of $\min_{1 \leq j \leq n} \| X - Y_j \| \leq t$ is

$$\mathbf{Pr}(\min_{1 \leq j \leq n} \| X - Y_j \| \leq t)$$

$$= 1 - \mathbf{Pr}(\| X - Y \| > t)^n$$

$$= 1 - \big(1 - \mathbf{Pr}(\| X - Y \| \leq t)\big)^n$$

$$= \begin{cases} 1 - \big(1 - \pi t^2 + \frac{8}{3}t^3 - \frac{1}{2}t^4\big)^n, & (0 \leq t \leq 1), \\ 1 - \big(\frac{2}{3} - \frac{4}{3}\sqrt{t^2 - 1} - \frac{8}{3}t^2\sqrt{t^2 - 1} \\ \quad + 2t^2 + \frac{1}{2}t^4 + 2t^2\arcsin(1 - 2t^{-2})\big)^n, & (1 < t \leq \sqrt{2}). \end{cases}$$

We again have that $\mathbf{Pr}(\min_{1 \leq j \leq n} \| X - Y_j \| \leq t)$ equals 0 if $t < 0$ and equals 1 if $t > \sqrt{2}$.

Let $f_n(z)$ be the probability density function of $\min_{1 \leq j \leq n} \| X - Y_j \|$. Then it is $\frac{d}{dz} \mathbf{Pr}(\min_{1 \leq j \leq n} \| X - Y_j \| \leq z)$. That is, $f_n(z) = 0$ for $z < 0$ and $z > \sqrt{2}$, and for $0 \leq z \leq \sqrt{2}$,

$$
f_n(z) = \begin{cases}
n\left(2\pi z - 8z^2 + 2z^3\right)\left(1 - \pi z^2 + \frac{8}{3}z^3 - \frac{1}{2}z^4\right)^{n-1}, & (0 \leq z \leq 1), \\[2mm]
n\Big(\dfrac{-8z + 8z^3}{\sqrt{z^2 - 1}} - 4z - 2z^3 - 4z \arcsin(1 - 2z^{-2})\Big) \\[2mm]
\quad \times \Big(\frac{2}{3} - \frac{4}{3}\sqrt{z^2 - 1} - \frac{8}{3}z^2\sqrt{z^2 - 1} + 2z^2 + \frac{1}{2}z^4 \\[2mm]
\quad + 2z^2 \arcsin(1 - 2z^{-2})\Big)^{n-1}, & (1 < z \leq \sqrt{2}).
\end{cases}
$$

Further, if $f_n(z)$ reaches its *peak* at $z = d(n)$, then $d(n)$ is the solution to $f_n'(z) = 0$ with $0 \leq z \leq 1$, or equivalently,

$$
(n-1)\left(2\pi z - 8z^2 + 2z^3\right)^2 - \left(2\pi - 16z + 6z^2\right)\left(1 - \pi z^2 + \frac{8}{3}z^3 - \frac{1}{2}z^4\right) = 0.
$$

Thus, as $n \to \infty$,

$$
d(n) \sim \frac{1}{\sqrt{2\pi n}}.
$$

Yet another important problem is about the expected value $D(n)$ of $\min_{1 \leq j \leq n} \| X_i - Y_j \|$ with $1 \leq i \leq n$. We have

$$
D(n) = \mathbf{E}\left[\frac{1}{n}\sum_{i=1}^{n} \min_{1 \leq j \leq n} \| X_i - Y_j \|\right] = \frac{1}{n}\sum_{i=1}^{n} \mathbf{E}\left[\min_{1 \leq j \leq n} \| X_i - Y_j \|\right]
$$

$$
= \mathbf{E}\left[\min_{1 \leq j \leq n} \| X - Y_j \|\right] = \int_0^{\sqrt{2}} \mathbf{Pr}(\min_{1 \leq j \leq n} \| X - Y_j \| > t)\, dt
$$

$$
= \int_0^1 S_1(t)\, dt + \int_1^{\sqrt{2}} S_2(t)\, dt,
$$

where

$$
S_1(t) = \left(1 - \pi t^2 + \frac{8}{3}t^3 - \frac{1}{2}t^4\right)^n,
$$

$$
S_2(t) = \left(\frac{2}{3} - \frac{4}{3}\sqrt{t^2 - 1} - \frac{8}{3}t^2\sqrt{t^2 - 1} + 2t^2 + \frac{1}{2}t^4 + 2t^2 \arcsin(1 - 2t^{-2})\right)^n.
$$

We also introduce

$$
S_0(t) = \left(1 - \pi t^2\right)^n,
$$

and rewrite $D(n)$ as

$$
D(n) = \int_0^{1/\sqrt{\pi}} S_0(t)\, dt - \int_{n^{-5/12}}^{1/\sqrt{\pi}} S_0(t)\, dt + \int_0^{n^{-5/12}} \left(S_1(t) - S_0(t)\right) dt
$$

$$
+ \int_{n^{-5/12}}^1 S_1(t)\, dt + \int_1^{\sqrt{2}} S_2(t)\, dt.
$$

Now, we approximate each integral as $n \to \infty$. First,

$$\int_0^{1/\sqrt{\pi}} S_0(t)dt = \frac{\Gamma(n+1)}{2\Gamma(n+\frac{3}{2})} \sim \frac{1}{2\sqrt{n}},$$

where the Gamma function has the asymptotic approximation $\Gamma(x+\alpha) \sim \Gamma(x)x^\alpha$ for $\alpha \in \mathbf{C}$ as $x \to +\infty$. Next, noticing that $S_0(t)$ is a decreasing function on $[0, 1/\sqrt{\pi}]$ with $0 \le S_0(t) \le 1$, we have

$$\left| \int_{n^{-5/12}}^{1/\sqrt{\pi}} S_0(t)dt \right| < \frac{1}{\sqrt{\pi}} S_0(n^{-5/12}) = o\left(\frac{1}{n^{1/2}}\right),$$

since $S_0(n^{-5/12})$ decays exponentially to zero as $n \to \infty$. For the third integral, we use the trivial identity $a^n - b^n = (a-b)(a^{n-1} + a^{n-2}b + \cdots + ab^{n-2} + b^{n-1})$, and deduce that for $0 \le a, b \le 1$, the inequality $|a^n - b^n| \le n|a-b|$ holds true. Thus,

$$\left| \int_0^{n^{-5/12}} (S_1(t) - S_0(t))dt \right| \le \int_0^{n^{-5/12}} |S_1(t) - S_0(t)| \, dt$$

$$\le n \int_0^{n^{-5/12}} \left(\frac{8}{3}t^3 - \frac{1}{2}t^4\right) dt = o\left(\frac{1}{n^{1/2}}\right).$$

For the fourth integral, noticing that $S_1(t)$ is decreasing on $[0, 1]$ with $0 \le S_1(t) \le 1$, we have

$$\left| \int_{n^{-5/12}}^{1} S_1(t)dt \right| < S_1(n^{-5/12}) = o\left(\frac{1}{n^{1/2}}\right),$$

since $S_1(n^{-5/12})$ decays exponentially to zero as $n \to \infty$. Finally, since $S_2(t)$ is decreasing on $[1, \sqrt{2}]$ with $0 \le S_2(t) < 1$ and $S_2(1)$ decays exponentially to zero as $n \to \infty$, we have

$$\left| \int_1^{\sqrt{2}} S_2(t)dt \right| < (\sqrt{2}-1)S_2(1) = o\left(\frac{1}{n^{1/2}}\right).$$

The above argument then leads us to the approximation as $n \to \infty$,

$$D(n) \sim \frac{1}{2\sqrt{n}}.$$

2. Supplementary Figures
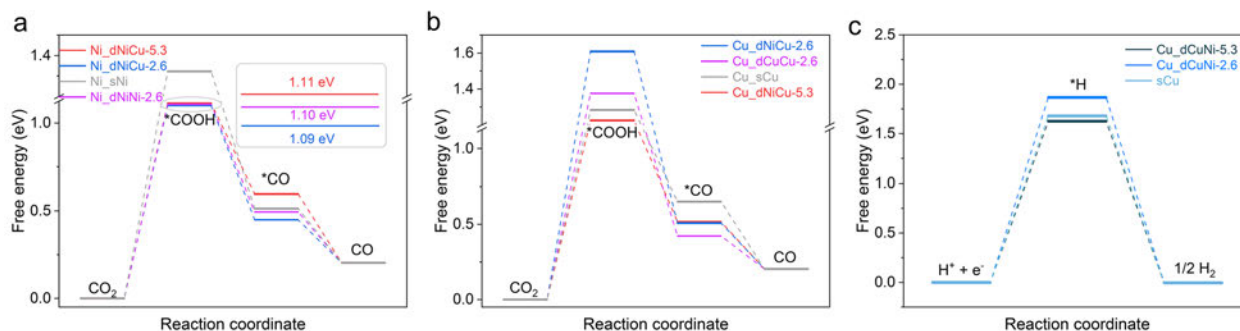
Figure S1. Free energy diagrams of CO_2 electroreduction to CO on (a) Ni sites and (b) Cu sites for dNiCu-5.3, dNiCu-2.6, dimer atom models (i.e., dNiNi-2.6 and dCuCu-2.6) and sNi/sCu models (U = 0 eV; pH = 6.8), and Free energy diagrams of (c) HER on the Cu sites of dNiCu-5.3, dNiCu-2.6 and sCu models.
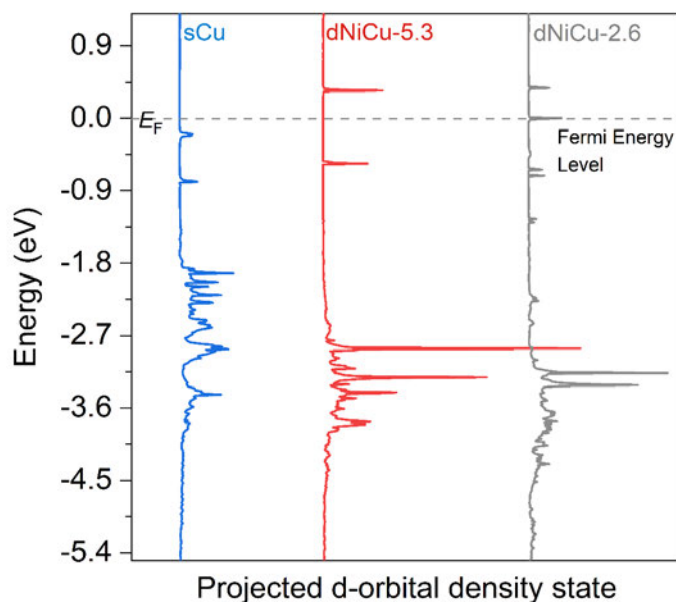
Figure S2. Computed pDOS of the Cu d-orbital for dNiCu-5.3, dNiCu-2.6 and sCu models.
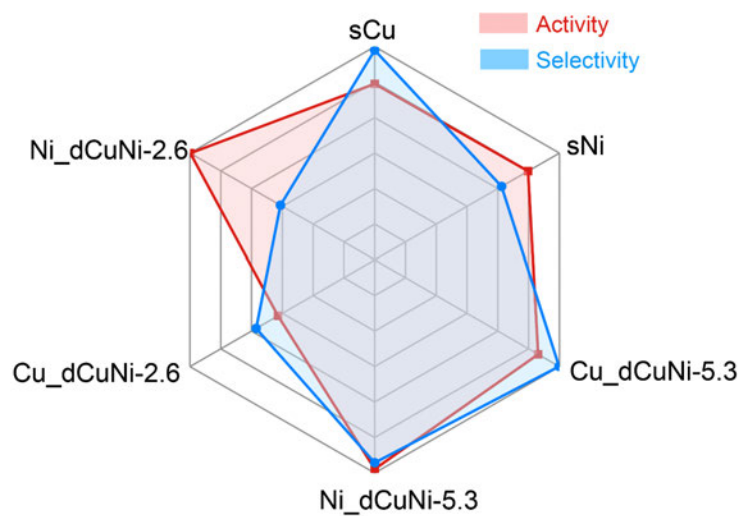
Figure S3. Radar chart summarizing CRR activity and selectivity of different SACs and DACs.
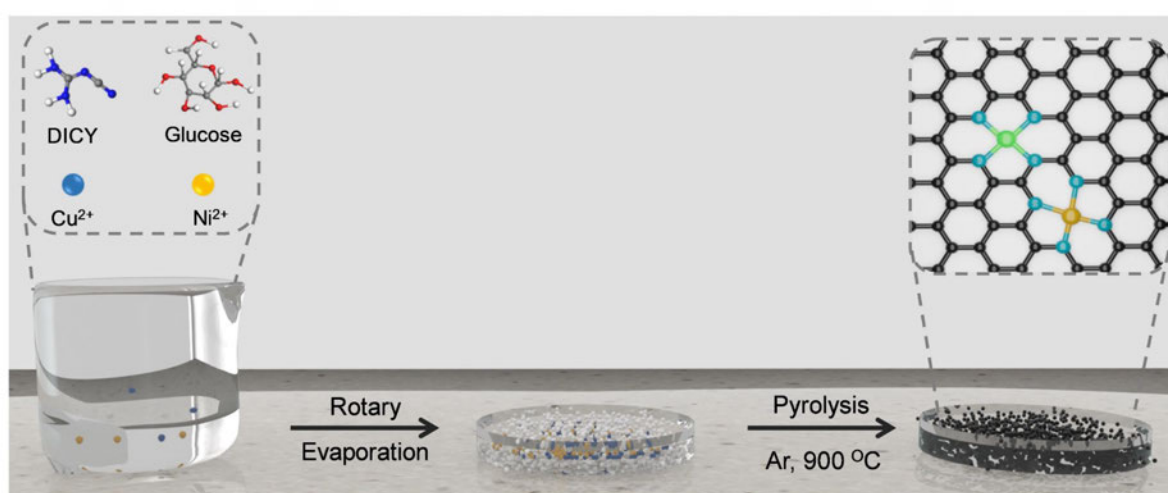
Figure S4. Schematic of the fabrication procedure for NiCu-NC DACs. DICY is dicyandiamide.
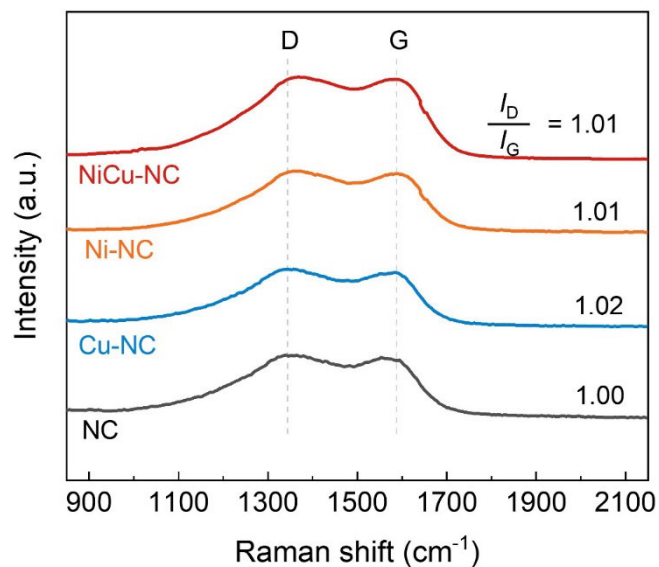
Figure S5. Raman spectra of the as-obtained NiCu-NC, Ni-NC, Cu-NC and NC. The dashed lines are assigned to D and G bands at ~1350 cm^{-1} and ~1580 cm^{-1}, respectively.
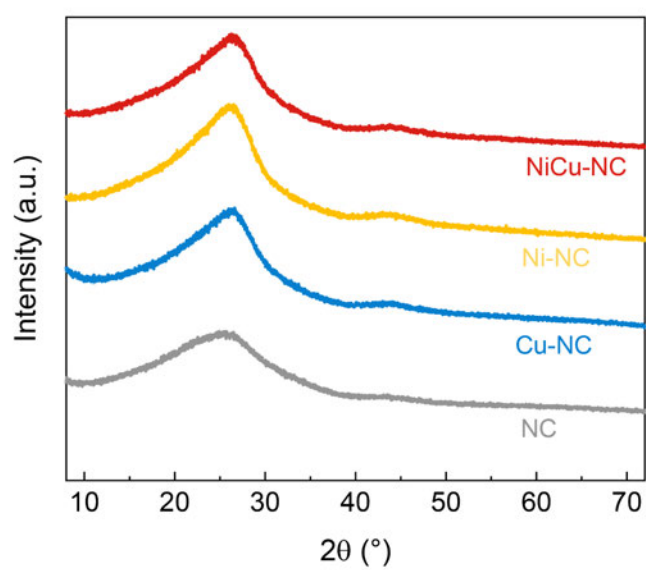
Figure S6. Powder XRD patterns of the as-obtained NiCu-NC, Ni-NC, Cu-NC and NC.
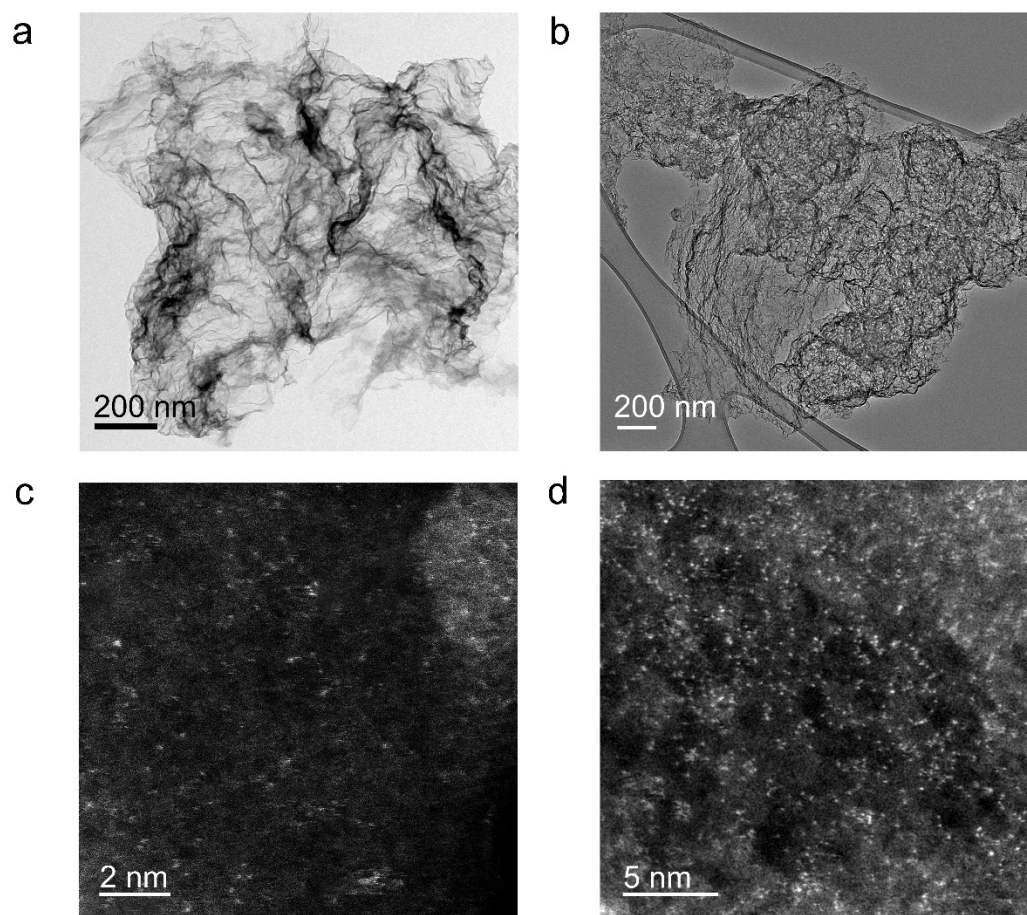
Figure S7. High-resolution TEM images of the as-obtained (a) Ni-NC and (b) Cu-NC. HAADF-STEM images of (c) Ni-NC and (d) Cu-NC.
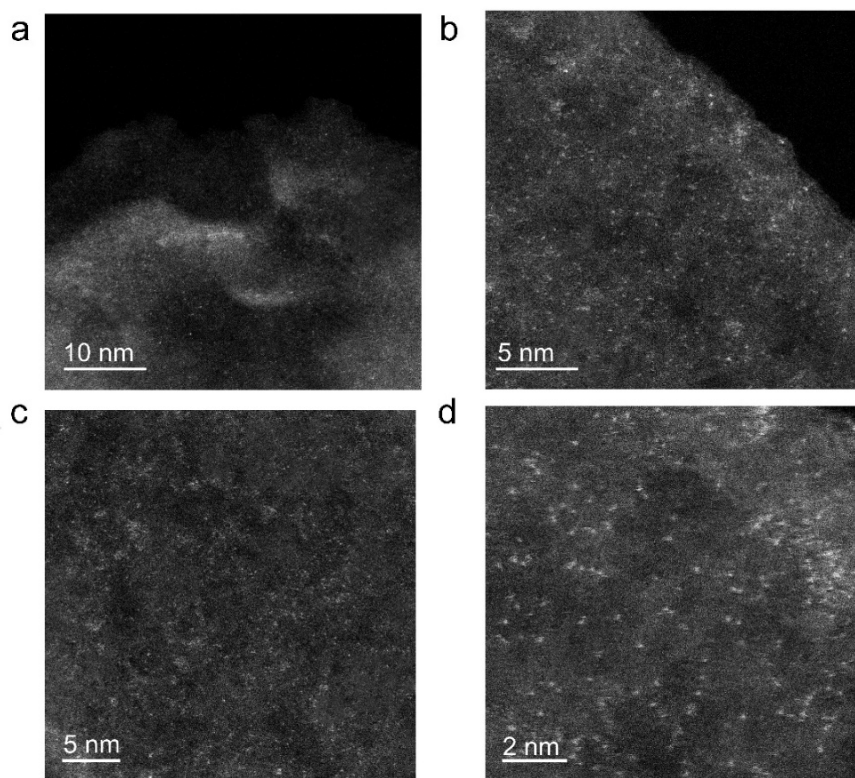
Figure S8. HAADF-STEM images of the as-obtained NiCu-NC in different magnification.
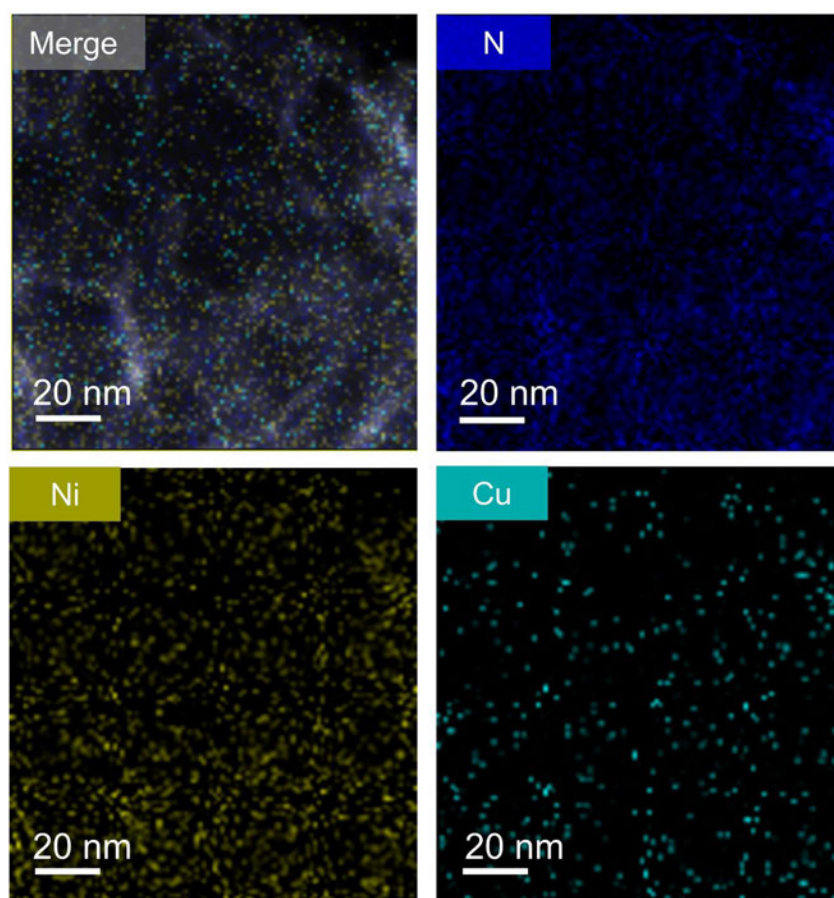
Figure S9. EDX Elemental mapping of the NiCu-NC.
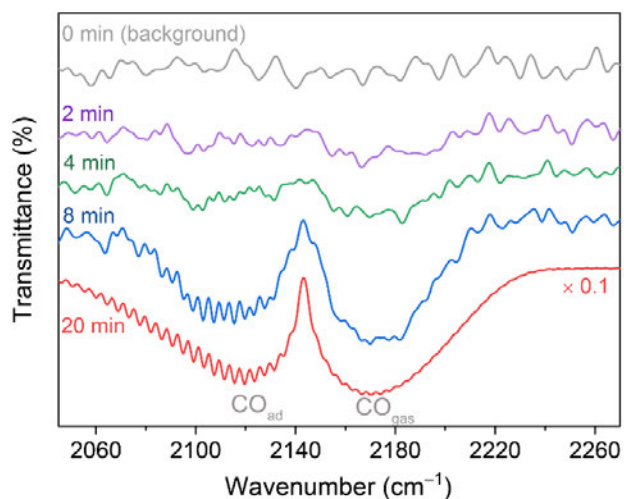
Figure S10. Time-dependent in situ DRIFT responses for CO adsorption on the NiCu-NC.
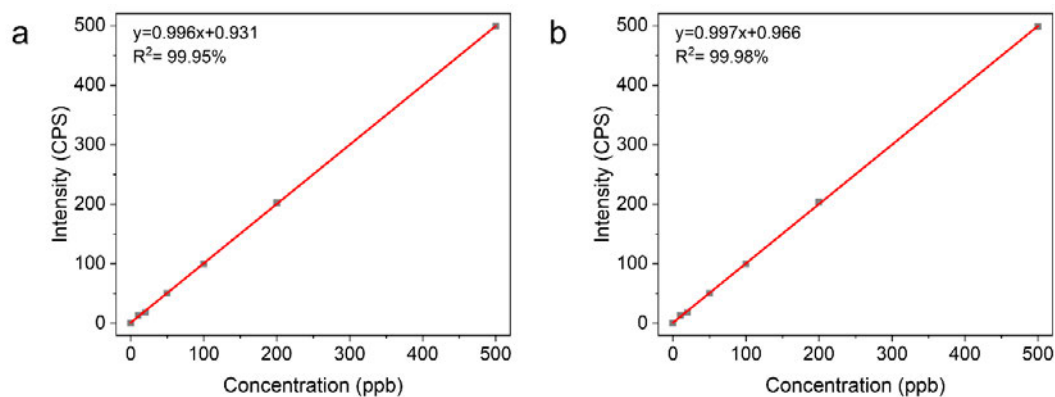
Figure S11. ICP-MS determination of (a) Ni and (b) Cu contents by using the standard Ni and Cu calibration solutions, ranging from 0 ppb to 500 ppb.
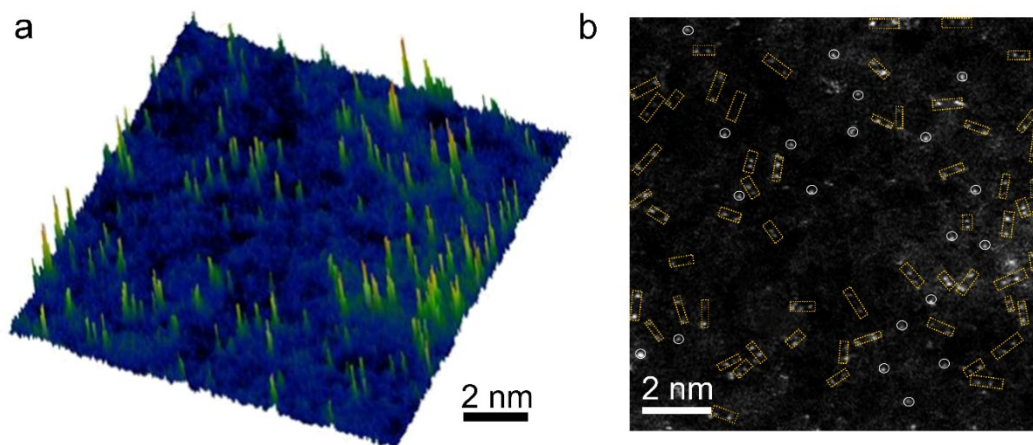
Figure S12. The analysis of the inter-metal distance in NiCu-NC DACs based on the (a) 3D transformed image from the marked area in Figure 2c and (b) the counting method and result for the atomic arrangement. Yellow squares stand for the dual-atom pairs (DACs), while white circles represent the isolated single atom (SACs). The percentage of dual-atom pairs over isolated single-atom is listed in Figure 2e.
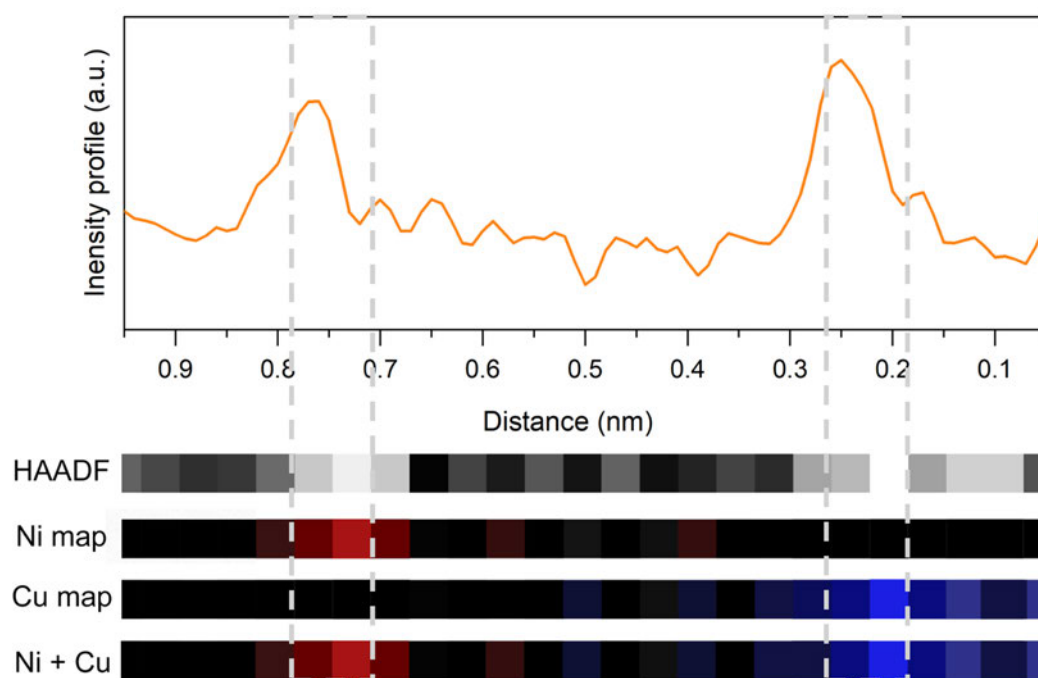
Figure S13. The line analysis of the intensity profile in the acquired HAADF-STEM image (Figure 2f), accompanied by atomic-resolution EELS mapping of the Ni/Cu pair.
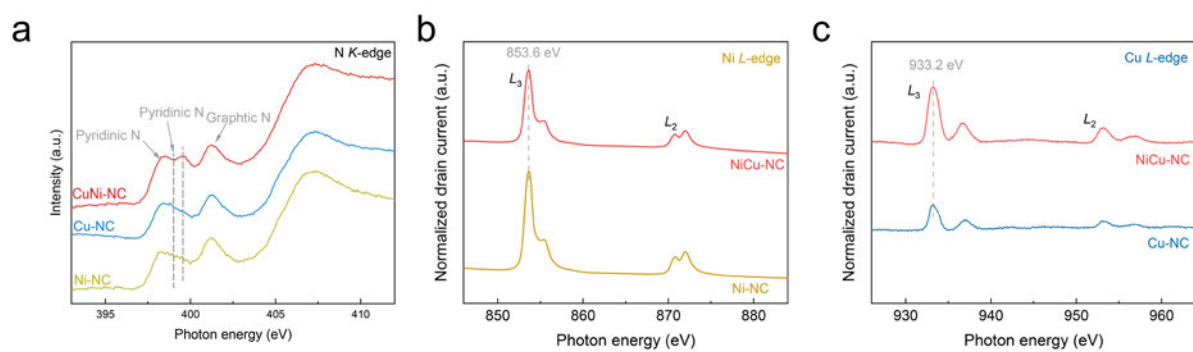
Figure S14. NEXAFS of (a) N *K*-edge, (b) Ni *L*-edge and (c) Cu *L*-edge for NiCu-NC, Ni-NC and Cu-NC respectively.
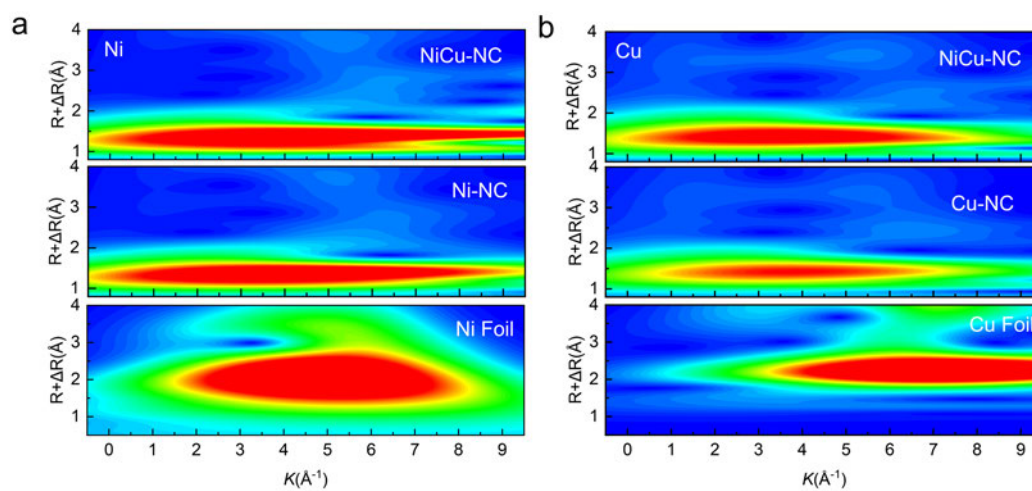
Figure S15. WT-EXAFS spectra of (a) Ni *K*-edge and (b) Cu *K*-edge for NiCu-NC, Ni/Cu-NC, and Ni/Cu metal foil reference respectively.
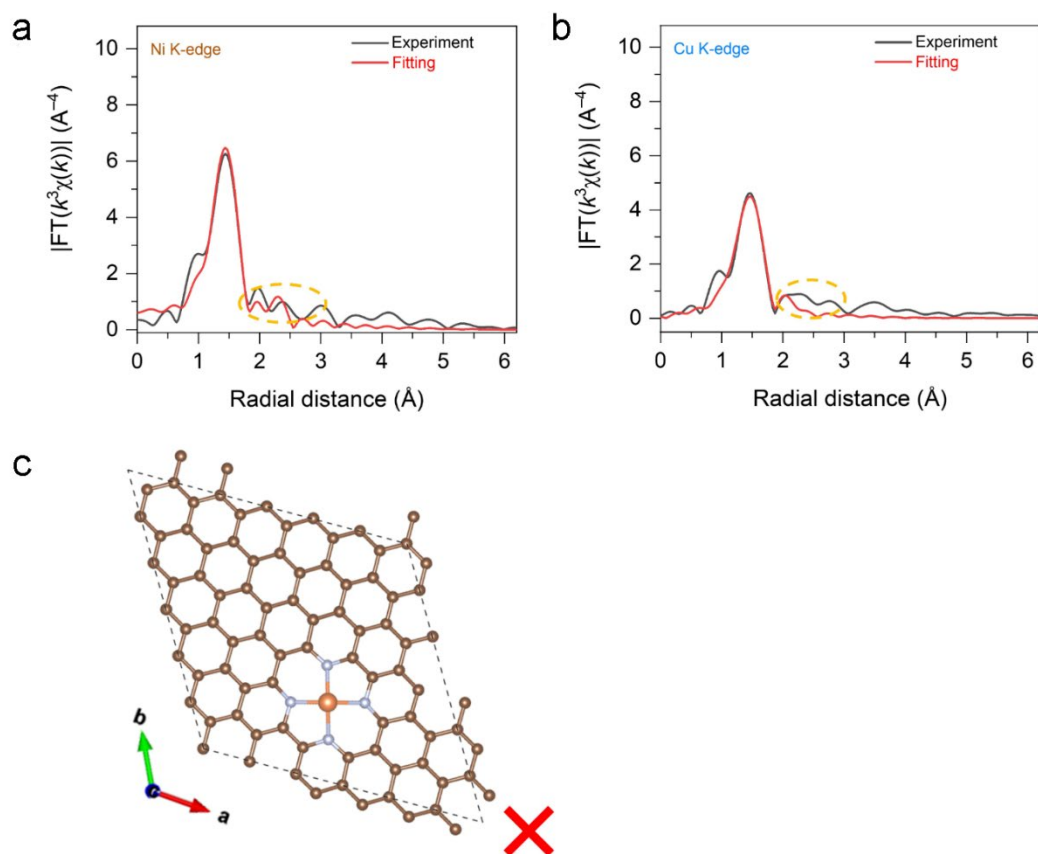
Figure S16. The *R*-space EXAFS-fitting curves of the as-obtained NiCu-NC sample at (a) Ni *K*-edge and (b) Cu *K*-edge by using (c) the sNi/sCu model for curve fitting.The brown, grey, orange balls represent C, N, and Ni/Cu atoms, respectively.
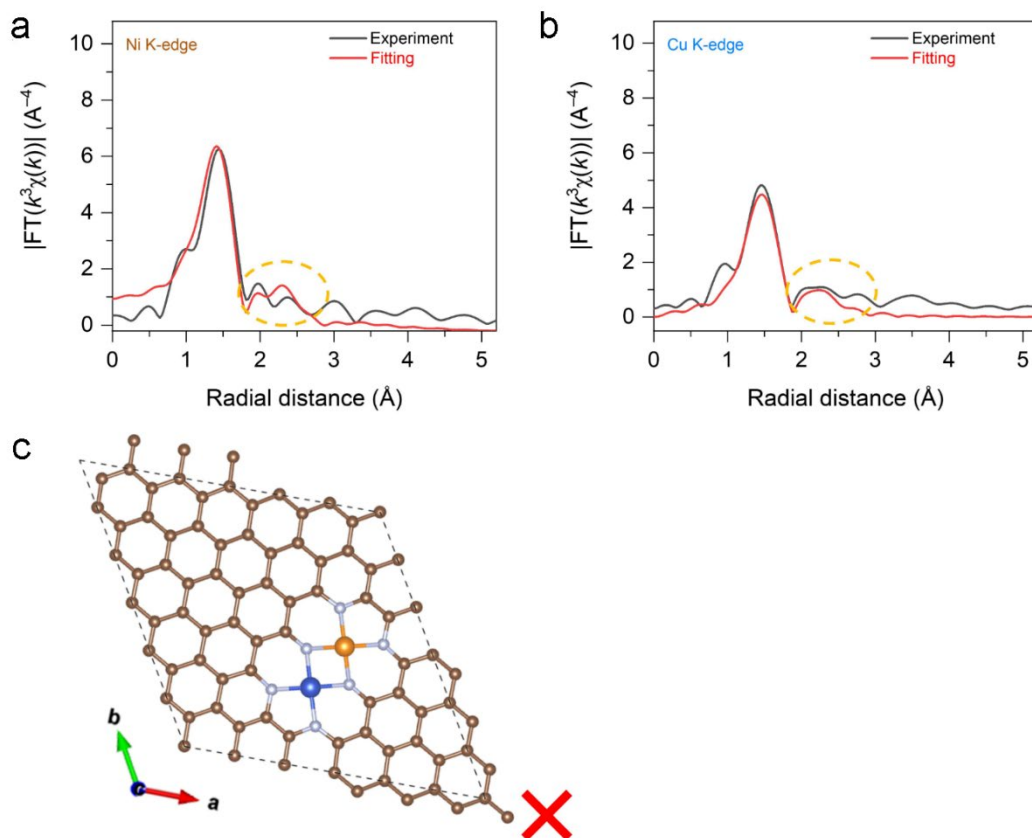
Figure S17. The *R*-space EXAFS-fitting curves of the as-obtained NiCu-NC sample at (A) Ni *K*-edge and (b) Cu *K*-edge by using (c) the dNiCu-2.6 model for curve fitting. The brown, grey, orange balls represent C, N, and Ni/Cu atoms, respectively.
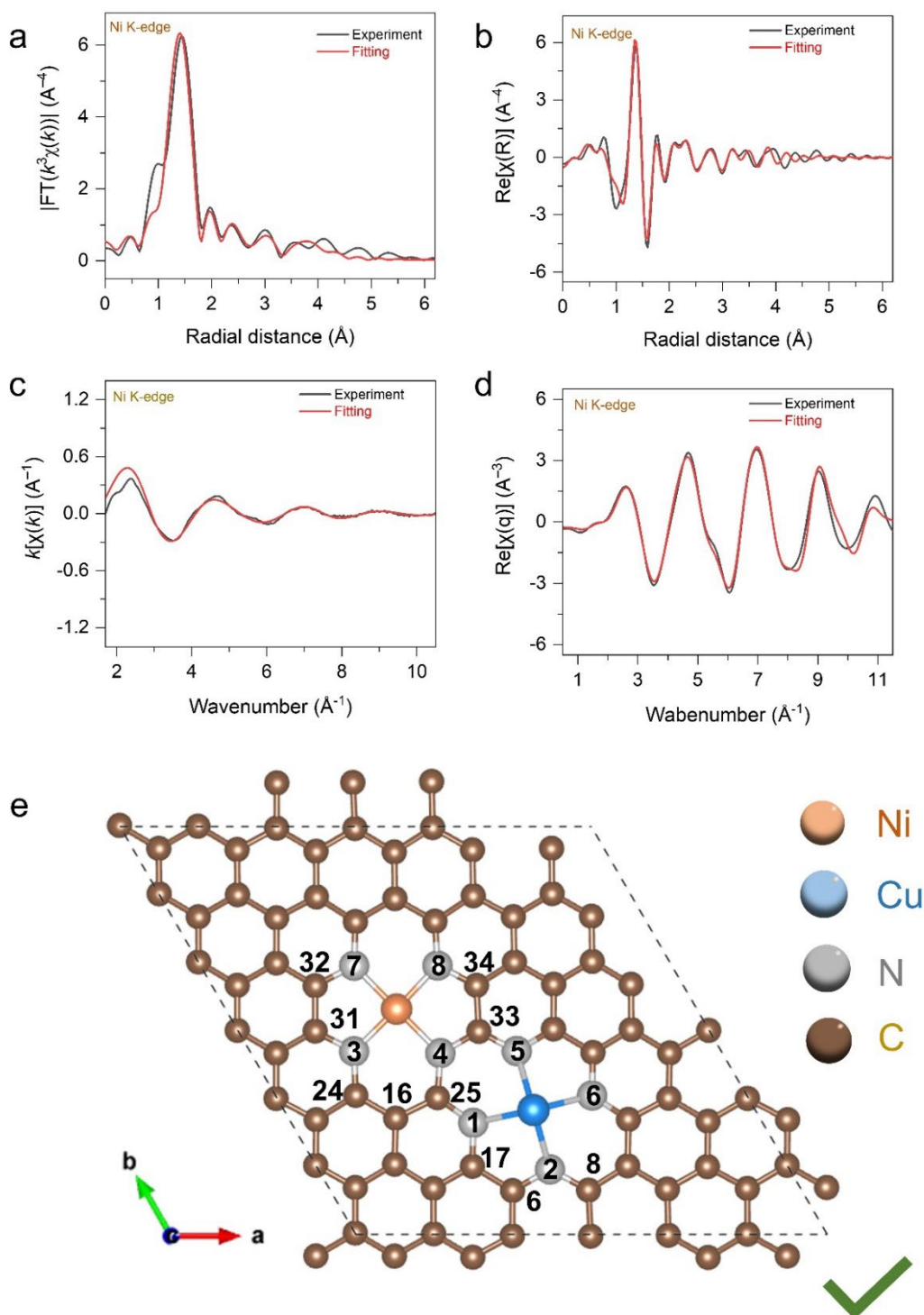
Figure S18. The EXAFS-fitting for the NiCu-NC sample at Ni *K*-edge. (a) The magnitude and (b) real component of FT-EXAFS spectra in *R*-space. (c) *k*-space plot and (d) the real component in *q*-space. (e) The most likely structural model (dNiCu-5.3) used for fitting. The brown, grey, orange and blue balls represent C, N, Ni and Cu atoms, respectively.
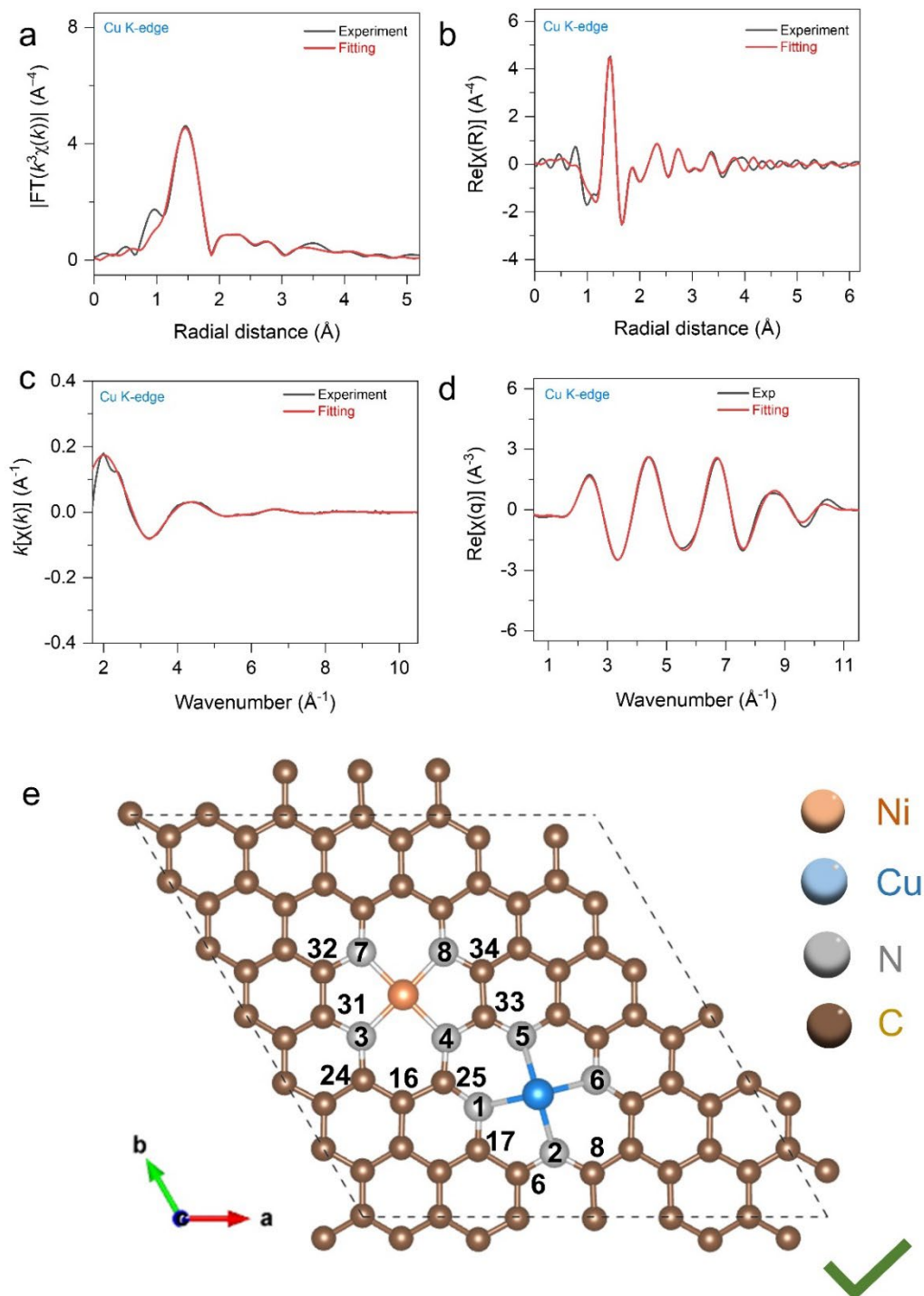
Figure S19. The EXAFS-fitting for the NiCu-NC sample at Cu *K*-edge. (a) The magnitude and (b) real component of FT-EXAFS spectra in *R*-space. (c) *k*-space plot and (d) the real component in *q*-space. (e) The most likely structural model (dNiCu-5.3) used for fitting. The brown, grey, orange and blue balls represent C, N, Ni and Cu atoms, respectively.
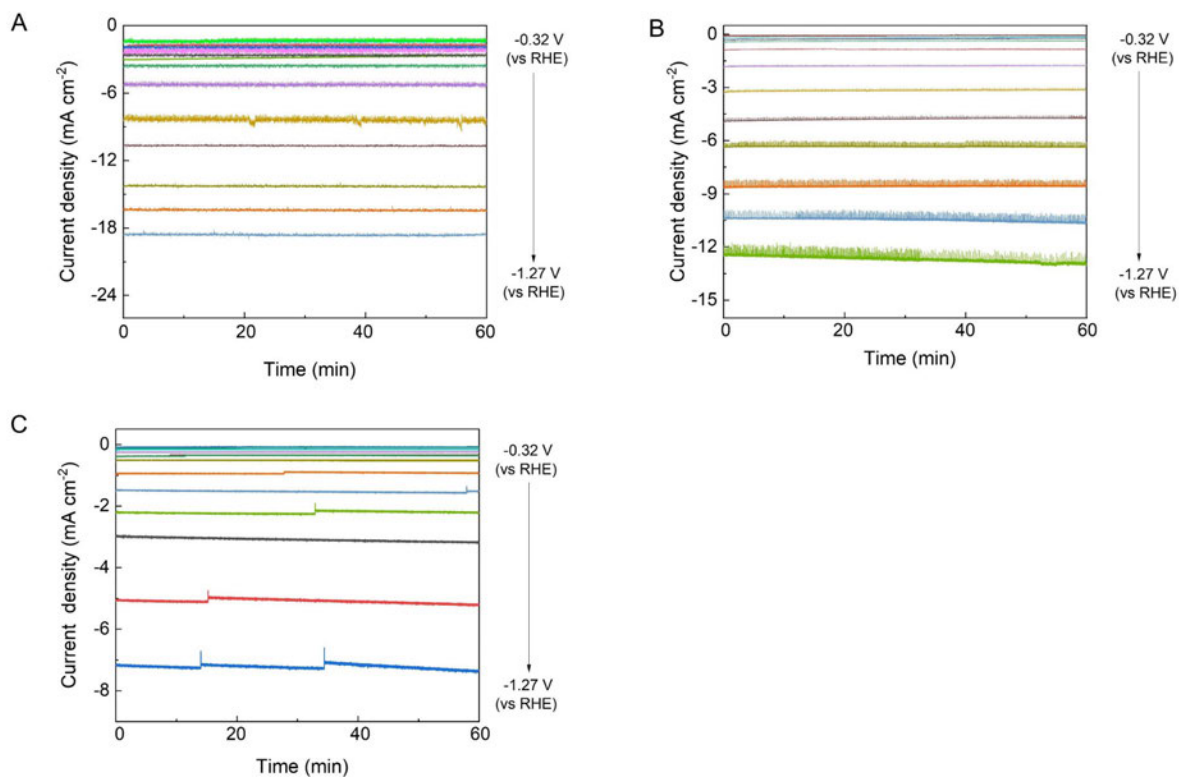
Figure S20. Chronoamperometry responses tested in the H-cell for (a) NiCu-NC, (b) Ni-NC and (c) Cu-NC, at different potentials in CO$_2$-saturated 0.1 M KHCO$_3$.
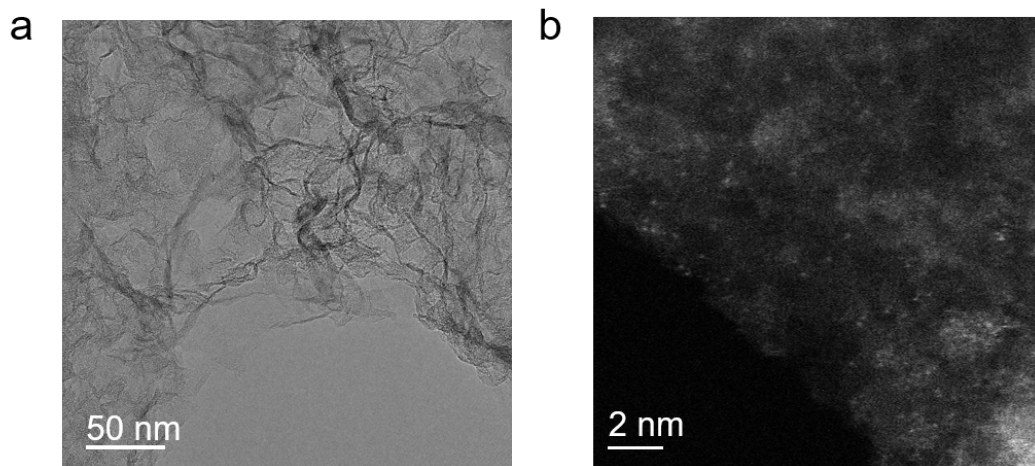
Figure S21. Post-catalysis (a) high-resolution TEM image and (b) HAADF-STEM image characterization of NiCu-NC DACs after CRR.
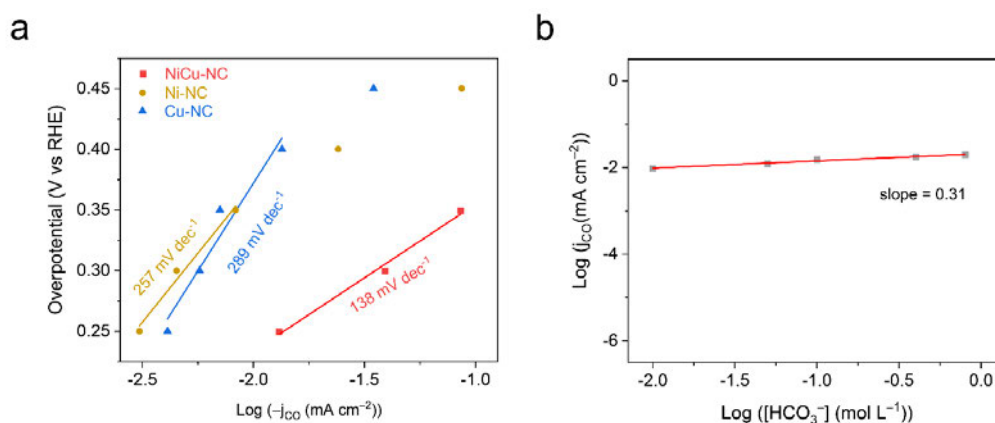
Figure S22. Kinetics studies of CO₂-to-CO. (a) Tafel slopes for CO evolution on NiCu-NC, Ni-NC and Cu-NC, and (b) Rate dependencies on [HCO₃⁻] for NiCu-NC.
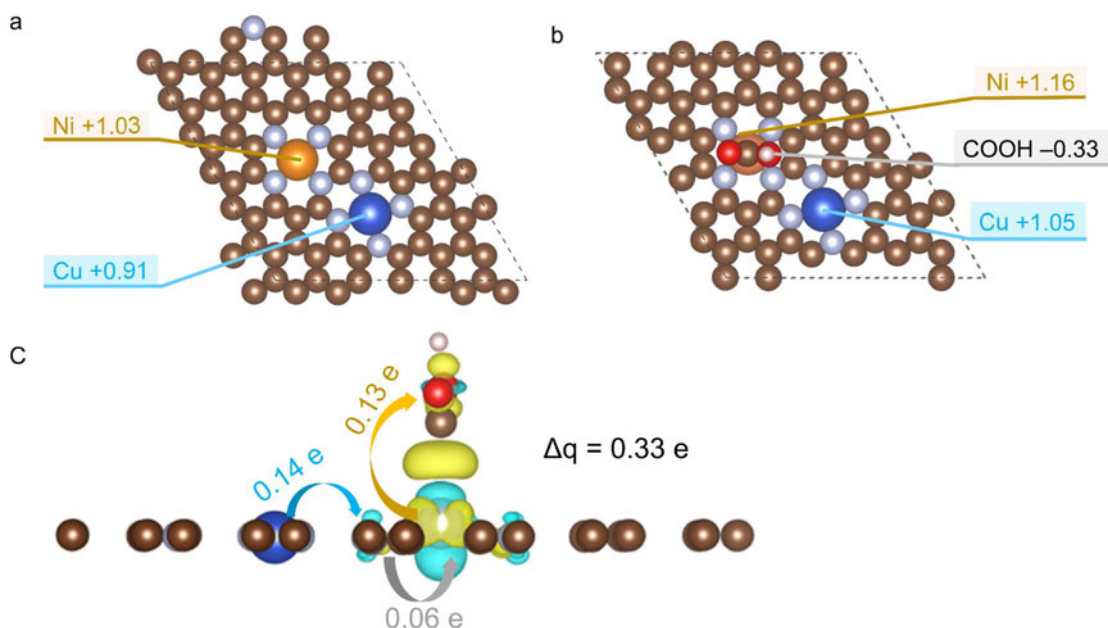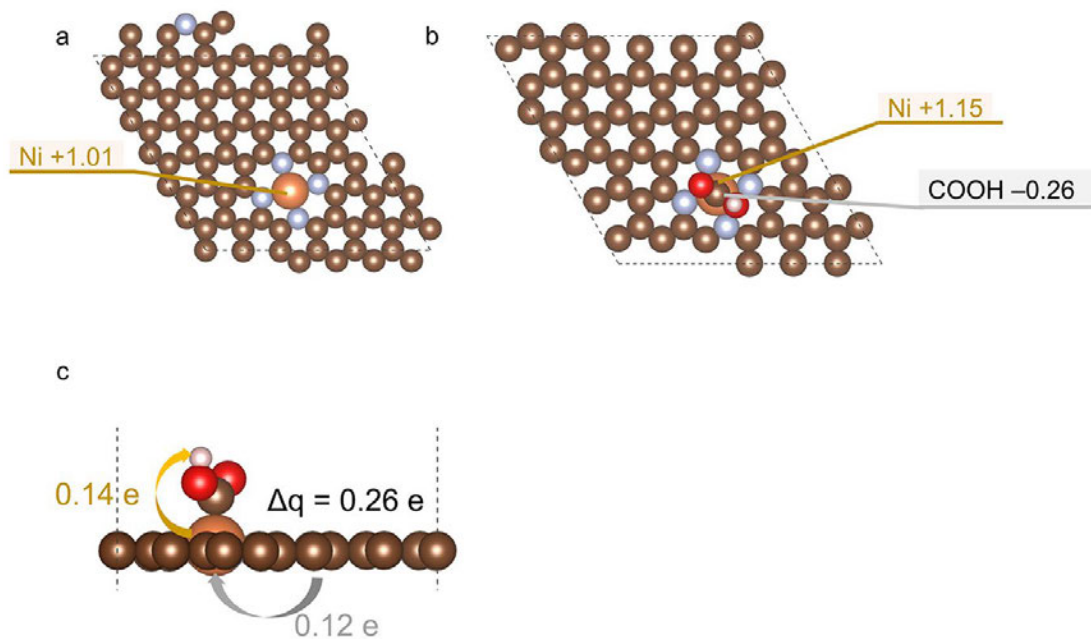

Figure S23. Bader charge analysis for dNiCu-5.3 model on the Ni site at top-view (a) without *COOH adsorption and (b) with *COOH adsorption. (c) Electron charge difference for dNiCu-5.3 model with *COOH adsorption on the Ni site. Positive and negative values in this Figure represent the electron depletion and accumulation respectively. Cyan regions show electron depletion, and yellow regions show electron accumulation. The isosurface value is 0.004 e⁻ Å⁻³. Brown, grey, orange and blue spheres represent C, N, Ni and Cu atoms, respectively. Charge difference (ρ_{diff}) is calculated according to the following equation: $\rho_{diff} = \rho_{total} - \rho_{*COOH} - \rho_{substrate}$, where ρ_{total} is the total charge density of the model with the adsorbed *COOH intermediate on the Ni site; ρ_{*COOH} and $\rho_{substrate}$ are the charge densities of *COOH intermediate and the initial system (dNiCu-5.3 model).

Figure S24. Bader charge analysis for sNi model on the Ni site at top-view (a) without *COOH adsorption and (b) with *COOH adsorption. (c) Electron transfer for sNi model with *COOH adsorption on the Ni site. Positive and negative values in this Figure represent the electron depletion and accumulation respectively.
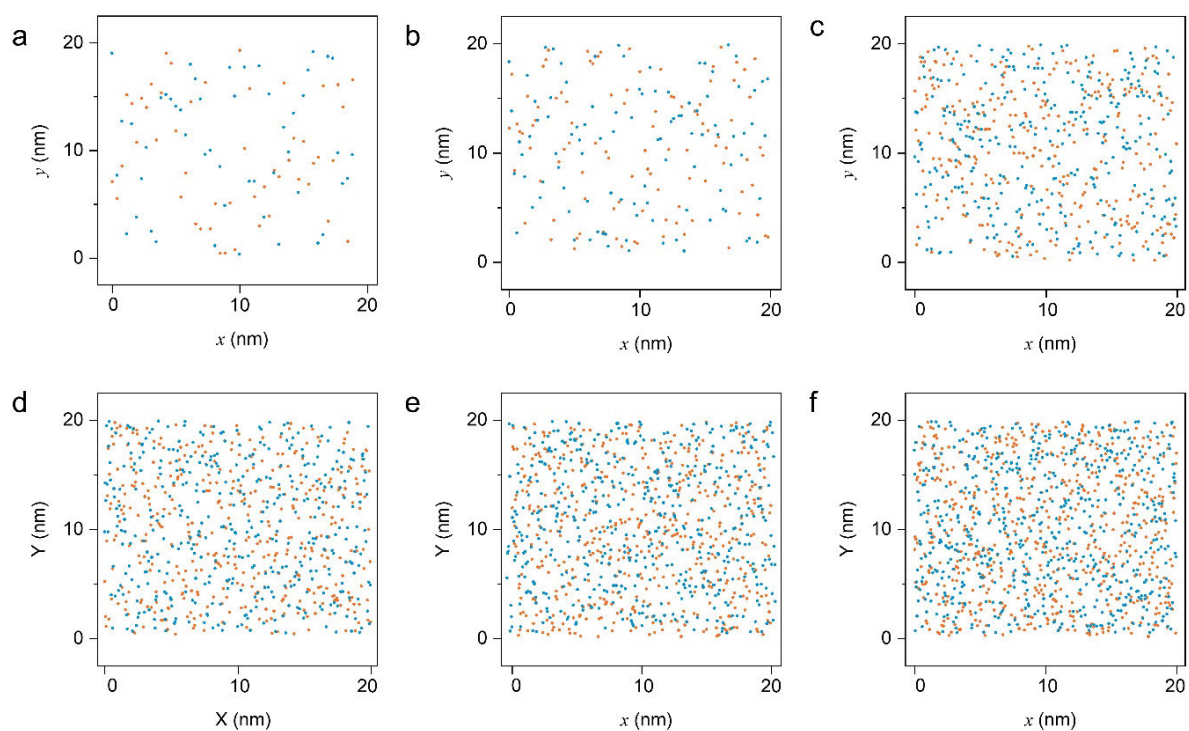
Figure S25. The typical position of dispatching (a) 100, (b) 200, (c) 600, (d) 800, (e) 1000, and (f) 1200 spheres on the 20 nm × 20 nm grid after random simulations.
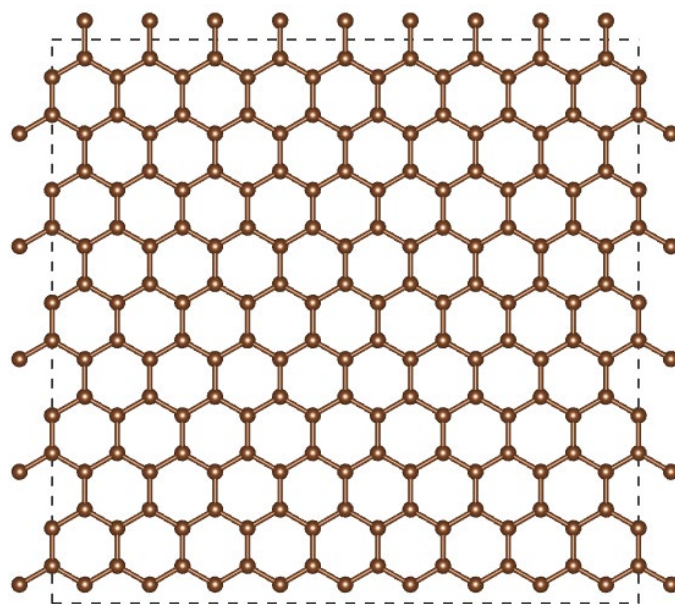
Figure S26. The monolayer graphene contains 180 carbon atoms with lattice parameter of $a =$ 22.13 Å, $b = 21.3$ Å, $c = 1$ Å.

3. Supplementary Tables

Table S1. Thermodynamic energy corrections (in eV) for gaseous molecules and reaction intermediates.

Gas molecule/ adsorbate	ZPE	−TS
CO_2	0.31	−0.66
CO	0.13	−0.61
H_2	0.27	−0.40
H_2O	0.57	−0.54
*COOH	0.61	−0.24
*CO	0.15	−0.27
*H	0.17	−0.02

Table S2. Optimized configurations showing top view and side view of reaction intermediates explored in this research.

Adsorption site_Model	*COOH	*CO	*H
Cu_dCuNi-5.3			
Ni_dCuNi-5.3			
Cu_sCu			
Ni_sNi			
Cu_dCuNi-2.6			
Ni_dCuNi-2.6			
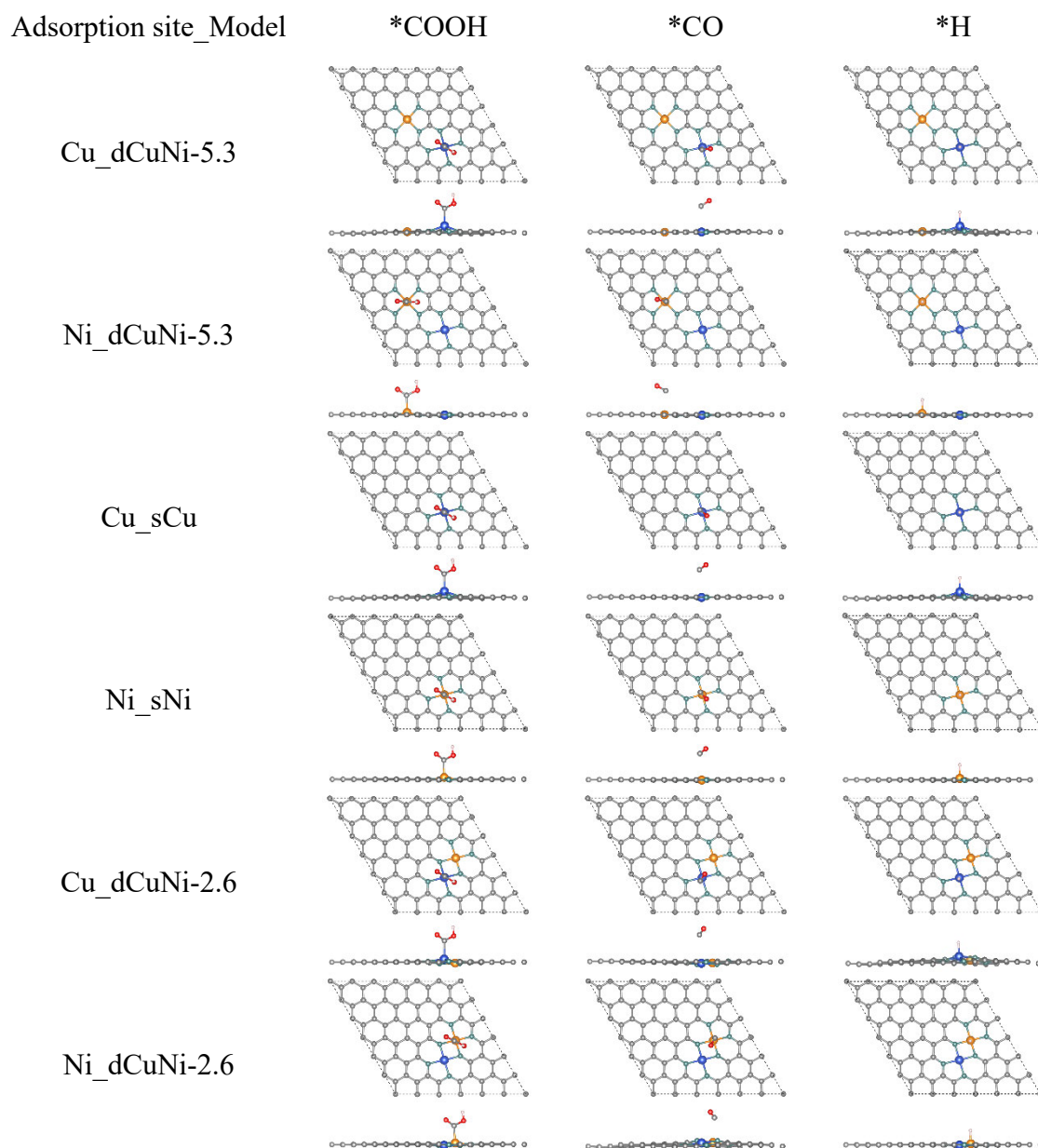
Table S3. The mass loading of Ni and Cu for NiCu-NC, Ni-NC and Cu-NC determined by ICP-MS.

Sample	Ni content (wt.%)	Cu content (wt.%)	Total metal content (wt.%)
NiCu-NC	0.67	0.88	1.55
Ni-NC	1.10	0.04	1.14
Cu-NC	0.05	1.39	1.44

Table S4. Ni *K*-edge and Cu *K*-edge EXAFS curve-fitting parameters for NiCu-NC and reference samples based on different DFT-simulated models.

Sample	*K*-edge	Path	R_{eff}	*N*	S_0^2	σ^2	ΔE_0	*R*-factor	Reference Model
Ni Foil	Ni	Ni–Ni	2.479	12	0.750	0.005	0.764	0.001	--
Cu Foil	Cu	Cu–Cu	2.561	12	0.850	0.004	0.923	0.001	--
NiCu-NC	Ni	Ni–N	1.952	5.031	0.750	0.005	0.296	0.026	sNi/sCu (Figure S16)
	Cu	Cu–N	1.952	4.435	0.850	0.010	2.852	0.036	
	Ni	Ni–N	1.852	4.675	0.750	0.005	1.725	0.0188	dNiCu-2.6 (Figure S17)
		Ni–Cu	2.574	0.033	0.750	0.018			
	Cu	Cu–N	1.882	4.344	0.850	0.009	4.361	0.018	
		Cu–Ni	2.574	−1.179	0.750	0.029	48.01		
	Ni	Ni–N(4)	1.958	4.317		0.005			dNiCu-5.3 (Figure S18)
		Ni–C(31)	2.624	4.264		0.007			
		Ni–C(16)	3.429	2.002	0.750	0.009	0.5133	0.028	
		Ni–N(5)	3.998	1.058		0.014			
		Ni–N(1)	4.312	1.357		0.006			
		Ni–Cu	2.574	0.001		0.432			
	Cu	Cu–N(1)	1.921	4.075		0.008			dNiCu-5.3 (Figure S19)
		Cu–C(17)	2.623	3.932	0.850	0.005	4.664	0.007	
		Cu–C(8)	3.008	4.002		0.010			
		Cu–N(4)	3.412	1.127		0.005			

Note: *N*, coordination number; R_{eff}, distance between absorber and backscatter atoms; σ^2, Debye-Waller factor for both thermal and structural disorders; ΔE^0, Energy shifts for inner potential correction; *R*-factor indicates the goodness of the fitting result. S_0^2 was fixed for the NiCu-NC sample according to the Ni/Cu foil reference. The number shown in the listed path represents the atomic number in the corresponding model.

Table S5. Summary and comparison of CRR performance on some typical atomically dispersed electrocatalysts including Ni sites or Cu sites.

Catalyst	Electrolyte	Potential (V vs RHE)	FE_{CO} (%)	j_{CO} (mA cm^{-2})	Potential Range (mV, FE_{CO} > 80%)	Reference
NiCu-NC DAC	**0.1 M KHCO₃**	**−0.77**	**95.3**	**3.54**	**~800**	**This work**
Ni1Fe1-N-C	0.5 M KHCO3	−0.50	96.2	2.4	~500	[S13]
Ni-Zn-N-C	0.5 M KHCO₃	−0.80	>95	~14	>500	[S14]
NiFe-DASC	0.5 M KHCO₃	−0.80	94.5	50.4	~500	[S15]
Ni/Cu-N-C	0.5 M KHCO₃	−0.69	99	22.4	700	[S10]
Ni/Fe-N-C	0.5 M KHCO₃	−0.70	98	7.4	700	[S16]
CuFe/N-C	0.5 M KHCO₃	−0.40	95.5	2.1	~500	[S17]
Cu-Fe-N₆-C	0.1 M KHCO₃	−0.70	98	3.8	~500	[S18]
Ni SAC	0.5 M KHCO₃	−0.60	95.2	14.3	~400	[S19]
Ni-N-Gr	0.1 M KHCO₃	−0.65	90	~0.2	~350	[S20]
Ni SAs /N-C	0.5 M KHCO₃	−1.0	71.9	10.48	--	[S21]
Ni-NCB	0.5 M KHCO₃	−0.68	99	~7	~500	[S22]
Cu-N₄-NG	0.1 M KHCO₃	−1.00	80.6	~6	~100	[S23]
Cu-N₂ /GN	0.1 M KHCO₃	−0.50	81	~4	--	[S24]
Cu-N-C	0.1 M KHCO₃	−0.80	28	~1.5	--	[S25]
Cu-C₃N₄	0.1 M KHCO₃	−1.10	36	~2	--	[S26]

4. Supplementary References

[S1]   G. Kresse, J. Furthmüller, *Phys. Rev. B* **1996**, *54*, 11169.

[S2]   J. K. Nørskov, J. Rossmeisl, A. Logadottir, L. Lindqvist, J. R. Kitchin, T. Bligaard, H. Jónsson, *J. Phys. Chem. B* **2004**, *108*, 17886.

[S3]   A. A. Peterson, F. Abild-Pedersen, F. Studt, J. Rossmeisl, J. K. Nørskov, *Energy Environ. Sci.* **2010**, *3*, 1311.

[S4]   a) X. Zhi, Y. Jiao, Y. Zheng, A. Vasileff, S. Z. Qiao, *Nano Energy* **2020**, *71*, 10460; b) Y. Wang, L. You, K. Zhou, *Chem. Sci.* **2021**, *12*, 14065; c) S. Fu, X. Liu, J. Ran, Y. Jiao, S. Z. Qiao, *Appl. Surf. Sci.* 2021, 540, 148293.

[S5]   C. Xu, A. Vasileff, D. Wang, B. Jin, Y. Zheng, S. Z. Qiao, *Nanoscale Horiz.* **2019**, *4*, 1411.

[S6]   D. Liu, C. Wu, S. Chen, S. Ding, Y. Xie, C. Wang, T. Wang, Y. A. Haleem, Z. ur Rehman, Y. Sang, Q. Liu, X. Zheng, Y. Wang, B. Ge, H. Xu, L. Song, *Nano Res.* **2018, *11*, 2217.

[S7]   B. Ravel, M. Newville, *J. Synchrotron. Radiat.* **2005**, *12*, 537.

[S8]   P. Wang, H. Yang, C. Tang, Y. Wu, Y. Zheng, T. Cheng, K. Davey, X. Huang, S. Z. Qiao, *Nat. Commun.* **2022**, *13*, 3754.

[S9]   Y. Wang, B. J. Park, V. K. Paidi, R. Huang, Y. Lee, K.-J. Noh, K.-S. Lee, J. W. Han, *ACS Energy Lett.* **2022**, *7*, 640.

[S10]   H. Cheng, X. Wu, M. Feng, X. Li, G. Lei, Z. Fan, D. Pan, F. Cui, G. He, *ACS Catal.* **2022**, *11*, 12673.

[S11]   J. C. Slater, *J. Chem. Phys.* **1964**, *41*, 3199.

[S12]   G. Marsaglia, B. Narasimhan, A. Zaman, *Commun. Stat. - Theory Methods* **1990, *19*, 4199.

[S13]   L. Jiao, J. Zhu, Y. Zhang, W. Yang, S. Zhou, A. Li, C. Xie, X. Zheng, W. Zhou, S. H. Yu, H. L. Jiang, *J. Am. Chem. Soc.* **2021**, *143*, 19417.

[S14]   Y. Li, B. Wei, M. Zhu, J. Chen, Q. Jiang, B. Yang, Y. Hou, L. Lei, Z. Li, R. Zhang, Y. Lu, *Adv. Mater.* **2021**, *33*, 2102212.

[S15]   Z. Zeng, L. Y. Gan, H. Bin Yang, X. Su, J. Gao, W. Liu, H. Matsumoto, J. Gong, J. Zhang, W. Cai, Z. Zhang, Y. Yan, B. Liu, P. Chen, *Nat. Commun.* **2021**, *12*, 4088.

[S16]   W. Ren, X. Tan, W. Yang, C. Jia, S. Xu, K. Wang, S. C. Smith, C. Zhao, *Angew. Chem. Int. Ed.* **2019**, *58*, 6972.

[S17]   F. Wang, H. Xie, T. Liu, Y. Wu, B. Chen, *Appl. Energy* **2020**, *269*, 115029.

[S18] R. Yun, F. Zhan, X. Wang, B. Zhang, T. Sheng, Z. Xin, J. Mao, S. Liu, B. Zheng, *Small* **2020**, *17*, 2006951.

[S19] W. Zhu, J. Fu, J. Liu, Y. Chen, X. Li, K. Huang, Y. Cai, Y. He, Y. Zhou, D. Su, J. J. Zhu, Y. Lin, *Appl. Catal. B: Environ.* **2020**, *264*, 118502.

[S20] P. Su, K. Iwase, S. Nakanishi, K. Hashimoto, K. Kamiya, *Small* **2016**, *12*, 6083.

[S21] C. Zhao, X. Dai, T. Yao, W. Chen, X. Wang, J. Wang, J. Yang, S. Wei, Y. Wu, Y. Li, *J. Am. Chem. Soc.* **2017**, *139*, 8078.

[S22] T. Zheng, K. Jiang, N. Ta, Y. Hu, J. Zeng, J. Liu, H. Wang, *Joule* **2019**, *3*, 265.

[S23] C. Xu, X. Zhi, A. Vasileff, D. Wang, B. Jin, Y. Jiao, Y. Zheng, S. Z. Qiao, *Small Struct.* **2021**, *2*, 2000058.

[S24] W. Zheng, J. Yang, H. Chen, Y. Hou, Q. Wang, M. Gu, F. He, Y. Xia, Z. Xia, Z. Li, B. Yang, L. Lei, C. Yuan, Q. He, M. Qiu, X. Feng, *Adv. Funct. Mater.* **2020**, *30*, 1907658.

[S25] L. Takele Menisa, P. Cheng, C. Long, X. Qiu, Y. Zheng, J. Han, Y. Zhang, Y. Gao, Z. Tang, *Nanoscale* **2020**, *12*, 16617.

[S26] Y. Jiao, Y. Zheng, P. Chen, M. Jaroniec, S. Z. Qiao, *J. Am. Chem. Soc.* **2017**, *139*, 18093.

Chapter 6

Sonication Production of Noble-metal Single-atom Catalysts for Electrocatalytic Nitrate Reduction

6.1 Introduction and Significance

It is highly desirable to develop simplistic and efficient method for synthesizing singl-atom catalysts (SACs) under mild conditions with potential to work at an industrial production scale. Here we report on harnessing the cavitation generated from the ultrasound effect to synthesize noble-metal SACs (including platinum, palladium, silver and gold) on the C_3N_4 matrix. The highlights of this work include:

(1) Ex situ spectroscopic characterizations unravel the crucial steps in the growth of SACs assisted by sonication, i.e., trapping and binding. The first trapping process requires some active sites to capture metal precursors, like interplanar defects and vacancies, while the sonication treatment contributes to the formation of atomic binding between metal atoms and the matrix.

(2) No further post-treatments and sophisticated procedures are required in the process, and gram-level yield can be obtained in a single run and under ambient conditions.

(3) The practical application validaty of this strategy is corroborated by the excellent green ammonia production which is achieved on the Pt-CN-s via electrocatalytic nitrate reduction.

This work deepens the understanding of the growth mechanism of SACs, explores some new insights into employing traditional wet chemistry in SACs preparation, and also paves the way for their future industrial productions.

6.2 Sonication Production of Noble-metal Single-atom Catalysts for Electrocatalytic Nitrate Reduction

This chapter is presented as a manuscript format for research paper by Dazhi Yao, Yanzhao Zhang, Cheng Tang, Junyu Zhang, Bernt Johannessen, and Shi-Zhang Qiao. Sonication production of noble-metal single-atom catalysts for electrocatalytic nitrate reduction, In preparation.

Statement of Authorship

Title of Paper	Sonication production of noble-metal single-atom catalysts for electrocatalytic nitrate reduction
Publication Status	☐ Published ☐ Accepted for Publication ☐ Submitted for Publication ☑ Unpublished and Unsubmitted work written in manuscript style
Publication Details	D. Yao, Y. Zhang, C. Tang, J. Zhang, B Johannessen, S. Z. Qiao, Unsubmitted

Principal Author

Name of Principal Author (Candidate)	Dazhi Yao
Contribution to the Paper	Designed and conducted the experiments, analysed the data, wrote the manuscript.
Overall percentage (%)	70%
Certification:	This paper reports on original research I conducted during the period of my Higher Degree by Research candidature and is not subject to any obligations or contractual agreements with a third party that would constrain its inclusion in this thesis. I am the primary author of this paper.
Signature	Date 28/09/2022

Co-Author Contributions

By signing the Statement of Authorship, each author certifies that:

i. the candidate's stated contribution to the publication is accurate (as detailed above);

ii. permission is granted for the candidate in include the publication in the thesis; and

iii. the sum of all co-author contributions is equal to 100% less the candidate's stated contribution.

Name of Co-Author	Cheng Tang
Contribution to the Paper	Guided to design the whole experiment, helped data analysis, and revised the manuscript
Signature	Date 28/09/2022

Name of Co-Author	Yanzhao Zhang
Contribution to the Paper	Assisted in designing the experiment and data analysis.
Signature	Date 28/09/2022

Name of Co-Author	Junyu Zhang		
Contribution to the Paper	Helped the experiment, discussed and analysed the data		
Signature	175	Date	28/09/2022

Name of Co-Author	Bernt Johannessen		
Contribution to the Paper	Collected XAS data and assisted in the analysis thereof. Revised the manuscript.		
Signature		Date	28/Sep/2022

Name of Co-Author	Shi-Zhang Qiao		
Contribution to the Paper	Supervision of the work, discussion and conceptualization of this manuscript and manuscript evaluation and revision.		
Signature		Date	28/Sep/2022

Sonication production of noble-metal single-atom catalysts for electrocatalytic nitrate reduction

Dazhi Yao[1], Yanzhao Zhang[1], Cheng Tang[1], Junyu Zhang[1], Bernt Johannessen[2], Shi-Zhang Qiao[1*]

[1]Centre for Materials in Energy and Catalysis, School of Chemical Engineering and Advanced Materials, The University of Adelaide, Adelaide, SA 5005, Australia
[2]Australian Synchrotron, 800 Blackburn Rd, Clayton, VIC 3168, Australia

*Corresponding author. Email: s.qiao@adelaide.edu.au

Abstract

Developing a simplistic strategy to fabricate atomically dispersed catalysts under mild conditions is crucial for industrial scale production and use. Here we report on harnessing the cavitation generated from the ultrasound effect to synthesize noble-metal SACs (including platinum, palladium, silver and gold) on the C_3N_4 matrix. Ex situ spectroscopic characterizations unravel the critical steps in the growth of SACs assisted by sonication, i.e., trapping and binding. The first trapping process requires active sites to capture metal precursors such as interplanar defects and vacancies. While the sonication treatment contributes to the formation of atomic binding between metal atoms and the matrix. No further post-treatments and sophisticated procedures were required in the process, and gram-level yield can be obtained in a single run and under ambient conditions. The validity of the practical application of the strategy is corroborated by the excellent green ammonia production achieved on the Pt-CN-s via electrocatalytic nitrate reduction. This work deepens the understanding of the growth mechanism of SACs, explores some new insights into employing traditional wet chemistry in SACs preparation, and also paves the way for their future industrial production and application.

Introduction

Single-atom catalysts (SACs) have attracted considerable interests recently. Their unique structure, i.e., the atomically metal atoms dispersed onto a host matrix, offers maximized atom utilization and provides higher activity, which has sparked their potential applications in both heterogeneous and homogeneous catalysis.[1-4] For the fabrication of SACs, the "bottom-up" route based on the "impregnation-binding" strategy is commonly utilized, especially via high-temperature annealing for the synthesis of the carbon matrix-supported SACs.[5-9] However, the atoms inevitably tend to aggregate into nanoclusters or particles to decrease their surface energy.[2, 9-12] Thus, acid washing is usually required as a post-treatment step for the cleaning of SACs.[13, 14] Notably, some noble metal elements, due to their intrinsic electrical potentials, cannot react with common acid without damaging the carbon matrix.[15, 16] The necessity of requiring expensive equipment, sophisticated techniques and operations, and time-consuming procedures, along with the low yield production, also burden the development of the synthesis and practical application of SACs.[10, 17-19] Therefore, it is desirable to find alternatives for the synthesis of SACs toward high-yield production with ease of operation and under mild conditions.

Traditional solution synthesis is one of the mature and facile methods for the preparation of nanomaterials. It has been developed as a method capable of industrial scale or automated fabrication of materials.[14, 20-22] However, it is challenging to synthesize SACs by solution chemistry due to the difficulties in precisely tailoring diffusion, aggregation and nucleation of the product atoms in the liquid phase.[23-25] Recently, inspired by the growth mechanism of high-entropy nanoalloys, the high temperature and short residence time generally enable the homogeneous mixing of elements and minimize particle agglomeration.[26-28] Sonochemistry is one of the suitable candidates to meet the requirements mentioned, which has been developed into a mature method for nanomaterial synthesis.[29-31] Bubbles in the solution act as a micro-reactor like annealing in the furnace. The acoustic cavitation from the ultrasound effect, especially during the collapse of these bubbles, can generate significant energy (>1000°C, ~2000 atm) occurring in momentary timespans ($\leqslant 10^{-9}$ s), which can accelerate the metal atom binding process.[27, 31, 32] Thus, a proposal for the synthesis of SACs through wet chemistry assisted by sonication treatment comes to our mind. It is imagined that the experiment protocol should include two critical steps. First, the metal precursors are first trapped onto the host matrix. Second, the mixture will be transferred into the ultrasonicator for the atomic binding with the substrate.

Herein, we report a general "sonication" strategy and successfully fabricate precious element metal SACs on the C_3N_4, including Pt, Au, Pd, and Ag, denoted as X-CN-s (X = Pd, Pt, Ag and Au; Scheme 1). By introducing ex situ scanning transmission electron microscope (STEM) and X-ray photoelectron spectroscopy (XPS) to follow the development process, we unravel that the sonochemistry-assisted SACs strategy includes two crucial steps: (1) capture of metal precursors onto the matrix (adsorption), via the highly active sites (such as defects, vacancies and edge sites); and (2) formation of the atomic binding between metal precursors and matrix under the sonicating treatment (Scheme 1). Additionally, acid washing and other post-treatment procedures are not required for this sonication method of SACs preparation. Notably, the resultant yield of this sonication method reaches gram-levels in single runs. The practical application of the SACs obtained from the "sonication" method is further supported by measuring the electrocatalytic nitrate reduction (NitRR) performance for ammonia production on the Pt-CN-s. This work reports a novel and straightforward method of synthesizing noble-metal SACs under mild conditions with great energy efficiency, and also extends the practical applications of noble-metal SACs to green ammonia production.
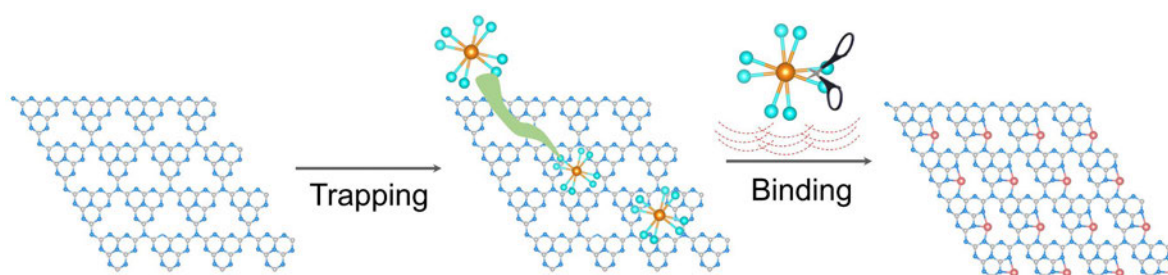
Scheme 1. Illustration of the SAC synthetic procedure based on the two-step strategy via "adsorption-trapping and sonication-binding".

Results and Discussions

First, C_3N_4 was fabricated via the pyrolysis of urea at 550°C in the air. High-resolution transmission electron microscopy (HRTEM) (Figure S1) reveals that the prepared C_3N_4 has a thin, sheet-like morphology with wrinkles. X-ray powder diffraction (XRD) results identify two pronounced diffraction peaks located at ~13° and 27.4°, corresponding to the (100) and (002) peaks of typical graphite C_3N_4 (Figure S2). [33]After sonicating the mixture of C_3N_4 metal precursors (Na_2PdCl_4 as an example), Pd atoms can be atomically dispersed on the C_3N_4 substrate. The high-resolution high-angle annular dark-field scanning transmission electron microscopy (HAADF-STEM) confirmed the formation of the Pd single atom. As shown in Figure 1a and Figure S3, there are no metal clusters or nanoparticles on the C_3N_4. Instead,

highly dispersed bright spots are visible (Figure 1b–e), which are ascribed to Pd metallic atoms because of the higher atomic mass compared to carbon and nitrogen. XRD patterns of the prepared Pd-CN-s show similar features of carbon nitride, without any metal signals (Figure S4). The absence of diffraction peaks for metallic nanoparticles, together with no agglomeration in high-resolution TEM images, indicates the formation of isolated Pd atoms supported on the C_3N_4. The energy-dispersive spectroscopy (EDS) spectrum and mapping images further demonstrate the presence of Pd element and their uniform distribution and the absence of larger aggregates (Figure 1c and Figure S5). The Pd metal mass loading amount of Pd-CN-s sample is quantified by the inductively coupled plasma mass spectrometry (ICP–MS), to be ~1.47 % (Table S1).
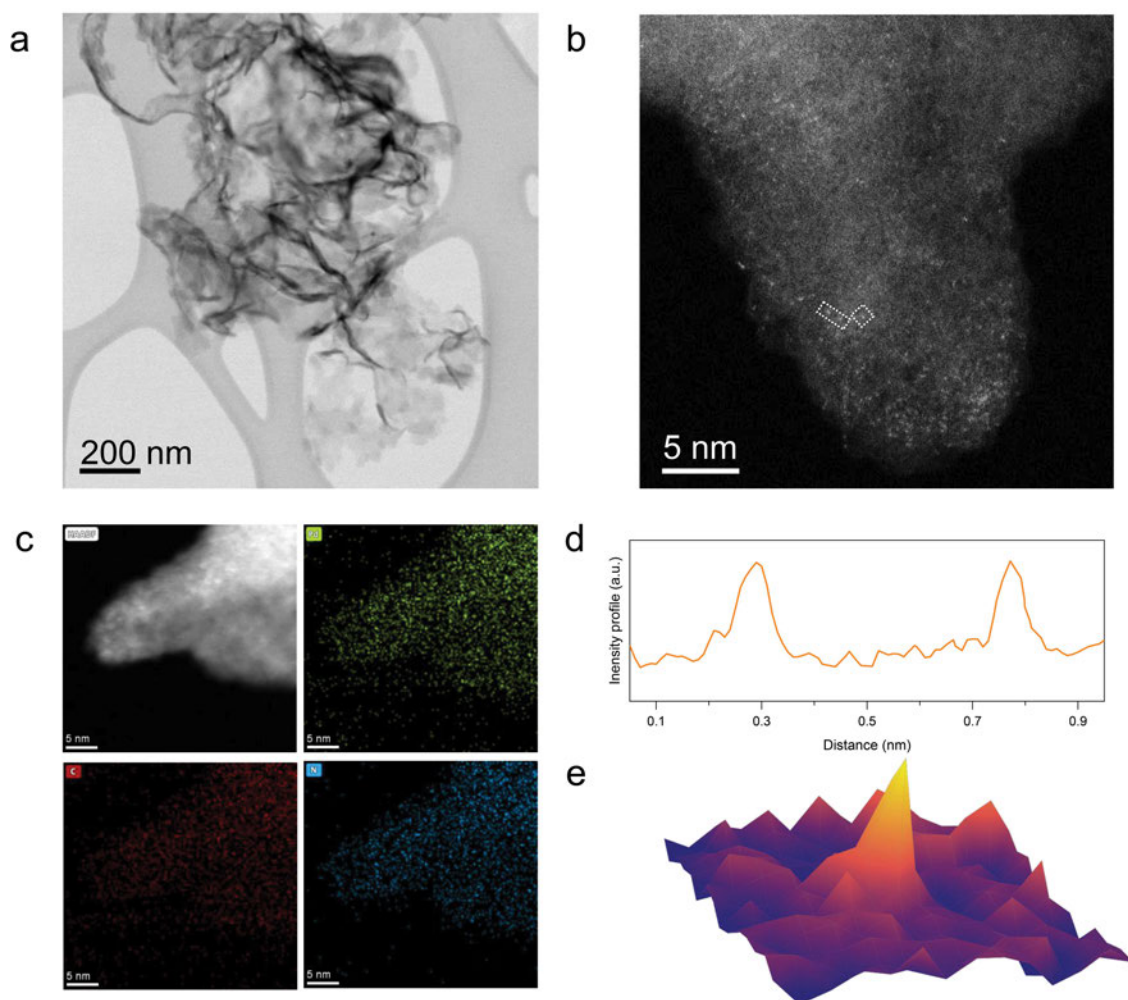
Figure 1. Morphological and atomic characterization of the as-obtained Pd-CN samples. The typical (a) TEM image, (b) HAADF-STEM image, and (c) corresponding EDS mapping of Pd-CN-s samples. (d) The intensity profile along the marked area in Figure 1b. (e) 3D transformed atom-overlapping fitting of the highlighted area in Figure 1b.

The dispersion of Pd species on the C_3N_4 matrix was also confirmed by X-ray absorption near edge structure (XANES) and extended X-ray absorption fine structure (EXAFS) to identify the structure of the as-obtained Pd-CN-s at the atomic level. As shown in Figure 2a, the *K*-edge of Pd-CN-s is located between the metallic Pd^0 and PdO, indicating the positive oxidation state of Pd in Pd-CN is situated between Pd^0 and Pd^{2+} (Figure 2a). Figure 2b shows the Fourier transform (FT) of the Pd *K*-edge EXAFS oscillations of Pd-CN-s, with reference to standard PdO and Pd foil. The peak at approximately 1.48 Å, belonging to the Pd−N path, and no obvious Pd−Pd path (2.50 Å) was observed in the Pd-CN-s sample. Therefore, by combing the results from the HAADF-STEM images and XAFS analysis, Pd atoms are revealed to be atomically dispersed on the C_3N_4 matrix.
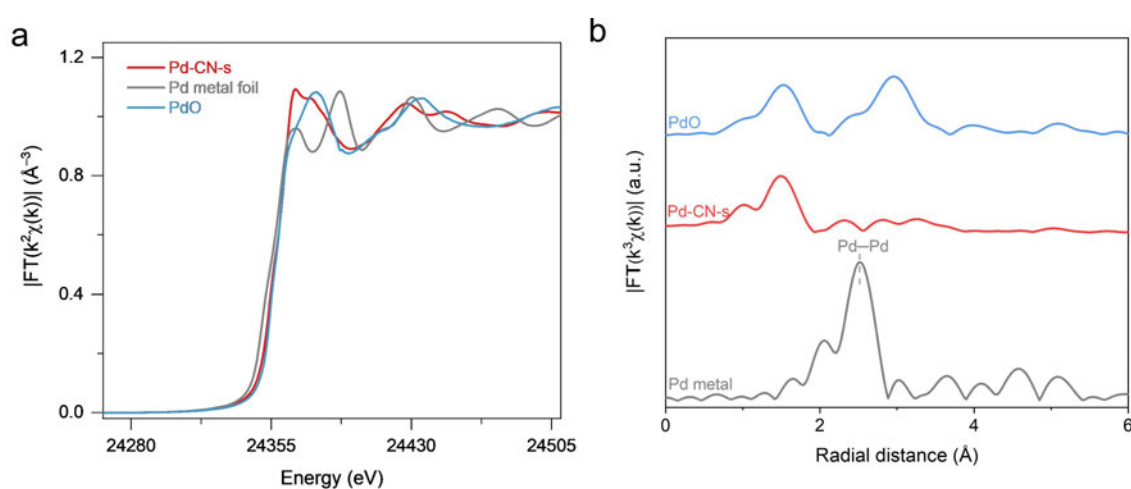
Figure 2. (a) XANES spectra of Pd *K*-edge and (b) Fourier transform *R*-space spectra at the Pd K-edge of Pd-CN-s, Pd metal foil and standard PdO samples.

To investigate the effectivity of the two-step strategy and the possible production process, we employed ex situ STEM imaging to follow the Pd-CN-s at different stages. As mentioned above, the general "capture-and-bonding" process requires active adsorption sites to combine metal precursors. The vacancy defects in the C_3N_4, especially those surrounded by nitrogen atoms, can capture the free metal precursor (like $[PdCl_4]^{2-}$) in the solution owing to the physical confinement effect and electrostatic/coordination interaction.[33, 34] Thus, we examined the morphology of C_3N_4 after the addition of Na_2PdCl_4 but without sonication (i.e., Pd-CN-a) to determine the effect of the adsorption process. As shown in Figure S6, the HADDF-STEM image of Pd-CN-a exhibits many densely populated bright dots with a diameter of approximately 0.2 nm, which are similar to those on the Pd-CN-s (Figure 1b). The contrast under the electron probe, combined with the results from EDS mapping results, ascribed these dots to the atomic Pd metal dispersed on the Pd-CN-a (Figure S7). Notably, Pd single atoms

are uniformly distributed on the whole C_3N_4 nanosheet. By imaging alongside the edge toward the inner sheet as shown in Figure S8, the density of bright spots is not significantly decreased with the change of imaging position. Pd single atoms are not only densely populated around the edge of C_3N_4, but are distributed inside the nanosheet. Such findings indicate that the higher energy sites including structural defects and the active edge of the C_3N_4 can effectively capture metal precursors, thus achieving the adsorption step of the single-atom synthesis.

To further verify the necessity of the adsorption step for the single-atom synthesis, we employed two typical two-dimensional (2D) materials (MoS_2 and BN) as comparisons to support the claim because of their similar structure but different intrinsic defects compared to C_3N_4. MoS_2 and BN were directly utilized from commercial samples without further modification (Experimental Section in the Supporting Information). Prior to the addition of Na_2PdCl_4 to a MoS_2/BN dispersion, HADDF-STEM images of both samples only exhibit corresponding lattice and atomic arrangement from crystal, while no bright spots from the highly contrasted heavy elements were detected (Figure S9). However, after mixing the matrix dispersion with $[PdCl_4]^{2-}$, Pd atoms were presented on the margin of the MoS_2 nanosheet, or at the junction of several nanosheets, but did not show up in the bulk phase (Figure S10). Contrastively, no Pd atoms were formed on either edge or inside of the BN nanosheet (Figure S11). It is inferred that no interplanar defects are presented in the bulk of commercial MoS_2 and BN, so there are no accessible sites to capture precursors. The dangling bonds from unsaturated Mo atoms at the edge serve as higher energy sites for adsorption, leading to the formation of Pd single atoms concentrated around the margin.[35, 36] These results confirm the necessity of adsorption sites to trap metal precursors as the first step for SAC synthesis.

The in-depth mechanism of the adsorption and atomic binding process was also studied by ex situ X-ray photoelectron spectroscopy (XPS) to monitor the change in the chemical status during the fabrication process. As shown in Figure 3 and Figure S12, four elements including C, N, Cl, and Pd were analysed for the pristine CN, Pd-CN-a and Pd-CN-s samples. Two peaks at the bonding energy of 284.6 and 287.9 eV in C 1s spectra were observed, which are assigned to sp^2 and sp^3 C–N bonds.[37, 38] The N 1s peaks of the pristine C_3N_4 can be deconvoluted into three peaks at approximately 398.5, 399.1 and 400.7 eV, which are related to C=N–C, N–C_3, and –NH_2 respectively.[37, 38] The capture of $[PdCl_4]^{2-}$ precursors onto the C_3N_4 matrix (i.e., Pd-CN-a) was corroborated by the presence of Cl 2p and Pd 3d spectra (Figure 3c-d). The Pd 3d peaks at 338.0 eV and 343.2 eV are ascribed to the Pd (II) in the $[PdCl_4]^{2-}$.
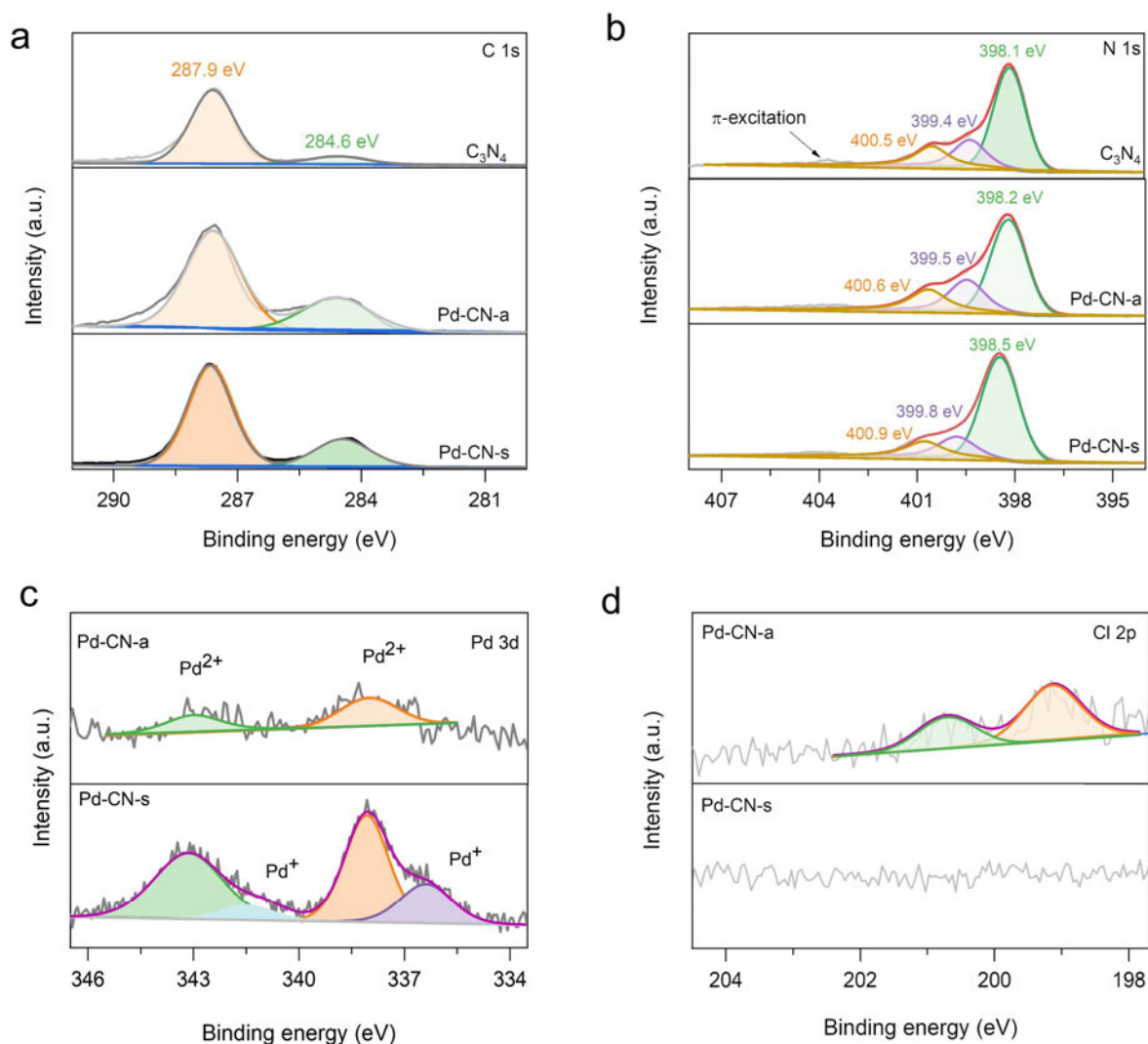
Figure 3. Deconvolution of the high-resolution XPS of (a) carbon 1s spectra, (b) nitrogen 1s spectra, (c) palladium 3d spectra, and (d) chloride 2p spectra for C_3N_4, Pd-CN-a and Pd-CN-s samples.

After sonication treatment of Pd-CN-a, the C=N–C (398.2 eV), N–C$_3$ (399.5 eV) peaks of the N 1s spectra shift to higher binding energy (398.5 eV and 399.8 eV respectively), indicating the interaction between Pd atom and N species. Notably, two different forms of Pd can be seen in the Pd-CN-s, namely Pd$^+$ and Pd^{2+} located around 336.2 and 338.0 respectively[39, 40]. This suggests bonding of the single-atom Pd with nearby N atoms, indicating that Pd is introduced in the form of a single atom rather than as nanoparticles. The Cl 2p$_{3/2}$ XPS (199.2eV) evidences that ultrasound sonication treatment triggered the complete removal of Cl ligands, further denoting the cleavage of Pd–Cl in the [PdCl$_4$]$^{2-}$, and the formation of Pd–N (Figure 3d). Combined with previous studies, we speculate that cavitation is the driving factor for atomic binding for the fabrication of Pd-CN-s. It is believed in the sonication process that high pressure

(~2000 atm) and temperature (>1000°C) can be generated, which offers similar reaction conditions to pyrolysis for SACs synthesis at ambient pressures and temperatures rapidly. These results demonstrate the successful synthesis of Pd-CN based on the "adsorption-sonication" strategy.
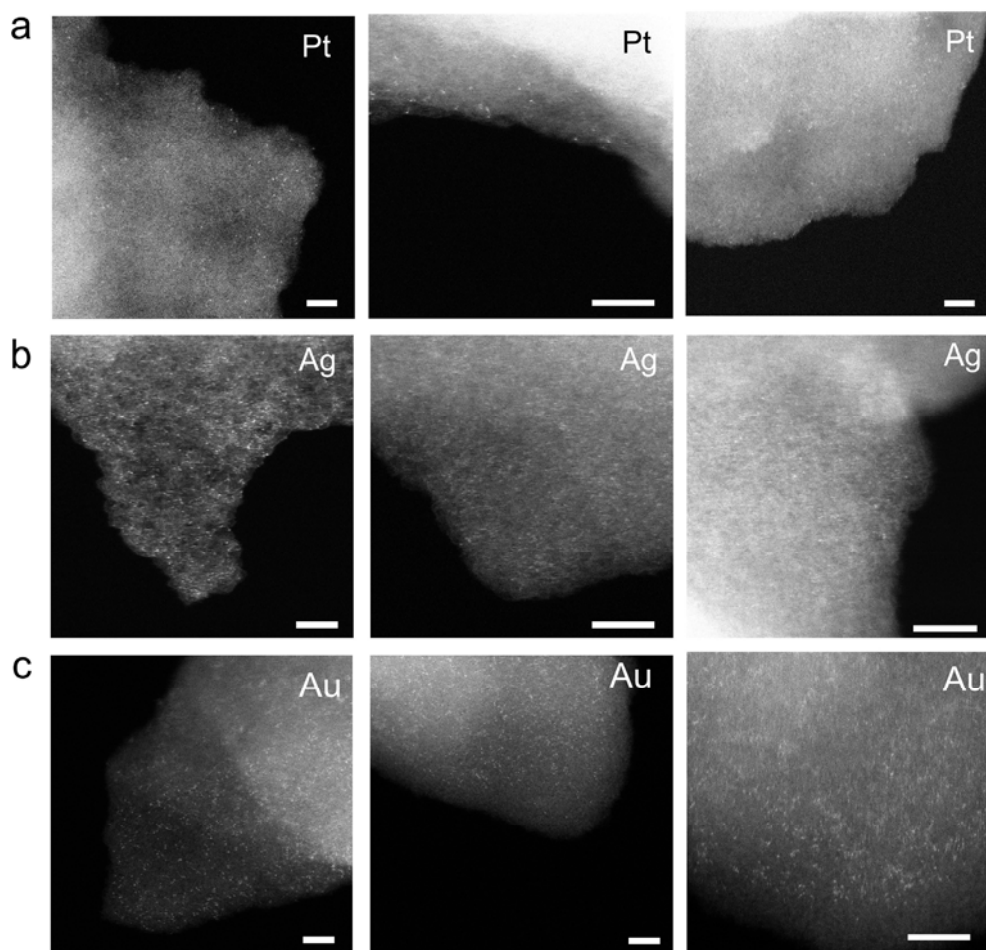
Figure 4. Visualization of the universality of the proposed synthetic strategy. Typical HAADF-STEM images of (a) Pt-CN-s, (b) Ag-CN-s and (c) Au-CN-s (left column), and magnified STEM images from the edge of nanosheet (middle column) or focusing on the inner part (right column). All scale bars inserted in the figure are 5nm.

The universality of the "adsorption-sonicating" strategy in the synthesis of single-atom catalysts was also investigated on other noble-metal atoms dispersed on the C_3N_4 matrix (i.e., X-CN-s, X=Pt, Au, and Ag). As shown in Figure 4, HAADF-STEM images exhibited many bright spots on the support. The EDS mapping suggests the element composition and uniform distribution of metal atoms on the C_3N_4 (Figure S13-S15). No obvious large metal particles are found under STEM images, consistent with the results of their corresponding XRD patterns (Figure S16). Notably, noble-metal atoms are distributed on the edge and inner areas. This is

similar to the results of Pd-CN-s, indicating that the growth mechanism of other atomically dispersed catalysts follows the "adsorption-sonication" strategy. ICP results revealed the loading amount of different metals on C_3N_4 by using this strategy (Table S1). In addition, such route is suitable to scale to industrial production levels. By proportionally magnification of ingredients, the resultant Pd-CN-s with gram-level yield is obtained in a single run (Figure S17). Consequently, these findings indicate that the proposed "adsorption-sonication" strategy is a universal route to the simplistic synthesis of atomically dispersed catalysts under ambient conditions.

To explore the practical application of as-synthesized SACs, we evaluated the performance of representative Pt-CN-s in the electrocatalytic nitrate reduction reaction (NitRR), because Pt SACs on C_3N_4 were predicted to achieve the promising technological potential for ammonia production via NitRR but were seldomly studied.[41, 42] The electrocatalytic experiments were undertaken in a gas-tight H-cell under ambient conditions. The Pt-CN-s samples were drop-cast onto carbon paper (1×1 cm^2) as the working electrode with a mass loading of 0.2 mg cm^{-2}. As shown in Figure 5a, the linear scan voltammograms (LSV) suggest that Pt-CN-s exhibits higher current density on addition or absence of 0.1M KNO_3 to the electrolyte (0.5M K_2SO_4), implying its superior NitRR performance. Product selectivity was investigated in K_2SO_4/KNO_3 electrolyte by amperometry i-t testing of the Pt-CN-s sample at different applied potentials for 30 min (Figure S18). Ammonia (NH_3) and nitrite (NO_2^-) were quantified by ultraviolet-visible (UV–Vis) spectrophotometry (Figure S19-S20; Experimental Section). Gas product (H_2) was determined by online gas chromatography (GC; Experimental Section). As shown in Figure 3b, the Pt-CN-a exhibits high selectivity for electrocatalytic NO_3^--to-NH_3 conversion. The NitRR started at -0.35 V versus RHE, with an overall current density (j) of -2.72 mA cm^{-2} and faradaic efficiency of NH_3 (FE_{NH_3}) of ~ 30% (Figure 4b). Pt-CN-s achieved a maximum NH_3 yield of 10.65 µmol cm^{-2} h^{-1} at -0.80 V versus RHE and maximum FE_{NH_3} of 81.42 % at -0.45 V versus RHE (Figure 4b-c). The stability of Pt-CN-s is also evidenced by its long-term testing at -0.45 V versus RHE for continuous 8 hours. No obvious variations in ammonia yield are noticed during cycles, and the FE_{NH_3} keeps around 80% (Figure 4d).
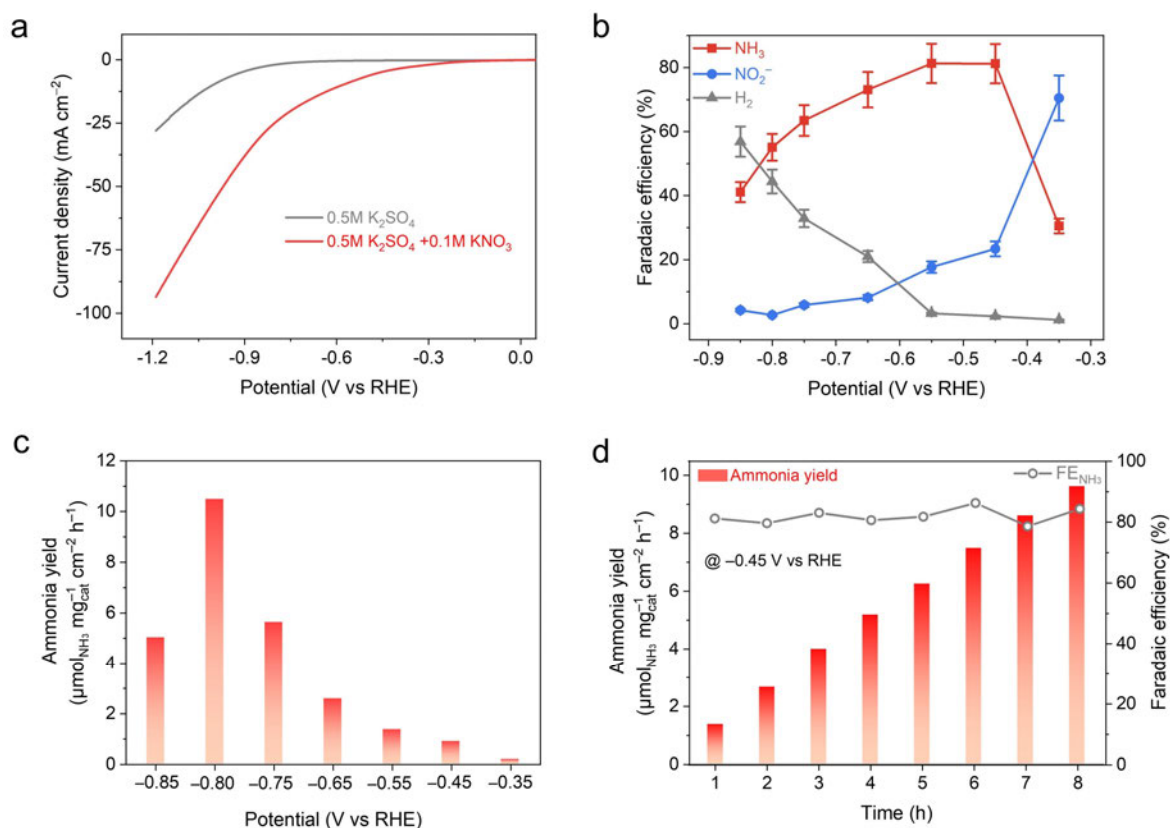
Figure 5. Electrocatalytic nitrate reduction performance of Pt-CN-s. (a) LSV responses of Pt-CN-s in 0.5M K_2SO_4 aqueous solution with addition or absence of 0.1M KNO_3. (b) Faradaic efficiency for different products and (c) potential-dependent ammonia yield determined in the 0.1 M KNO_3 + 0.5 M K_2SO_4 electrolyte. (d) Time-dependent ammonia yield and Faradaic efficiency for ammonia at −0.45V versus RHE in the 0.5 M KNO_3 + 0.5 M K_2SO_4 electrolyte.

To exclude possible nitrogen contamination from the carbon nitride, a series of control tests including blank experiments and isotope labelling tests were conducted. As shown in Figure S21, the bare C_3N_4 electrode achieved negligible nitrate reduction activity, corroborated by the current density in the LSV curves with the addition/absence of KNO_3 to the electrolyte. No noticeable production of ammonia is detected on the bare C_3N_4 electrode after electrolysis at −0.8 V versus RHE in Ar-saturated 0.5 M K_2SO_4/0.1 M KNO_3 electrolyte (Figure S22). Further, isotope labelling experiments by using ^1H NMR spectroscopy demonstrated that a doublet around 7.2 ppm (J = 72 Hz) assigned to $^{15}NH_4^+$ can be detected using $K^{15}NO_3$ (98 atom % ^{15}N, CAS: 57654-83-8) as the feeding N-species origin (Figure S23). Therefore, we confirm that the ammonia product originates from the electrochemical reduction of nitrate in the electrolyte.

Conclusion

In summary, a simplistic method for synthesis of SACs under ambient conditions based on the "adsorption-sonication" strategy successfully achieved to obtain noble-metal atoms supported on the C_3N_4 matrix (X-CN, X = Pd, Pt, Au, and Ag). A two-step synthetic route is revealed by ex situ STEM and XPS characterizations. The capture of metal precursors through an active site is the prerequisite, while the following sonication treatment realizes the atomic binding, thus facilitating their large-scale preparation at mild temperature. As an example, the electrocatalytic nitrate reduction performance was studied on the as-obtained Pt-CN-s. By rigid blank experiment and isotope labelling testing, the Pt-CN-s achieved the maximized FE for ammonia of 80.42 % at −0.45 V versus RHE and the highest ammonia yield of 10.65 μmol cm^{-2} h^{-1} at −0.8 V in 0.1 M KNO_3 + 0.5 M K_2SO_4 electrolyte. The onset potential of around −0.30 V versus RHE and long-term stability of 8 h in the presence of KNO_3 electrolyte denotes the potential application of SACs in future green ammonia production. This study provides a novel strategy for the construction of SACs and also facilitates a new route in the field of energy catalysis in the future.

Supporting Information

Supporting Information is available from the Wiley Online Library or from the author.

Acknowledgements

References

[1]   A. Wang, J. Li, T. Zhang, *Nat. Rev. Chem.* **2018**, *2*, 65.

[2]   L. Han, H. Cheng, W. Liu, H. Li, P. Ou, R. Lin, H.-T. Wang, C.-W. Pao, A. R. Head, C.-H. Wang, X. Tong, C.-J. Sun, W.-F. Pong, J. Luo, J.-C. Zheng, H. L. Xin, *Nat. Mater.* **2022**, *21*, 681.

[3]   X. He, Q. He, Y. Deng, M. Peng, H. Chen, Y. Zhang, S. Yao, M. Zhang, D. Xiao, D. Ma, B. Ge, H. Ji, *Nat. Commun.* **2019**, *10*, 3663.

[4]   Q. Liang, W. Li, L. Xie, Y. He, B. Qiu, H. Zeng, S. Zhou, J. Zeng, T. Liu, M. Yan, K. Liang, O. Terasaki, L. Jiang, B. Kong, *Nano Lett.* **2022**, *22*, 2889.

[5]   J. Wang, Z. Li, Y. Wu, Y. Li, *Adv. Mater.* **2018**, *30*, 1801649.

[6]   Y. Yang, Y. Yang, Z. Pei, K.-H. Wu, C. Tan, H. Wang, L. Wei, A. Mahmood, C. Yan, J. Dong, S. Zhao, Y. Chen, *Matter* **2020**, *3*, 1442.

[7]   E. Zhang, T. Wang, K. Yu, J. Liu, W. Chen, A. Li, H. Rong, R. Lin, S. Ji, X. Zheng, Y. Wang, L. Zheng, C. Chen, D. Wang, J. Zhang, Y. Li, *J. Am. Chem. Soc.* **2019**, *141*, 16569.

[8]   W. Ren, X. Tan, W. Yang, C. Jia, S. Xu, K. Wang, S. C. Smith, C. Zhao, *Angew. Chem. Int. Ed.* **2019**, *58*, 6972.

[9]   J. Jones, H. Xiong, A. T. DeLaRiva, E. J. Peterson, H. Pham, S. R. Challa, G. Qi, S. Oh, M. H. Wiebenga, X. I. Pereira Hernández, Y. Wang, A. K. Datye, *Science* **2016**, *353*, 150.

[10]   W. Fu, J. Wan, H. Zhang, J. Li, W. Chen, Y. Li, Z. Guo, Y. Wang, *Nat. Commun.* **2022**, *13*, 5496.

[11]   L. Wang, M.-X. Chen, Q.-Q. Yan, S.-L. Xu, S.-Q. Chu, P. Chen, Y. Lin, H.-W. Liang, *Sci. Adv.* **2019**, *5*, eaax6322.

[12]   C. Xia, Y. Qiu, Y. Xia, P. Zhu, G. King, X. Zhang, Z. Wu, J. Y. Kim, D. A. Cullen, D. Zheng, P. Li, M. Shakouri, E. Heredia, P. Cui, H. N. Alshareef, Y. Hu, H. Wang, *Nat. Chem.* **2021**, *13*, 887.

[13]   M. Li, H. Wang, W. Luo, P. C. Sherrell, J. Chen, J. Yang, *Adv. Mater.* **2020**, *32*, 2001848.

[14] A. Han, B. Wang, A. Kumar, Y. Qin, J. Jin, X. Wang, C. Yang, B. Dong, Y. Jia, J. Liu, X. Sun, *Small Methods* **2019**, *3*, 1800471.

[15] X. Li, X. Yang, Y. Huang, T. Zhang, B. Liu, *Adv. Mater.* **2019**, *31*, 1902031.

[16] F. Zhang, Y. Zhu, Q. Lin, L. Zhang, X. Zhang, H. Wang, *Energy Environ. Sci.* **2021**, *14*, 2954.

[17] Y. Shi, W.-M. Huang, J. Li, Y. Zhou, Z.-Q. Li, Y.-C. Yin, X.-H. Xia, *Nat. Commun.* **2020**, *11*, 4558.

[18] J. Lin, A. Wang, B. Qiao, X. Liu, X. Yang, X. Wang, J. Liang, J. Li, J. Liu, T. Zhang, *J. Am. Chem. Soc.* **2013**, *135*, 15314.

[19] Y. Qu, Z. Li, W. Chen, Y. Lin, T. Yuan, Z. Yang, C. Zhao, J. Wang, C. Zhao, X. Wang, F. Zhou, Z. Zhuang, Y. Wu, Y. Li, *Nat. Catal.* **2018**, *1*, 781.

[20] Y. Wu, D. Wang, Y. Li, *Sci. China Mater.* **2016**, *59*, 938.

[21] C. Tan, H. Zhang, *Nat. Commun.* **2015**, *6*, 7873.

[22] S. Lu, J. Liang, H. Long, H. Li, X. Zhou, Z. He, Y. Chen, H. Sun, Z. Fan, H. Zhang, *Acc. Chem. Res.* **2020**, *53*, 2106.

[23] H. Wei, K. Huang, D. Wang, R. Zhang, B. Ge, J. Ma, B. Wen, S. Zhang, Q. Li, M. Lei, C. Zhang, J. Irawan, L.-M. Liu, H. Wu, *Nat. Commun.* **2017**, *8*, 1490.

[24] N. D. Loh, S. Sen, M. Bosman, S. F. Tan, J. Zhong, C. A. Nijhuis, P. Král, P. Matsudaira, U. Mirsaidov, *Nat. Chem.* **2017**, *9*, 77.

[25] X. Wang, J. Zhuang, Q. Peng, Y. Li, *Nature* **2005**, *437*, 121.

[26] M. Liu, Z. Zhang, F. Okejiri, S. Yang, S. Zhou, S. Dai, *Adv. Mater. Interfaces* **2019**, *6*, 1900015.

[27] H. Li, H. Zhu, S. Zhang, N. Zhang, M. Du, Y. Chai, *Small Struct.* **2020**, *1*, 2000033.

[28] E. P. George, D. Raabe, R. O. Ritchie, *Nat. Rev. Chem.* **2019**, *4*, 515.

[29] H. Xu, B. W. Zeiger, K. S. Suslick, *Chem. Soc. Rev.* **2013**, *42*, 2555.

[30] M. Hujjatul Islam, M. T. Y. Paul, O. S. Burheim, B. G. Pollet, *Ultrason. Sonochem.* **2019**, *59*, 104711.

[31] Z. Li, T. Zhuang, J. Dong, L. Wang, J. Xia, H. Wang, X. Cui, Z. Wang, *Ultrason. Sonochem.* **2021**, *71*, 105384.

[32] A. Moghtada, R. Ashiri, *Ultrason. Sonochem.* **2016**, *33*, 141.

[33] G. Liu, Y. Huang, H. Lv, H. Wang, Y. Zeng, M. Yuan, Q. Meng, C. Wang, *Appl. Catal. B.* **2021**, *284*, 119683.

[34] P. Zhou, F. Lv, N. Li, Y. Zhang, Z. Mu, Y. Tang, J. Lai, Y. Chao, M. Luo, F. Lin, J. Zhou, D. Su, S. Guo, *Nano Energy* **2019**, *56*, 127.

[35] Y. Lou, Y. Zhao, H. Liu, Q. Gu, B. Yang, Y. Shi, T. Yao, B. Yang, *ChemCatChem* **2021**, *13*, 2783.

[36] C. Tsounis, B. Subhash, P. V. Kumar, N. M. Bedford, Y. Zhao, J. Shenoy, Z. Ma, D. Zhang, C. Y. Toe, S. Cheong, R. D. Tilley, X. Lu, L. Dai, Z. Han, R. Amal, *Adv. Funct. Mater.* **2022**, *32*, 2203067.

[37] A. P. Dementjev, A. de Graaf, M. C. M. van de Sanden, K. I. Maslakov, A. V. Naumkin, A. A. Serov, *Diam. Relat. Mater.* **2000**, *9*, 1904.

[38] D. Hao, J. Ren, Y. Wang, H. Arandiyan, M. Garbrecht, X. Bai, H. K. Shon, W. Wei, B.-J. Ni, *Energy Mat. Adv.* **2021**, *2021*, 9761263.

[39] X. Xu, J. Luo, L. Li, D. Zhang, Y. Wang, G. Li, *Green Chem.* **2018**, *20*, 2038.

[40] G. Liu, H. Lv, Y. Zeng, M. Yuan, Q. Meng, Y. Wang, C. Wang, *Trans. Tianjin Univ.* **2021**, *27*, 139.

[41] L. Lv, Y. Shen, J. Liu, X. Meng, X. Gao, M. Zhou, Y. Zhang, D. Gong, Y. Zheng, Z. Zhou, *J. Phys. Chem. Lett.* **2021**, *12*, 11143.

[42] J.-X. Liu, D. Richards, N. Singh, B. R. Goldsmith, *ACS Catal.* **2019**, *9*, 7052.

Supporting Information

Sonication production of noble-metal single-atom catalysts for electrocatalytic nitrate reduction

Dazhi Yao[1], Yanzhao Zhang[1], Cheng Tang[1], Junyu Zhang, Bernt Johannessen[2], Shi-Zhang Qiao[1]*

*Corresponding author. Email: s.qiao@adelaide.edu.au

This PDF file includes:

1. Experimental Section

2. Supplementary Figure (Figure S1 to Figure S23)

3. Supplementary Table (Table S1)

1. Experimental Section

Chemicals and materials. Ammonia chloride (NH$_4$Cl, 99.998%), boron nitride (BN), chloroplatinic acid hydrate (H$_2$PtCl$_6 \cdot x$H$_2$O), concentrated hydrochloric acid (HCl, 36%), gold (III) chloride trihydrate (HAuCl$_4 \cdot$ 3H$_2$O), molybdenum(IV) sulfide (MoS$_2$), N-(1-Naphthyl)ethylenediamine dihydrochloride (>98%), sodium nitrite (≥97%), sulfanilamide (≥99%), palladium(II) oxide (PdO) , palladium(II) acetylacetonate(Pd(acac)$_2$), platinum(IV) oxide (PtO$_2$), platinum(II) acetylacetonate (Pt(acac)$_2$), potassium sulfate (K$_2$SO$_4$), potassium (KNO$_3$), silver nitrate (AgNO$_3$), potassium sodium tartrate hydrate (NaKC$_4$H$_4$O$_6 \cdot$4H$_2$O), para-(dimethylamino) benzaldehyde ((CH$_3$)$_2$NC$_6$H$_4$CHO, 99%), sodium nitroferricyanide (C$_5$FeN$_6$Na$_2$O, ≥ 99%), sodium hypochlorite (available chlorine 10–15 %), sodium salicylate (S3007, ≥ 99.5%), sodium tetrachloropalladate(II) (Na$_2$PdCl$_4$), sulfuric acid (H$_2$SO$_4$, ACS reagent, 95.0–98.0%), urea(CO(NH$_2$)$_2$), were purchased from Sigma-Aldrich Chemical Reagent Co. Ltd. Isopropanol (≥99.8%), sodium hydroxide (NaOH, anhydrous pellets, ≥98%), ethanol (99.9% AR), and concentrated nitric acid (HNO3, 70%) were ordered from Chem-Supply Pty. Ltd. Carbon paper and Nafion 117 membrane (Dupont) were purchased from Fuelcell store. Ultra-high purity Ar (99.999%) were supplied by BOC gas, Australia. Ultrapure water (18.2 MΩ·cm, PURELAB OptionQ) was used in all experiments. All chemicals were used in this work without further purification.

Synthesis of carbon nitride (C$_3$N$_4$). 10.0 g of urea was first ground in a mortar into fine urea powder. Then, the as-obtained powder was transferred into lidded crucibles in a muffle furnace. The powder was annealed at 550°C for four hours with a heating rate of 5°C min^{-1}. Once cooling down to room temperature, the product was washed with water three times, followed by centrifuging and drying at 70°C in the oven.

Synthesis of noble-metal single atom supported on the C$_3$N$_4$ (X-CN, X= Pd/Pt/Ag/Au). For a typical procedure, the synthesis of Pd-CN was followed by two steps. First, 50 mg of C$_3$N$_4$ was dispersed in 20 mL of deionized H$_2$O under ultrasound for 30 min. Then, 100 μL Na$_2$PdCl$_6$ aqueous solution (20 mM) was added to the above C$_3$N$_4$ dispersion, and the mixed solution was kept in vigorous stirring for around 16 h. The as-obtained dispersion was then collected by centrifugation, washed with water and ethanol three times, and re-dispersed into 30 mL nitrogen-saturated deionized water. The as-obtained dispersion was transferred into the nitrogen-filled airtight flask, followed by treatment in the ultrasound waves (40kHz; Branson ultrasonic bath) for 4 hours. The final product, Pt-CN, was collected by centrifugation, washed with water and ethanol, and freeze dried for future use. Other X-CN samples (i.e., Pd-CN, Ag-

CN, and Au-CN) were prepared using a similar method but with a change of noble-metal precursor H_2PtCl_6, $AgNO_3$ or $HAuCl_4$. The samples before and after ultrasonic treatment are named X-CN-a and X-CN-s respectively.

Synthesis of Pd single atom supported on the MoS₂ and BN (Pd-MoS₂/BN). Pd-MoS₂ and Pd-BN samples were prepared using a similar method as mentioned above, but the substrates were changed to cleaned MoS₂ and BN. The cleaned MoS₂ and BN were obtained from corresponding commercial samples and washed with water and ethanol.

Materials characterization. The crystal structure of the samples was characterized by powder X-ray diffraction spectroscopy (Rigaku MiniFlex 600 X-ray Diffractometer). The morphology was characterized by the transmission electron microscope (TEM, Philips CM 200, 200 kV). HADDF-STEM imaging and EDX mapping were taken on the FEI Titan Themis 80-200 (200 kV voltage) equipped with a Super-X high-sensitivity windowless EDX detector for rapid compositional analysis. XPS measurement was performed on a VGESCALAB 210 XPS spectrometer with Mg Kα source. The X-ray absorption spectra (XAS) were performed at the Australia Synchrotron, Clayton, Victoria, Australia (ANSTO). The XANES and EXAFS of the samples at Pd *K*-edge (24350 eV) were collected from 1.9 T Wiggler XAS beamline using liquid nitrogen-cooled Si (111) crystal at Hutch B experimental station (19−31 keV). Samples were mounted using standard sample holders and analysed at room temperature. Pd Foil and PdO standard samples were provided by ANSTO and used as references. All data of metal foils were obtained via transmission mode, while other samples were tested using fluorescence mode.

Electrochemical experiment. Electrochemical nitrate reduction performance was evaluated in a gas-tight standard three-electrode H-cell with the cathodic and anodic compartments separated by a Nafion 117 membrane. Nafion 117 membrane was preconditioned before use by boiling in 5% H_2O_2 solution and deionized water at 80 °C for 1 h, respectively, followed by treatment in 0.05 M H_2SO_4 for 3 h and deionized water for another 1h. A RuO_2 and a saturated Ag/AgCl electrode served as the counter and reference electrodes, respectively. All experiments were carried out at room temperature (25 °C). Potentials (E) in this study were calibrated to the RHE reference scale by E (V versus RHE) = E (V versus Ag/AgCl) + 0.0591 × pH + 0.217. The electrolyte was purged with ultrahigh purity Ar (99.999%) for 20 min before and during electrolysis.

Quantification of liquid products. In brief, the quantification of ammonia is based on the indophenol blue method. Chromogenic reagents were prepared according to our previous studies. For nitrite (NO_2^-) determination, 0.50 g of sulfanilamide was dissolved in 50.0 mL of 2.0 M HCl solution to prepare sulfanilamide solution (A). 20.0 mg of N-(1-Naphthyl) ethylenediamine dihydrochloride was then dissolved in 20.0 mL of deionized water to prepare N-(1-Naphthyl) ethylenediamine dihydrochloride solution (B). For UV-vis measurement of NO_2^-, 5.0 mL of sample solutions, 0.10 mL of A and 0.10 mL of B were mixed up for measurement. The ammonia and nitrite standard curves were established with the increase of the concentration of NH_4^+ and NO_2^- in the aqueous solution (Figure S19 and S20).

Qualification of gaseous H_2 products. Briefly, the headspace gas in the cathode chamber was injected into the gas chromatograph (Agilent 8890B GC) configured with a thermal conductivity detector (TCD) detector and flame ionisation detector (FID). The concentration of H_2 (ppm) is calculated by the peak area ratio according to the standard curve, calibrated by the customized standard gas supplied from BOC gas, Australia.

Isotope labelling testing and NMR determination. Isotope labelling tests were conducted using $K^{15}NO_3$ as the N-source. After electrolysis for 30 min at –0.8 V vs RHE in Ar-saturated 0.10 M $K^{15}NO_3$/0.50 M K_2SO_4 solution, the obtained electrolyte was acidified to a pH of 1. Then, 125 μL of the acidified electrolyte was mixed with 125 μL of D_2O and 750 μL of d_6-DMSO and then determined by ^1H nuclear magnetic on a Bruker Ascend 600 MHz system with water suppression.

2. Supplementary Figures
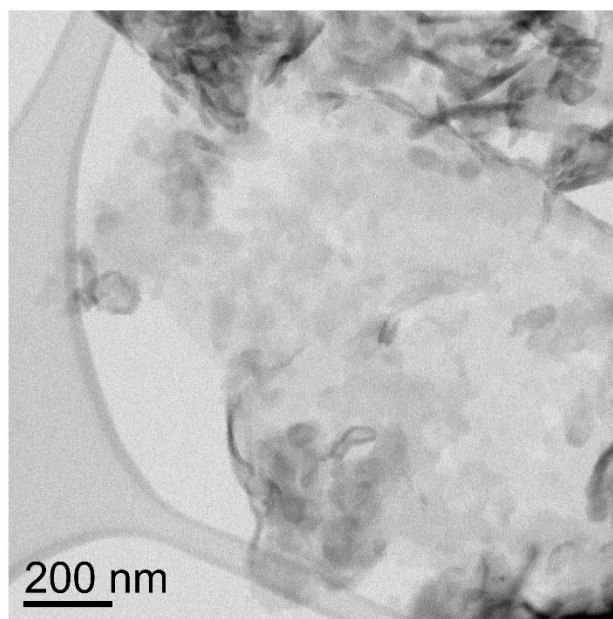
Figure S1. High-resolution TEM image of the pristine C_3N_4 nanosheet.
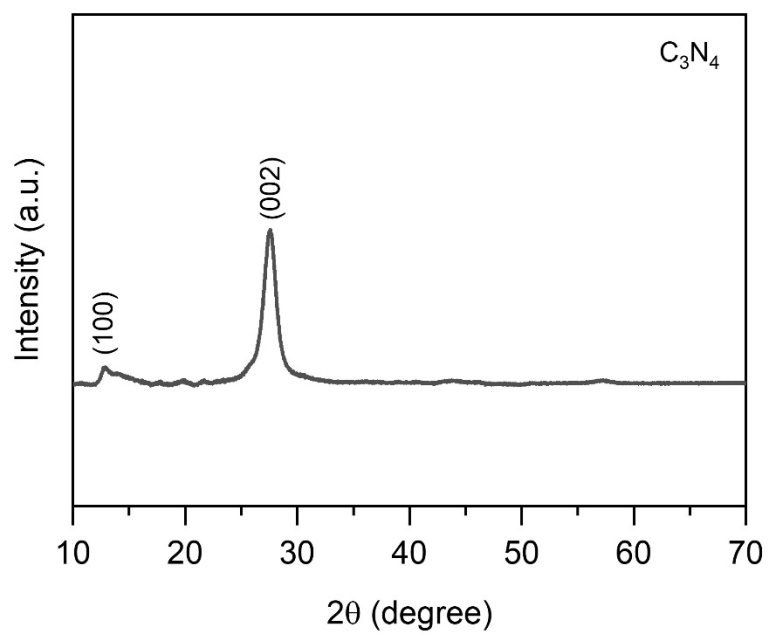
Figure S2. XRD pattern of the as-obtained C_3N_4.
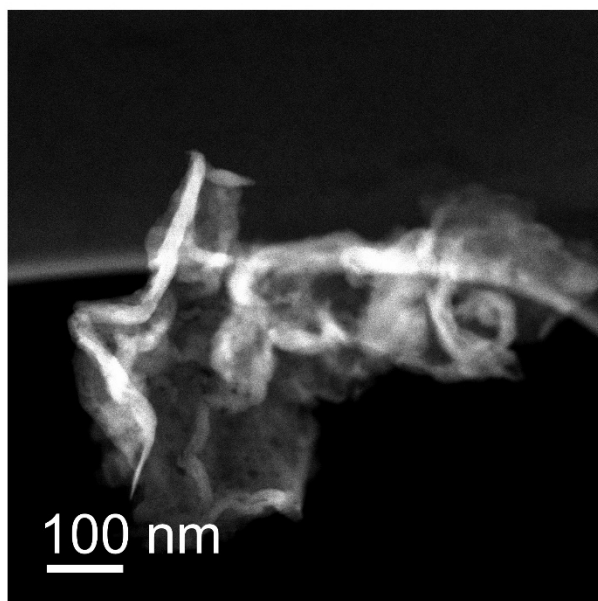
Figure S3. The typical STEM image of the as-obtained Pd-CN-s sample.
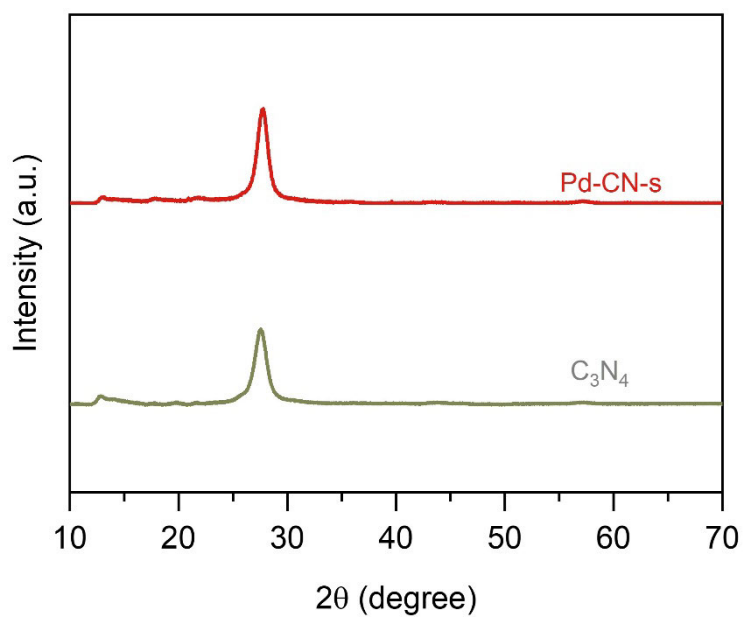
Figure S4. XRD pattern of Pd-CN-s in comparison to that of C_3N_4.
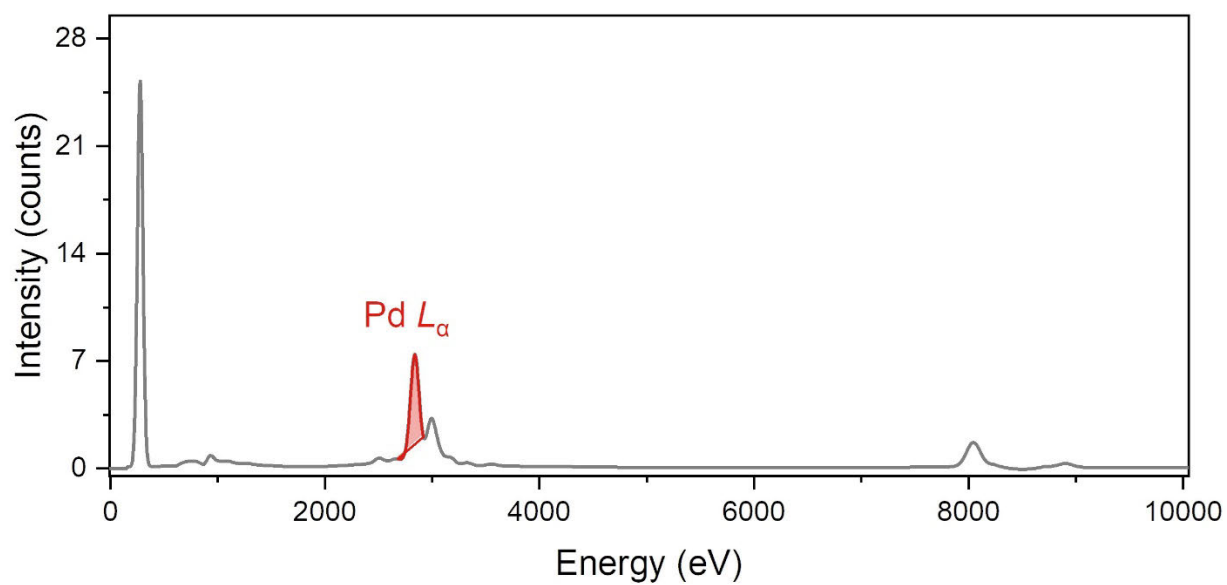
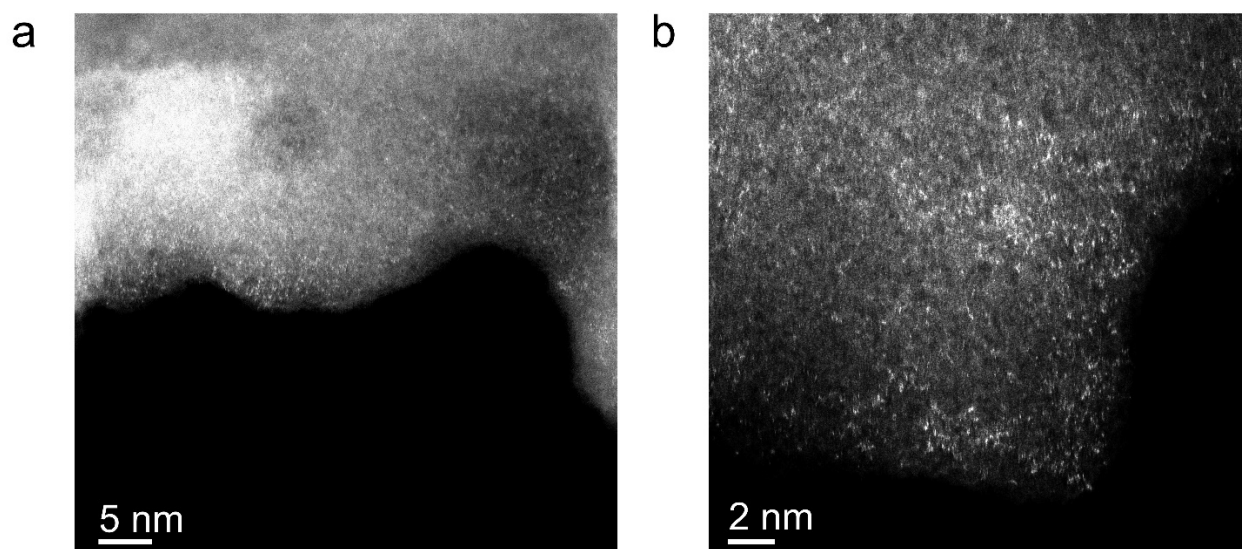**Figure S5.** EDS spectrum of the Pd-CN-s sample, highlighting the presence of the Pd element.
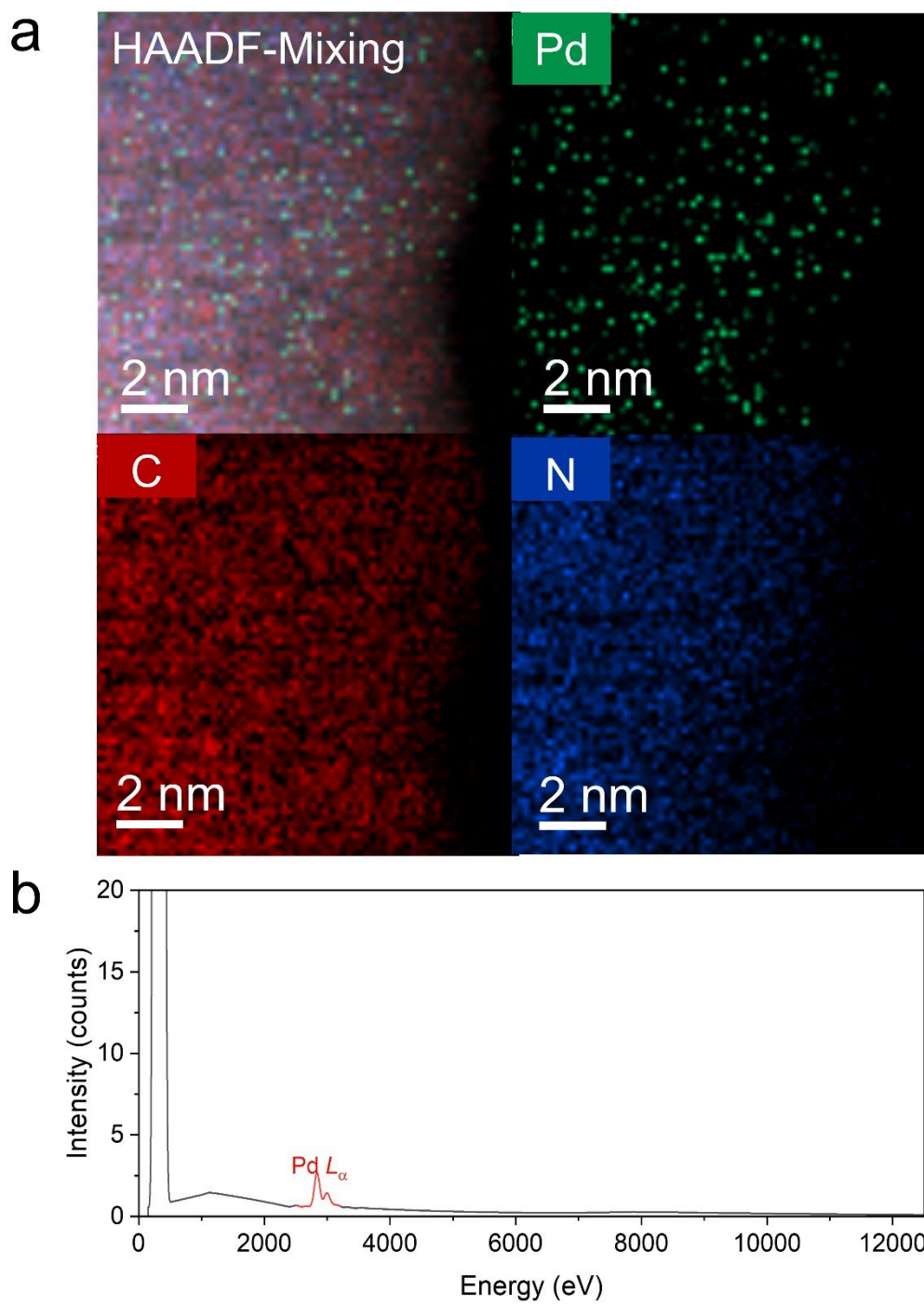

Figure S6. HAADF-STEM images of the Pd-CN-a samples at different areas.

Figure S7. (a) EDS mapping and (b) EDS spectrum of the Pd-CN-a sample. The presence of the Pd element before sonication treatment confirms the origin and necessity of the adsorption-trapping process.
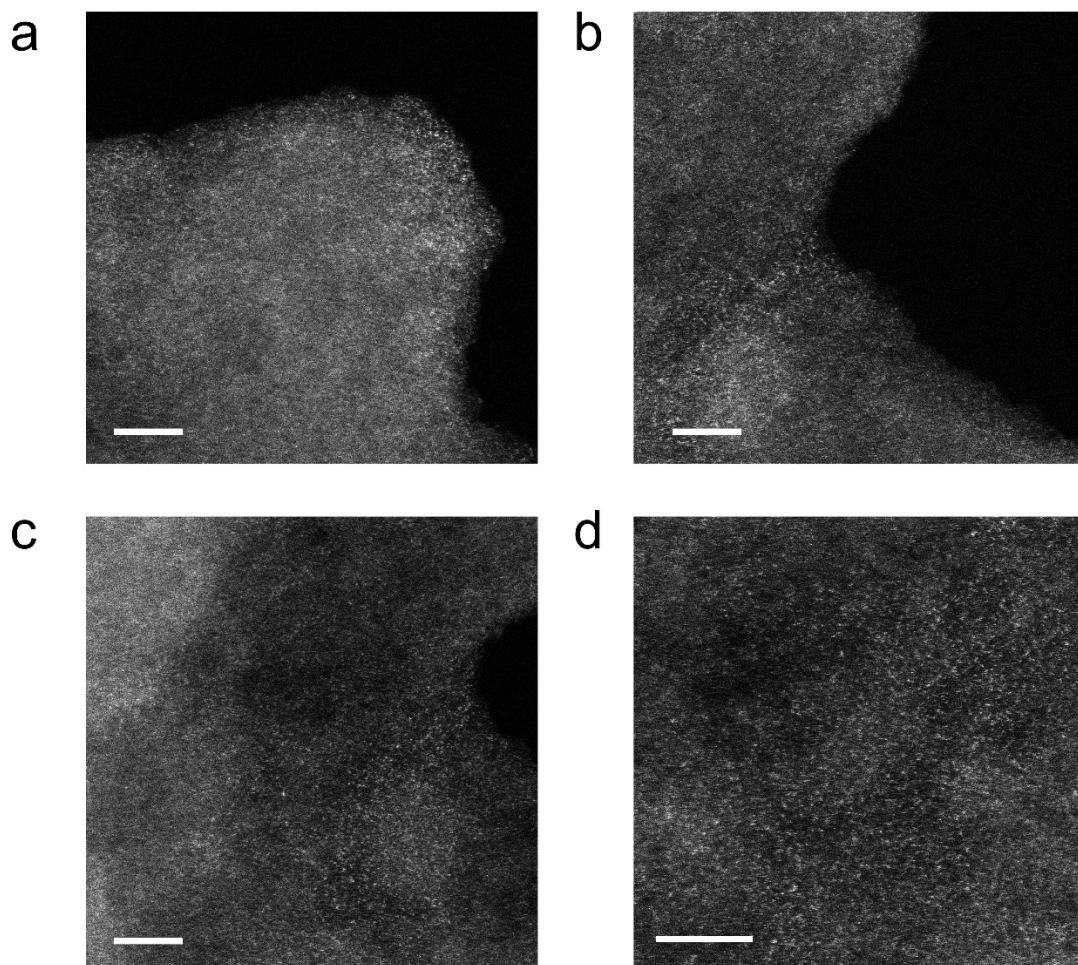
Figure S8. HAADF-STEM pictures of Pd-CN-a imaged from (a, b) the edge area of a thick sheet to (c, d) its inner part, indicating the uniform distribution of Pd atoms on the matrix. The scale bar in each figure is 5 nm.
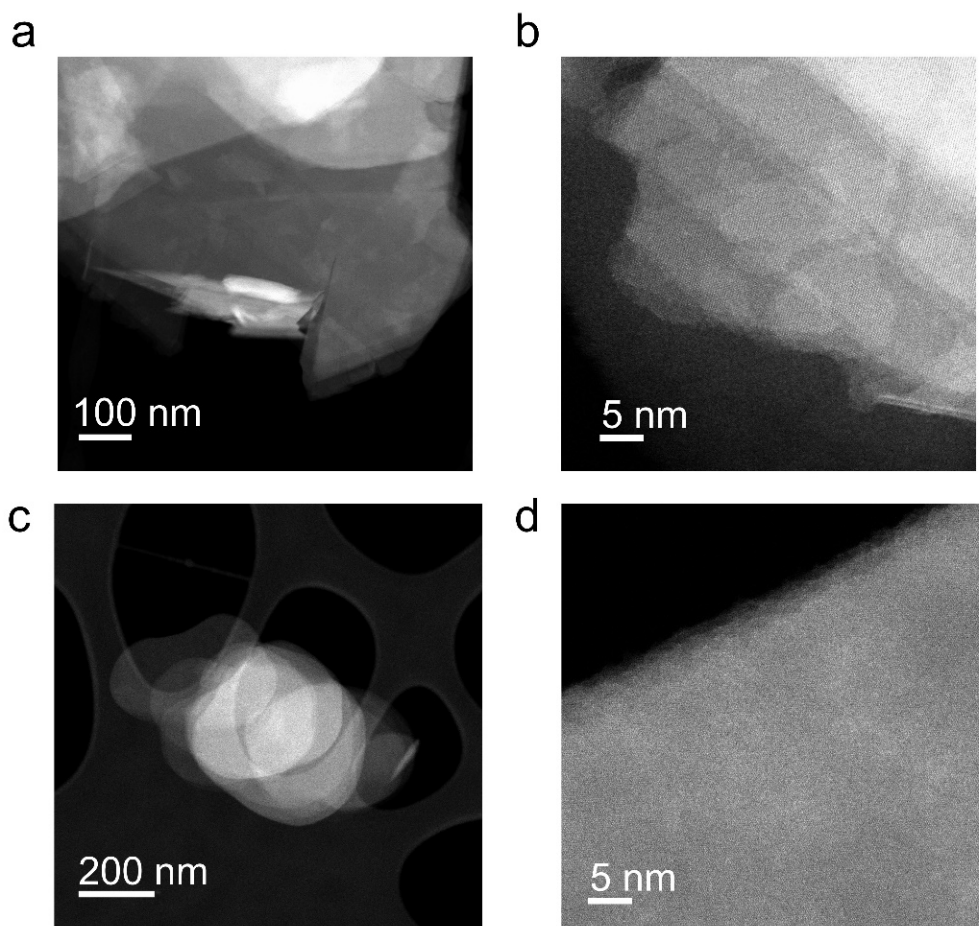
Figure S9. HAADF-STEM images of (a,b) MoS_2 and (c, d) BN in different magnification. Samples are obtained from commercial suppliers (sigma-aldrich) and are not purified or treated.
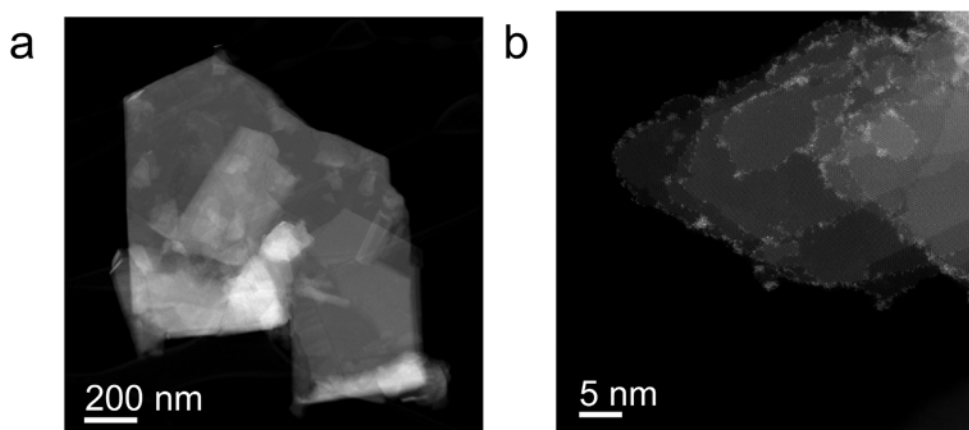
Figure S10. HAADF-STEM images of the Pd-MoS_2-s sample in different magnification.
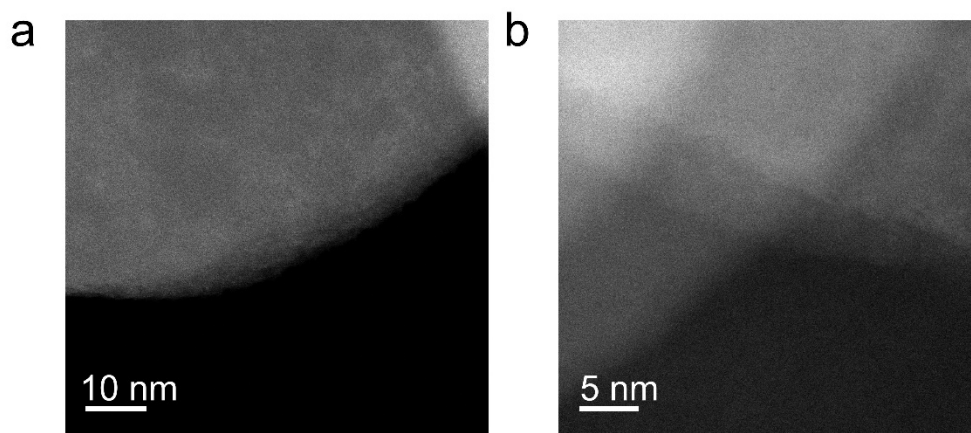
Figure S11. HAADF-STEM images of the Pd-BN-s sample in different magnification. No contrasted spots in the images denote the absence of Pd atoms hosted on the BN.
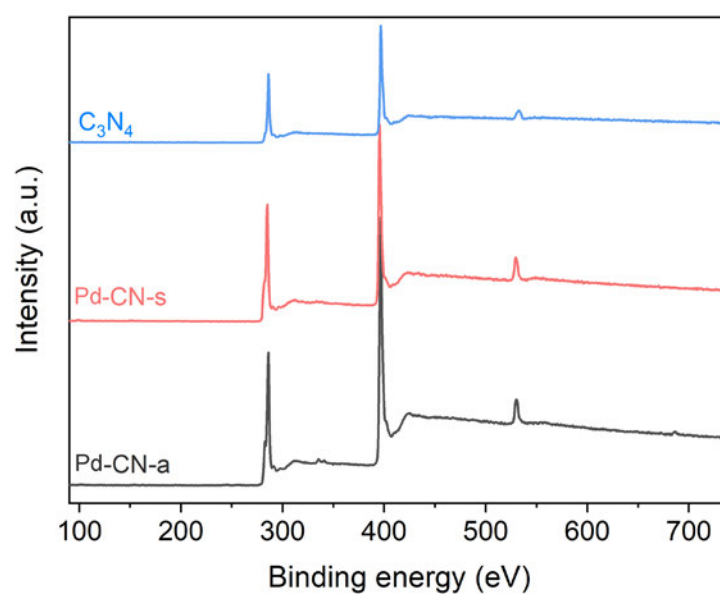
Figure S12. XPS surveys of the C_3N_4, Pd-CN-a, and Pd-CN-s samples/
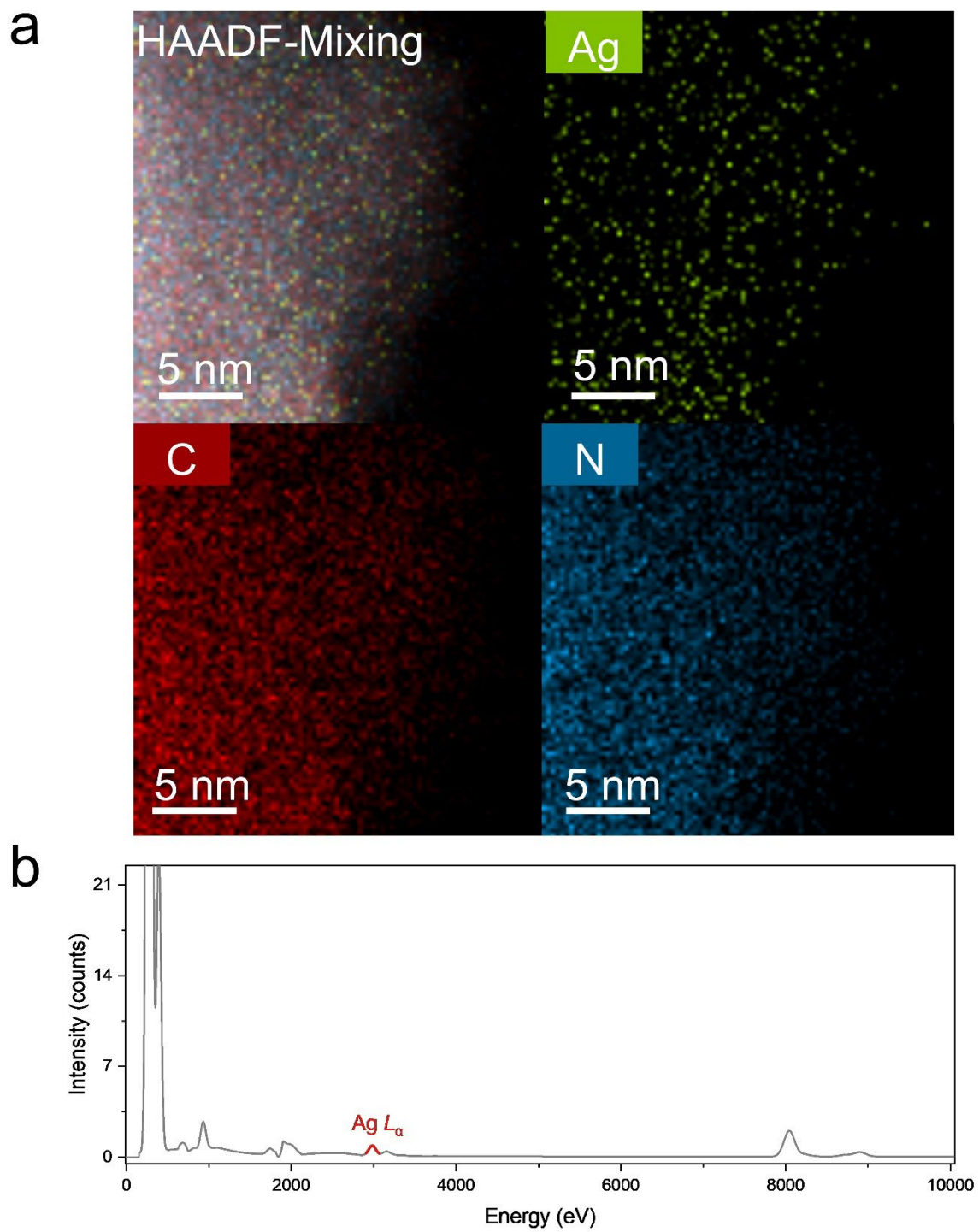
Figure S13. (a) EDS mapping and (b) EDS spectrum of the Ag-CN-s sample.
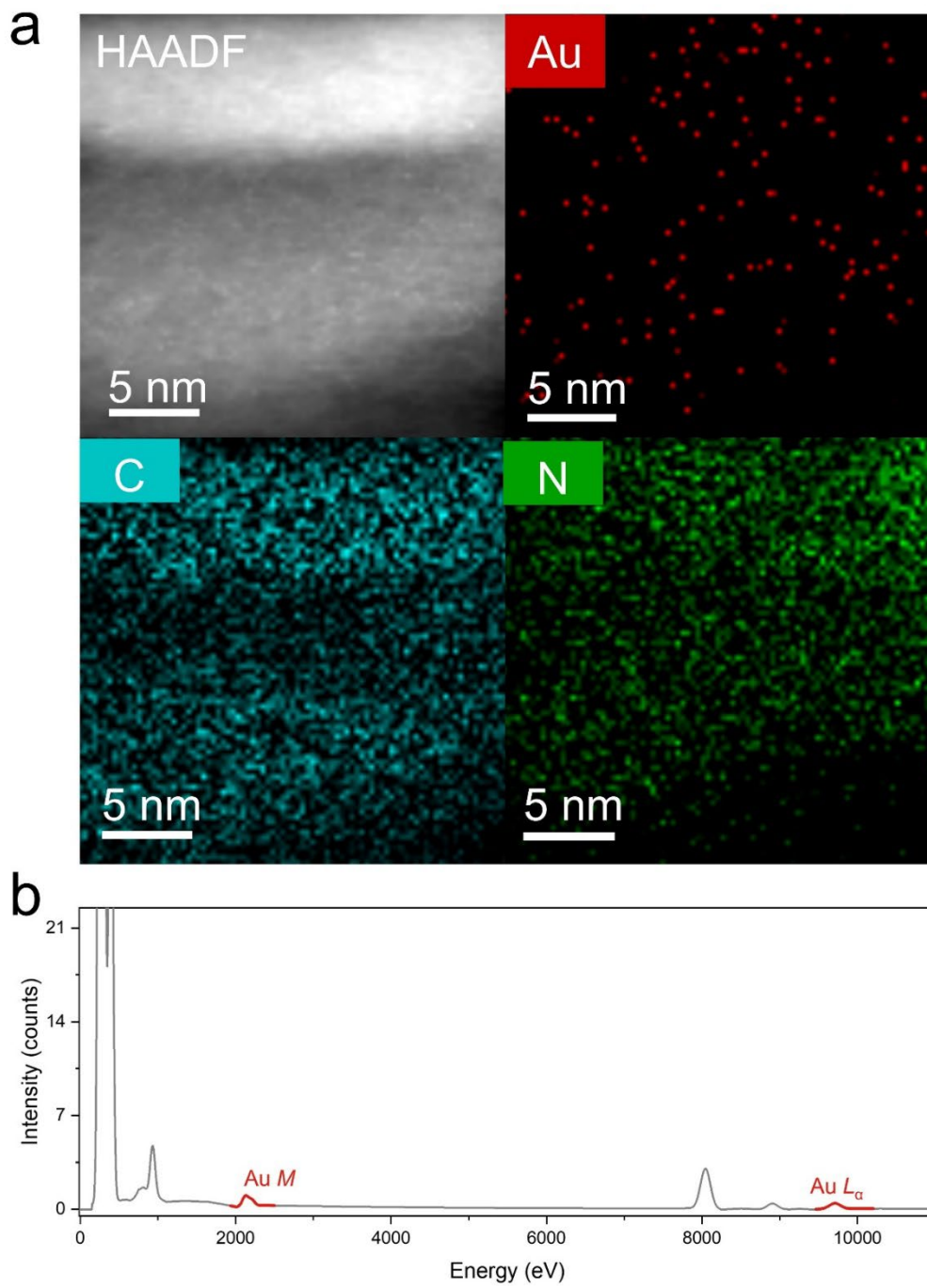
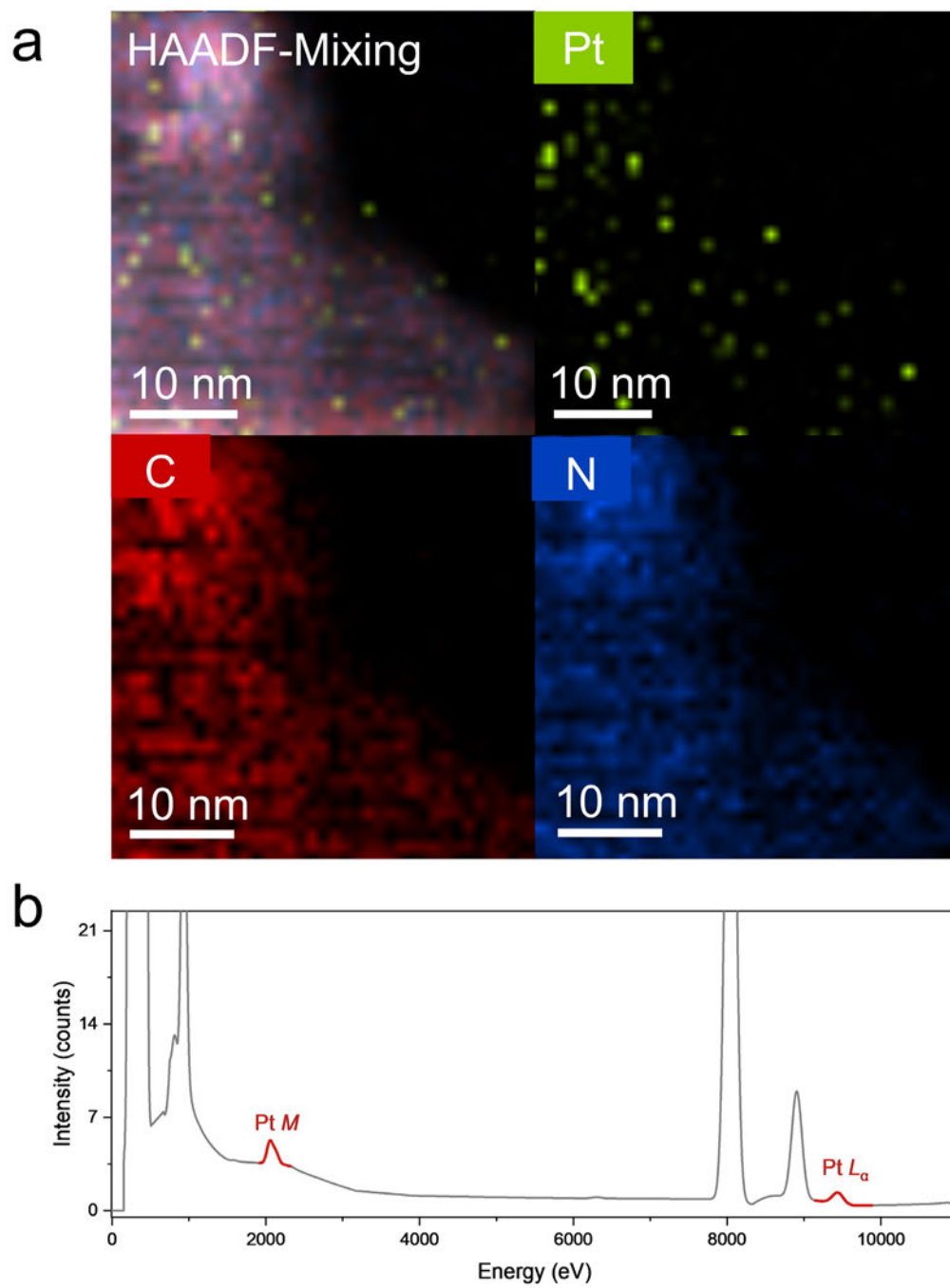**Figure S14.** (a) EDS mapping and (b) EDS spectrum of the Au-CN-a sample.

Figure S15. (a) EDS mapping and (b) EDS spectrum of the Pt-CN-a sample.
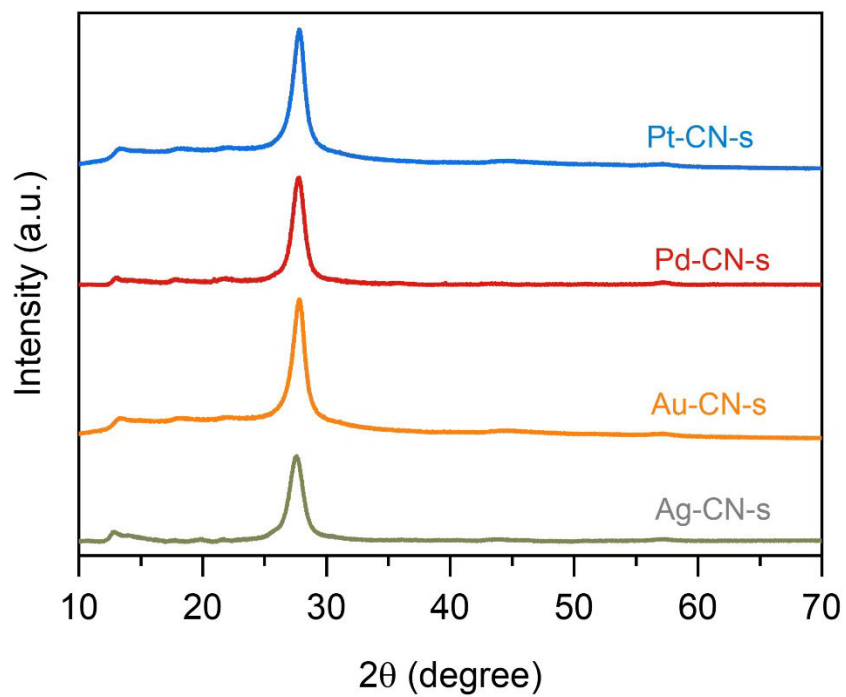
Figure S16. XRD patterns of the as-obtained Pt-CN-s, Au-CN-s and Ag-CN-s, in comparison to that of Pd-CN-s.
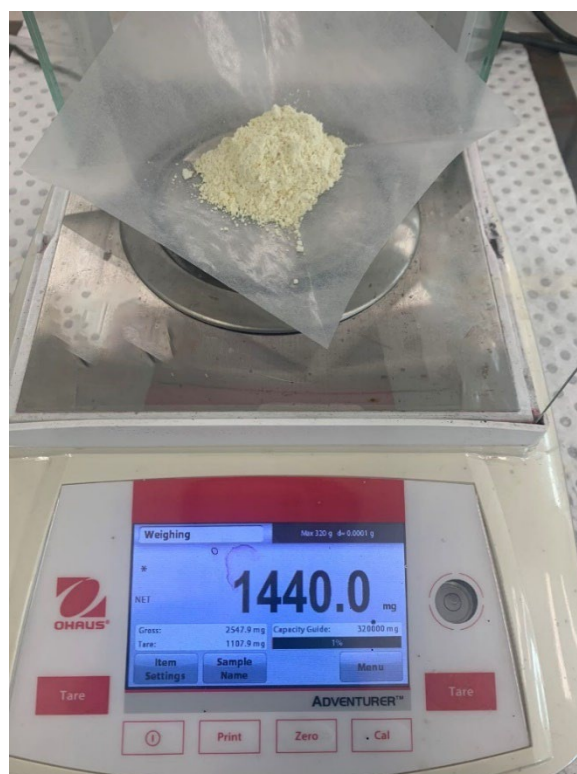
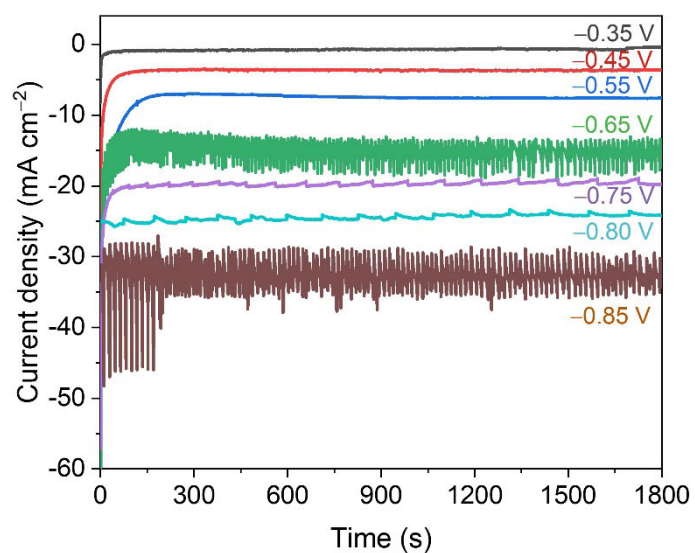**Figure S17.** The photograph for Pd-CN-s synthesized in large scale.

Figure S18. Chronoamperometry responses of Pt-CN-s at different applied potentials in Ar-saturated 0.50 M K_2SO_4 with the addition of 0.10 M KNO_3.
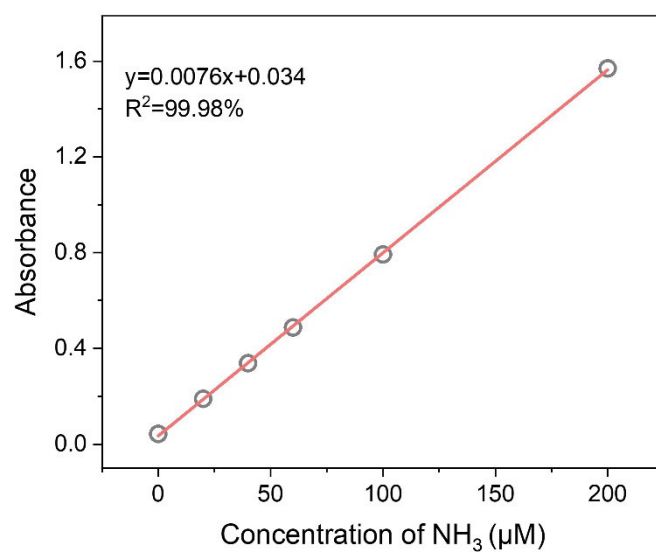
Figure S19. Standard curve for NH4Cl solution with different concentrations in 0.50 M K2SO4 by indophenol blue colorimetric method. Corresponding linear fitting between absorbance and NH4Cl concentration is inserted.
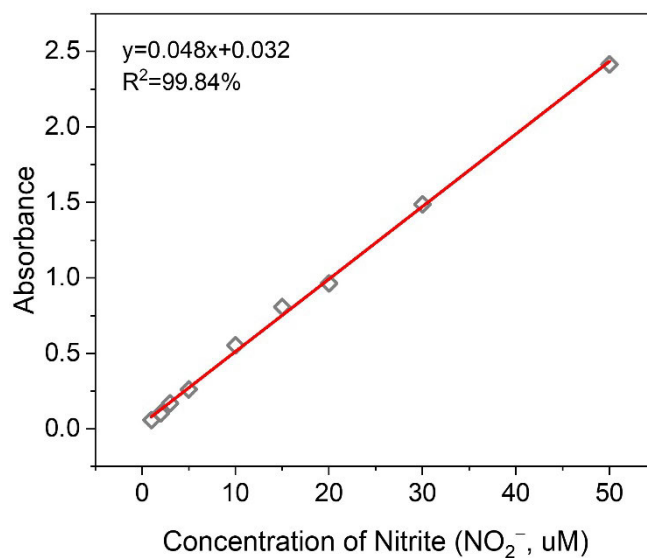

Figure S20. Standard curve for NaNO2 solution with different concentrations in 0.50 M K2SO4 by indophenol blue colorimetric method. Corresponding linear fitting between absorbance and nitrite (NO_2^-) concentration is inserted.
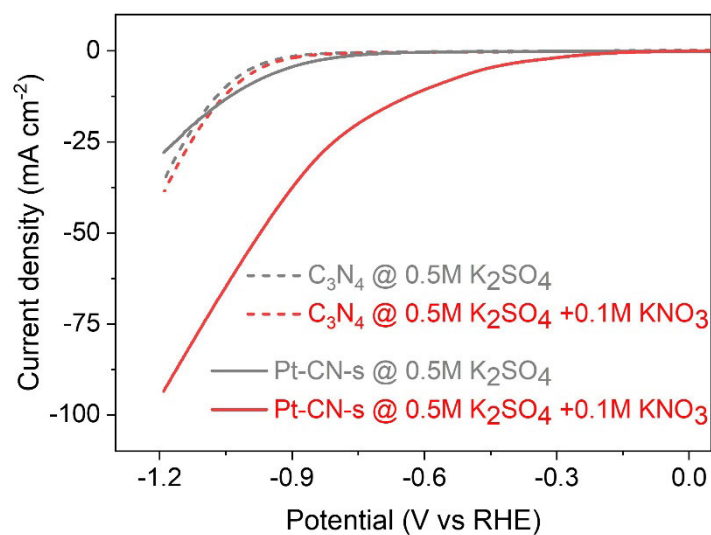
Figure S21. LSV curves for C_3N_4 and Pt-CN-s in Ar-saturated 0.50 M K_2SO_4 with the absence of 0.10 M KNO_3 (grey line) and addition of the 0.10 M KNO_3 (red line).
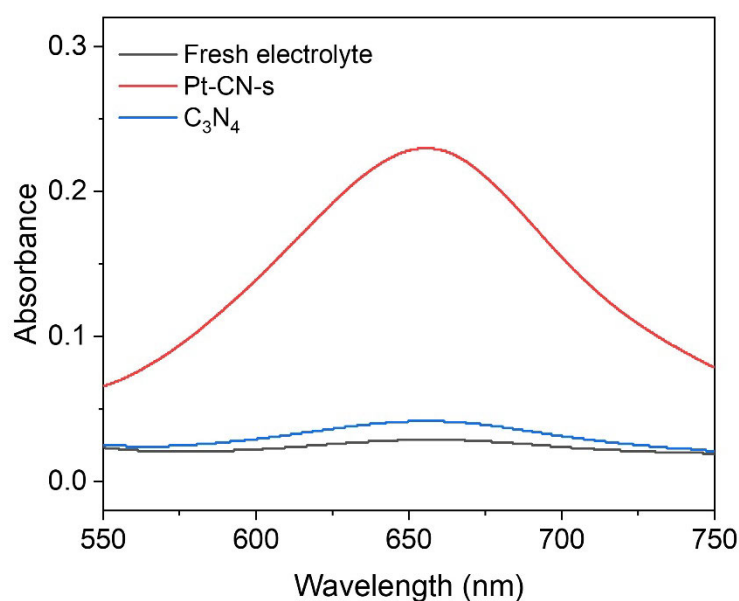

Figure S22. UV–vis spectra of cathodic electrolytes stained with indophenol indicator for control tests. Electrolysis of C_3N_4 in the 0.1M KNO_3/0.5M K_2SO_4 solution at −0.8 V vs RHE for 30 min brings about a negligible amount of ammonia. The cathodic electrolyte for Pt-CN-s was diluted 10 times before the colormetric assay.
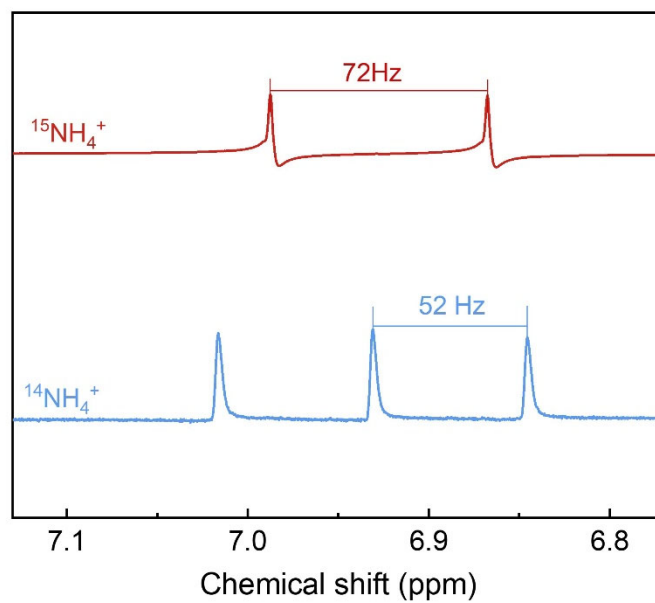
Figure S23. ^1H NMR spectra of $^{14}NH_4^+$ and $^{15}NH_4^+$ produced from NitRR of Pt-CN-s at −0.8 V vs RHE on using $K^{14}NO_3$ and $K^{15}NO_3$ as the feeding source, respectively.

3. Supplementary Table

Table S1. The metal mass loading of X-CN-s samples determined by ICP-MS.

Sample	Metal content (wt.%)
Pd-CN-s	1.47
Pt-CN-s	1.10
Au-CN-s	0.98
Ag-CN-s	1.25

Chapter 7

Conclusions and Outlooks

7.1 Conclusions

This Thesis aimed to develop the rational design and synthesis of nanomaterials for electrocatalytic N_2 and CO_2 reduction to produce value-added chemicals. Mechanistic investigations of electrocatalytic processes and "structure-to-performance" correlation are also included. On the basis of the works in this Thesis, the following conclusions are drawn:

1. The fragmented Bi^0 nanoparticles exhibit excellent NRR performance in both neutral and acidic electrolytes, with an ammonia yield of 3.25 ± 0.08 μg cm^{-2} h^{-2} at –0.7 V versus RHE and a Faradaic efficiency of $12.11 \pm 0.84\%$ at –0.6 V in 0.10 M Na_2SO_4. Online differential electrochemical mass spectrometry detects the production of NH_3 and N_2H_2 during NRR, suggesting a possible pathway through two-step reduction and decomposition.

2. The intricate reconstruction process of Bi-MOFs prior to CRR can be decoupled into two steps: electrolyte-mediated conversion of Bi-MOF NR to $Bi_2O_2CO_3$ by bicarbonate-initiated ligand substitution, and potential-mediated reduction of $Bi_2O_2CO_3$ to Bi. The first step controls the final morphology and defects, whilst the second step determines the final composition and valence states. For example, tuning the bicarbonate concentration can produce $Bi_2O_2CO_3$ and Bi with different thickness and catalytic performance. In situ reconstructed Bi NS with thickness of 3.5 nm achieved a FE of 92% towards formate production and was stable under operating conditions. Abundant unsaturated Bi atoms were formed adjacent to the surface vacancies during the two-step reconstruction, contributing to more favourable adsorption of *OCHO intermediates and ultimately benefiting the reaction process.

3. By taking NiCu-NC as an example, Ni and Cu atoms featuring the threshold distance of 5.3 Å exhibited non-bonding interaction but synergistically regulated the electronic structure and promoted intermediate adsorption, thus boosting the activity and selectivity of CO_2 electroreduction. The threshold-distributed NiCu-NC DACs

exhibited a low onset potential (300 mV) and a wide potential window of ~ 800 mV for selective CO_2 reduction to CO (> 80%), with a maximum FE of ~98% at -1.07 V vs RHE in 0.1 M $KHCO_3$. The random distribution simulation and mathematical analysis also revealed an effective macro-descriptor to correlate the inter-metal distance with structure features, such as the substrate thickness and metal loading.

4. A simplistic and effective method for synthesis of SACs under ambient conditions based on the "adsorption-sonication" strategy successfully achieved noble-metal atoms supported on the C_3N_4 matrix (X-CN, X = Pd, Pt, Au, and Ag). A two-step synthetic route is revealed by ex situ STEM and XPS characterizations. The capture of metal precursors through an active site is the prerequisite, while the following sonication treatment realizes the atomic binding, thus facilitating their large-scale preparation at mild temperature. As an example, the electrocatalytic nitrate reduction performance was studied on the as-obtained Pt-CN-s. By rigid blank experiment and isotope labelling testing, the Pt-CN-s achieved the maximized FE for ammonia of 80.42% at -0.45 V versus RHE and the highest ammonia yield of 10.65 μmol cm^{-2} h^{-1} at -0.8 V in 0.1 M KNO_3 + 0.5 M K_2SO_4 electrolyte. The onset potential of around -0.30 V versus RHE and long-term stability of 8 h on the presence of KNO_3 electrolyte denote the potential application of SACs in future green ammonia production.

In summary, these systematic studies in this Thesis shed light on the development of efficient electrocatalysts towards the production of portable fuels and value-added chemicals. By advanced characterizations, deep investigation of structure and elaborate mechanism studies, "structure-to-performance" correlations are also established to guide future design of optimized electrocatalysts and achieve promising performance.

7.2 Outlooks

Although extensive studies have been conducted and many strategies have been proposed for designing effective electrocatalysts on NRR and CRR toward value-added chemical productions, additional works are required to further develop and establish e-refinery for the sustainable production of fuels and value-added chemicals.

1. The investigation of some new aspects beyond materials science is believed to make breakthroughs in NRR, including the use of non-aqueous electrolytes, the regulation of ion effects, the design of Li-mediated pathway, and the operation under pressure and in flow cells.

2. The exploration of other electrocatalytic nitrogen transformation reactions are beneficial for both green NH_3 synthesis and nitrogen cycle closing, such as the oxidation of nitrogen to nitrate and nitric oxide. Alternative catalysis processes, such as plasma catalysis, bio-electrocatalysis, redox-mediated electrocatalysis, and photocatalysis offer new opportunities to address the challenge of N_2 activation and innovate the reaction process design.

3. The precise study and modulation on the structure of single-atom catalysts are of great importance. Particularly, their formation process, controlled by the precursor amount, reaction conditions, along with the dynamic change under working conditions, should be shed light on. Hopefully, with the advancement of in/ex situ characterization tools, more systematic understandings could be achieved to guide the rational design and development of atomically-dispersed catalysts, and clarify their "structure-to-performance" correlations (for example, the relationship between loading amount and their performance).

4. Reactor and electrolyte engineering may provide new solutions to obtain higher performance CRR. Detailed investigation of issues in the application of flow-cell in CRR, the optimization of the cell and optimizing the electrolyte can further improve

the performance and the stability of CRR. Developing CRR in the acid medium can effectively overcome the CO_2 loss and carbonate accumulations in CO_2 electrolyzers.

5. By coupling in situ generated intermediates or products, integrated reactions and tandem reactions can extend the framework of e-refinery. For examples, using in situ electrocatalytically generated Cl_2 and H_2O_2 species for sequential oxidation reactions have been verified as one effective pathway to fulfil propylene oxide and peroxyacetic acid productions.

Appendix: Publications During the PhD candidature

[1] **D. Yao**, C. Tang, A. Vasileff, X. Zhi, Y. Jiao, S. Z. Qiao The Controllable Reconstruction of Bi-MOFs for Electrochemical CO_2 Reduction through Electrolyte and Potential Mediation, ***Angew. Chem. Int. Ed.***, 2021, *60*, 18178.

[2] **D. Yao**, C. Tang, L. Li, B. Xia, A. Vasileff, H. Jin, Y. Zhang, S. Z. Qiao, In Situ Fragmented Bismuth Nanoparticles for Electrocatalytic Nitrogen Reduction, ***Adv. Energy Mater.***, 2020, *10*, 2001289.

[3] **D. Yao**, C. Tang, P. Wang, H. Cheng, H. Jin, L. X, Ding, S. Z. Qiao, Electrocatalytic Green Ammonia Production Beyond Ambient Aqueous Nitrogen Reduction, ***Chem. Eng. Sci.***, 2022, *257*, 117735.

[4] **D. Yao**, C. Tang, X. Zhi, B. Johannessen, A. Slattery, S. Chern, S. Z. Qiao, Inter-metal interaction with a threshold effect in NiCu dual-atom catalysts for CO_2 electroreduction, ***Adv. Mater.***, 2022, **accepted**. DOI: 10.1002/ adma.202209386.

[5] **D. Yao**, Y. Zhang, C. Tang, J. Zhang, B. Johannessen, S. Z. Qiao, Sonication production of noble-metal single-atom catalysts for electrocatalytic nitrate reduction, ***In preparation***.

[6] F. Xie, X. Cui, X. Zhi, **D. Yao**, B. Johannessen, Q. Zhang, J. Tang, T. Woodfield, Gu L., S. Z. Qiao, A General Approach to 3D Printed Single Atom Catalysts, ***Nat. Synth.***, 2022, **accepted**. DOI: 10.1038/s44160-022-00193-3.

[7] L. Li, C. Tang, **D. Yao**, Y. Zheng, S. Z. Qiao, Electrochemical nitrogen reduction: identification and elimination of contamination in electrolyte, ***ACS Energy Lett.***, 2019, *4*, 2111.

[8] Y. Zhang, **D. Yao**, B. Xia, M. Jaroniec, J. Ran, S. Z. Qiao, Photocatalytic CO_2 Reduction: Identification and Elimination of False-Positive Results, ***ACS Energy Lett.***, 2022, *7*, 1611.

[9] Y. Zhang, **D. Yao**, B. Xia, H. Xu, Y. Tang, K. Davey, J. Ran, S. Z. Qiao, ReS_2 Nanosheets with In Situ Formed Sulfur Vacancies for Efficient and Highly Selective Photocatalytic CO_2 Reduction, ***Small Sci.***, 2021, *1*, 2000052